



Jere Elfving

**DIRECT CAPTURE OF CO₂ FROM AIR USING
AMINE-FUNCTIONALIZED RESIN -
EFFECT OF HUMIDITY IN MODELLING AND
EVALUATION OF PROCESS CONCEPTS**



Jere Elfving

**DIRECT CAPTURE OF CO₂ FROM AIR USING
AMINE-FUNCTIONALIZED RESIN -
EFFECT OF HUMIDITY IN MODELLING AND
EVALUATION OF PROCESS CONCEPTS**

Dissertation for the degree of Doctor of Science (Technology) to be presented with due permission for public examination and criticism in the Auditorium 103 of the Student Union House at Lappeenranta-Lahti University of Technology LUT, Lappeenranta, Finland on the 17th of December, 2021, at noon.

Acta Universitatis
Lappeenrantaensis 1004

Supervisors Professor Tuomo Sainio
LUT School of Engineering Science
Lappeenranta-Lahti University of Technology LUT
Finland

Dr. Cyril Bajamundi
Soletair Power Ltd.
Finland

Reviewers Professor Marco Mazzotti
Department of Mechanical and Process Engineering
ETH Zurich
Switzerland

Assistant Professor Matteo Gazzani
Copernicus Institute of Sustainable Development
Utrecht University
Netherlands

Opponent Professor Arvind Rajendran
Chemical and Materials Engineering Department
University of Alberta
Canada

ISBN 978-952-335-764-8
ISBN 978-952-335-765-5 (PDF)
ISSN-L 1456-4491
ISSN 1456-4491

Lappeenranta-Lahti University of Technology LUT
LUT University Press 2021

Abstract

Jere Elfving

Direct capture of CO₂ from air using amine-functionalized resin - Effect of humidity in modelling and evaluation of process concepts

Lappeenranta 2021

125 pages

Acta Universitatis Lappeenrantaensis 1004

Diss. Lappeenranta-Lahti University of Technology LUT

ISBN 978-952-335-764-8, ISBN 978-952-335-765-5 (PDF), ISSN-L 1456-4491, ISSN 1456-4491

Direct air capture (DAC) using adsorbents is a promising negative emissions technology if coupled with CO₂ storage and is a viable option as a CO₂ source for producing truly carbon-neutral synthetic fuels. However, if this technology is to become a serious climate change mitigation tool with the capture potential of several Gt_{CO₂}/year, the cost needs to decrease significantly. To achieve this, the material and energy requirements of the process need to be minimized by adsorbent development and process design. Most of the developments in the field of DAC have focused on the synthesis of novel adsorbents, while some of the other aspects of the process have been less studied. This thesis aims to fill some of these gaps in DAC process research.

In this work, the performance of an amino resin for CO₂ capture was studied experimentally in a wide range of conditions. Humidity and cold conditions were found to nearly double the experimental CO₂ adsorption capacity of the studied amino resin in some cases. Based on a working capacity analysis using isotherm modelling, the typically proposed DAC process using temperature and vacuum swing adsorption (TVSA) with a closed inlet is severely limited in terms of CO₂ working capacity.

Using an improved fixed-bed experimental setup with automatic operation, a detailed comparison of DAC regeneration processes was carried out. By using a purge gas such as air in TVSA, CO₂ productivity was significantly increased. This method was also advantageous in terms of the specific energy requirement and adsorbent stability compared to the TVSA process with closed inlet. Therefore, in applications that do not require pure CO₂ such as greenhouses or microbial cultivation, using inert purge gas or air is beneficial in adsorbent regeneration.

A novel kinetic model was developed that takes into account the effect of humidity in CO₂ adsorption on amine-functionalized adsorbents. Using this model, humid CO₂ isotherms and adsorption column dynamics were accurately modelled. The kinetic model can be expected to be generally useful in DAC process modelling, and ultimately in DAC process design and optimization.

Keywords: direct air capture, CO₂ adsorption, adsorption isotherm, adsorbent regeneration, kinetic model

Acknowledgements

First of all, I'd like to thank three people who gave me the opportunity to start my scientific career at VTT: Dr. Jouni Hämäläinen for all his support and trust, Dr. Pasi Vainikka for letting me be a part of the Neo-Carbon Energy project, and my second supervisor Dr. Cyril Bajamundi for his guidance and help which was especially important at the start of this process. This dissertation is based on research carried out in VTT during 2015-2021 in several projects, supported by the funding from Tekes (now Business Finland) and Academy of Finland.

Thanks to my first supervisor Prof. Tuomo Sainio for his excellent guidance to steer this work in the right direction. The adsorption-filled discussions with him were always something I looked forward to. Acknowledgements also to the reviewers of this work, Prof. Marco Mazzotti and Ass. Prof. Matteo Gazzani.

I'd also like to acknowledge all the people at VTT and LUT University who helped me in this process and with whom I've had the pleasure to have useful and interesting discussions with, work-related and otherwise. Especially, I'd like to thank Juho Kauppinen for the great help and innovativeness in the development and building of the experimental devices that made this work possible. I'd also like to acknowledge Kari Paakkinen, Juha Knihtinen, Jukka Sulin-Saaristo and Ismo Pietikäinen for the help in the practical design and implementation of the second experimental setup used in this work. Thanks also to Mikko Jegoroff at VTT and Vesa Ruuskanen and Lauri Järvinen at LUT for implementation of the control software of the experimental setup. Moreover, I'd like to acknowledge Prof. Satu-Pia Reinikainen and the technical and research staff at the Chemical Technology Unit at LUT University for helping to gather and analyse the data related to the structural characterization of the adsorbent.

Finally, my deepest gratitude goes to my family and friends who have supported me during this time. I'm especially grateful to my wife for her unwavering support and love during these years.

Jere Elfving
December 2021
Jyväskylä, Finland

Contents

Abstract

Acknowledgements

Contents

List of publications **9**

Other publications **10**

Nomenclature **11**

1 Introduction **15**

- 1.1 CO₂ capture, storage and utilization..... 16
- 1.2 Direct air capture (DAC)..... 18
 - 1.2.1 DAC technologies 18
 - 1.2.2 DAC in climate change mitigation..... 19
- 1.3 Objectives and novelty 22
- 1.4 Thesis structure..... 22

2 Review of adsorbent-based direct air capture **25**

- 2.1 Adsorbent materials..... 25
 - 2.1.1 Supported amine adsorbents 25
 - 2.1.2 Amine-impregnated adsorbents 27
 - 2.1.3 Amine-grafted adsorbents 29
 - 2.1.4 Stability of amine-based adsorbents 31
 - 2.1.5 Other adsorbents 33
- 2.2 The adsorbent-based DAC process 36
 - 2.2.1 Process types in CO₂ adsorption 36
 - 2.2.2 Cost and specific energy requirement..... 39
 - 2.2.3 Alternative process configurations..... 43
 - 2.2.4 DAC process research gaps..... 44

3 Experimental and modelling methods **45**

- 3.1 Experimental methods 45
 - 3.1.1 Adsorbent characterization 45
 - 3.1.2 Fixed-bed CO₂/H₂O adsorption setup (Articles I-II) 45
 - 3.1.3 Automatic adsorption/desorption device (Articles III-IV)..... 47
 - 3.1.4 Adsorption/desorption experiments 48
 - 3.1.5 CO₂/H₂O capacity calculation..... 51
- 3.2 Calculation and modelling methods 54
 - 3.2.1 Isotherm models and working capacity analysis..... 55
 - 3.2.2 Specific energy requirement of regeneration (Article III) 57
 - 3.2.3 Kinetic CO₂ adsorption model (Article IV) 59

3.2.4	Dynamic CO ₂ adsorption model (Article IV)	61
4	Results and discussion	67
4.1	Physicochemical structure of the adsorbent (Article I)	67
4.2	CO ₂ /H ₂ O adsorption isotherms	69
4.2.1	Single-component CO ₂ /H ₂ O isotherms (Articles I-II, IV).....	69
4.2.2	CO ₂ isotherms with the effect of humidity (Article IV)	74
4.3	Working capacity analysis (Articles I-II)	78
4.4	Experimental regeneration method comparison (Article III)	80
4.4.1	CO ₂ working capacity	81
4.4.2	Regeneration energy and CO ₂ productivity	83
4.4.3	Cyclic adsorption/desorption tests	85
4.5	Dynamic modelling of CO ₂ adsorption from humid air (Article IV).....	88
5	Conclusions	97
	References	101
	Appendix A: Literature adsorbent data	123
	Publications	

List of publications

This dissertation is based on the following articles. The rights have been granted by the publishers to include the articles in this dissertation.

- I. Elfving, J., Bajamundi, C., and Kauppinen, J. (2017). Characterization and performance of direct air capture sorbent. *Energy Procedia*, 114, pp. 6087-6101.
- II. Elfving, J., Bajamundi, C., Kauppinen, J., and Sainio, T. (2017). Modelling of equilibrium working capacity of PSA, TSA and TVSA processes for CO₂ adsorption under direct air capture conditions. *Journal of CO₂ Utilization*, 22, pp. 270-277.
- III. Elfving, J., Kauppinen, J., Jegoroff, M., Ruuskanen, V., Järvinen, L., and Sainio, T. (2021). Experimental comparison of regeneration methods for CO₂ concentration from air using amine-based adsorbent. *Chemical Engineering Journal*, 404, pp. 126337.
- IV. Elfving, J., and Sainio, T. (2021). Kinetic approach to modelling CO₂ adsorption from humid air using amine-functionalized resin: Equilibrium isotherms and column dynamics. *Chemical Engineering Science*, 246, pp. 116885.

Author's contribution

Jere Elfving is the principal author and investigator in papers I – IV.

Contribution in Publications I-II: The author had the main responsibility for planning and carrying out experimental work, processing of results, modelling and writing of manuscripts. The experimental fixed-bed setup was designed and implemented by Jere Elfving in co-operation with Dr. Cyril Bajamundi and Juho Kauppinen. The initial version of the Matlab codes for experimental results processing were provided by Dr. Cyril Bajamundi and further developed by Jere Elfving. The co-authors also reviewed and commented on the manuscript.

Contribution in Publication III: The author had the main responsibility for the main design of the experimental device and the control and data acquisition software, in addition to planning and carrying out experimental work, processing of results, carrying out the energy requirement calculation and writing the manuscript. Juho Kauppinen helped with the practical design and implementation of the experimental setup. Mikko Jegoroff, Dr. Vesa Ruuskanen and Lauri Järvinen implemented the experimental device control and data acquisition software in LabVIEW. The co-authors also reviewed and commented on the manuscript.

Contribution in Publication IV: The author had the main responsibility for planning and carrying out the experimental work, processing of the results, kinetic and dynamic modelling and writing the manuscript. The kinetic model was developed in co-operation with Prof. Tuomo Sainio, who also reviewed and commented on the manuscript.

Other publications

Vázquez, V. F., Koponen, J., Ruuskanen, V., Bajamundi, C., Kosonen, A., Simell, P., Ahola, J., Frilund, C., Elfving, J., Reinikainen, M., Heikkinen, N., Kauppinen, J., Piermartini, P. (2018). Power-to-X technology using renewable electricity and carbon dioxide from ambient air: SOLETAIR proof-of-concept and improved process concept. *Journal of CO₂ Utilization*, 28, pp. 235-246.

Bajamundi, C. J. E., Koponen, J., Ruuskanen, V., Elfving, J., Kosonen, A., Kauppinen, J., Ahola, J. (2019). Capturing CO₂ from air: Technical performance and process control improvement. *Journal of CO₂ Utilization*, 30, pp. 232-239

Ruuskanen, V., Givirovskiy, G., Elfving, J., Kokkonen, P., Karvinen, A., Järvinen, L., Sillman, J., Vainikka, M., Ahola, J. (2021). *Journal of Cleaner Production*, 278, pp. 123423

Nomenclature

Latin alphabet

b	adsorption affinity	1/bar
b_1	adsorption affinity of reaction 1 (new kinetic model)	$\text{bar}^{-1}(\text{mol/kg})^{1-t_1}$
b_2	adsorption affinity of reaction 2 (new kinetic model)	$\text{bar}^{-2}(\text{mol/kg})^{1-t_2}$
c_i	concentration of species i	mol/m^3
c_p	specific heat capacity at constant pressure	$\text{J}/(\text{kg K})$
$c_{p,m}$	molar heat capacity at constant pressure	$\text{J}/(\text{mol K})$
C	GAB-isotherm parameter	-
d	diameter	m
D_L	Axial dispersion coefficient	m^2/s
E	specific energy requirement	J/kg
h	overall heat transfer coefficient	$\text{W}/(\text{m}^2 \text{K})$
ΔH	adsorption enthalpy	J/mol
$-\Delta H$	isosteric heat of adsorption	J/mol
ΔH_C	enthalpy difference between mono- and multilayer adsorption	J/mol
ΔH_K	enthalpy difference between H_2O condensation and multilayer adsorption	J/mol
$-\Delta H_1$	isosteric heat of adsorption parameter in reaction 1 (new kinetic model)	J/mol
$-\Delta H_2$	isosteric heat of adsorption parameter in reaction 2 (new kinetic model)	J/mol
k_{deg}	degradation rate	$(\text{mol}/\text{kg})/\text{nr. of cycles}$
$k_{f,1}$	forward reaction kinetic constant in reaction 1 (new kinetic model)	$\text{bar}^{-1}\text{s}^{-1}(\text{mol}/\text{kg})^{1-t_1}$
$k_{f,2}$	forward reaction kinetic constant in reaction 2 (new kinetic model)	$\text{bar}^{-2}\text{s}^{-1}(\text{mol}/\text{kg})^{1-t_2}$
k_{Fr}	Freundlich isotherm parameter	$\text{mol}/(\text{kg bar})$
$k_{i,\text{LDF}}$	linear driving force model kinetic constant of species i	1/s
K	GAB-isotherm parameter	-
L	length	m
m	mass	kg
M	molar mass	kg/mol
n	number of points	-
\dot{n}	molar flow rate	mol/s
n_{Fr}	Freundlich isotherm exponential parameter	-
n_{Sips}	Sips isotherm exponential parameter	-
N_{cycle}	cycle number	-
N_{cycles}	total number of adsorption/desorption cycles in a day	-
p_i	partial pressure of species i	bar
P	total pressure	bar
Δp	pressure drop	Pa

q	sorption capacity	mol/kg
q_m	maximum capacity (isotherm parameter)	mol/kg
\bar{q}_i	average adsorption capacity of species i in an adsorbent particle	mol/kg
R	radius	m
R_{id}	ideal gas constant	J/(mol K)
t	time	s
t_{Toth}	Toth isotherm exponential parameter	-
t_1	exponential parameter in reaction 1 (new kinetic model)	-
t_2	exponential parameter in reaction 2 (new kinetic model)	-
T	temperature	K
v	velocity	m/s
V	volume	m ³
\dot{V}	volume flow rate	m ³ /s
y_i	volume fraction of species i	-
z	axial coordinate	m

Greek alphabet

α	Toth model parameter	-
Δ	change	
∂	partial differential	
ε	adsorbent bed porosity	-
μ	dynamic viscosity	Pa·s
ν	kinematic viscosity	m ² /s
ρ	density	kg/m ³
Σ	sum	
σ	standard deviation	
χ	Toth model parameter	-

Dimensionless numbers

Re	Reynolds number
----	-----------------

Subscripts

a	adsorbent
ads	adsorption
b	backward
bed	(adsorbent) bed
chemi	chemisorption
cool	cooling
dry	dry conditions
des	desorption
eq	equilibrium
exp	experimental

f	forward
fit	fitted
g	gas
hum	humid
i	interstitial
<i>i</i>	adsorbing gas species (CO ₂ or H ₂ O)
in	inlet
meas	measured
mix	(gas) mixture
norm	normalized
out	outlet
p	particle
physi	physisorption
reg	regeneration
s	superficial
sat	saturation
sen	sensible
tot	total
vac	vacuum
w	wall
0	initial/reference

Abbreviations

ATR	attenuated total reflectance
BECCS	bioenergy with carbon capture and storage
BET	Brunauer-Emmett-Teller
BJH	Barrett-Joyner-Halenda
CCS	carbon capture and storage
CCU	carbon capture and utilization
CSA	concentration swing adsorption
DAC	direct air capture
DACCS	direct air capture and carbon storage
DACCU	direct air capture and carbon utilization
EOR	enhanced oil recovery
EWC	equilibrium working capacity
FTIR	Fourier-transform infrared spectroscopy
GAB	Guggenheim Anderson De Boer
GCF	gas conversion factor
GHG	greenhouse gas
HAS	hyperbranched aminosilica
IPCC	Intergovernmental Panel on Climate Change
LCA	life-cycle assessment
L/D	length/diameter
LDF	linear driving force

MCF	mesocellular foam
MFC	mass flow controller
MOF	metal-organic framework
NET	negative emissions technology
NFC	nanofibrillated cellulose
NIST	National Institute of Standards and Technology
NMR	nuclear magnetic resonance
ppm	parts per million
ppmv	parts per million by volume
PAA	polyallylamine
PCC	post-combustion capture
PEG	polyethylene glycol
PEI	polyethylenimine
PID	proportional-integral-derivative
PPI	polypropylenimine
PSA	pressure-swing adsorption
PtX	Power-to-X
PV	photovoltaics
RH	relative humidity
SATP	standard ambient temperature and pressure
SEM	scanning electron microscope
SER	specific energy requirement
TCSA	temperature-concentration swing adsorption
TEPA	tetraethylenepentamine
TGA	thermogravimetric analysis
TPSA	temperature-pressure swing adsorption
TREN	tris(2-amino ethyl)amine
TSA	temperature swing adsorption
TVCSA	temperature-vacuum-concentration swing adsorption
TVSA	temperature-vacuum swing adsorption
VSA	vacuum-swing adsorption
WC	working capacity
1-D	one-dimensional

1 Introduction

Based on Antarctic ice core data of air bubbles from the last 800 thousand years, a strong positive correlation has existed between the atmospheric CO₂ concentration and the mean temperature change [1]. However, significant changes of both have usually taken place on a scale of thousands or tens of thousands of years. In the last 800 thousand years, the atmospheric CO₂ concentration has never exceeded around 300 ppmv [1]. Since 1958 the atmospheric CO₂ concentration yearly average has risen from around 315 ppmv to 414 ppmv in 2020 [2]. This almost 100 ppmv increase in CO₂ concentration is caused by human-induced greenhouse gas (GHG) emissions and has already led to a global mean temperature increase, i.e., global warming, of around 1 °C compared to the pre-industrial era [3]. If the total greenhouse gas emissions continue at the current rate of around 50 GtCO₂-equivalent/year [4], the threshold for global warming of 1.5 °C by the end of the century will be reached already in the following couple of decades [3,4].

Global warming of 1.5–2 °C already leads to major negative ecological, social and economic impacts. These include the loss of biodiversity and harm to ecosystems, increased likelihood of extreme weather events such as storms and heat waves, reduced crop yields, lowered availability of fresh water and reduced economic growth. [3] Without any greenhouse gas emission reductions, the world is on a pathway to over 4 °C warming by the end of the century [4]. While the quantitative comparison of the effects of global warming is difficult, it is clear that increased warming leads to more severe consequences, such as increased sea level rise and more severe species loss [3]. It is thus necessary to mitigate climate change to avoid serious risks to the habitability of many regions of Earth already in the current century.

To follow the Paris Agreement and limit global warming to 1.5 or 2 °C requires reducing CO₂ emissions to net zero by 2050 or 2070, respectively [3]. This is an enormous challenge not only due to the requirement for the rapid reduction of huge amounts of emissions, but also because of the diversity of emission sources. Around ¾ of the total greenhouse gas emissions originate from energy use in industry, houses and transportation, while the rest originate mainly from agriculture, forestry, waste and by-product CO₂ of the chemical industry and cement production [4]. Many of these emission sources are scattered sources as opposed to point-source emissions from, e.g., production of electricity and heat in fossil-fuel based power plants, making them more difficult to control. The transport sector constitutes around 16% of the total greenhouse gas emissions [4], making it a major source of scattered emissions. In 2018, CO₂ emissions constituted around 36 GtCO₂-equivalent/year or ¾ of the total greenhouse gas emissions [5]. The most significant non-CO₂ greenhouse gases are methane and N₂O, constituting to emissions of 8 and 3 GtCO₂-equivalent/year in 2018, respectively [5].

Due to the complexity of greenhouse gas emissions, keeping global warming below 2 °C requires various effective mitigation methods. Seeing that a major part of all CO₂ emissions are generated by burning fossil fuels [4], the most impactful mitigation measures are related to decarbonisation of the power sector and transportation.

Decarbonisation of the energy sector can be achieved by replacing fossil-fuel based energy with nuclear power and renewable energy such as photovoltaic and wind power. Moreover, emission reductions can be achieved via switching the fuel, e.g., from coal to natural gas, as well as by achieving efficiency gains through efficient fuel combustion and waste heat recovery [6]. In transportation, important measures include the electrification of vehicles and the use of alternative fuels such as biofuels and hydrogen. In addition to these emission reductions, CO₂ neutrality requires CO₂ capture to capture or compensate for scattered and otherwise unavoidable emissions.

1.1 CO₂ capture, storage and utilization

CO₂ capture from point-sources combined with permanent CO₂ storage (CCS) can serve as an intermediate solution between the present and future with no reliance on fossil-based energy [7]. For industrial or power plant use, CO₂ capture constitutes mainly of three technologies: post-combustion capture (PCC), pre-combustion capture and oxyfuel combustion. PCC is based on the capture of CO₂ from flue gases in combustion or side-streams of industry. In pre-combustion capture, fuel is first reacted with steam and oxygen to produce syngas [8]. Carbon monoxide is converted together with steam to CO₂ and hydrogen, from which the CO₂ is separated to produce H₂-rich fuel [8]. In oxyfuel combustion, pure oxygen is introduced into the fuel combustion process, thus producing a flue gas with over 80% CO₂. However, the feasibility of this technology is reliant on the price of oxygen separation and purification. [9] On the other hand, pre-combustion capture requires a multi-stage process, and a separate CO₂ capture step based on similar separation technologies as in PCC [8]. Of these three CO₂ capture technologies, PCC has been by far the most studied [10].

In PCC, a capture process using amine-based solvents such as monoethanolamine (MEA) is seen as the benchmark technology [11]. However, disadvantages of amine-based solvents include corrosion of equipment and the emission of degradation compounds which are potentially harmful to nature and humans [11,12]. Therefore, alternative solvents have been studied, such as amino acid solutions with increased resistance to oxidative degradation [13]. Other options are the use of CO₂-selective membranes, stand-alone or in a combination with solvents [14], or solid adsorbents [15]. A typical case considered for PCC is the capture of CO₂ from the flue gas of a coal-fired power plant with a CO₂ concentration of 10-15%, targeting 90% removal rate. However, the CO₂ concentration varies from several percent in natural gas combustion up to 99-100% in industrial processes such as ammonia processing. Based on the calculations of the work of separation, the cost of PCC has been estimated to range from 14 USD/tCO₂ (~12 €/tCO₂ with the 10-year average exchange rate of 0.84 €/USD [16]) with high-purity CO₂ emissions up to 100 USD/tCO₂ (~84 €/tCO₂) in natural gas or petroleum-fired power plants. [7]

A complementary climate change mitigation technology to CCS is carbon capture and utilization (CCU), which mainly refers to the conversion of CO₂ into chemicals or fuels

(Power-to-X or PtX) and enhanced oil recovery (EOR). Examples of CO₂ conversion routes are electrochemical reduction into formic acid derivatives [17] and thermochemical routes such as CO₂ hydrogenation to produce methane [18] and methanol [19]. The captured CO₂ can also be indirectly utilized by first producing syngas in reverse-water gas shift reactor, and then utilizing the syngas, e.g., in the Fischer-Tropsch process to produce a variety of hydrocarbons [20]. Mac Dowell et al. [21] argued that the actual CO₂ sequestering potential of CCU without EOR is quite negligible and is likely to be less than 1% of the CO₂ emission mitigation challenge by 2050. The same authors estimated that PCC+CCS and EOR, on the other hand, could have sequestering rates of around 8 and 6-7 GtCO₂/year by 2050, respectively. Therefore, the prospects of conversion-based CCU are, rather than in CO₂ sequestration, to reduce the dependency of chemical and plastics manufacturing on fossil-based precursors [19,22] and to enable renewable energy by balancing the fluctuating solar photovoltaics (PV) and wind electricity production via chemical energy storage [23]. However, unless renewable energy is produced in large excess, the significant realization of carbon-neutral chemicals and fuels may not materialize [22].

While all other methods discussed above aim to reduce GHG emissions, negative emissions technologies (NETs) aim to remove CO₂ directly from the atmosphere. NETs are an important part of many of the 1.5-2 °C pathways for emission reductions proposed by the Intergovernmental Panel on Climate Change (IPCC) [3,24]. However, many NETs have large uncertainties in terms of the carbon removal potential, costs and environmental impacts [25]. Therefore, it has been argued that a climate change mitigation strategy relying on NETs could actually slow down the reduction of CO₂ emissions, and that the emission reductions excluding NETs should be more ambitious [24]. On the other hand, even if net zero global CO₂ emissions are reachable purely through emissions reduction (including PCC), the IPCC projects that NETs will still be required to remove already emitted CO₂ and thus even reverse climate change [3]. Moreover, NETs can be used to balance scattered emissions that cannot be reduced by other means such as electrification and CO₂-neutral fuels.

Based on the CO₂ removal potential, some of the most promising NETs are afforestation and reforestation, soil carbon sequestration, biochar, bioenergy with carbon capture and storage (BECCS), enhanced weathering and direct air capture (DAC) combined with carbon storage (DACCS) [25]. Fuss et al. [25] estimated that the CO₂ removal potential by 2050 for BECCS, soil carbon sequestration and direct air capture each is up to around 5 GtCO₂/year. However, BECCS and afforestation face serious limitations in terms of land and fresh water use and are relatively slow, while the carbon fixation potential in soil carbon sequestration will ultimately decline due to soil saturation [25]. In this regard, direct air capture can offer some advantages compared to other NETs, but requires significant technological development.

1.2 Direct air capture (DAC)

Direct air capture refers to processes in which CO₂ is captured directly from the air using solvents or solid sorbents. Some of the characteristic features of DAC include the selective capture of CO₂ from the air, a cyclic process and the production of high-purity CO₂. The first feature is important since the CO₂ concentration in the air can be described as ultra-dilute, corresponding to a partial pressure of around 0.0004 bar. The cyclicity of the process is paramount to minimize the cost of replacing the materials that capture CO₂. Therefore, the capture process is followed by a desorption phase, where the solvent or sorbent is regenerated and gaseous concentrated CO₂ is produced. The high purity of the produced CO₂ is crucial for the use of DAC in CCS or CCU applications. This is to limit pressurization costs in CCS and to meet the purity demands in CO₂ conversion processes [20].

1.2.1 DAC technologies

Often, the selectivity towards CO₂ in ultra-dilute conditions needs to be satisfied via materials that chemically react with CO₂. Thus, strongly basic hydroxide solutions were first proposed by Lackner et al. [26] and are the most mature solvent-based technology for DAC. In this process, air is first contacted with an aqueous NaOH [27–29] or KOH [30,31] solution that selectively captures CO₂ to form a carbonate salt solution. In the causticization step, the hydroxide solution is regenerated by adding solid CaOH to the carbonate salt solution. Thus formed calcium carbonate then needs to be calcined at temperatures of 800–900 °C [28,30] to produce gaseous CO₂. Carbon Engineering has piloted this process on a scale of 0.6 tCO₂/day [30] and are planning commercial-scale plants of 1 MtCO₂/year [32].

Although the use of amine-solvents such as MEA is common in PCC [11], their use in DAC conditions has only rarely been studied. The reason probably lies in a lower maximum capacity and a slower CO₂ capture rate compared to strongly basic hydroxide solutions [28]. Barzagli et al. [33] reported an extensive comparison of different alkanolamine solvents for DAC conditions, finding the best results for aqueous primary and secondary amines that form carbamates with CO₂. The capture efficiencies were reported to be comparable to aqueous NaOH. Recently, aqueous solutions of guanidines and amino-acids [34–36] or peptides [37], have been proposed as alternative solvents for DAC. The guanidines are regenerable at 60–150 °C [34,35] or at around 100–130 °C [36].

Naturally occurring limestone has also been suggested for DAC in fluidized-bed operation [38]. This process requires long times for carbon fixation of days or weeks [38,39] as well as a very high temperature of around 835 °C [38] for calcination of the calcium carbonate. Since one of the characteristic features of DAC is the rapid cyclic capture of CO₂ from air, this technology can be argued to resemble enhanced weathering rather than DAC.

Different porous solid materials can be functionalized with species that chemically bind CO₂. Primary, secondary and tertiary amines supported on porous materials can selectively adsorb CO₂ and humidity from the air based on an acid-base reaction between CO₂ and the amine sites [40]. The adsorbents can be regenerated by heating at relatively mild temperatures from under 100 °C [41–43] up to 110–140 °C [44–46]. This type of process has been commercialized by Climeworks [43]. Another option is to use supported quaternary ammonium cations, which operate via a moisture swing [47] instead of temperature swing. Other species such as alkali metal carbonates [48] have also been used to functionalize porous substrates for DAC purposes. As of yet, studies on other than amine-based sorbents have mainly been done on a laboratory-scale, and reports of piloting these technologies are lacking. Although the capture of CO₂ on some of these sorbents has in some cases been referred to as absorption [47,49], typically only the outer surface and the surface within the pores of the support material are functionalized. Thus, the CO₂ capture takes place on the outer and inner surface of the material, and all such materials are referred to as adsorbents in this thesis. Different adsorbents and the adsorbent-based DAC process are reviewed in more detail in Chapter 2.

1.2.2 DAC in climate change mitigation

As illustrated in Figure 1.1, direct air capture has several applications with direct or indirect impacts on climate change mitigation. Carbon Engineering has piloted the conversion of CO₂ from air into fuels and are planning 0.5-1 Mt_{CO2}/year scale DACCS plants to be established in the Permian Basin in the United States and in north-eastern Scotland [32]. The first commercial plant by Climeworks captures 0.9 kt_{CO2}/year and supplies it to a greenhouse [50]. Additionally, Climeworks is building a 4 kt_{CO2}/year scale plant in Iceland, where the captured CO₂ will be stored underground. The Climeworks technology is also planned to be used for CO₂ production for the Norsk e-fuel project to produce 10 and 100 million litres of renewable liquid fuel by 2023 and 2026, respectively [51]. Apart from these CCU and CCS applications, DAC can be used as the CO₂ source for the cultivation of protein-rich microbes [52]. However, noting the possibility that CCU will only play a small role in the total climate change mitigation challenge [21], the most effective strategy for climate change mitigation or reversal using DAC is CCS.

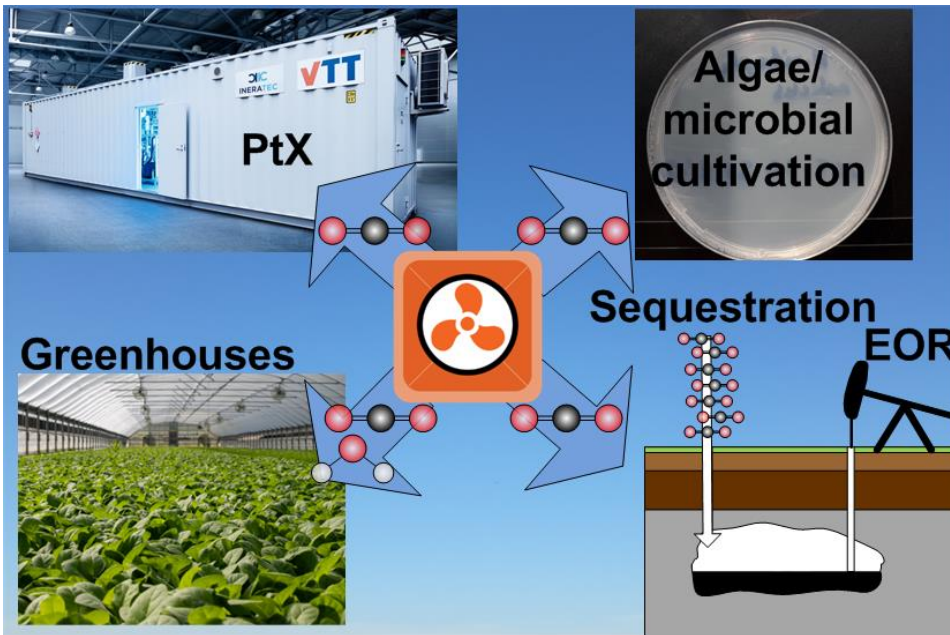


Figure 1.1: Some of the applications of DAC.

DACCS can offer some advantages with respect to other NETs, such as less land use [25,43]. Additionally, DAC does not require arable land, and the rate of CO_2 capture is fast compared to that of biomass and enhanced weathering. However, as with other CCS technologies, the water footprint especially in the solvent-based DACCS process could become significant [53]. In this regard, adsorption-based DAC with regeneration based on heating might be the preferable technology as it can produce liquid water from air [54,55] instead of consuming it like the moisture-swing [56] or solvent-based [57] processes. As noted above, DACCS could reach multi- $\text{GtCO}_2/\text{year}$ removal by 2050. Based on the growth of solar photovoltaics capacity and investments made, Breyer et al. [58] estimated that scaling DAC up to 10 $\text{GtCO}_2/\text{year}$ could be feasible already by 2050. The proposed maximum potentials are 30 $\text{GtCO}_2/\text{year}$ [59] or even near 40 $\text{GtCO}_2/\text{year}$ [60] by the end of the century. However, reaching such a massive CO_2 removal rate would require that no environmental side-effects or CO_2 storage capacity become severe limitations [25]. In addition, limitations related to material and energy demands need to be factored in.

Scaling-up the manufacturing of DAC units may not in itself be insuperable when compared to the production of other complicated and expensive units such as cars and other vehicles [59]. However, the application of DAC on a 30 $\text{GtCO}_2/\text{year}$ scale using solvent or solid adsorbent-based processes could lead to immense material demands that dwarf the current global production of the relevant chemicals [61]. Moreover, the energy demand required to operate the plants by 2100 would be more than half of the current total energy supply as estimated by Realmonte et al. [59]. In addition, Chatterjee and

Huang [61] estimated that the energy required to produce ammonia (for amine-based sorbents) alone could match the total current global energy supply. On the other hand, Realmonte et al. also noted that the development of the DAC technology may significantly reduce the energy demands of the process [62]. Furthermore, the material demands such as chemicals for the synthesis of adsorbents can be expected to decrease via improved sorbent and process design.

The role of the energy supply in the carbon-negativity of DAC is of utmost importance. The carbon removal efficiency of DAC is largely dependent on the carbon footprint of the electricity production [55,57], and with fossil-based electricity generation the captured CO₂ by DAC might not be enough to offset the emissions of the required power plants [25]. On the other hand, Van Der Giesen et al. [56] reported a life-cycle assessment (LCA) of humidity-swing DAC and concluded that this process with its electricity demand met with solar PV could be used to complement MEA-PCC to enable net-zero emissions from fossil-based electricity. A low energy demand for the moisture-swing process was assumed, based on wind for the convection of CO₂ during adsorption, and atmospheric drying of the sorbent during regeneration. Additionally, Azarabadi and Lackner evaluated that in some cases DAC may be even cheaper than retrofitting gas-fired power plants with PCC [63]. However, to maximize carbon removal, DACCS should be coupled with low-carbon energy production such as solar photovoltaics or wind power rather than compensate for the emissions of a fossil-based energy system [62].

Probably the main barrier currently for the large-scale application of DAC is the high cost compared to PCC or other NETs such as afforestation [25,64]. DAC cost analyses reported in the literature have a large range from below 100 USD/t_{CO2} [30,65] (~84 €t_{CO2}) to over 1000 USD/t_{CO2} [66,67] (~840 €t_{CO2}). It should be noted that some authors report only the cost of captured CO₂, while others report the cost of avoided CO₂ that takes into account the CO₂ emissions from building and operating the process. Solvent-based DAC using NaOH solutions was comprehensively first assessed in a report by the American Physical Society (APS), with estimated total costs of captured and avoided CO₂ around 430–550 USD/t_{CO2} (~361–462 €t_{CO2}) and 610–780 USD/t_{CO2} (~512–655 €t_{CO2}), respectively [28]. Carbon Engineering estimated the cost of captured CO₂ for their commercial 1 Mt_{CO2}/year plants to become 94–232 USD/t_{CO2} [30] (~79–195 €t_{CO2}). The main differences between the techno-economic assessment (TEA) by the APS [28] and the estimates by Carbon Engineering were related to improved rate of capture using KOH instead of NaOH, the contactor design as well as reduced energy consumption due to waste heat integration [30]. In 2018, Climeworks estimated the cost of capture with their first commercial plant to be around 600 USD/t_{CO2} (~504 €t_{CO2}), and that the cost would fall below 100 USD/t_{CO2} (~84 €t_{CO2}) in the coming 5–10 years [68]. Fasihi et al. [69] estimated that the cost of low-temperature (adsorbent-based) DAC even with conservative assumptions will decrease from around 300 €t_{CO2} to 80 €t_{CO2} by 2050.

Acknowledging the complexity of climate change mitigation challenge, no single technology will be enough to reach the 1.5–2 °C climate warming targets. Even if the costs of DAC were not a barrier, the immense material and energy demands might prevent

its utilization on a scale matching current global CO₂ emissions. Additionally, it has been projected that without ambitious reductions in GHG emissions in line with the IPCC 1.5 °C or 2.0 °C pathways, over 2–3 °C warming will be reached even with massive deployment of DAC by 2100 [70]. Therefore, DAC coupled with CCS and CCU are complementary to other NETs, like argued by Realmonte et al. [59]. Moreover, NETs are in turn complementary to significant emissions reductions. However, for DAC to reach the carbon removal scale of several GtCO₂/year it requires the reduction of material and energy demands and thus the cost of the technology. DAC is still at an early stage of development, and continued material and process design is needed to achieve sufficient cost-effectiveness to enable its large-scale commercialization.

1.3 Objectives and novelty

This thesis examines the adsorption-based direct air capture process using a proprietary amine-based CO₂ adsorbent. Most of the DAC literature so far has focused on the development of novel materials for DAC, while some of the other important aspects of the process have been all but neglected. Rather than developing new materials, this thesis aims to fill these gaps in the research, while complementing others. The focus of this work is on the experimental study and modelling of the DAC process in different conditions. Ultimately, the main goal of this thesis is to help reduce the cost and energy requirements of the DAC process. This is done by providing new experimental data and models that are useful in the design and optimization of the process.

The main novel aspects and results of the DAC research introduced in this work are as follows:

- Experimental and modelled performance of an amine-functionalized resin in a wide range of conditions relevant to atmospheric CO₂ capture, including humid conditions and sub-zero temperatures.
- Comprehensive comparison of different regeneration processes for DAC in terms of CO₂ capacity, kinetics and cyclic adsorbent stability.
- The evaluation of a novel regeneration method for DAC coupling vacuum and temperature swing with air as purge gas.
- A novel kinetic model of CO₂ adsorption from air on an amine-based adsorbent that takes into account the effect of humidity. The model is used to model humid CO₂ isotherms and adsorption column dynamics.

1.4 Thesis structure

Chapter 2 comprehensively reviews the literature related to solid adsorbent-based direct air capture to give an overall understanding of the developments and challenges of the field. In the first section of the review, the most important part of the process, the

adsorbent materials, are reviewed. The second section discusses the proposed DAC adsorption processes and their cost and energy requirements. The section closes with the discussion of some of the important but less studied aspects in the field of amine adsorbent-based DAC. In the first section of Chapter 3, the experimental setups and methods to carry out the experiments in this thesis are discussed. In the second section of this chapter, the calculation and modelling methods are described in detail. Chapter 4 describes and discusses the results of this work with the research topics divided into five different sections. Finally, a brief summary and conclusions of this work are given in Chapter 5.

2 Review of adsorbent-based direct air capture

The research on direct air capture involves a combination of scientific fields, ranging from synthesis chemistry to the study of the process life-cycle and economics. This review focuses on the technical side of the DAC process. While adsorbent synthesis is not performed in this work, it is important to understand the working principles, main parameters, current development and challenges of the adsorbent materials used in DAC research and applications. Therefore, the first part of this review is focused on reviewing the research related to DAC adsorbents. The latter part of the review is focused on the aspects of the overall DAC process to review the process types and configurations, and the cost and energy requirements related to the DAC process. This section aims to identify the main parts of the process that need more development. Finally, some of the less researched topics in the field of DAC are reviewed, which are studied in this thesis.

2.1 Adsorbent materials

The most important part of the CO₂ adsorption process is the adsorbent material. One of the most important qualities of the adsorbent to enable selective capture of CO₂ from air is the sufficient strength of binding with CO₂, which is also referred to as the heat of adsorption. Amine-based adsorbents used for DAC typically have high isosteric heats of adsorption in the order of 70-90 kJ/mol [71–74] due to the chemical adsorption mechanism between CO₂ and amines. The high heat of adsorption coupled with a high number of easily reached amine groups (adsorption sites) typically enables a high adsorption capacity even at low CO₂ partial pressures. Another important parameter is adsorption kinetics, which is dependent not only the adsorption mechanism, but also the mass transfer of CO₂ within the adsorbent. Other important characteristics of a good adsorbent are regenerability at moderate desorption temperature and stability in various conditions, including cyclic operation. In the sections below, literature related to direct air capture using solid adsorbents is reviewed, while focusing on supported amine adsorbents.

2.1.1 Supported amine adsorbents

Due to the low concentration of CO₂ in air, using porous adsorbents based only on weak physical interactions between the adsorbent surface and CO₂ typically cannot produce adsorption capacities large enough for practical use in the DAC process. Also, air humidity surpasses the concentration of CO₂ even in desert conditions, which causes competition of the captured species in materials based on physical adsorption [75]. Thus, so far, most of the reported solid adsorbents for DAC have been based on supported amines [76,77]. These materials combine the high capacity and selectivity of amines towards CO₂ with high porosity of the support to retain good gas diffusion and adsorption kinetics. The mechanism of CO₂ capture on primary and secondary supported amines is based on the formation of a zwitterion intermediate [40]:



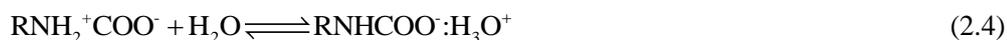
The zwitterion is then stabilized via deprotonation by another amine group or water molecule. Thus, in dry conditions the reaction proceeds by forming ammonium carbamate:



On the other hand, it has been found in FTIR and NMR studies [78,79] that in humid conditions ammonium bicarbonate salt is formed between a water molecule and the zwitterion via:



The formation of bicarbonate in humid conditions is also the only known mechanism for tertiary amines and CO₂, thus resulting in negligible adsorption of CO₂ in dry conditions [46]. On the other hand, Li et al. [40] studied the mechanism of CO₂ capture on silica-supported PEI in dry and humid conditions, and concluded that the formation of bicarbonate is less likely than hydronium carbamate. Thus, the zwitterion is stabilized by water via:



Therefore, in dry conditions, two amine groups are required to capture one CO₂ molecule, while in humid conditions only one amine group is required per CO₂ molecule. The implication is that theoretically the CO₂ adsorption capacity in humid conditions is twice the capacity in dry conditions. It should be noted, that other interactions between CO₂ and amines can also exist from those presented, as for example carbamic acid has been suggested to exist in humid [80,81] or dry [81,82] CO₂ adsorption conditions. Moreover, Miller et al. [83] suggested that in humid conditions hydrated hydronium carbamate is formed, leading to an increased binding energy.

Based on the reaction mechanisms of CO₂ with amines, the preferred amine types for amine-based adsorbents are primary and secondary amines. Tertiary amines should only be able to adsorb CO₂ in humid conditions, although this should not pose a problem in ambient conditions where moisture is always present. However, even in humid conditions the CO₂ adsorption performance on supported tertiary amines is rather low [46]. Moreover, primary amines have been found to perform better than secondary amines in terms of CO₂ adsorption. Didas et al. [84] found that primary amine-grafted adsorbents had higher than double the amine efficiency, i.e. CO₂ capacity divided by amine loading, compared to adsorbents functionalized with secondary amines. However, Alkhabbaz et al. [74] found that primary and secondary aminosilane-containing adsorbents had similar heats of adsorption of around 90 kJ/mol, even though using primary amines led to higher CO₂ adsorption capacities. Thus, rather than differences in heats of adsorption, steric

hindrances caused by hydrocarbon side-chains may explain the performance differences of different amines in these cases [74,85].

Materials used as supports in amine-based adsorbents typically have a high surface area and pore volume. Varieties of porous silica are a widely used group of materials as supports for amines, including fumed silica [41], silica gel [86] and mesoporous silica such as MCM-41 [87], SBA-15 [46] and mesocellular foam (MCF) [88]. Both SBA-15 and MCF are prepared via hydrothermal synthesis, but MCF has larger pores due to using a pore-expanding solvent [89]. The resulting mesoporous types of silica are powder-like substances with surface areas from 500 up to 1000 m²/g [89]. Other support materials used in DAC adsorbents include mesoporous alumina [90], mesoporous carbon [91], porous polymers [44,92] and nanofibrillated cellulose (NFC) [93]. An especially promising and wide group of materials are metal-organic frameworks (MOFs) that are based on well-ordered networks of metal centers and organic ligands [94]. These materials have very high surface areas well over 1000 m²/g [94] and can be post-functionalized to host different types of amines [95,96]. Many of these support materials have been studied extensively as physisorbents for higher-concentration CO₂ capture such as 10–15% in PCC [15].

Usually, supported amine adsorbents for DAC have been prepared by post-functionalization of the support with amines. An exception to this are certain MOFs that can be directly synthesized to incorporate amino-groups in their structure [97]. The main methods for post-functionalization are amine impregnation and amine grafting. Materials belonging to these main groups are discussed in detail below.

2.1.2 Amine-impregnated adsorbents

In amine impregnation, the porous support is wet-impregnated typically with a polyamine such as linear [98] or branched polyethylenimine [95] (PEI) mixed in methanol. At low amine loadings in the support material, polyamines only coat the surface of the support, while at higher loadings complete filling of mesopores will occur [99]. The final adsorbent is received after drying out the solvent. In the literature, these materials are also referred to as class 1 amine adsorbents [76,77,100].

In the literature, CO₂ adsorption capacities of polyamine-impregnated sorbents range from 0.5 mmol_{CO₂}/g_{sorbent} [93] up to over 3 mmol_{CO₂}/g_{sorbent} [101,102] in conditions relevant to ambient air. Most of the promising amine-impregnated materials in terms of adsorption capacity are based on using high loadings of low-molecular weight branched PEI in mesoporous or macroporous supports. Choi et al. [103] reported one of the first trials to use PEI-impregnated porous silica for direct air capture, obtaining up to 2.36 mmol_{CO₂}/g_{sorbent} from dry 400 ppm CO₂ at 25 °C with an amine loading of 10.5 mmol_N/g_{sorbent}. Chen et al. [104] impregnated macroporous commercial resins with PEI, with the most promising sample HP20 with 50 w-% PEI adsorbing 2.26 mmol_{CO₂}/g_{sorbent} from (practically) dry 400 ppm CO₂ at 25 °C. Goepfert et al. [41] measured the highest adsorption capacity of 2.44 mmol_{CO₂}/g_{sorbent} from dry air at 25 °C when using 50 w-% of

branched PEI with molecular weight of 800 g/mol supported by fumed silica. With similar loading of heavier PEI (25 000 g/mol), the adsorption capacity was lower of 1.67 mmol_{CO₂}/g_{sorbent}. Data for the amine-impregnated adsorbents reported in the literature can be found in Table A1.

In some cases, adsorbents with higher polyamine loadings can become partially pore-blocked, affecting gas diffusion. This can lead to lowered adsorption kinetics and thus lower measured CO₂ capacity within certain adsorption time [41], the practical implication of which is reduced productivity under process conditions. Therefore, there often exists an optimum in terms of amine loading, over which the observed adsorption capacities start to decrease. This optimum amine loading is dependent on the used amine type and support material. For example, a significant decrease in the capacity and amine efficiency have been reported to occur using PEI on resins at loadings above 50 w-% [104], PEI on NFC at loadings over 44 w-% [93] and polyallylamine (PAA) on silica at loadings over 40 w-% [105]. Furthermore, pore-filled adsorbents may yield unintuitive results, where maximum adsorption capacities are gained at relatively high temperatures such as at 46 °C [106] or even at 75 °C [91]. Thus, to achieve the maximum adsorption capacity in conditions relevant to DAC, the most commonly utilized amine loading of PEI has been near 50 w-% for mesoporous silica, carbon and resins (see Table A1).

Several authors have used different additives to improve the accessibility of amine-sites in amine-impregnated sorbents, thus also potentially increasing the optimal amine loading. Wang et al. [91] used a surfactant (Span 80) on mesoporous carbon with a high PEI loading of 55 w-% to boost adsorption capacity from 1.5 to 2.25 mmol_{CO₂}/g_{sorbent} at 25 °C in dry DAC conditions. Sakwa-Novak et al. [107] studied the effect of polyethylene glycol (PEG) as an additive, reporting slightly higher CO₂ capacities for additive-modified samples compared to the native PEI/SBA-15 adsorbent. Sayari et al. [87] functionalized the surface of pore-expanded MCM-41 with cetyltrimethylammonium cations as an additive. Apparently, the surface-modification led to a better dispersion of PEI, since the maximum capacity from dry 400 ppm CO₂ at 25 °C increased from under 1 mmol_{CO₂}/g_{sorbent} to 2.2 mmol_{CO₂}/g_{sorbent}.

The selection of the support material also affects the dispersion of polyamines and the maximum optimal amine loadings. Zhu et al. [108] used an Mg-Al-oxide support to offer better dispersion of impregnated PEI, finding a maximum capacity of 2.27 mmol_{CO₂}/g_{sorbent} at a PEI loading of 67 w-% in dry DAC conditions at 25 °C. The adsorption capacity of an SBA-15-supported adsorbent with a similar PEI-loading was slightly lower (1.92 mmol_{CO₂}/g_{sorbent}). Additionally, support materials with extra-large pores can achieve a higher amine loading without hindering the accessibility of the amine sites. For example, Kwon et al. [102] prepared a so-called hierarchical silica support with meso- and macropores, taking up large PEI loadings and adsorbing 2.4 mmol_{CO₂}/g_{sorbent} from dry simulated air at 30 °C.

Polyethylenimine has been the common choice for preparing class 1 adsorbents, since it hosts a large amount of primary and secondary amines, and it is commercially available.

However, other amines have also been used, with varying results in direct air capture conditions. Chaikittisilp et al. [105] used PEI- and polyallylamine (PAA)-impregnated MCF for CO₂ capture from dry simulated air (400 ppm CO₂) at 25 °C, with optimal results of 1.74 mmol_{CO₂}/g_{sorbent} and 0.86 mmol_{CO₂}/g_{sorbent} using branched PEI and PAA, respectively. Brillman and Veneman [109] reported a high capacity of 2.50 mmol_{CO₂}/g_{sorbent} from dry 400 ppm CO₂ at 35 °C on silica impregnated with 38 w-% tetraethylenepentamine (TEPA). Pang et al. [99] impregnated SBA-15 with linear polypropylenimine (PPI), finding improved oxidative stability of the adsorbents compared to using PEI. Sujan et al. [110] aimed to combine the diffusion-enhancing properties of PEG with the CO₂ affinity of PEI by synthesizing polyglycidylamine-impregnated SBA-15 adsorbents. However, the resulting adsorbents had significantly lower adsorption capacities than PEI-impregnated adsorbents with similar loadings, although slightly improved oxidative resistance. Kumar et al. [111] synthesized alkyl-aryl amine impregnated SBA-15 but found no clear benefits in terms of oxidative stability or adsorption capacity compared to PEI-impregnated sorbents. Park et al. [112] prepared polypropylene guanidine impregnated SBA-15 adsorbents, and found that these adsorbents lost their capacity more rapidly in cyclic experiments than PEI-loaded SBA-15.

As discussed in section 2.1.1 above, humidity increases the theoretical amine efficiency to one mole of CO₂ per mole of amine. On several occasions, higher adsorption capacities have been measured in the presence of humidity compared to dry conditions (see Table A1). For example, Wang et al. [101] measured 3.16 mmol_{CO₂}/g_{sorbent} at 10% RH, which is a 61% capacity improvement from dry conditions for the PEI-loaded resin. Kwon et al. [102] reported one of the highest adsorption capacities in DAC conditions of 3.36 mmol_{CO₂}/g_{sorbent} at 19% RH, which was a 40% improvement on dry conditions. Sehaqui et al. [93] found a remarkable improvement of CO₂ capacity from 0.5 mmol_{CO₂}/g_{sorbent} at 20% RH to 2.2 mmol_{CO₂}/g_{sorbent} at 80% RH. However, in some cases, no clear improvement has been found in the presence of humidity. Wang et al. [91] measured 2.58 mmol_{CO₂}/g_{sorbent} at 80% humidity with PEI- and additive-loaded mesoporous carbon, which was only around 15% improvement compared to dry conditions. Goepfert et al. [113] found a slight decrease in the adsorption capacity from 1.70 mmol_{CO₂}/g_{sorbent} to 1.41 mmol_{CO₂}/g_{sorbent} at 67% RH on a 50-% PEI-loaded fumed silica adsorbent. Therefore, to reliably predict the performance of amine-based adsorbents in varying conditions, it is important to measure the CO₂ adsorption capacity in both conditions of variable humidity and temperature.

2.1.3 Amine-grafted adsorbents

Although polyamine impregnation produces adsorbents that can have high CO₂ adsorption capacities in DAC conditions, one of the main disadvantages of this method often encountered in the literature is the rapid loss of CO₂ capacity in repeated adsorption/desorption cycles. This is caused by the loss of amine that is only physically bound to the support surface. To counter this rapid amine loss, amines can be covalently bound to the support. For example, Rao et al. [114] compared the stability of amine-

impregnated and covalently grafted CO₂ adsorbents, finding clear advantage in terms of thermal and cyclic stability in the latter.

Amine-grafted adsorbents can be referred to as class 2 amine adsorbents [76,77,100]. A typical method to prepare grafted amine adsorbents is to use amine-containing silanes that can react with the silanol or hydroxyl groups on the surface of the support material. In this method, a high density of silanol or hydroxyl groups is important, which is why supports such as SBA-15 [46], MCF [84] and NFC [115] have been used. On the other hand, in MOFs, the amine grafting can be achieved by the reaction of an amine with the unsaturated open metal sites of the MOF [96]. Another way is by tethering the amine onto the organic ligands of the MOF [116].

In terms of CO₂ capacity, some of the most promising class 2 adsorbents based on aminosilanes include tri-aminosilane-functionalized MCM-41 with a capacity of 0.9-1 mmolCO₂/g_{sorbent} [117] and mono-aminosilane-functionalized NFC with a capacity of 1.1 mmolCO₂/g_{sorbent} [73] in dry DAC conditions at 23-25 °C. Moreover, Gebald et al. [73] reported 2.13 mmolCO₂/g_{sorbent} at 23 °C and 90% RH on the aminosilane-functionalized NFC, which was a 92% capacity improvement compared to dry conditions. Results reported in the literature using amine-grafted materials can be found in Table A2.

As mentioned, MOFs are different from other support materials in that they have open-metal sites that can react with free amines, thus creating covalently bound amine adsorbents. Darunte et al. [95] used MIL-101(Cr) as a support for tris(2-amino ethyl) (TREN) and PEI. Evidently, a significant part of the free amine groups in these polyamines reacted with the MOF surface metal sites, thus leading to very low CO₂ adsorption capacities when the amine loadings were low. The authors were able to boost the adsorption capacities by increasing the polyamines, although in this case the additional polyamines were probably only physically bound with the polyamine-coated surface of the MOF. Thus, significant capacity losses occurred already in three cycles for both adsorbents. Zhu et al. [118] reported an interesting composite material combining a polymeric substrate with HKUST- type MOF and covalently bound PEI. The best result in dry DAC conditions at 25 °C was 1.78 mmolCO₂/g_{sorbent} with 70 w-% PEI.

Perhaps the most promising and widely reported amine-functionalized MOF adsorbents for DAC are diamine-grafted Mg₂(dobdc) [45,119] and Mg₂(dobpdc) [96,120]. The highest reported capacities using these materials are 3.89 mmolCO₂/g_{sorbent} [45] and 2.83 mmolCO₂/g_{sorbent} [120] in dry DAC conditions at 25 °C, respectively. The first result is the highest reported capacity so far with a solid adsorbent material in dry or humid DAC conditions. Additionally, Darunte et al. [121] grew diamine-functionalized Mg₂(dobpdc) as a coating on a cordierite monolith in an attempt to develop a more practical, low-pressure drop adsorbent. However, a slight drop of CO₂ capacity and a substantial loss of surface area was found after exposure to humid conditions. The CO₂ adsorption performance of these materials in conditions relevant to humid DAC has not been reported in detail.

The third group of amine-based adsorbent materials (class 3) are prepared by grafting the amine from the support by using different techniques of in-situ polymerization [76,100]. Choi et al. [122] prepared so-called hyperbranched aminosilica (HAS) adsorbents via acid-catalyzed ring-opening polymerization of aziridine using SBA-15 as a support. The resulting adsorbents had a high nitrogen loading of up to 9.9 mmol_N/g_{sorbent} and a good adsorption capacity of 1.72 mmol_{CO₂}/g_{sorbent} from 400 ppm CO₂ at 25 °C. However, these materials were also reported to have long adsorption times, evidently due to partly blocked pores by the amino polymer.

Another means of in-situ amine polymerization is to first functionalize the support material with a suitable initiator, followed by the addition of a monomer and subsequent polymerization. Liu et al. [123] used aminosilane-functionalized macroporous silica to prepare adsorbents with linear L-alanine polymers. The resulting adsorbents had even higher amine loadings than HAS materials of up to 11 mmol_N/g_{sorbent} and 2.65 mmol_{CO₂}/g_{sorbent} from 400 ppm CO₂ at 50 °C. Qi et al. [124] functionalized MCF silica with iodine-containing aminosilane to act as initiator on the support surface for the ring-opening polymerization of 2-methyl-2-oxazoline. The resulting adsorbent had linear chains of PEI, resulting in a very high amine content of over 15 mmol_N/g_{sorbent} and an outstanding adsorption capacity of 11.8 mmol_{CO₂}/g_{sorbent} from humid 8% CO₂ at 25 °C. Interestingly, the adsorbent was reported to yield only 0.82 mmol_{CO₂}/g_{sorbent} in the 2-hour TGA test using dry CO₂ at the same temperature, which was attributed to hindered diffusion in dry conditions. However, no results relevant to direct air capture conditions have been reported so far using this promising adsorbent.

2.1.4 Stability of amine-based adsorbents

Degradation of amine adsorbents remains one of the main challenges to their large-scale application in both PCC and DAC [125]. Although some control over degradation can be achieved in the design of the desorption process, this factor should be taken into account already in the design of the adsorbent to maximize cyclic stability and CO₂ productivity.

Resistance of amine-based adsorbents to elevated temperatures and repeated adsorption/desorption cycles is important in terms of maximal CO₂ desorption. However, in some cases polyamine-impregnated sorbents have been found to suffer a significant capacity loss in only a few cycles [93,95,102,103,112,126]. As mentioned in section 2.1.3, covalently bound aminosilanes can be more stable against amine evaporation as opposed to physically impregnated polyamines. Better thermal stability and cyclic stability in inert desorption conditions at over 100 °C have been reported for aminosilane-grafted silica compared to PEI-impregnated silica [114,127]. However, although the evaporation of amines can be countered via covalent grafting of the amine, other significant mechanisms also contribute to the degradation of amine-functionalized adsorbents in the DAC process. These include degradation of the support in humid conditions and/or at high temperatures, amine leaching by steam, amine oxidation and urea formation at high concentrations of CO₂ [125].

Steam-stripping is a widely proposed method for CO₂ desorption from amine-based adsorbents [65,128–131], but steam may cause structural changes to the support material and may leach the amines, thus eventually reducing the CO₂ adsorption capacity [129,132]. Chaikittisilp et al. [90] reported mesoporous alumina to be a more stable support for PEI than SBA-15 silica, which lost its adsorption capacity almost completely after being subjected to steam at 105 °C for 24 hours. Sakwa-Novak and Jones [132] found that after a 24-hour steam treatment the CO₂ adsorption capacity of PEI-loaded mesoporous alumina dropped from 1.71 to 0.66 mmol_{CO₂}/g_{adsorbent} using humid 400 ppm CO₂ at 30 °C. It was noted that the capacity drop was mostly due to the leaching of PEI rather than degradation of the support as in the case of silica. The loss of CO₂ capacity after steam treatment has been reported also for aminosilane-grafted SBA-15, but without the loss or degradation of amines [133]. Thus, in the development of steam-stable adsorbents, the robustness of both the support material and the amine-functionalization are important.

Chemical degradation of the amine groups via different mechanisms is one of the main challenges encountered in applications of CO₂ adsorption on amine-based adsorbents. The formation of urea-groups from the amines takes place in the presence of concentrated CO₂, even in mild conditions [134,135]. Such a condition in DAC can take place when using CO₂ as a purge gas, or when CO₂ is desorbed without a purge gas, subjecting the adsorbent to a concentrated CO₂ atmosphere. Sayari et al. [136] found that primary amines were more susceptible to urea formation than secondary or tertiary amines. However, it was found that only isolated secondary amines were more resistant to urea formation [137]. Additionally, Didas et al. [135] found that highly-loaded adsorbents degrade more than materials with low amine loadings, indicating that neighbouring amines assist urea formation. On the other hand, Sayari and Belmabkhout [134] found that humidity had a significantly stabilizing effect, preventing urea formation. In fact, an already deactivated amine-grafted silica adsorbent could be regenerated under a humid flow of N₂ at 200 °C, apparently via hydrolysis of the urea groups back to amines [134].

Another significant deactivation mechanism of supported amines is via oxidative degradation. The species resulting from the oxidation of amine groups in supported PEI have been found to be mainly imine and carbonyl groups [138]. Primary amines are more resistant to oxidative degradation than secondary amines [139,140], which is problematic for the use of polyamines such as PEI that are rich in secondary amines. Another affecting factor seems to be the length of the hydrocarbon chain between amine groups. Polypropylenimine-impregnated adsorbents have been found to be much more resistant to oxidative degradation than PEI-containing adsorbents, while having comparable adsorption capacities [99]. PPI-functionalized adsorbents have been found to maintain most of their adsorption capacity even after 1.5 years in atmospheric conditions [141]. Another method suggested to improve oxidative and thermal stability is to use hybrid adsorbents with both grafted and impregnated amines [103,142].

Tests with extended exposure to varying conditions are important in the study of degradation mechanisms and for finding the boundaries of reasonable operating

conditions. However, to predict the longevity of an adsorbent in practical DAC conditions, cyclic adsorption/desorption tests are needed. Typically, tests with fewer than 20 cycles have been conducted [125], which may be enough for comparison purposes between materials, but not for the prediction of long-term stability. However, on some occasions, more cycles have been conducted. Wijesiri et al. [129] conducted 50 adsorption/desorption cycles in varying steam-stripping conditions on PEI-impregnated MCF pellets, finding a capacity drop from 1.69 to 1.56 mmol_{CO₂}/g_{sorbent}. Pang et al. [99] found a consistent working capacity of 0.76 mmol_{CO₂}/g_{sorbent} for a PPI-loaded sample in 50 adsorption/desorption cycles with desorption in inert conditions at 110 °C. Bos et al. [44] found no capacity drop in over 60 adsorption/desorption cycles in varying regeneration conditions for the commercial Lewatit VP OC 1065 adsorbent. The same adsorbent was also tested by Parvazinia et al. [143] for 275 cycles with desorption in inert conditions, resulting in less than 5% capacity loss. Gebald et al. [144] conducted 100 cycles using temperature-vacuum swing adsorption on the aminosilane-functionalized NFC sorbent, finding around a 5% capacity drop.

Even though carrying out adsorption/desorption cycles in the dozens or hundreds of cycles may be time and resource consuming, even this may not be enough to prove the feasibility of an adsorbent material. For the DAC process to be economically feasible, an adsorbent may have to survive thousands if not tens of thousands of cycles without losing the majority of its adsorption capacity [145]. For many of the otherwise promising adsorbent materials discussed above, there is either not enough data to prove such stability exists, or multicycle experiments have shown rapid degradation. However, further material development could bring improvements also in terms of long-term stability. For example, Choe et al. [146] increased the hydrophobicity of the diamine-functionalized Mg₂(dobpdc) by silane functionalization, thus significantly improving the stability of the material in humid ambient conditions. Moreover, Kim et al. [147] developed a tetra-amine-functionalized variant of the Mg₂(dobpdc) MOF with increased stability. The adsorbent exhibited stable performance over 1000 cycles of adsorption and desorption in humid CO₂-containing gases. These recent advances, and those discussed in the sections above, show that despite the many challenges faced in terms of the practicality of amine-based adsorbents in DAC, these challenges can be overcome with continued adsorbent development.

2.1.5 Other adsorbents

Other amine-based adsorbents have been developed that do not quite fit the two categories discussed in sections 2.1.2 and 2.1.3. Rim et al. [148] encapsulated silica nanoparticles functionalized with PEI into polymeric shells, combining the good gas diffusion of solid adsorbents with the high capacity of amine solvents. Thus, the materials were reported to have significantly increased kinetics compared to amine solvents in PCC, while having a fairly high capacity of 1.7 mmol_{CO₂}/g_{sorbent} from humid air at 80% RH at 25 °C. Another interesting alternative to the amine-based adsorbents discussed above are amine-based adsorbents without a separate support material. Xu et al. [149] reported the use of cross-linked PEI sorbent, obtaining around 1.3 mmol_{CO₂}/g_{sorbent} in breakthrough testing from

laboratory air. Abhilash et al. [150] prepared amine-containing polysilsesquioxane-based adsorbents via a direct synthesis route by reacting aminosilane with vinyl triethoxysilane. An adsorption capacity of 1.68 mmol/g was gained from 400 ppm CO₂ at 30 °C and 60% RH. No degradation of the adsorbent was observed in 50 cycles of adsorption/desorption with desorption at 80 °C using dry inert gas.

To reduce the heat demand for CO₂ desorption or counter other disadvantages of primary, secondary or tertiary amine-functionalized adsorbents such as amine degradation, other adsorbents have also been studied for DAC. These include quaternary-ammonium functionalized materials, metal-carbonate loaded adsorbents, ion-exchanged zeolites and MOFs without amine functional groups.

Quaternary ammonium cations have been supported on materials such as polymeric resins [47,151–154], cellulose [155] and chitosan [156] as DAC adsorbents. The process is operated via a moisture-swing cycle, where CO₂ is captured from (relatively) dry air and released when exposed to liquid water or humid air [47]. The CO₂ capture mechanism is based on the reaction of H⁺- and OH⁻-ions with CO₃²⁻-ions and CO₂, respectively, to form bicarbonate ions that become bound to the cationic surface [157]. On the other hand, Song et al. [158] reported a resin ion-exchanged with PO₄³⁻ ions, with improved kinetics and capacity compared to sorbents based on mobile carbonate ions. Therefore, the advantage of the moisture-swing technology vs. amine-based adsorbents is that no heat is required to desorb the CO₂. On the other hand, the requirement to humidify air or the use of liquid water may restrict the geographical applicability of this technology [56].

Alkali metal carbonate-loaded materials such as mesoporous alumina [49,159] or zirconia aerogel [48] have been studied for DAC. The materials are based mainly on the formation of potassium bicarbonate and require a higher desorption temperature of 200-350 °C for full regeneration compared to amine-based adsorbents [48,49,159]. Rodríguez-Mosqueda et al. used activated carbon honeycombs impregnated with sodium [160] or potassium carbonate [161,162]. The authors combined a low temperature of 50-80 °C with a moisture swing to partially regenerate the sorbents. However, the attained working capacities were quite small and consequently the estimated specific energy requirements were huge [162]. Cuesta and Song [163] reported a proof-of-concept study of a novel adsorbent type incorporating K₂CO₃, a nitrogen-containing polymer and carbonic anhydrase for direct air capture. The adsorbent captured CO₂ in basic conditions as bicarbonate, releasing it in acidic conditions. The adsorbent is thus regenerable via a pH-swing via an N₂ flow with ammonium-bicarbonate solution vapour. The authors mentioned minimal energy consumption as one of the important benefits compared to amine-functionalized adsorbents for CO₂ capture. However, the used CO₂ concentration was 1 vol-% instead of 400 ppm, and the actual direct air capture performance has not yet been reported.

In percent-scale CO₂ concentrations relevant to PCC [7], physical adsorbents have been widely proposed using adsorbents such as activated carbon [164], MOFs [165], zeolites and other materials [15]. However, few physisorbent materials have sufficient heat of

adsorption to enable meaningful amounts of CO₂ to be adsorbed from the air. Thus, zeolites and physisorbing MOFs usually have very low capacities for adsorbing CO₂ from air, especially in the presence of humidity [75,166]. Stuckert and Yang [167] studied the use of cation-exchanged zeolites for direct air capture. The zeolites had slightly lower heats of adsorption (48–60 kJ/mol) compared to amine-grafted SBA-15 (65 kJ/mol) used as a benchmark material. The zeolites adsorbed up to 1.34 mmol/g from dry simulated air at 25 °C. However, the materials lost most of their capacity in humid conditions.

Certain MOFs without amine functional groups have been reported to have CO₂ capacities even over 1 mmol/g from 400–500 ppm CO₂ [168–171]. Bien et al. [171] used ligand-exchanged MOFs for trace CO₂ capture, finding a very sharply increasing CO₂ isotherm shape with 2.2 mmol_{CO₂}/g_{sorbent} at 0.4 mbar CO₂ at 27 °C. In breakthrough experiments with simulated dry air, the capacity was lower but still rather impressive (1.4 mmol_{CO₂}/g_{sorbent}), while having a relatively low desorption temperature of 100 °C compared to up to 150 °C for the diamine-functionalized Mg₂(dobpdc) MOFs discussed in section 2.1.3 above. However, in humid breakthrough testing, immediate CO₂ breakthrough was observed, referring to poor adsorption performance in humid conditions.

Bhatt et al. [170] measured around 1.3 mmol_{CO₂}/g_{sorbent} in dry conditions from 0.4 mbar CO₂ on NbOFFIVE-1-Ni MOF. However, in breakthrough experiments with 1% CO₂, significant CO₂ roll-up was observable from their results with 74% relative humidity. Similar behaviour can be observed in humid 1000 ppm CO₂ adsorption on SIFSIX-3 MOFs [168]. These materials have seemingly good performance for CO₂ capture from dry air. However, as the roll-up typically takes place in competitive adsorption for the less strongly adsorbed components, reducing its adsorption capacity, the results do not bode well for the performance of these materials in real humid atmospheric conditions. Another problem in certain MOF materials arises from degradation due to their high affinity towards H₂O [169], but the MOFs discussed above were claimed to have good stability in humid conditions [168,170,171].

Recently, attempts have been made to improve the properties of MOFs in humid DAC conditions. Mukherjee et al. [169] engineered MOF pore properties to become more hydrophobic to improve both their selectivity and stability under humid trace CO₂ capture conditions. However, the adsorption capacities in humid conditions were only around half of those in dry conditions. Additionally, a significant capacity decrease of several percent was observed after only a few cycles in both dry and humid adsorption conditions. Guo et al. [172] synthesized a promising DAC physisorbent (heat of adsorption 56.2 kJ/mol_{CO₂}) with NbOFFIVE-1-Ni grown in situ on hydrophobic polyacrylate beads. The material was tested for CO₂ capture from air using a bubbling fluidized bed, maintaining a working capacity of 0.84 mmol_{CO₂}/g_{sorbent} in 2000 short cycles at 25 °C in humid conditions. Although more studies on CO₂ capture performance and stability in varying conditions is warranted, these types of MOFs seem a promising alternative to using amine-based adsorbents. Moreover, in search of new MOF alternatives that show promise

in DAC conditions, computational methods such as Monte Carlo method, molecular simulations and machine learning can be utilized [173].

2.2 The adsorbent-based DAC process

The adsorption step is typically common in principle to all cyclic adsorption/desorption DAC process types, involving the blowing of air through the adsorbent. Thus, the desorption step is typically the step that determines the type of the process. These process types, and the main cost and energy requirement components are discussed in the sections below. Some considerations for lowering the energy requirement are also given based on the literature. While the most commonly proposed DAC process is based on amine-based adsorbents in a cyclic adsorption/desorption process, some of the alternative processes are also briefly reviewed. Finally, some of the gaps in the DAC process research so far, that have relevance to this thesis, are discussed.

2.2.1 Process types in CO₂ adsorption

The basis for the design of an adsorbent-based DAC process, like any adsorption process, is determining the CO₂ adsorption isotherms. As depicted in Figure 2.1, CO₂ adsorption isotherms determined at different temperatures allow the prediction of the working capacity in given pressure and temperature conditions. Due to the shape of CO₂ isotherms, no strict points of temperature or partial pressure exist where all CO₂ is removed. Rather, the amount of CO₂ desorbed increases gradually by increasing the temperature and decreasing the partial pressure. Figure 2.1 also depicts the process types in adsorption, which are concentration swing adsorption (CSA), pressure swing adsorption (PSA), temperature swing adsorption (TSA), temperature-concentration swing adsorption (TCSA) and temperature-pressure swing adsorption (TPSA).

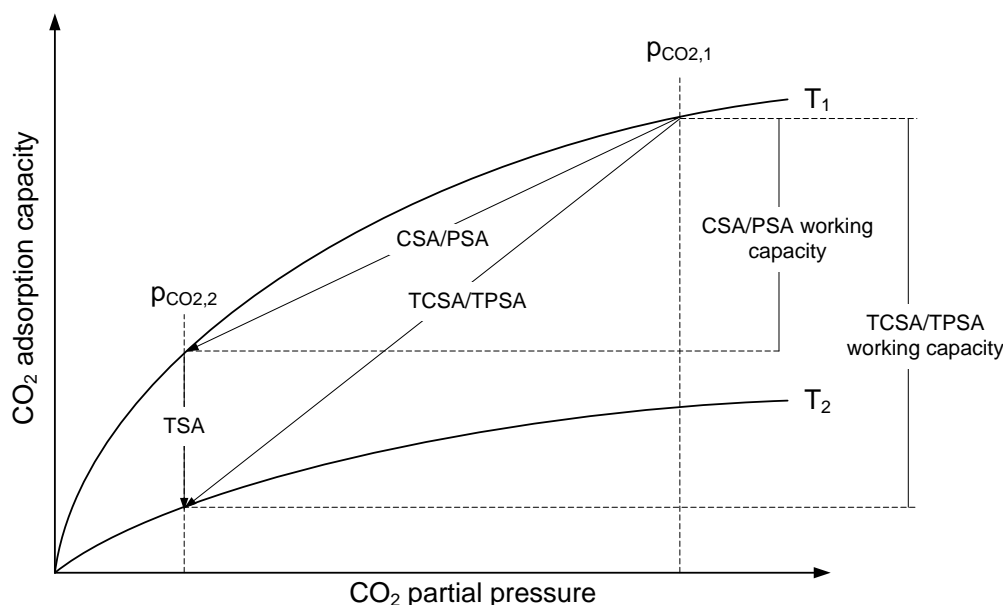


Figure 2.1: The concept of working capacity in the adsorption process.

Concentration swing adsorption means changing the concentration of the adsorbed species, such as by using an inert purge gas, to a lower level during desorption while temperature is not changed. This type of process cannot be considered practical for CO₂ capture, since the desorbed CO₂ is diluted. Pressure swing adsorption, on the other hand, has been widely considered for CO₂ capture using physisorbents such as zeolite 13X [174–176]. This process is typically based on using increased pressure during adsorption and lowered pressure during desorption. Evacuation can be applied during the desorption phase, and in this case the process can also be referred to as vacuum swing adsorption (VSA). However, PSA cannot be considered a practical method for direct air capture due to the very low partial pressure of CO₂ in air [86]. This is also shown and discussed in detail in section 4.3 and in Articles I and II. While temperature is not changed by design in CSA, VSA or PSA, the conditions during adsorption or regeneration are never truly isothermal due to the heat of adsorption, consequently heating up the bed when CO₂ is adsorbed and cooling it down when CO₂ is released.

Combined temperature and concentration swing adsorption using an elevated temperature and an inert gas during desorption is the most commonly-used scheme in laboratory-scale CO₂ adsorption studies for effective adsorbent regeneration [125]. A significant challenge in using inert gases such as nitrogen arises from the cost of the gas, which may become significant enough to render the TCSA method uneconomical on a process-scale [177]. On the other hand, when using air as a feed during the desorption step, the oxidation of an amine-based adsorbent may become a major problem at elevated temperatures as discussed in section 2.1.4 above. Moreover, in TSA or TCSA, the produced CO₂ is eventually diluted. On the other hand, this might not be a major problem in some

applications such as algae cultivation [178], microbial cultivation [52] or greenhouses [160,162], where only slightly concentrated, instead of pure CO₂, is required. Steam-stripping is a variation of TSA, where steam acts as both a heat source and a stripping gas. Moreover, the moisture can be removed from the product stream as liquid water via condensation, thus allowing the production of high-purity CO₂ [128].

Another method for producing highly concentrated CO₂ is to use combined temperature-vacuum swing adsorption (TVSA), requiring at least three steps, which are adsorption, column evacuation (blow-down) and desorption with combined heating and vacuuming. After adsorption, the adsorption column is evacuated to remove air from the column. Then, under continued vacuuming, the adsorption column is heated to desorb the CO₂ and H₂O. Water can then be condensed to produce a high-purity CO₂ stream [54]. One of the major drawbacks of the TVSA process is that the attainable CO₂ working capacity is limited compared to methods that use a purge gas [86]. The reason for this is, that during desorption the adsorption column is filled by an atmosphere with a high concentration of CO₂, shifting the partial pressure of CO₂ to a much higher value from that of the adsorption conditions. On the other hand, adsorption from humid air limits the partial pressure of CO₂ during regeneration due to co-desorbed H₂O, thus increasing the CO₂ working capacity compared to dry conditions [44,86,179]. Increasing the desorption temperature well above 100 °C may increase the attainable CO₂ working capacity, but also induces the risk of thermal or oxidative degradation of the adsorbent [177]. To avoid confusion between different regeneration methods, the TVSA method discussed above, with closed inlet during desorption, is referred to as “closed TVSA” further in the text.

To remove the working capacity penalty in closed TVSA, a stripping gas could also be utilized. Thus, the combination of two promising methods, TVSA and steam-stripping, have been studied for DAC [44,65,129–131]. In addition to increased working capacity, the advantage of using steam-stripping and TVSA may be the increased kinetics of desorption [129]. On the other hand, the use of steam can increase the thermal energy consumption of the process [131]. Additionally, steam may cause structural changes in the adsorbent and eventually reduce the adsorption capacity, as discussed in section 2.1.4 above.

Another method to increase the working capacity in TVSA is to use air or an inert stripping gas such as nitrogen. In the latter case, the method can be referred to as temperature-concentration-vacuum swing adsorption (TVCSA). Again, using stripping gas introduces the disadvantage of product dilution. Moreover, using a vacuum together with a stripping gas may lead to high vacuum energy costs. On the other hand, using an inert dry gas for stripping can increase the long-term stability of the adsorbent. For example, Yu et al. [177] found that the commercial amino resin Lewatit VP OC 1065 is stable up to 150 °C in inert conditions, while significantly degrading at 120 °C in a CO₂ atmosphere and already at 70 °C in air. On the other hand, using a stripping gas in TVSA leads to a lowered partial pressure for CO₂, which should in turn lead to decreased desorption temperature required to attain similar working capacities as in closed TVSA at a higher temperature. In addition, when using air as a stripping gas, the partial pressure

of oxygen is lowered compared to isobaric TSA. Thus, based on measurements of oxidative degradation at different oxygen concentrations [177], the detrimental effect of air during desorption should be limited when applying vacuum. However, TVCSA or TVSA with an air purge have not been studied in detail as regeneration methods for direct air capture.

The typically suggested process configuration for direct air capture using solid adsorbents is based on a fixed-bed [42,44,86,131] or a monolithic structure [65,180] of the adsorbent. The most commonly studied process option in experimental [42,54,86,129] or simulation [65,130,131] studies is based on the TVSA scheme, with or without steam stripping. Some differences exist in the practical cyclic DAC processes. In the DAC unit reported by Bajamundi et al. [54], CO₂ desorption is carried out by constantly vacuuming and heating. The produced CO₂ is collected into a buffer tank by using a compressor after the vacuum pump. No separate cooling step is used, leading to partial temperature swing desorption after the actual desorption step, as air is blown through the hot adsorbent beds. This is suboptimal in that a part of the adsorbed CO₂ is wasted after each cycle, and also induces a risk of adsorbent oxidation. The steam-assisted TVSA cycle simulated by Sinha et al. [65] only uses vacuuming for removing air before initiating steam-stripping, and during a separate cooling step before initiating adsorption.

2.2.2 Cost and specific energy requirement

As discussed in section 1.2.2, the cost estimates for DAC range from around 80 €/t_{CO₂} up to over 800 €/t_{CO₂}. An even wider cost range can be obtained when varying different process parameters from optimistic to pessimistic extremes, although the mid-range estimates for the cost of captured CO₂ lie somewhere between under 100 €/t_{CO₂} up to under 200 €/t_{CO₂} (e.g. 86-221 USD/t_{CO₂} [181]) or up to 250 €/t_{CO₂} for DACCS (100-300 USD/t_{CO₂} [25]). Similarly, future projections of the DAC cost development are highly uncertain, relying strongly on assumptions about technical parameters and learning rates [69]. While the immaturity of the DAC technology can explain some of the higher cost values, there is clearly a need for more detailed technical data about the process for more accurate cost estimates. Therefore, rather than comparing cost numbers reported in the literature directly with each other, a more useful approach from an engineering point-of-view is to identify the most important cost components of the process.

The cost of the adsorbent-based DAC process in an automated system can be roughly divided into the capital cost of the process equipment and adsorbent, and the operational costs, which mainly arise from the energy demand of the process. The process equipment such as air blowers, vacuum pumps and adsorption columns are mostly mature technology, and can be argued to be easily optimized for DAC. The cost of these components can be expected to come down with economies of scale and general development of technology, such as novel materials. However, the development of CO₂ adsorbents is yet an emerging field, with significant challenges, especially in terms of CO₂ capacity and adsorbent stability, as discussed in section 2.1 above.

Some of the main challenges of amine-based adsorbents also make the estimation of the effect of adsorbent cost on the total cost of DAC difficult. Sinha et al. [65] simulated the DAC process using two amine-functionalized MOFs, finding that depending on the adsorbent price and lifetime, the cost of the adsorbent can become the dominant factor of the capital cost and even the total cost of captured CO₂. For example, using diamine-functionalized Mg₂(dobpdc), the capital cost of the adsorbent was estimated to be 16-72% of the total costs of the produced CO₂ [65,182]. On the other hand, Azarabadi and Lackner [145] evaluated the profitability of DAC by calculating the maximum allowable budget (MAB) of the adsorbent to allow the process to economically break even at some point in the process lifetime. For example, they evaluated that with a 1-year adsorbent lifetime, neither of the MOF adsorbents evaluated by Sinha et al. [65] could be affordable. On the other hand, they found that if the adsorbent has a low adsorption capacity, it cannot reach a high MAB even if stable for tens of thousands of cycles. Thus, they concluded that high stability cannot compensate for a low adsorption capacity and kinetics. The authors also emphasized the need for more data about the degradation rate and the kinetics of CO₂ sorbents.

The contribution of the energy requirements to the total cost of DAC are highly dependent on the contribution of other uncertain components, especially the adsorbent cost discussed above. In the diamine-functionalized Mg₂(dobpdc) steam/TVSA case evaluated by Sinha et al. [65,182], the operating costs were 15-47% of the total cost, being heavily dependent on the contribution of the adsorbent cost. In a later work, Sinha and Realf [181] evaluated that the operating costs arising from the energy requirements could contribute to around 10-13% of the total cost. Thus, based on these numbers, it would seem that the capital cost, especially due to the adsorbent cost, dominates the total cost of DAC. However, the energy requirement values may vary significantly depending on the process configuration and are subject to uncertainties. Therefore, the energy requirement of the process should not be overlooked as a component of the total cost of CO₂ capture from air.

The energy requirement of the cyclic DAC process typically mainly consists of the electricity consumption of the air blowers, vacuum pump and compressor, and the heat demand of the adsorbent regeneration. The heat demand originates from the sensible heat of the adsorbent and the adsorbed species as well as the (latent) heat of desorption of CO₂ and H₂O. Typically, the heat demand dominates the total energy requirement. For example, Kulkarni and Sholl [180] estimated the total energy demand of a steam-stripping DAC process to be around 6.3 GJ/tCO₂, of which heat demand contributed 94%. In the amine/MOF-based DAC processes simulated by Sinha et al. [65,182], a major part of the total energy consumption was sensible heat of the adsorbent and monolith wall. For example, using diamine-functionalized Mg₂(dobpdc), the energy consumed by air blowers was around 0.66 GJ/tCO₂, while the sensible heats of the adsorbent and the monolith were around 0.50 GJ/tCO₂ and 1.80 GJ/tCO₂, respectively [182]. On the other hand, the energy consumed by vacuum pumps was only 0.07 GJ/tCO₂. In later work, Sinha and Realf [181] evaluated that the contributions of electrical and thermal energy in a steam-assisted TVSA DAC process using MOFs were up to 1.12 GJ/tCO₂ and 4.8 GJ/tCO₂, respectively. Stampi-Bombelli et al. [131] also simulated the TVSA process with a steam

purge, finding an even higher contribution due to the thermal demand in the process. At maximum CO₂ productivity, the energy requirement for heat was high, being around 35 GJ/tCO₂. On the other hand, the electrical energy consumed by air fans and vacuum pumps was only around 0.35 GJ/tCO₂, perhaps due to the flat fixed-bed structure.

Achieving both maximal CO₂ productivity and minimal specific energy requirement in DAC may be challenging, and rather a trade-off between these typically exists [130,131]. Stampi-Bombelli et al. [131] concluded, that to maximize CO₂ productivity, it is most reasonable to use low vacuum pressures such as 50-100 mbar together with a steam purge during desorption. On the other hand, to minimize the energy requirement, higher vacuum pressures should be used, while limiting the amount of steam used. Zhu et al. [130] also simulated a steam-TVSA DAC process, finding optimized cases in terms of the CO₂ productivity and the specific energy requirement. With a maximal productivity of 5.5 molCO₂/(kg_{sorbent}·day), the specific energy requirement was 11.6 GJ/tCO₂. On the other hand, by reducing the desorption time and steam flow rate, the energy requirement could be reduced to around half, while the CO₂ productivity would decrease below 4 molCO₂/(kg_{sorbent}·day). Thus, by varying parameters such as the cycle times, vacuum pressure and amount of steam or temperature during desorption, the DAC process can be tailored for either maximal CO₂ productivity or minimal energy requirement. The optimal selection of parameters in each case may depend on the cost of the electricity and the availability of waste heat. The cost of heat for adsorbent regeneration may be avoided by integration of DAC in e.g. the power-to-gas process, where even autothermal operation can be achieved [183]. It should also be taken into account that based on the evaluations of the operating vs. capital costs [65,181,182], an increase in CO₂ productivity probably has more leverage on the total cost of the process than a similar percentage decrease in the specific energy requirement.

As discussed above (sections 2.1.2 and 2.1.3), the co-adsorption of H₂O usually increases the CO₂ capacity in amine-based adsorbents. However, co-adsorbed water may also have a negative impact on the process by increasing the heat demand during regeneration. For example, Drechsler and Agar [184] reasoned that the heat demand of the process may increase by up to several times from that of dry adsorption. The heat demand can be expected to be especially high with adsorbents that have high adsorption capacities toward water. For example, Gebald et al. [73] measured around 7.4 mmolH₂O/g_{sorbent} on amine-functionalized NFC at 80% RH at 23 °C, being around 4 times the CO₂ adsorption capacity from air in similar conditions. It may be difficult to avoid the water co-adsorption even with more hydrophobic support materials such as polymeric resins, since it has been found that most of the H₂O adsorption takes place on the supported amines in these materials [72]. On the other hand, Bos et al. [44] found that the enhancing effect of water on the CO₂ working capacity led to a decreased specific energy requirement, even though the sensible heat of the adsorbed H₂O increased. Thus, it is important to take the contribution of H₂O properly into account in the evaluation of CO₂ productivity and the specific energy requirement of the process.

The specific energy requirement of DAC can be reduced via process design. To lower the electrical energy consumption of the adsorption step, a commonly proposed method is to use a monolithic adsorbent to minimize the pressure drop of blowing air through the adsorbent [65,180,185]. However, achieving a high amine loading while maintaining the openness of the monolith apertures may be a difficult task. On the other hand, if the adsorbent monolith has too much open space in the apertures, diffusion resistance increases in the bulk of the pore, i.e., most of the incoming air will not get in contact with the amine sites and the fraction of captured CO₂ is lowered, which will prolong the adsorption step. If using a fixed-bed configuration, the pressure drop can be minimized by using a low bed length to diameter (L/D) ratio [54,131]. Also, an optimum needs to be established in terms of the adsorption step time. A too short adsorption time will leave most of the adsorbent bed unsaturated, thus wasting much of the available adsorption capacity. On the other hand, because the adsorption rate is eventually lowered [186–188], aiming at full saturation of the bed will lead to a prolonged adsorption step, and thus leads to an increased specific energy consumption and reduced daily productivity.

To minimize the regeneration energy requirement, the heat demand is the top priority, since it typically dominates the total energy requirement, as discussed above. To minimize heat losses in adsorbent regeneration, resistive heating of the adsorbent or the monolith could be used instead of separate heat transfer elements. Sadiq et al. [189] reported the pilot-scale results of a DAC system utilizing a proprietary MOF-polymer composite adsorbent that is coated onto resistive heating sheets. The process cycle was based on a similar type TVSA technology as described in section 2.2.1 above but uses resistive heating by applying a voltage. The regeneration energy requirement was evaluated to be around 5.8 GJ/tCO₂, which is on a similar scale to results of the simulation studies reported above. On the other hand, to limit the parasitic heat demand caused by co-adsorbed water, heat recovery could be utilized [184].

Another proposed method to reduce the energy requirement of DAC is to utilize natural temperature cycling, e.g., by adsorbing during the night time and desorbing at a naturally higher temperature during the day. However, while this can minimize the heat demand, it also severely restricts the productivity of the process by only allowing one adsorption/desorption cycle per day. Thus, Kulkarni and Sholl [180] found that only using diurnal heating and cooling not only reduced CO₂ productivity but also increased the overall specific energy requirement of the process. However, lowering the product CO₂ purity could reduce the energy requirement of DAC, as argued by Wilcox et al. [190] based on work of separation calculations. A lower product purity allows the use of process types such as TSA and TVCSA, leading to a higher working capacity (see section 2.2.1). In addition to the methods discussed here, attempts have been made to improve the energy requirement and other aspects of the DAC process through alternative process configurations, which are discussed briefly in the next section.

2.2.3 Alternative process configurations

Other process configurations than the cyclic TVSA process relying on amine-based adsorbents have also been suggested for DAC. Yu and Brillman [191,192] studied a radial flow configuration for DAC, arguing that this process could have a lower pressure drop and would be more easily scalable compared to a conventional axial flow fixed bed configuration. Using the commercial Lewatit VP OC 1065 as adsorbent, the energy requirement of adsorption was evaluated to be 0.7-1.5 GJ/tCO₂. Zhang et al. [193] studied a fluidized-bed process for DAC, using PEI-loaded mesoporous silica with an adsorption capacity of around 1.7 mmol_{CO₂}/g_{sorbent}. A high CO₂ removal rate of almost 100% was obtained using a bubbling fluidized bed configuration. However, it should be noted that such a high removal rate should not be a design criterion, because DAC is a separation rather than a purification process. The observed fast kinetics of this design came with a high pressure drop of 2500 Pa. Consequently, the authors proposed a circulating fluidized bed (CFB) concept to lower the pressure drop to 572 Pa and allow the continuous feed of air into the system. The heat and electricity demands of a 40 tCO₂/day CFB process were evaluated to be 3.2 and 3.4 GJ/tCO₂, respectively. Drechsler and Agar [194] suggested a moving belt DAC to allow for more complete recovery of sensible heat compared to the cyclic adsorption/desorption process.

Despite the disadvantage of low selectivity towards CO₂ in ambient conditions, zeolites have also been suggested for process-scale direct air capture. Wilson and Tezel [195] studied the use of zeolites in a TVSA process, using a purification-type adsorption bed configuration with a high L/D ratio and thus high pressure drop of 0.35 atm. Additionally, the suggested process required very high regeneration temperatures of up to 350 °C. Thus, the specific energy requirement for CO₂ capture was around 16-17 GJ/tCO₂, which is fairly high compared to the values estimated in section 2.2.2 above. Moreover, due to the severe competition of H₂O with CO₂, the incoming air needs to be dried, leading to significant additional energy demands. For example, the authors evaluated that at 23.5 °C with 22% RH, the energy demand for air drying is 16.8 GJ/tCO₂. Santori et al. [196] proposed a different type of DAC process based on a series of zeolite adsorbent beds where CO₂ is adsorbed from the air in the first bed. When heating the first bed, CO₂ is desorbed, thus producing a slightly concentrated CO₂ flow that is adsorbed in the second bed. This is repeated for a number of beds until the CO₂ concentration and pressure in the last bed are sufficient for underground storage. It was claimed that the process worked with a specific energy requirement below 40 GJ/tCO₂, producing >95% CO₂ at close to a 10 bar pressure. However, again, the feed air would require pre-drying, which would increase the energy demand significantly. The results of these studies point out the importance of adsorbent selectivity towards CO₂ in the DAC process.

The alternative processes discussed in this section do not seem to offer significant improvements in terms of the CO₂ productivity or the specific energy requirement compared to the cyclic adsorption/desorption process with an axial flow configuration, an amine-based adsorbent and desorption using steam or other heat source coupled with

a vacuum. However, some of these concepts are at a very early stage of development, and detailed process comparisons are needed.

2.2.4 DAC process research gaps

Although the most important cost components of the DAC process have been identified and evaluated in the literature, the cost estimates of DAC are still uncertain. For improved techno-economic analysis and the process optimization of DAC, more data is required, especially about the amine-functionalized adsorbents. Often, the evaluation of CO₂ adsorption capacity has been done in a very limited set of conditions, such as using dry gases at room temperature. Although important in terms of the specific energy requirement, the H₂O adsorption performance data is often lacking, except for a few cases (see e.g. [72,73]). The lack of knowledge about adsorbent degradation means there is a difficulty in estimating the rate at which the CO₂ capacity drops, and how the drop rate evolves over successive adsorption/desorption cycles [145]. Thus, more comprehensive cyclic adsorption/desorption testing in varying conditions is required. Decreasing the cost of DAC also requires innovative process design. However, a comprehensive evaluation of other process types than closed TVSA or steam-assisted TVSA for DAC, experimentally or otherwise, is lacking in the literature.

A significant deficiency in the simulation of amine adsorbent-based direct air capture in the literature [65,130,187] is the lack of comprehensive models that take into account the enhancing effect of humidity on CO₂ adsorption capacity. Wurzbacher et al. 2016 [179] used bilinear interpolation from a few points of CO₂ and H₂O co-adsorption to consider the effect of humidity on the CO₂ capacity. Stampi-Bombelli et al. [131] used a modified Toth isotherm model with two additional parameters to consider the effect of humidity. However, the accuracy of these efforts in describing humid CO₂ isotherms has not been assessed. Jung and Lee [197] reported a CO₂ isotherm model based on the reaction mechanisms of CO₂ and H₂O on amine-functionalized adsorbents (Equations 2.1-2.3) to consider the effect of humidity in PCC conditions. However, it was not deducible whether the reported model could accurately describe the co-adsorption of CO₂ and H₂O in DAC conditions. Thus, significant scientific effort is required in several areas to improve the knowledge of the DAC process utilizing amine-based adsorbents. This thesis aims to improve the understanding in these areas of DAC research.

3 Experimental and modelling methods

In this thesis, experimental and modelling work was combined to study CO₂ adsorption from air using an amine-functionalized resin. The experimental and modelling work was done in VTT Technical Research Centre of Finland Ltd., except for structural characterizations of the adsorbent. The sections below describe the used experimental and modelling methods in this work.

3.1 Experimental methods

The adsorbent used in this thesis is a proprietary amine-functionalized resin used e.g. in a demonstration DAC device delivered to VTT by Oy Hydrocell Ltd. The DAC device has been used in experimental campaigns that demonstrated PtX [20] and the cultivation of protein-rich microbes [52]. The operation and performance of the device has been reported in detail by Bajamundi et al. [54]. The experimental work in this thesis is based on using the resin in laboratory-scale experiments as described in the chapters below.

3.1.1 Adsorbent characterization

The structural characterization of the adsorbent was carried out in LUT University, except for the elemental analysis that was conducted by Eurofins Labtium Oy. The surface area and pore volume were studied by Micromeritics Gemini V via a BET-BJH analysis. The particle size distribution was obtained using a Malvern Mastersizer 3000 Aero Laser diffractometer. The chemical structure of the adsorbent and adsorption mechanism were studied using a PerkinElmer Frontier FTIR with Attenuated Total Reflectance (ATR) sampling. More details on the physicochemical characterizations can be found in Article I [198].

3.1.2 Fixed-bed CO₂/H₂O adsorption setup (Articles I-II)

By far the most used experimental devices in the literature related to DAC use either thermogravimetric analysis (TGA), volumetric measurement or fixed-bed adsorption for the determination of adsorption capacities and adsorption kinetics. The advantage of TGA is that the amount of adsorbed CO₂ is easily calculated from the mass change, also giving an indication of adsorption kinetics. Additionally, the required sample amount is typically only on the mg-scale. However, in humid conditions the adsorption capacities of CO₂ and H₂O can be difficult to discern, usually requiring saturating the sample with H₂O before CO₂ adsorption is initiated. Moreover, the ultra-dilute concentration of CO₂ increases the significance of mass transfer resistance at the gas-solid interface, thus potentially limiting the kinetics in a TGA setup. In TGA, slow kinetics may be promoted if the crucible holding the sample does not allow the gas to flow through the sample. In this work, fixed-bed adsorption was used due to flexibility in the study of both adsorption and desorption conditions.

The first experimental device for fixed-bed gas adsorption used in Articles I-II is illustrated in Figure 3.1. A sample of amine-functionalized resin was fixed into the adsorption column with quartz wool. The adsorption column was assembled from stainless steel Swagelok parts, and the temperature was controlled using laboratory heating tape and a PID-controller (Article I). The temperature was measured from the middle of the adsorbent bed and outside the column wall. The different CO₂ concentrations needed for isotherms in the dilute region (100-5000 ppmv) were acquired by using an Environics series 2000 gas mixer to mix 1% CO₂/N₂ and pure N₂. In humid experiments, the gas mixture was humidified using a Hovacal digital 122-SP moisture calibrator. Gasmeter online FTIR gas analyzers before and after the column were used to measure the CO₂ and H₂O concentrations. The pressure drop was also measured.

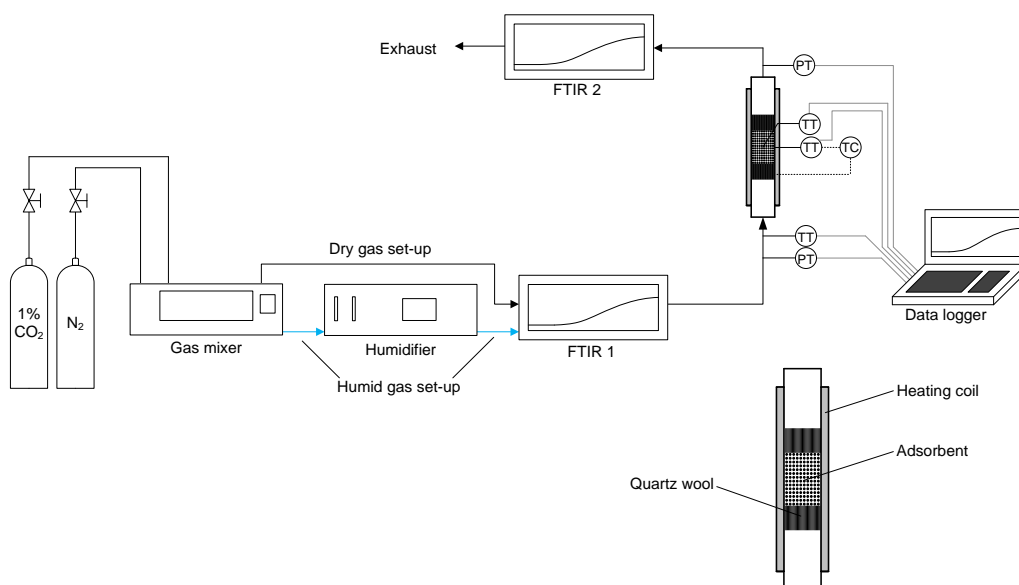


Figure 3.1: The experimental set-up for adsorption capacity determination. From Article II.

The experimental setup was operated with a manual change of gas composition in the gas mixer and temperature set point in the temperature controller. In Article II [199], the adsorption was also measured below 25 °C. To achieve 0 °C and -10 °C, the heating tape had to be removed and the column placed into a dewar containing salt solution and ice. Optionally, a Liebig-condenser with cooling liquid circulation was used to reach -10 °C and 13 °C. Due to the practical limitations of the experimental setup such as lack of pressure control and laborious control of temperature and the feed gas composition, a new experimental device was designed that is described in the following section.

3.1.3 Automatic adsorption/desorption device (Articles III-IV)

The improved experimental setup for studying CO₂ adsorption and desorption with solid adsorbents was designed and built in VTT and is depicted in Figure 3.2. The setup has several mass-flow controllers (MFCs) which allow the convenient change of gas composition. The gas can be directed to the adsorption column via two routes, or the column can be bypassed. This allows, e.g., purging the column with inert gas while measuring the feed concentration of gas directed through the column bypass. The feed gas can also be humidified. Pressure in the adsorption column can be controlled via two pressure control valves and a vacuum pump, which allow either normal/overpressure or vacuum operation. The temperature of the column is controlled by circulating either cool or hot liquid in the adsorption column jacket using two Julabo Corio CD 200 F circulators.

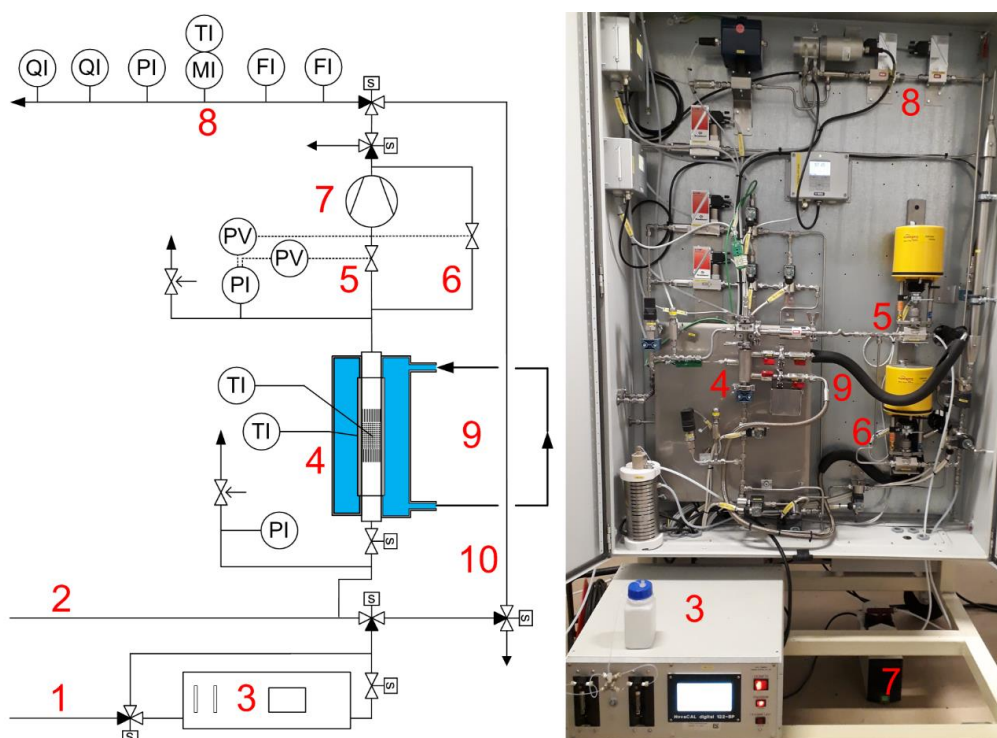


Figure 3.2: Scheme (left) and a photo (right) of the experimental device for adsorption and desorption of CO₂ and H₂O. The numbers show the main sections and components of the device as follows: 1) inlet route 1; 2) inlet route 2; 3) humidity calibrator; 4) the adsorption column; 5) vacuum route and pressure control valve; 6) normal/overpressure route and pressure control valve; 7) vacuum pump; 8) outlet measurements; 9) heating/cooling liquid circulation; 10) column bypass route.

The gas composition of the gas in the outlet is measured via ppm- and %-scale CO₂ analyzers and a humidity measurement. The flow-rate is measured with two Bronkhorst

mass flow meters calibrated to measure up to 21 ml/min and 2100 ml/min. The pressure is measured before and after the adsorption column and in the outlet. Temperature is measured inside the column and outside the adsorption column wall. The probe inside the column is 1 cm into the bed, being approximately in the middle and $\frac{1}{4}$ of the bed length with 0.5 g and 1 g of the amino resin, respectively. A more detailed description of the device and its components is found in Article III [200].

The device is operated via a LabVIEW-based data acquisition and control software. The device can be operated by manually changing the parameters in the process chart or by using stepwise sequences that allow automatic operation. The sequences are built in a spreadsheet by listing the set-points of MFCs, pressure control valves and magnetic valves in steps.

The operating condition limits in the adsorption column are:

- Pressure: from 11-12 mbar vacuum up to approximately 5 bar overpressure.
- Temperature: from sub-zero up to 100 °C, depending on flow-rate. A lower minimum and a higher maximum temperature may be possible depending on the bath fluid in the heating/cooling liquid circulators.
- Flow rate (MFC upper limits): 0.1 l/min, 1 l/min and 10 l/min.

The operating conditions allow the study of CO₂ adsorption and desorption conditions relevant to direct air capture. The automatic sequence-based experimental runs allow more efficient use of time and resources with excellent repeatability. Moreover, the device is modifiable e.g. by introducing a larger adsorption column. The types of fixed-bed experiments done in this thesis are described in the following section.

3.1.4 Adsorption/desorption experiments

In most experiments, 0.5 g of the amino resin adsorbent was loaded into the adsorption column and fixed with quartz wool. However, in Article III, in experiments where the dynamics of regeneration were studied more closely, 1 g samples were used. In all experiments, the adsorbent sample placed in the adsorption column was first regenerated via TCS (Articles I-III) or TVCS (Articles III-IV). The sample was then cooled down to the adsorption temperature in an N₂ flow, and adsorption was started by introducing the wanted CO₂/H₂O/N₂ mixture or dry or humidified compressed air into the column. Adsorption was followed by regeneration, which was done in various ways, as explained below. Figure 3.3 below shows an example of a full adsorption/desorption cycle.

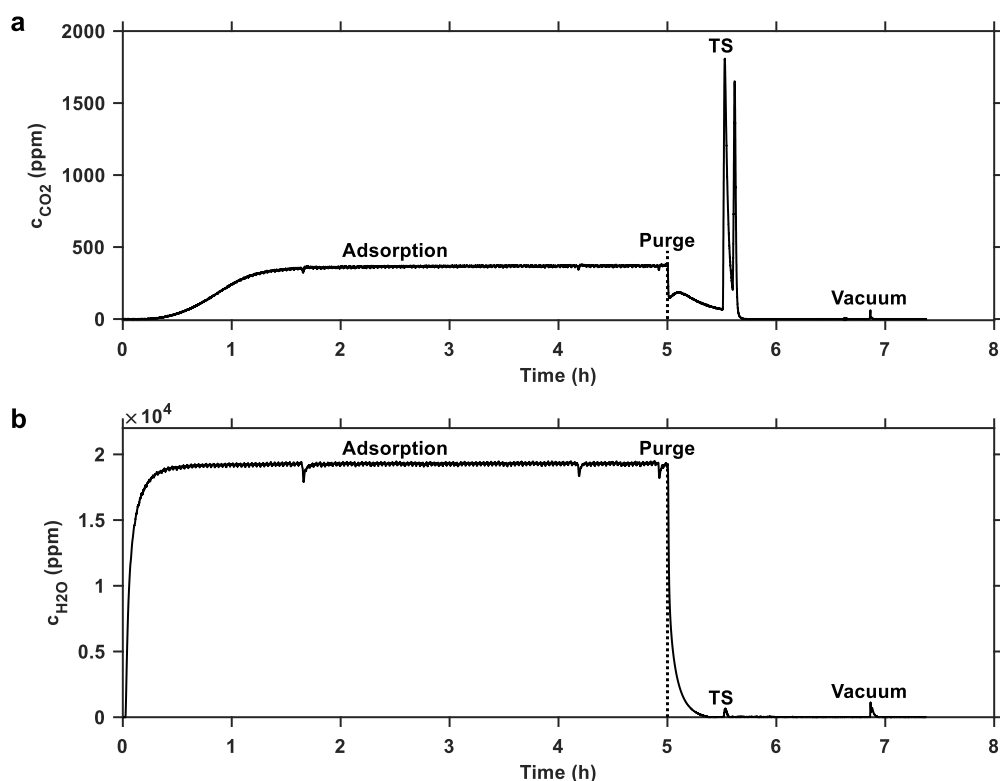


Figure 3.3: Experimental TVCSA cycle showing the concentration profiles of a) CO₂; b) H₂O at 500 ml/min at 25 °C. Dashed lines show the end of the adsorption phase. ‘Purge’ is N₂ flow at 1000 ml/min and ‘TS’ is a temperature swing to 100 °C followed by vacuum and flow rate decrease to 100 ml/min. The ‘TS’ peak is split due to temperature ramping.

In Articles I-II, only TCSA experiments were done due to lack of total pressure control in the first experimental setup, and because the focus was to measure the CO₂ isotherms. After 120 min of adsorption in dry or humid conditions, a concentration swing was initiated by changing the feed gas from the adsorption mixture to an N₂ purge for 30 min. Then, a temperature swing was initiated by heating the column to 90 °C for 60 min. For a new isotherm point measurement, the sample was then cooled down back to the adsorption temperature, followed by adsorption in the new conditions. The total flow rate was kept at 1 l/min for the whole cycle. The adsorption temperature was varied from 25 °C to 50 °C in Article I and from -10 °C to 90 °C in Article II. The CO₂ isotherms were measured using CO₂ concentration in the range of 100-5000 ppmv.

Article III focused on the desorption phase, and thus the adsorption phase was kept similar by using dry near 400 ppm CO₂/N₂ or compressed air at 25 °C for 120 min at a total flow rate of 1 l/min. However, the desorption phase was varied to study different regeneration methods. A temperature swing was used in each method, and was done by using

temperature ramping in two steps, consisting of 60 min 'TS1' at 60 °C and 60 min 'TS2' at 100 °C. The TCOSA scheme was similar to that used in Articles I-II, except temperature ramping was used. TSA was conducted by directly introducing the temperature swing after the adsorption, and for full regeneration an N₂ purge was initiated after 'TS2'. In TVSA with air purge, a CO₂-containing flow was maintained after adsorption while applying a vacuum, followed by a temperature swing. The sample was then fully regenerated by initiating an N₂ purge after the second temperature swing step. TVCSA was similar to TVSA with air purge, but instead of using a CO₂-containing gas after adsorption, the gas flow was switched to N₂. The vacuum pressure in TVSA and TVCSA was controlled via the pressure control valve in the range of 25-500 mbar. In closed TVSA, the column inlet was closed after the adsorption phase, and a vacuum was applied, followed by a temperature swing. Full regeneration of the sorbent was achieved at the end of the run by opening the column inlet and introducing an N₂ purge.

In Article III, different flow rates during desorption were used depending on the purpose of the experiment. For the working capacity study comparison and cyclic experiments, a total flow rate of 1 l/min was used during both adsorption and desorption phases. However, in experiments where desorption kinetics and specific energy requirement were studied, the total flow rate of the feed was 40 ml/min during desorption. The cyclic experiments were conducted by repeating the cycle for up to 23 times.

In Article IV [201], a TVCSA scheme was used in all experiments. For measuring humid pseudo-equilibrium isotherms, adsorption was carried out for 5-6 hours using 200-4000 ppmv CO₂ with approximately 0.2-2 vol-% H₂O balanced with N₂. The adsorption temperature was 25-50 °C. During adsorption phase the flow rate was 500 ml/min except for the 35 °C isotherm with 0.2 vol-% H₂O, where the flow rate was 200 ml/min. Adsorption was followed by an N₂ purge at 1000 ml/min, a temperature swing up to 100 °C and finally a vacuum with purge flow rate changed to 100 ml/min. A cyclic experiment was carried out also using TVCSA with an otherwise similar scheme to the isotherm experiments but using a flow rate of 1000 ml/min during adsorption and an adsorption time of 120 min. Moreover, a nearly 2-day adsorption test was carried out using 100 ml/min of humidified compressed air with approximately 400 ppmv CO₂ and 2 vol-% H₂O. A summary of the regeneration schemes used in this work is found in Table 3.1.

Table 3.1: The used regeneration method schemes.

Process	Article(s)	Purge 1	TS 1	TS 2	Purge 2
TCSA	I,II	0 ppm CO ₂	-	90 °C	-
TCSA	III	0 ppm CO ₂	60 °C	100 °C	-
TSA	III	-	60 °C	100 °C	0 ppm CO ₂
TVSA	III	400 ppm CO ₂ , vacuum	60 °C	100 °C	0 ppm CO ₂
TVCSA	III	0 ppm CO ₂ , vacuum	60 °C	100 °C	-
closed TVSA	III	No inflow. Column inlet closed, vacuum	60 °C	100 °C	0 ppm CO ₂
TVCSA	IV	0 ppm CO ₂ , vacuum	-	100 °C	-

3.1.5 CO₂/H₂O capacity calculation

The capacity calculation in this work was based on the numerical integration of the mass balance of adsorbed or desorbed species i in the fixed-bed column. The resulting equation for calculating the volume of the adsorbed species $V_{i,\text{exp}}$ is:

$$V_{i,\text{exp}} = \int_{t_0}^t \dot{V}_{\text{tot}} (y_{i,\text{in}} - y_{i,\text{out}}) \quad (3.1)$$

where t is time, \dot{V}_{tot} is the total flow rate and y_i is the volume fraction of species i . More specifically, $y_{i,\text{in}}$ is the volume fraction in the gas coming into the adsorption column (feed) and $y_{i,\text{out}}$ is the volume fraction in the gas leaving the column. For the desorption capacity, the feed volume fraction is subtracted from the outlet volume fraction in the mass balance of Equation 3.1. The experimental adsorbed species capacity $q_{i,\text{exp}}$ was then calculated by using ideal gas law:

$$q_{i,\text{exp}} = \frac{PV_{i,\text{exp}}}{R_{\text{id}}T \cdot m_{\text{a}}} \quad (3.2)$$

where P is total pressure, R_{id} is the ideal gas coefficient, T is temperature and m_{a} is the mass of the adsorbent. In Articles I-II, no corrections to the measured volume fractions of CO₂ and H₂O were made, and the conditions for capacity calculation were selected based on the gas mixer specifications of 273.15 K and 1.01325 bar. Additionally, the total volume flow rate used in Equation 3.1 was a constant 1 l/min.

In Articles III-IV, the calculations were made using standard ambient temperature and pressure (SATP) of 298.15 K and 1.01325 bar. Although the true volume fraction does not change with changing pressure or temperature, the measured CO₂ volume fractions

had to be compensated for the measured temperature and pressure due to the measurement technique in the following equation [202]:

$$y_{\text{CO}_2,\text{SATP}} = \frac{P_{\text{SATP}}}{T_{\text{SATP}}} \cdot \frac{y_{\text{CO}_2,\text{meas}} \cdot T_{\text{out,meas}}}{P_{\text{out,meas}}} \quad (3.3)$$

where $y_{\text{CO}_2,\text{SATP}}$ is the temperature- and pressure-compensated CO_2 volume fraction, subscripts ‘SATP’ and ‘meas’ denote the SATP and measured outlet conditions, respectively. Due to the effect of humidity on the absorption strength of CO_2 [203], the temperature- and pressure-compensated volume fraction gained from the ppm-scale measurement (Vaisala GMP343) also had to be compensated for humidity using the following equation:

$$y_{\text{CO}_2,\text{SATP,dry}} = (1 - 1,51 \cdot 10^{-7} y_{\text{H}_2\text{O}} - 2,10 \cdot 10^{-7} y_{\text{CO}_2} - 8,18 \cdot 10^{-11} y_{\text{H}_2\text{O}} y_{\text{CO}_2} + 3,16 \cdot 10^{-11} y_{\text{CO}_2}^2) y_{\text{CO}_2,\text{SATP}} \quad (3.4)$$

The function used to multiply the SATP-corrected CO_2 volume fraction $y_{\text{CO}_2,\text{SATP}}$ in Equation 3.4 was obtained from a linear regression using absolute humidity and measured CO_2 volume fraction as the predictor variables and the ratio of humidity-compensated and non-compensated CO_2 volume fraction as the response variable. The response variable data was gained by measuring a feed gas with 400-4000 ppm CO_2 with and without the internal humidity compensation of the ppm-scale sensor at different humidity levels. As this internal compensation could only be applied with a constant humidity set-point, the regression model was required to conduct this compensation with varying humidity. It should be noted that this humidity compensation is different from the calibration done in Article IV (see Supplementary data of Article III). This is why the results in sections 4.2.2 and 4.5 and Figure 4.18a are slightly different from those in Article IV. However, the differences are so small that they may not be apparent when comparing the figures in Article IV to the corresponding results in sections 4.2.2 and 4.5 and Figure 4.18a.

The volume fraction of water $y_{\text{H}_2\text{O}}$ was calculated from the measured relative humidity RH_{meas} and total pressure at the outlet:

$$y_{\text{H}_2\text{O}} = p_{\text{H}_2\text{O},\text{sat}} \cdot \frac{RH_{\text{meas}}}{100} \cdot \frac{1}{P_{\text{out,meas}}} \quad (3.5)$$

where $p_{\text{H}_2\text{O},\text{sat}}$ is the water vapour saturation pressure at outlet temperature $T_{\text{out,meas}}$. This value along with many thermodynamic constants was acquired using a user-built function ‘refpropm’ in Matlab developed by the National Institute of Standards and Technology (NIST), which uses the REFPROP software to access the NIST database using given temperature and pressure.

With the new experimental device in Articles III-IV, a measured flow rate was used in Equation 3.1 instead of a constant value. Since the mass flow meters were calibrated for air and the density of the measured gas varied due to changes in gas composition, the measured flow rate \dot{V}_{meas} had to be corrected by $\dot{V}_{\text{meas,corr}} = GCF_{\text{N}_2/\text{CO}_2} \cdot \dot{V}_{\text{meas}}$. The gas conversion factor $GCF_{\text{N}_2/\text{CO}_2}$ was calculated in dry conditions based on the volume fraction of CO_2 in the gas mixture:

$$GCF_{\text{N}_2/\text{CO}_2} = \frac{1}{\frac{y_{\text{CO}_2,\text{SATP,dry}}}{GCF_{\text{CO}_2}} + \frac{1 - y_{\text{CO}_2,\text{SATP,dry}}}{GCF_{\text{N}_2}}} \quad (3.6)$$

where GCF_{CO_2} and GCF_{N_2} are the gas conversion factors for CO_2 and N_2 , respectively. In Article III, $\dot{V}_{\text{meas,corr}}$ was used to calculate the capacities ($\dot{V}_{\text{tot}} = \dot{V}_{\text{meas,corr}}$), because the experiments were carried out in dry conditions. However, in humid conditions (Article IV) another correction was required because of humidity to acquire the final corrected total flow rate used for capacity calculation via $\dot{V}_{\text{tot}} = GCF_{\text{hum}} \cdot \dot{V}_{\text{meas,corr}}$. Here the gas conversion factor for the correction for the humidity was calculated by

$$GCF_{\text{hum}} = \frac{c_{p,\text{dry}} \cdot \rho_{\text{g,mix,dry}}}{c_{p,\text{hum}} \cdot \rho_{\text{g,mix,hum}}} \quad (3.7)$$

where c_p and $\rho_{\text{g,mix}}$ are the specific heat capacity and density of the dry or humid gas mixture, respectively [204]. The specific heat capacities were obtained from the NIST library. The densities of the dry and humid gas mixtures in Equation 3.7 were replaced with the molar mass of each gas mixture because the temperature and pressure are identical for both mixtures.

The experimental error was evaluated differently in the articles. In Article II, the experimental uncertainty was evaluated based on the propagation of error using the uncertainty of the gas mixer and FTIR-analyzers. However, as this analysis is based on known uncertainty components, it can be argued that not every factor is taken into account in the resulting uncertainty.

In Article III, the uncertainty was calculated based on repeated experiments. Repeatability in consequent experiments with the same sample was calculated as the standard error of the cyclic experiments. In-house reproducibility was then calculated by subtracting the (average) adsorption repeatability component from the standard error for the adsorption capacities gained in similar conditions with different sample batches of the amino resin. The in-house reproducibility calculated this way and repeatability in different cyclic experiments were combined to calculate the total uncertainty for the different experiment types. In Article IV, repeatability was calculated based on the standard error of the humid

cyclic experiment similarly to Article III. Details of the uncertainty calculations can be found in the Supplementary Data of Articles II and III.

Due to lower uncertainty compared to adsorption capacities, only experimental desorption capacities were used in all the isotherm modelling described in section 3.2.1 below. The capacity obtained from the whole desorption phase with an N₂ purge, temperature swing and vacuum (where used) combined is referred to as the total desorption capacity in this work. The total desorption capacity was mostly used in all the isotherm modelling of this thesis. The difference between the total CO₂ desorption capacity and adsorption capacity was typically found to be negligible, and thus it is warranted calling the modelled CO₂ isotherms adsorption isotherms. However, in Article I, the N₂ purge and temperature swing capacities were also separately calculated. The capacities obtained during the N₂ purge and temperature swing were referred to as the physisorption capacity and chemisorption capacity, respectively. This was based on the assumption that CO₂ desorbed during the concentration swing would be weakly bound, while the strongly bound CO₂ would be removed during the temperature swing.

All capacities presented in this work were corrected for the capacity obtained without a sample, except for the dynamic capacity profiles in section 4.4.1 and thus the productivities calculated from these. In Articles I-II, the capacities were calculated per mass of as-received resin. In Articles III-IV, the capacities were calculated per mass of fully regenerated resin. Additionally, in Article IV, the isotherm capacities were corrected with Equation 3.8:

$$q_{i,\text{corr}} = q_{i,\text{exp}} \cdot \left(1 + \frac{k_{\text{deg}}}{q_{i,0}} N_{\text{cycle}} \right) \quad (3.8)$$

where $q_{i,\text{corr}}$ is the capacity corrected for adsorbent degradation, k_{deg} is the degradation rate, $q_{i,0}$ is the pristine capacity and N_{cycle} is the current cycle number. The degradation rate and pristine capacity were obtained from cyclic tests as the slope and the intercept from linear fit to cyclic desorption capacities, respectively.

3.2 Calculation and modelling methods

The experimental data using the amine-functionalized resin was used in modelling of the CO₂ and H₂O adsorption in DAC conditions. Well-known single-component isotherm models were used to model the equilibrium capacity of CO₂ and H₂O. A kinetic model was developed for modelling the CO₂ adsorption capacity in humid conditions. These models were used for the dynamic modelling of the CO₂ adsorption process. Moreover, the specific energy requirement was calculated for different regeneration processes using models found in the literature. These models and their use are described in detail below.

3.2.1 Isotherm models and working capacity analysis

Various isotherm models can be used to describe the equilibrium adsorption capacity q_i of adsorbed species i by the adsorbent at a given temperature and partial pressure p_i . These models were fitted for their parameters using experimental CO₂ and H₂O capacities. In Article I, the goodness of fit of different well-known isotherm models to experimental total desorption CO₂ capacities was compared. The comparison was made using the Langmuir, Freundlich, Sips and Toth isotherms. The Langmuir isotherm is given by:

$$q_i = \frac{q_m b p_i}{1 + b p_i} \quad (3.9)$$

where q_m is the maximum adsorption capacity at any p_i , and b is adsorption affinity. The Freundlich isotherm is given by:

$$q_i = k_{Fr} p_i^{1/n_{Fr}} \quad (3.10)$$

where k_{Fr} is a parameter specific to the Freundlich model and n_{Fr} is the Freundlich model exponential parameter. The Sips model is a combination of the two models above:

$$q_i = \frac{q_m (b p_i)^{1/n_{Sips}}}{1 + (b p_i)^{1/n_{Sips}}} \quad (3.11)$$

where n_{Sips} is the Sips model exponential parameter. The Toth model is given by:

$$q_i = \frac{q_m b p_i}{(1 + (b p_i)^{t_{Toth}})^{1/t_{Toth}}} \quad (3.12)$$

where t_{Toth} is the Toth model exponential parameter.

In Article I, an attempt was also made to quantify the physisorption and chemisorption capacities separately as described in section 3.1.5. Thus, these capacities were used for isotherm fitting of a derivative of the Toth model reported by Serna-Guerrero et al. [71], which can be used to separately account for physisorption and chemisorption:

$$q_i = \left[\frac{q_{m,physi} b_{physi} p_i}{(1 + (b_{physi} p_i)^{t_{Toth,physi}})^{1/t_{Toth,physi}}} \right]_{physi} + \left[\frac{q_{m,chemi} b_{chemi} p_i}{(1 + (b_{chemi} p_i)^{t_{Toth,chemi}})^{1/t_{Toth,chemi}}} \right]_{chemi} \quad (3.13)$$

The temperature dependence for the Toth equations was obtained by:

$$q_m = q_{m,0} \exp \left[\chi \left(1 - \frac{T}{T_0} \right) \right] \quad (3.14)$$

$$b = b_0 \exp \left[\frac{-\Delta H}{R_{id} T_0} \left(\frac{T_0}{T} - 1 \right) \right] \quad (3.15)$$

$$t_{Toth} = t_{Toth,0} + \alpha \left(1 - \frac{T_0}{T} \right) \quad (3.16)$$

where $q_{m,0}$, b_0 and $t_{Toth,0}$ are the reference parameters of the Toth model at a reference temperature T_0 , χ and α are dimensionless parameters and $-\Delta H$ is the isosteric heat of adsorption at zero fractional loading.

While the CO₂ adsorption capacity on amine-functionalized adsorbents can be described with the type I isotherm models above such as the Toth model [71–73,205], the H₂O adsorption on such materials follows a type III isotherm shape with multilayer adsorption [72,73]. The Guggenheim Anderson De Boer (GAB) isotherm has been used to depict the multilayer type III adsorption of H₂O on e.g. polymeric sorbents [206], foods such as corn and starch [207] and amine-functionalized nanofibrillated cellulose [73]. Thus, the adsorption of H₂O on the amino resin in this work was modelled using the GAB model:

$$q_{H_2O} = \frac{q_{m,mono} CK (p_{H_2O} / p_{H_2O,sat})}{(1 - K (p_{H_2O} / p_{H_2O,sat})) (1 + K (p_{H_2O} / p_{H_2O,sat}) (C - 1))} \quad (3.17)$$

where q_{H_2O} is the H₂O adsorption capacity, p_{H_2O} is the partial pressure of water, $p_{H_2O,sat}$ is the saturation vapour pressure of water and $q_{m,mono}$ is the monolayer adsorption capacity of H₂O. Parameters C and K are temperature-dependent:

$$C = C_0 \exp \left(\frac{\Delta H_C}{R_{id} T} \right) \quad (3.18)$$

$$K = K_0 \exp \left(\frac{\Delta H_K}{R_{id} T} \right) \quad (3.19)$$

where C_0 and K are dimensionless parameters, ΔH_C is the enthalpy difference between mono- and multilayer adsorption and ΔH_K is the enthalpy difference between H₂O condensation and multilayer adsorption. [73,131,206,207]

Isotherm fitting was done by minimizing the residual sum of squares of modelled and experimental capacities using the 'lsqnonlin' -function in Matlab. The normalized standard deviation used in Article I to study the goodness of isotherm fits was calculated by:

$$\sigma_{\text{norm}} = \sqrt{\frac{\sum_{j=1}^n [(q_{i,\text{exp}} - q_{i,\text{fit}}) / q_{i,\text{exp}}]^2}{n-1}} \quad (3.20)$$

where n is the number of experimental points and $q_{i,\text{fit}}$ is the fitted isotherm capacity with the given isotherm model.

In Articles I-II, the equilibrium working capacity of CO₂ was evaluated in different DAC processes by $EWC = q_{\text{CO}_2}(p_{\text{CO}_2,\text{ads}}, T_{\text{ads}}) - q_{\text{CO}_2}(p_{\text{CO}_2,\text{des}}, T_{\text{des}})$, where subscripts ‘ads’ and ‘des’ refer to adsorption and desorption conditions, respectively. The total CO₂ capacity was thus calculated in adsorption and regeneration conditions using the parameters gained from isotherm fitting of the Toth model in Equations 3.13, 3.14, 3.15 and 3.16 (Article I) or 3.12, 3.14, 3.15 and 3.16 (Article II). For pressure-swing adsorption (PSA) and temperature-vacuum swing adsorption (TVSA), impurities were assumed to be removed prior to the regeneration phase. The adsorption column was assumed to be closed from the inlet side in these processes. Therefore, the partial pressure of CO₂ during regeneration could be assumed to be equal to the total pressure inside the column in PSA and TVSA. Thus, working capacity matrices were calculated for different p_i and T conditions to compare regeneration methods. These matrices were then visualized using contour plots.

In Article III, the working capacities were measured experimentally. To compare the regeneration options with the desorption rate taken into account, daily CO₂ productivities were calculated. The productivity was calculated by $WC \cdot N_{\text{cycles}} \cdot M_{\text{CO}_2}$, where WC is working capacity and N_{cycles} is the number of adsorption and desorption cycles in a day. The number of daily cycles was calculated by $N_{\text{cycles}} = (24 \cdot 60 \text{ min}) / (t_{\text{ads}} + t_{\text{des}} + t_{\text{cool}})$, where t_{ads} , t_{des} and t_{cool} are the adsorption time, desorption time and cooling time, respectively. The calculation was based on an adsorption/desorption cycle with a 120 min adsorption step, followed by the desorption time required to reach 90% and 99% of the maximum capacity at 60 °C and 100 °C, respectively. Finally, a 30 min cooling step was assumed at the end of each cycle. The results are discussed in section 4.4.2.

3.2.2 Specific energy requirement of regeneration (Article III)

To compare the energy cost related to different regeneration processes of DAC, the specific energy requirements (SER) of regeneration were calculated. These numbers were calculated using theoretical correlations for the energy requirement of each component and experimental data in dry conditions. The specific energy requirements were evaluated cumulatively by using the total gas volume and CO₂ capacity acquired until time t . The temperature and pressure level measured at time t were used. No energy losses were taken into account, and therefore the SER numbers are ideal. The total SER of regeneration was calculated by $E_{\text{reg,tot}} = E_{\text{fan}} + E_{\text{sen,a}} + E_{\text{sen,CO}_2} + E_{\text{des,CO}_2} + E_{\text{vac}}$, where E_{fan} , $E_{\text{sen,a}}$, $E_{\text{sen,CO}_2}$, $E_{\text{des,CO}_2}$ and E_{vac} are specific energy requirements related to air blowers, sensible heat of the adsorbent, sensible heat of CO₂, desorption enthalpy of CO₂ and vacuum pump. The blower energy was calculated by:

$$E_{\text{fan}} = \int_0^t \Delta p \dot{V}_{\text{tot}} dt \quad (3.21)$$

where Δp is the pressure drop over the adsorbent bed calculated by the Ergun equation:

$$\Delta p = \frac{150 \mu L_{\text{bed}} (1-\varepsilon)^2 v_s}{d_p^2 \varepsilon^3} + \frac{1.75 L_{\text{bed}} \rho_g (1-\varepsilon) v_s^2}{d_p \varepsilon^3} \quad (3.22)$$

where μ is the dynamic viscosity of the gas, L_{bed} is the length of the adsorbent bed, ε is the bed voidage (porosity), v_s is the superficial velocity of the gas, d_p is the particle diameter and ρ_g is the gas density [208]. Sensible heat of the adsorbent without adsorbed species was calculated by:

$$E_{\text{sen,a}} = m_a c_{p,a} \Delta T \quad (3.23)$$

where $c_{p,a}$ is the specific heat capacity of the adsorbent and ΔT is the temperature difference of the temperature swing from adsorption temperature to temperature at time t . The sensible heat of desorbed CO_2 was calculated by

$$E_{\text{sen,CO}_2} = m_{\text{CO}_2} c_{p,\text{CO}_2} \Delta T \quad (3.24)$$

where m_{CO_2} is the mass of desorbed CO_2 and c_{p,CO_2} is the specific heat capacity of CO_2 . The desorption heat of CO_2 was calculated by:

$$E_{\text{des,CO}_2} = \int_0^t (-\Delta H_{\text{CO}_2}) \dot{n}_{\text{CO}_2} dt \quad (3.25)$$

where $-\Delta H_{\text{CO}_2}$ is the desorption enthalpy of CO_2 and \dot{n}_{CO_2} is the molar flow rate of CO_2 during desorption. Desorption enthalpy was gained by fitting the Toth isotherm to dry CO_2 isotherms. The energy consumed by the vacuum pump was calculated according to [180]:

$$E_{\text{vac}} = -P_{\text{out}} \int_0^t \dot{V}_{\text{tot}} dt \left(\frac{P_1}{P_{\text{out}}} - \frac{P_2}{P_{\text{out}}} + \ln \left(\frac{P_2}{P_1} \right) \right) \quad (3.26)$$

where P_{out} is the mean atmospheric pressure measured from the outlet, P_1 is the column pressure before vacuuming and P_2 is the column pressure at time t . The column pressure was measured from after the adsorption column. The parameters used for the SER calculations can be found in Table 3.2 below. For details of the measurements used in the calculations, refer to section 3.1.3, Figure 3.2 and Article III.

Table 3.2: The constants and variables used to calculate the specific energy requirement of regeneration in section 4.4.2. *NIST database values were obtained with the ‘refpropm’ - user-built function in Matlab and REFPROP software using the specified gas composition, temperature and pressure as inputs. Parameter values from Supplementary Data of Article III.

Quantity	Parameter	Value	Source
\dot{V}_{tot}	Total flow rate	Variable	Measured from the outlet.
μ	Dynamic viscosity	Variable	NIST database*.
L_{bed}	Bed length	0.034-0.035 m	Calculated from the sample mass, column dimensions and bulk density.
ϵ	Bed voidage	0.375	Adsorbent SDS.
v_s	Superficial velocity	~ 0.01 m/s	Calculated from the measured flow rate.
d_p	Particle diameter	$6 \cdot 10^{-4}$ m	Median value (see section 4.1).
ρ_g	Gas density, nitrogen	Variable	NIST database*.
m_a	Adsorbent sample mass	$0.98-0.99 \cdot 10^{-3}$ kg	Measured. Mass of the pre-adsorbed species subtracted.
$c_{p,a}$	Specific heat capacity of the adsorbent	1580 J/(kg K)	From [209]. Resin matrix similar type.
ΔT	Temperature difference of adsorption and desorption	Up to 75.6 °C	Measured from inside the adsorbent. The difference between the heating starting point and the current temperature.
c_{p,CO_2}	Specific heat capacity of CO ₂	851-917 J/(kg K)	NIST database*
$-\Delta H_{\text{CO}_2}$	CO ₂ desorption enthalpy.	62200 J/mol	From the Toth isotherm fitting using dry isotherm data (Table 4.1).
\dot{n}_{CO_2}	Molar flow rate of CO ₂	Variable	Calculated from the capacity profile and sample mass.
P_{out}	Outlet pressure	~ 1.013 bar	The measured mean outlet pressure during given step.
P_1	Pressure before vacuuming	~ 1 bar	Measured from after the column at the start of vacuuming.
P_2	Pressure after vacuuming	11-500 mbar	Measured from after the column.
ρ_B	Bulk density	450 kg/m ³	Measured using the pre-dried sample.

3.2.3 Kinetic CO₂ adsorption model (Article IV)

As described in section 2.1, the adsorption of CO₂ in amine-functionalized adsorbents occurs via formation of a zwitterion that is stabilized by another amine in dry conditions or water in humid conditions. Based on the reaction mechanism presented in Equations 2.1, 2.2 and 2.4, the adsorption rates r of CO₂ using primary amines can be presented by:

$$r_1 = k_{f,1}[\text{R-NH}_2]^2[\text{CO}_2] - k_{b,1}[\text{RNHCOO}^-:\text{RNH}_3^+] \quad (3.27)$$

$$r_2 = k_{f,2}[\text{R-NH}_2][\text{CO}_2][\text{H}_2\text{O}] - k_{b,2}[\text{RNHCOO}^-:\text{H}_3\text{O}^+] \quad (3.28)$$

where k_f and k_b are the kinetic constants of forward and backward reactions, respectively. Subscripts 1 and 2 refer to reactions in dry and humid conditions, respectively. Species in square brackets are the concentrations of the given reaction species. It should be noted that the reaction stoichiometry should be similar in the case of secondary amines, and the resulting mass balance equations can thus be assumed valid for both primary and secondary amines. To determine the mass balance equations of CO₂, the gas species concentrations can be replaced with partial pressures and the product concentrations can be replaced with CO₂ adsorption capacities such as in the model presented by Jung and Lee [197]. The available amine sites concentration is represented as the balance $q_{m,amine} - 2q_{1,CO_2} - q_{2,CO_2}$, where $q_{m,amine}$ is the maximum capacity of amines that can adsorb CO₂ in the adsorbent, and q_{1,CO_2} and q_{2,CO_2} are the CO₂ capacities for reactions in dry and humid conditions, respectively. Additionally, the backward reaction rate constant is written in terms of the adsorption affinity by $k_b = k_f/b$. The mass balance of CO₂ is thus:

$$\frac{dq_{1,CO_2}}{dt} = k_{f,1} (q_{m,amine} - 2q_{1,CO_2} - q_{2,CO_2})^2 p_{CO_2} - \frac{k_{f,1}}{b_1} q_{1,CO_2} \quad (3.29)$$

$$\frac{dq_{2,CO_2}}{dt} = k_{f,2} (q_{m,amine} - 2q_{1,CO_2} - q_{2,CO_2}) p_{CO_2} p_{H_2O} - \frac{k_{f,2}}{b_2} q_{2,CO_2} \quad (3.30)$$

where b_1 and b_2 are the adsorption affinities for reactions in dry and humid conditions, respectively. In Equations 3.29 and 3.30 the exponents of the available amine sites concentration are based on stoichiometry. However, these exponents can also be acquired from data fitting, resulting in equations:

$$\frac{dq_{1,CO_2}}{dt} = k_{f,1} (q_{m,amine} - 2q_{1,CO_2} - q_{2,CO_2})^{t_1} p_{CO_2} - \frac{k_{f,1}}{b_1} q_{1,CO_2} \quad (3.31)$$

$$\frac{dq_{2,CO_2}}{dt} = k_{f,2} (q_{m,amine} - 2q_{1,CO_2} - q_{2,CO_2})^{t_2} p_{CO_2} p_{H_2O} - \frac{k_{f,2}}{b_2} q_{2,CO_2} \quad (3.32)$$

where t_1 and t_2 are exponential parameters for dry and humid reactions, respectively. The adsorption affinities in Equations 3.29, 3.30, 3.31 and 3.32 are temperature dependent via:

$$b_1 = b_{0,1} \cdot \exp\left(\frac{-\Delta H_1}{R_{id} \cdot T_0} \cdot \left(\frac{T_0}{T} - 1\right)\right) \quad (3.33)$$

$$b_2 = b_{0,2} \cdot \exp\left(\frac{-\Delta H_2}{R_{id} \cdot T_0} \cdot \left(\frac{T_0}{T} - 1\right)\right) \quad (3.34)$$

where $b_{0,1}$ and $b_{0,2}$ are the reference parameters at reference temperature T_0 , and $-\Delta H_1$ and $-\Delta H_2$ are the isosteric heats of adsorption for reactions in dry and humid conditions, respectively. By summing Equations 3.29 and 3.30 or 3.31 and 3.32, the total rate of change of CO₂ adsorption can be calculated by $dq_{\text{tot,CO}_2}/dt = dq_{1,\text{CO}_2}/dt + dq_{2,\text{CO}_2}/dt$, where $q_{\text{tot,CO}_2}$ is the total CO₂ adsorption capacity. The kinetic model based on Equations 3.29, 3.30, 3.33 and 3.34 is referred to as the 5-parameter model, while the model using Equations 3.31-3.34 is referred to as the 7-parameter model.

In humid CO₂ adsorption isotherm modelling, the two kinetic models were used to calculate the equilibrium CO₂ adsorption capacity in humid conditions by integrating until equilibrium using the 'ODE15s'- solver in Matlab. The equilibrium parameters q_m , b_1 , b_2 , $-\Delta H_1$, $-\Delta H_2$, t_1 and t_2 were gained by fitting the kinetic models to experimental CO₂ isotherm data in humid conditions using 'lsqnonlin' in Matlab. The equilibrium state of CO₂ and H₂O adsorption on supported amines is determined by the ratio of forward and backward reaction constants rather than their absolute values. Thus, the kinetic parameters $k_{f,1}$ and $k_{f,2}$ could be set to an arbitrary value ($k_{f,1}=k_{f,2}=1$) during isotherm fitting. The actual values of these kinetic parameters could be acquired later from kinetic CO₂ adsorption data. In this work, these parameters were used to describe the overall kinetics of CO₂ adsorption, including reaction kinetics and mass transfer. Thus, the kinetic parameters were gained by using the kinetic models in a dynamic model and fitting this model to experimental fixed-bed data, as described in the next section.

3.2.4 Dynamic CO₂ adsorption model (Article IV)

A dynamic non-isothermal 1-D model of a fixed-bed column filled with the amino resin was coded in Matlab. The axial mass and heat balances were solved using the method of lines. The used assumptions were:

- A negligible effect of the balance gas (N₂) or O₂ adsorption on CO₂ or H₂O adsorption.
- Ideal gas law valid for gas-phase calculations.
- A constant gas velocity.
- A negligible pressure drop and constant total pressure.
- Thermal equilibrium between solid phase (adsorbent particles) and gas.
- Specific heat capacity of the gas neglected in the transient heat transfer term.
- Constant adsorbent bed properties.
- Constant case-dependent thermodynamic parameters during simulation.

The case-dependent thermodynamic parameters refer to the density, kinematic viscosity and specific heat capacity of the gas, which are dependent on the feed gas mixture composition, temperature and pressure. The component concentration balance for adsorbed species i can be represented using:

$$\frac{\partial c_i}{\partial t} = D_L \frac{\partial^2 c_i}{\partial z^2} - v_i \frac{\partial c_i}{\partial z} - \frac{\rho_{\text{bed}}}{\varepsilon} \frac{\partial q_i}{\partial t} \quad (3.35)$$

where c_i is the adsorbing species concentration, D_L is the axial dispersion coefficient, z is length in the axial direction, v_i is interstitial gas velocity and ρ_{bed} is the adsorbent bed density [176,205,208]. The concentration balance was calculated for both CO₂ and H₂O. The axial dispersion coefficient was calculated using the Chung & Wen correlation [210]:

$$D_L = \frac{2R_p v_i \varepsilon}{0.2 + 0.011 Re^{0.48}} \quad (3.36)$$

where R_p is the adsorbent particle radius. Re is the particle Reynold's number calculated by $Re = 2R_p v_i \varepsilon / \nu$, where ν is the kinematic viscosity. The source term for adsorption kinetics $\partial q_i / \partial t$ was replaced with the 5-parameter or 7-parameter kinetic model in the case of CO₂ as described in section 3.2.3 above. However, for H₂O adsorption kinetics the linear driving force (LDF) model [211] was used:

$$\frac{d\bar{q}_i}{dt} = k_{i,\text{LDF}} (q_{i,\text{eq}} - \bar{q}_i) \quad (3.37)$$

where $q_{i,\text{eq}}$ is the local equilibrium adsorption capacity from isotherm model, $k_{i,\text{LDF}}$ is the overall mass transfer coefficient of the LDF model and \bar{q}_i is the average adsorption capacity in the adsorbent particle. The heat balance is given by:

$$\begin{aligned} & \frac{1-\varepsilon}{\varepsilon} \rho_p \left(c_{p,a} + c_{p,m,\text{CO}_2} \cdot q_{\text{tot,CO}_2} + c_{p,m,\text{H}_2\text{O}} \cdot q_{\text{H}_2\text{O}} \right) \frac{\partial T}{\partial t} = \\ & \frac{K_z}{\varepsilon} \frac{\partial^2 T}{\partial z^2} - \rho_g c_{p,g} v_i \frac{\partial T}{\partial z} - \frac{1-\varepsilon}{\varepsilon} \rho_p \left(c_{p,m,\text{CO}_2} \frac{dq_{\text{tot,CO}_2}}{dt} + c_{p,m,\text{H}_2\text{O}} \frac{dq_{\text{H}_2\text{O}}}{dt} \right) T \\ & - \frac{1-\varepsilon}{\varepsilon} \rho_p \left(-\Delta H_1 \frac{dq_{1,\text{CO}_2}}{dt} + (-\Delta H_2) \frac{dq_{2,\text{CO}_2}}{dt} + (-\Delta H_{\text{H}_2\text{O},0}) \frac{dq_{\text{H}_2\text{O}}}{dt} \right) - \frac{2h}{\varepsilon R_{\text{bed}}} (T - T_w) \end{aligned} \quad (3.38)$$

where ρ_p is the adsorbent particle density, c_{p,m,CO_2} and $c_{p,m,\text{H}_2\text{O}}$ are the molar heat capacities of CO₂ and water, respectively, q_{CO_2} is the total CO₂ adsorption capacity gained using the kinetic model as described in the previous section and $q_{\text{H}_2\text{O}}$ is the H₂O adsorption capacity gained from the GAB isotherm (Equations 3.17, 3.18, 3.19). $c_{p,g}$ is the specific heat capacity of the gas mixture coming into the column, K_z is the axial effective heat conductivity, h is the overall heat transfer coefficient from the column wall to the adsorbent bed, R_{bed} is the adsorbent bed radius and T_w is the column wall temperature. The isosteric heats of CO₂ adsorption $-\Delta H_1$ and $-\Delta H_2$ were obtained from the humid isotherm fitting as described in section 3.2.3. The isosteric heat of H₂O adsorption at zero loading $-\Delta H_{\text{H}_2\text{O},0}$ was obtained from fitting of the temperature

dependent GAB model to experimental H₂O desorption isotherms as described in more detail in section 4.2.1 below.

The Danckwert's boundary condition was used for concentration balances, and an analogous equation for temperature [176] was used at the inlet boundary:

$$D_L \left. \frac{\partial c_i}{\partial z} \right|_{z=0} = -v_1 (c_{i,\text{feed}} - c_i|_{z=0}) \quad (3.39)$$

$$K_z \left. \frac{\partial T}{\partial z} \right|_{z=0} = -\varepsilon v_1 \rho_g c_{p,g} (T_{\text{feed}} - T|_{z=0}) \quad (3.40)$$

where $c_{i,\text{feed}}$ and T_{feed} are the concentration of species i and temperature of the feed gas, respectively. $c_i|_{z=0}$ and $T|_{z=0}$ are the concentration of species i and temperature at the adsorption column inlet boundary, respectively. At the outlet boundary, the boundary conditions are:

$$\left. \frac{\partial c_i}{\partial z} \right|_{z=L} = 0 \quad (3.41)$$

$$\left. \frac{\partial T}{\partial z} \right|_{z=L} = 0 \quad (3.42)$$

The initial conditions were: $q_{\text{H}_2\text{O}}(0)=0$; $q_{\text{CO}_2,1}(0)=0$; $q_{\text{CO}_2,2}(0)=0$; $q_{\text{CO}_2,\text{tot}}(0)=0$; $c_{\text{CO}_2}(0)=0$; $c_{\text{H}_2\text{O}}(0)=0$; $T(0)=T_w=T_{\text{feed}}$.

The dynamic model was fitted against scaled experimental CO₂ and H₂O breakthrough curves and column temperature using the 'lsqcurvefit' function in Matlab to obtain parameters $k_{f,1}$, $k_{f,2}$, $k_{\text{H}_2\text{O,LDF}}$, K_z and h . The number of control volumes was 200. The parameters and boundary conditions used in the simulation can be found in Table 3.3. For details of the measurements used in the calculations, refer to section 3.1.3, Figure 3.2 and Article III. Details of the discretization of the partial differentials and scaling of data can be found in the Supplementary Data of Article IV.

Table 3.3: Parameters used in the fixed-bed modelling of section 4.5. *NIST database values were obtained with the ‘refpropm’- user-built function in Matlab and REFPROP software using the specified gas composition, temperature and pressure as inputs.

Quantity	Parameter	Value	Source
<i>Adsorbent bed properties</i>			
L_{bed}	Bed length	0.017-0.018 m	Calculated from the column dimensions and bulk density.
R_{bed}	Bed radius	0.0045 m	The inner radius of the column.
ϵ	Bed voidage	0.375	Adsorbent SDS.
ρ_{bed}	Adsorbent bed density	450 kg/m ³	Measured.
R_p	Particle radius	$3 \cdot 10^{-4}$ m	From the particle size distribution median (see section 4.1).
ρ_p	Particle density	720 kg/m ³	Calculated from the voidage and bulk density.
$c_{p,a}$	Specific heat capacity of adsorbent	1580 J/(kg K)	From [209]. Resin matrix similar type.
<i>Inlet gas properties</i>			
$y_{\text{CO}_2,\text{feed}}$	Feed molar fraction of CO ₂	0.00037-0.00040	Measured from the outlet.
$y_{\text{H}_2\text{O},\text{feed}}$	Feed molar fraction of H ₂ O	0.0016-0.0193	Measured from the outlet.
T_{feed}	Feed gas temperature	298-308 K	Set equal to the measured bed temperature.
ρ_g	Gas mixture density	1.13-1.20 kg/m ³	NIST database.
v_i	Interstitial velocity	0.070-0.349 m/s	Calculated from the measured flow rate (outlet) and voidage.
ν	Kinematic viscosity of gas mixture	$1.48-1.61 \cdot 10^{-5}$ m ² /s	NIST database.
c_{p,m,CO_2}	Molar heat capacity of CO ₂	37.45-37.87 J/(mol K)	NIST database.
$c_{p,m,\text{H}_2\text{O}}$	Molar heat capacity of H ₂ O	75.27-75.31 J/(mol K)	NIST database.
$c_{p,g}$	Specific heat capacity of gas mixture	1050-1060 J/(kg K)	NIST database.
<i>Process conditions</i>			
T_w	Column wall temperature	298-308 K	Set equal to the measured bed temperature.
P_{tot}	Total pressure in the column	$1.03-1.07 \cdot 10^5$ Pa	Average of the pressures measured before and after the column.

For CO₂ at ultra-dilute concentrations, the effect of dispersion was very small and thus could be neglected in the breakthrough curve fitting. However, this was not the case for H₂O. Therefore, the effect of the empty volume on the H₂O curve was taken into account in the dynamic model by adding the “empty column” adsorption capacity to the equilibrium H₂O capacity $q_{i,\text{eq}}$ in Equation 3.37. This “empty column” adsorption capacity was gained from Langmuir model (Equation 3.9), the parameters of which were gained

by fitting the model to empty column adsorption capacities measured in various partial pressures of H₂O, as shown in Figure 3.4.

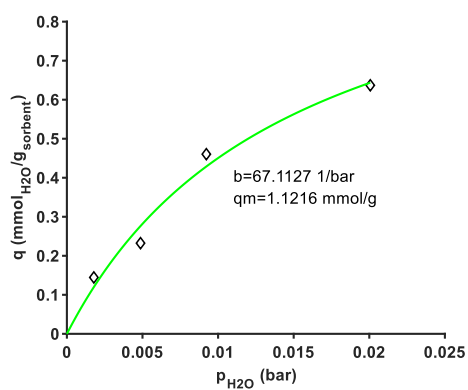


Figure 3.4: Langmuir fit and isotherm parameters with H₂O adsorption capacity results obtained without adsorbent. The capacities are calculated for a sample mass of 0.5 g. From Supplementary Data of Article IV.

4 Results and discussion

4.1 Physicochemical structure of the adsorbent (Article I)

The physical and chemical structure of the amine-functionalized resin was studied in Article I. The adsorbent was found to have a BET surface area of $32 \text{ m}^2/\text{g}$ and a median size of 0.58 mm . The SEM-image in Figure 4.1 shows that the resin particles have a round shape with different-sized pores.

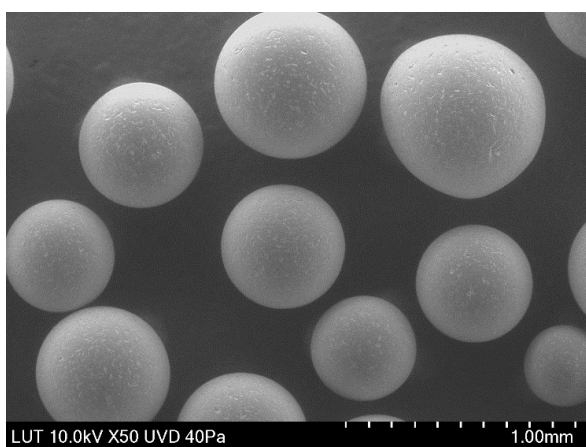


Figure 4.1: SEM-image showing different-sized amine-functionalized resin particles.

Figure 4.2 shows the FTIR spectrum of the amine-functionalized resin. The polystyrene backbone of the resin is strongly evident in the FTIR spectrum with several clear peaks at around $2850\text{-}3050 \text{ cm}^{-1}$ and $700\text{-}1200 \text{ cm}^{-1}$. On the other hand, peaks found in the region of approximately $3250\text{-}3400 \text{ cm}^{-1}$ could be attributed to N-H stretching, referring to the existence of primary or secondary amines.

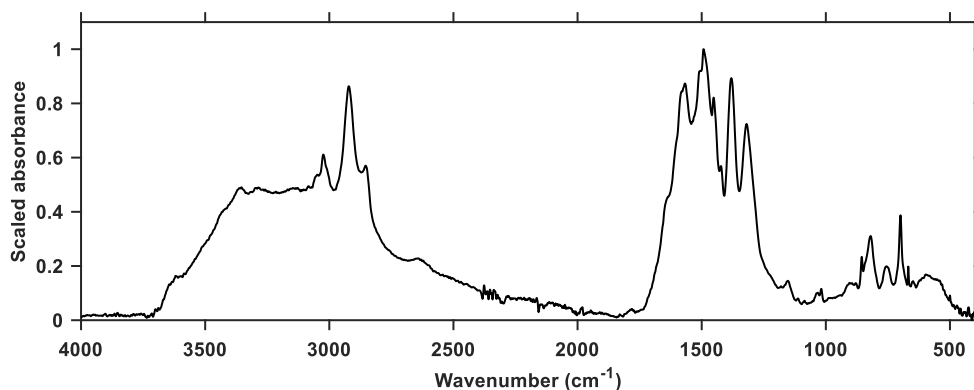


Figure 4.2: FTIR spectrum of the amine-functionalized resin. Absorbance is scaled between 0-1, corresponding to the minimum and maximum of the spectrum.

The capture mechanism of CO_2 on the resin was also studied by comparing the wavenumber regions of the found peaks to literature findings [212–215]. Based on this comparison, some peaks found in the wavenumber region of $1300\text{--}1700\text{ cm}^{-1}$ could be attributed to COO^- or NH_3^+ species. For example, a shoulder peak observed at 1636 cm^{-1} could be assigned to NH_3^+ deformation [213,215,216]. On the other hand, a shoulder peak at 1580 cm^{-1} and peaks at 1567 cm^{-1} and 1381 cm^{-1} are at or very close to peaks assigned to the carbamate ion observed in CO_2 adsorption on aminosilane-functionalized mesoporous silica adsorbents [213,215,216]. Additionally, the highest peak observed at 1493 cm^{-1} assigned to polystyrene may overlap a peak referring to the ammonium ion [215,216] or carbamate [212].

A strong peak at 1380 cm^{-1} has been assigned to the carbamate ion [213,215,216], but also to quaternary ammonium groups [217]. However, the sorption mechanism on quaternary-amine functionalized groups is based on moisture swing where the CO_2 capture capacity typically reduces as a function of humidity [47,217]. As will be shown in the next section below, the capture capacity of the amino resin in this work increases with increasing humidity, and thus it is unlikely that the amine groups on this resin are quaternary ammonium groups with an ion-exchange capture mechanism related to moisture swing resins reported in the literature [47,217]. The peaks analysed above in the region of $1300\text{--}1700\text{ cm}^{-1}$ could refer to the formation of ammonium carbamate, which should be the main product of CO_2 adsorption in dry conditions on primary and secondary amine-based adsorbents. On the other hand, no clear evidence of bicarbonate formation was found based on the FTIR-spectra.

However, it should be taken into account that in this study, it was not possible to control the gas atmosphere or other conditions during the FTIR-analysis. Therefore, it was not possible to systematically study the appearance or disappearance of each peak in different conditions. Examples of such control of conditions during the analysis, also referred to as in situ FTIR spectroscopy, can be found in the literature [212,215].

4.2 CO₂/H₂O adsorption isotherms

The CO₂ adsorption and desorption capacities of the amine-functionalized resin were calculated in a wide range of temperature, pressure and humidity conditions relevant to ambient CO₂ capture. Instead of just measuring single adsorption points, a more useful approach was to utilize adsorption isotherm modelling. Modelling of single-component adsorption isotherms was done using generally known isotherm models. To take into account the effect of co-adsorbing H₂O on CO₂ isotherms, a kinetic approach was used. The results of these approaches are discussed below.

4.2.1 Single-component CO₂/H₂O isotherms (Articles I-II, IV)

In Article I, a comparison of isotherm models was made in terms of the goodness of fit to experimental total desorption capacities with adsorption at 25–50 °C. The Langmuir model gave the lowest coefficients of determination and highest normalized standard deviations in most cases. As shown in Figure 4.3, the Langmuir isotherm was found to be unsuitable for describing the shape of the experimental CO₂ isotherm at 25 °C at any partial pressure range. The Freundlich model led to a much better representation of the data, but the normalized standard deviations using total desorption data were still high (4.1–5.5%) compared to Sips and Toth isotherms (1.1–3.8%). The Sips and Toth isotherms led to similar fits and parameters of goodness of fit. Based on these results, the Toth isotherm was selected for modelling of CO₂ isotherms in following work.

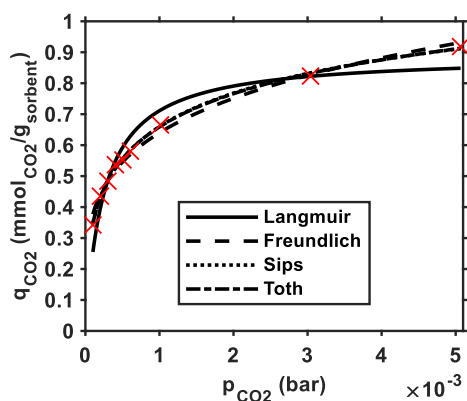


Figure 4.3: A comparison of adsorption isotherm model fits to experimental CO₂ capacities (markers) with adsorption at 25 °C.

The contribution of chemi- and physisorbed CO₂ on the amino resin was investigated by separating the desorption data as described in section 3.1.5. Figure 4.4 shows the fits to this data using the combined Toth model (Equation 3.13) with temperature dependence (Equations 3.14, 3.15, 3.16). The physisorption capacities (N₂ purge) shown in Figure 4.4a were not clearly affected by the adsorption temperature. However, temperature had a clear effect on the chemisorption (temperature swing) capacities in Figure 4.4b.

Moreover, the presence of humidity during adsorption did not significantly affect the physisorption capacities at 50 °C in the low partial pressure range (0.1-0.3 mbar CO₂). Meanwhile, the chemisorption capacities increased in the whole partial pressure range in humid conditions. The contribution of the chemisorption capacity to the total capacity was dominant in DAC conditions with 0.4 mbar CO₂ or less. The combined physi- and chemisorption data were used to successfully represent the total desorption capacity with equal or less than 3.8% error to experimental data.

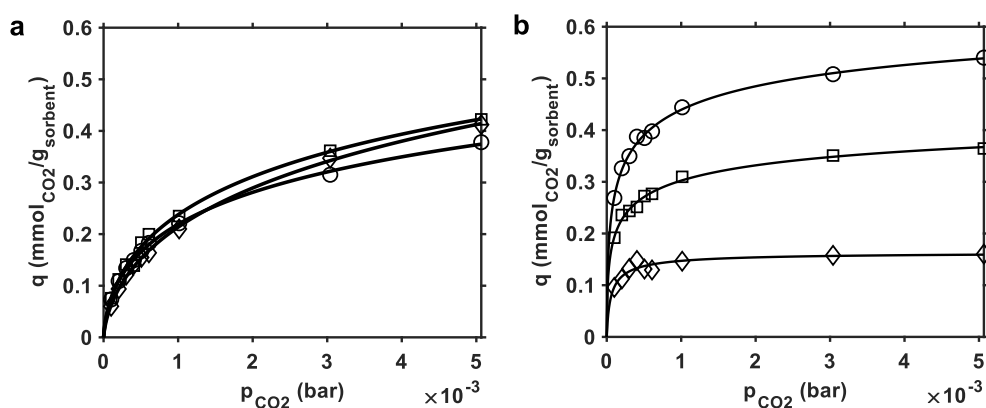


Figure 4.4: Combined Toth model fit to CO₂ desorption capacities obtained from a) N₂ purge; b) temperature swing part of the desorption curve. The adsorption was carried out at 25 °C (spheres), 35 °C (squares) and 50 °C (diamonds) in dry conditions.

As noted in section 3.1.5, the proposed method for separating the desorption data into chemi- and physisorption data was only based on the assumption that CO₂ species captured via chemisorption are not released without a temperature swing. To verify this, however, the N₂ purge step should be continued until equilibrium, which was not reached in 30 min. Additionally, the N₂ purge step was not similar between experiments, since it was carried out at the same temperature as the adsorption, which was between 25-50 °C. Moreover, the fitted isosteric heat of adsorption was actually smaller for “chemisorption” data (35.0 kJ/mol) than for “physisorption” data (52.5 kJ/mol) (see Table 4.1). This should be vice versa, if the data represented actual chemisorption and physisorption capacities. Therefore, it is likely that only a fraction of the CO₂ desorbed during N₂ purge is associated with physisorption.

It should be taken into account that the amino resin has a low surface area compared to mesoporous adsorbents. Even with physisorbent materials that exhibit surface areas in the hundreds or even thousands of m²/g such as MOFs and zeolites CO₂ capacities of less than 0.2 mmol/g have been measured in DAC conditions [75]. For an actual measurement of physisorption on the resin, the adsorption tests should be carried out on a reference resin without the amine groups. However, it is likely that only a negligibly small amount of the adsorbed CO₂ is physisorbed on the amino resin in conditions relevant to DAC.

In Article II, a temperature dependent Toth model (Equations 3.12, 3.14, 3.15, 3.16) was used to model CO₂ adsorption isotherms, as shown in Figure 4.5. Figure 4.5a shows that the CO₂ adsorption capacities increase with decreasing adsorption temperature, even below 0 °C. The highest experimental CO₂ capacity in dry DAC conditions (0.4 mbar CO₂) of 0.80 mmol_{CO₂}/g_{sorbent} was obtained at 0 °C. Humidity was also found to improve the CO₂ adsorption capacity, as shown in Figure 4.5b. The experimental CO₂ capacity from 0.4 mbar CO₂ improved from 0.54 mmol_{CO₂}/g_{sorbent} in dry conditions to 0.89 mmol_{CO₂}/g_{sorbent} with 2 vol-% of humidity at 25 °C. A single cold humid test done at -10 °C with 0.2 vol-% H₂O resulted in the highest capacity of 1.06 mmol_{CO₂}/g_{sorbent} from 0.4 mbar CO₂. The highest capacity using 5 mbar CO₂ was 1.28 mmol_{CO₂}/g_{sorbent} in cold dry conditions or humid conditions at 25 °C. Thus, the measured CO₂ capacities in dry DAC conditions are on the lower end compared to other amine-functionalized materials (see Tables A.1 and A.2). However, in humid conditions, the adsorption capacity nearing 1 mmol_{CO₂}/g_{sorbent} is somewhat mediocre compared to capacities gained with other amine-based adsorbents in DAC conditions.

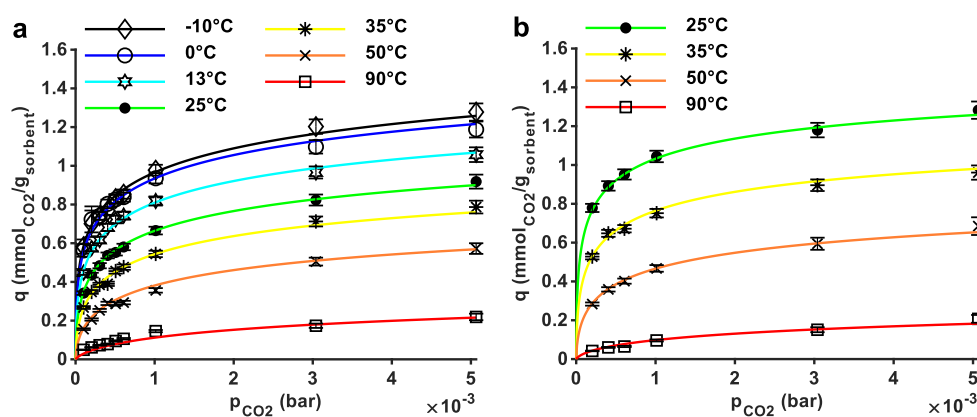


Figure 4.5: The temperature-dependent Toth model fit to experimental CO₂ adsorption isotherms in a) dry conditions; b) humid conditions. Markers correspond to experimental points and lines correspond to the model fit. Experimental uncertainty is shown by the error bars.

It was thus found that temperatures below 0 °C do not seem to significantly further improve CO₂ adsorption capacity. Additionally, with increasing CO₂ partial pressure the enhancing effect of cold temperature or humidity was relatively less pronounced. The results suggest that the obtained capacities in dry cold conditions neared the maximum CO₂ capacity with the studied CO₂ partial pressures. However, introducing humidity did improve the capacity further in cold conditions. Moreover, the sample in the humid cold test was not saturated, and the equilibrium CO₂ capacity was even higher. Thus, longer adsorption steps than two hours would be required in humid cold conditions to reach the maximum capacity.

Table 4.1 shows the parameters of all the CO₂ isotherm fits using the Toth model. The isosteric heats of adsorption from the total desorption isotherm fits are on the lower end

compared to those measured in the literature for other amine-based adsorbents. For example, 73 kJ/mol_{CO₂} was determined for aminosilane-functionalized NFC [73], 87 kJ/mol_{CO₂} for the commercial amino resin Lewatit VP OC 1065 [72] and around 90 kJ/mol_{CO₂} for primary or secondary amine-containing SBA-15 adsorbents [74]. However, it should be taken into account that the CO₂ isotherms in this work were only measured up to 5000 ppm CO₂, which is why the isosteric heat values gained from the isotherm fitting are directional.

Table 4.1: The fitted parameters of the Toth model to CO₂ isotherm data. Data from Articles I and II.

Data	$q_{m,0}$ (mmol _{CO₂} /g _{sorbent})	b_0 (1/bar)	t_0	α	χ	$-\Delta H$ (kJ/mol)
Dry CO ₂ , “physisorption” ^a	1.72	$7.60 \cdot 10^3$	0.234	1.26	2.13	52.5
Dry CO ₂ , “chemisorption” ^b	0.807	$3.25 \cdot 10^5$	0.286	2	17.1	35
Dry CO ₂ , total desorption	1.71	$1.13 \cdot 10^5$	0.265	0.601	4.53	62.2
Humid CO ₂ , total desorption	1.75	$2.60 \cdot 10^5$	0.311	0.046	4.7	67.9

^aDesorption capacity in N₂ purge. ^bDesorption capacity in temperature swing.

In Article II, only one humidity content was used for measuring CO₂ isotherms, and thus the CO₂ and H₂O adsorption data was insufficient for modelling humid DAC. This topic was revisited in Article IV, and Figure 4.6 shows the single-component H₂O isotherms modelled using the GAB isotherm (Equation 3.17). Figure 4.6a shows that at 35 °C and 50 °C, the H₂O isotherms seem fairly linear, but at 25 °C curvature is seen especially at higher partial pressures. The H₂O capacities are around 0.3 mmol_{H₂O}/g_{sorbent} at 1.7 mbar H₂O and 3.9 mmol_{H₂O}/g_{sorbent} at 19 mbar H₂O at 25 °C. The GAB isotherm yields an excellent representation of the H₂O isotherm data at each temperature.

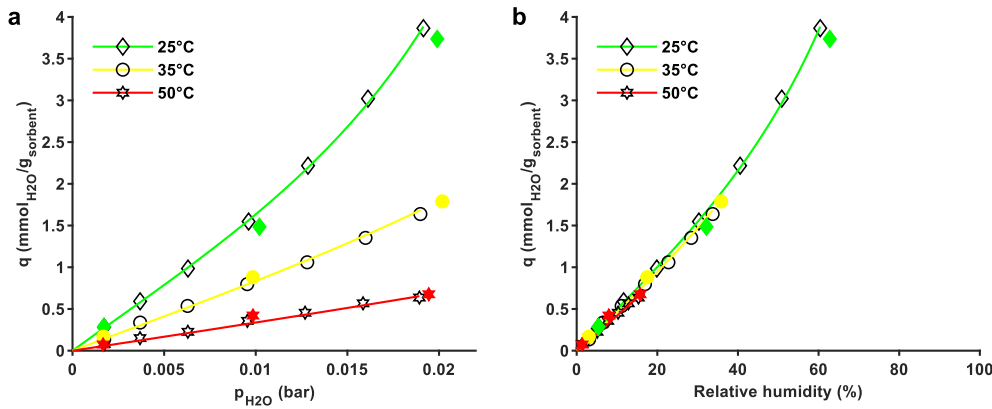


Figure 4.6: Single-component H₂O desorption isotherms. Filled markers show H₂O desorption capacities in co-adsorption of 370-380 ppm CO₂ and humidity. From Article IV.

Figure 4.6b shows that the H₂O isotherms are close to each other when presented as a function of relative humidity. This may indicate, that it is sufficient to measure H₂O capacities at different relative humidities, rather than changing both H₂O concentration and temperature. Thus, the GAB isotherm could model the H₂O adsorption capacity without temperature dependence. However, as data was not gathered from the whole relative humidity range at each temperature to verify the above, temperature dependence was retained in the GAB model.

Figure 4.6 also shows, that the H₂O capacities measured in co-adsorption conditions with 0.4 mbar CO₂ are similar to those gained in single-component adsorption. This is in line with the literature findings about the co-adsorption of CO₂ and H₂O on amine-functionalized adsorbents in DAC [73] or PCC [72] conditions. Therefore, there is no need for a separate co-adsorption model in DAC conditions in terms of H₂O adsorption, and the single-component GAB model parameters can be used in the source term of the dynamic model (Equation 3.37). The isosteric heat of H₂O adsorption at zero loading was calculated via $-\Delta H_{H_2O,0} = \Delta H_C + \Delta H_K + \Delta H_{H_2O,vap}$ [73,206,207], where $\Delta H_{H_2O,vap}$ is the heat of H₂O vaporization of 44.1 kJ/mol_{H₂O}. The resulting 50.7 kJ/mol_{H₂O} was used in the heat balance of the dynamic model to account for the heat released by H₂O adsorption (Equation 3.38). Table 4.2 shows the fitted parameters of the GAB isotherm model.

Table 4.2: Parameters of the GAB model fitted to single-component H₂O desorption isotherms, and the isosteric heat of H₂O adsorption at zero loading. From Article IV.

$q_{m,mono}$ (mmol _{H₂O} /g _{sorbent})	C_0	K_0	ΔH_C (kJ/mol)	ΔH_K (kJ/mol)	$-\Delta H_{H_2O,0}$
2.58	0.155	0.871	6.6	0	50.7

4.2.2 CO₂ isotherms with the effect of humidity (Article IV)

To model the effect of humidity on the CO₂ adsorption capacity in DAC conditions, experimental CO₂ isotherms were measured at three humidity conditions in the dilute CO₂ partial pressure region. The CO₂ adsorption capacities were around 0.6 and 0.9 mmol_{CO₂}/g_{sorbent} at 25 °C with 1.7 mbar and 20 mbar H₂O, respectively. Therefore, the H₂O/CO₂ capture ratios are around 0.5 and 4 in these conditions. The CO₂ capacities obtained with 2 vol-% humidity were thus similar to those measured using the first experimental setup in section 4.2.1.

For modelling of humid CO₂ adsorption isotherms, the 5-parameter and 7-parameter kinetic models were used to calculate the equilibrium capacity as described in section 3.2.3. Figure 4.7 shows a good fit to the pseudo-equilibrium CO₂ isotherms using the 5-parameter model. However, at the lowest humidity content of 0.2 vol-% H₂O the 5-parameter model over-estimates the CO₂ capacity at low partial pressures, and under-estimates the capacity at high partial pressures somewhat. For example, at 25 °C and 0.2 vol-% H₂O the experimental CO₂ capacity is 0.57 mmol_{CO₂}/g_{sorbent} while the model value is 0.06 mmol_{CO₂}/g_{sorbent} higher. The shape of the isotherms changes with temperature, and thus the partial pressure below which the capacity is over-estimated is around 1 mbar at 25 °C and 2 mbar at 35 °C. On the other hand, with 2 vol-% H₂O the model under-estimates the CO₂ capacities slightly at partial pressures below 1 mbar.

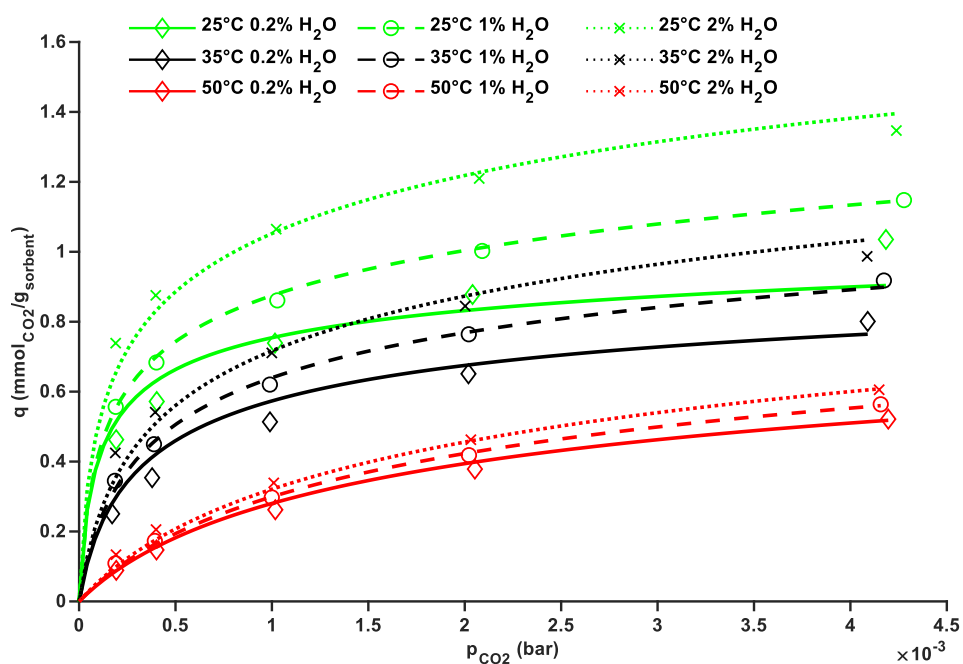


Figure 4.7: Experimental (markers) and modelled (lines) CO₂ isotherms using the 5-parameter co-adsorption model.

It could be expected that even better isotherm fits could be obtained by allowing the exponential parameters t_1 and t_2 to freely vary in the isotherm fitting, rather than using pre-determined values based on reaction stoichiometry. Consequently, using the 7-parameter model with relaxed boundaries for the exponential parameters t_1 and t_2 lead to a nearly perfect fit to the experimental data, as shown in Figure 4.8.

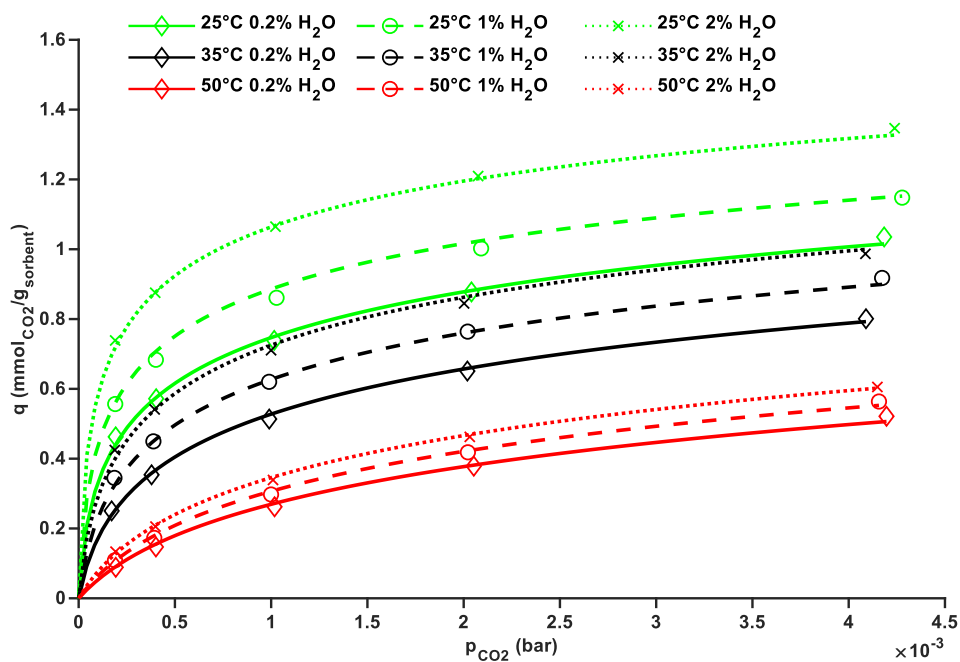


Figure 4.8: Experimental (markers) and modelled (lines) CO₂ isotherms using the 7-parameter co-adsorption model with relaxed upper boundaries for parameters t_1 and t_2 .

Moreover, to limit the computational effort of the model caused by excessively high exponential parameters, an upper limit of 3 for the exponential parameters was used. In this case, the 7-parameter model also gave an excellent fit, as shown in Figure 4.9. Only at 25 °C with 0.2 vol% H₂O and partial pressures higher than 2 mbar the model starts to diverge significantly from the experimental data.

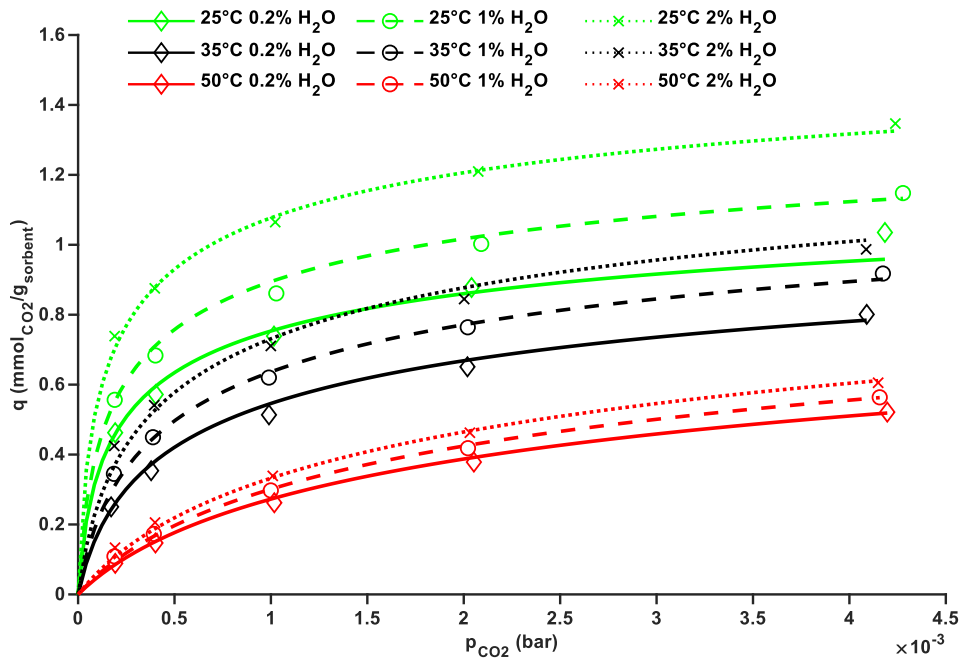


Figure 4.9: Experimental (markers) and modelled (lines) CO₂ isotherms using the 7-parameter co-adsorption model with exponential parameter upper boundary fixed at 3.

Overall, good fits to the pseudo-equilibrium CO₂ isotherms were gained using the kinetic model. These results indicate that the proposed kinetic model could be used to accurately describe the adsorption equilibrium of CO₂ in humid conditions. Parameters of the fits are found in Table 4.3. The isosteric heats of adsorption are higher in humid conditions, which could be explained with species such as hydrated hydronium carbamate being formed in humid conditions with higher binding energies than ammonium carbamate [80,83]. However, it should be noted, that the physicality of the parameters in the case of the 7-parameter model fits, especially the exponential parameters, cannot be proven with the current data. The equilibrium parameters for the 5-parameter model and its derivative the 7-parameter model with $t_1=t_2=3$ were used to model CO₂ adsorption kinetics in the dynamic fixed-bed model (Article IV), which is discussed in section 4.5. However, in Articles I-II, the temperature dependent Toth model was used to analyse the equilibrium working capacity using different regeneration options as described in the next section.

Table 4.3: Parameters of the kinetic models obtained from fitting to CO₂ isotherms in humid conditions. The forward rate constants $k_{f,1}$ and $k_{f,2}$ were set constant to $1 \text{ bar}^{-1}\text{s}^{-1} (\text{mol/kg})^{1-r_1}$ and $1 \text{ bar}^{-2}\text{s}^{-1} (\text{mol/kg})^{1-r_2}$.

Model	q_m (mmol _{amine} /g _{sorbent})	$b_{0,1}$ (bar ⁻¹) (mol/kg) ^{1-r₁}	$b_{0,2}$ (bar ⁻²) (mol/kg) ^{1-r₂}	t_1	t_2	$-\Delta H_1$ (kJ/mol)	$-\Delta H_2$ (kJ/mol)
5-parameter	1.93	3.02E+03	7.06E+04	2	1	97.2	111.5
7-parameter	2.63	4.00E+02	2.38E+04	3 ^b	3 ^b	84.3	124.0
7-parameter	6.30	2.53E-04	1.12E-04	9.35	12.44	81.6	126.8

^aParameter value fixed. ^bParameter upper boundary fixed to 3.

4.3 Working capacity analysis (Articles I-II)

In Articles I-II, different regeneration methods were evaluated in terms of the equilibrium working capacity, which is the maximum amount of CO₂ that could be produced in any given condition. Because in dry conditions it can be assumed that the CO₂ partial pressure equals the total pressure during regeneration in pressure-swing adsorption, no CO₂ can be produced at total pressures higher than 0.4 mbar. The pressure-swing adsorption working capacity contours are shown in Figure 4.10.

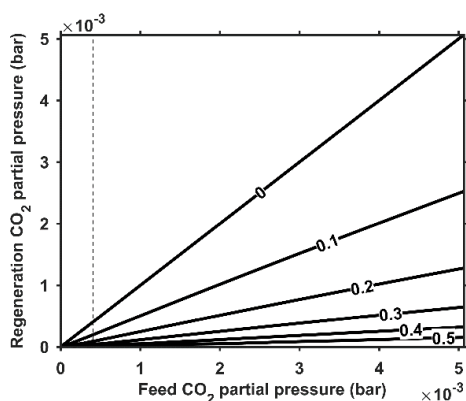


Figure 4.10: Contours of the modelled equilibrium working capacity (mmol_{CO2}/g_{sorbent}) for pressure swing adsorption at 25 °C. The dashed line depicts CO₂ partial pressure in air (0.4 mbar). From Article II.

Taking into account the ratios of captured CO₂ vs. H₂O (see section 4.2.2), even with H₂O present, the partial pressure of the CO₂ is not lowered enough to reach industrially reasonable regeneration vacuum levels. For the current adsorbent, to produce working capacity nearing 0.5 mmol_{CO2}/g_{sorbent} in dry conditions, a regeneration vacuum pressure below $1 \cdot 10^{-6}$ bar is required. Only around half of this capacity could be obtained by increasing the pressure to 12.5 bar during adsorption and using an already very low

vacuum pressure of 1 mbar. Moreover, these values are for equilibrium operation, which is not the case in a real DAC process. Therefore, unless the adsorbent exhibits high capacities and a very steep isotherm shape in ultra-dilute conditions, PSA cannot be an economically feasible option for DAC.

To regenerate the amine-functionalized adsorbent at pressure levels relevant to process conditions, a temperature swing is required. Figure 4.11 shows the equilibrium working capacities for isobaric temperature swing adsorption. Given the effect of the temperature on the CO₂ isotherms seen in Figure 4.5, it is no surprise that the highest working capacities in TSA can be obtained at an adsorption temperature below 0 °C, as shown in Figure 4.11a. With adsorption in cold conditions, the working capacity can rise over 0.5 mmolCO₂/g_{sorbent} with the regeneration temperature as low as 50 °C. However, such working capacity levels with adsorption in warm conditions (20-30 °C) require a regeneration temperature of 90 °C. With adsorption at room temperature, a 60 °C regeneration temperature yields 0.32 mmolCO₂/g_{sorbent}.

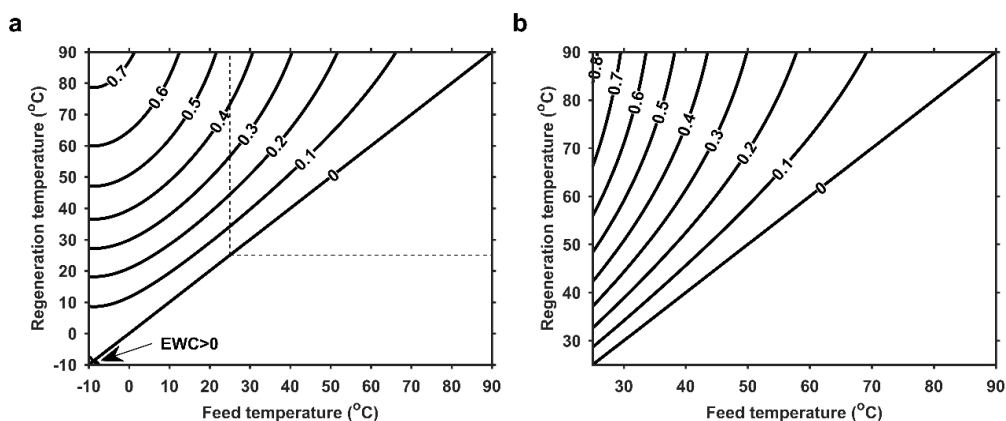


Figure 4.11: The contours of the modelled equilibrium working capacity (mmolCO₂/g_{sorbent}) for isobaric temperature-swing adsorption at a CO₂ partial pressure of 0.4 mbar in a) dry conditions; b) humid conditions with 2 vol-% H₂O. The dashed line segment in a) corresponds to the temperature range in b). From Article II.

The effect of humidity on the CO₂ isotherms is also transferred to the working capacity levels, which are almost doubled, as shown in Figure 4.11b. The maximum benefit of humidity on the working capacity of almost 80% is realized with adsorption at 25 °C and desorption at 90 °C. On the other hand, working capacities over 0.5 mmolCO₂/g_{sorbent} are achievable with a regeneration temperature of 50 °C. Such low regeneration temperatures warrant the use of low-grade waste heat for desorption of CO₂.

As discussed in section 2.2.1, it is required to evacuate the adsorption column prior to heating to avoid dilution of the desorbed CO₂. Additionally, unless the incoming purge gas is steam that can be condensed later, pure CO₂ cannot be produced unless the column inlet is closed. Calculation of equilibrium working capacities for dry (closed)

temperature-vacuum swing adsorption showed that even when using a low regeneration pressure of 1 mbar the working capacity falls below $0.4 \text{ mmol}_{\text{CO}_2}/\text{g}_{\text{sorbent}}$ (Article I). The used regeneration pressures in a real DAC process are much higher, however. Therefore, 13 mbar was selected as the vacuum pressure in the (closed) TVSA process, and Figure 4.12 shows the achievable working capacities. Cold adsorption can maintain the working capacity at $0.5 \text{ mmol}_{\text{CO}_2}/\text{g}_{\text{sorbent}}$ even without compression of the feed, as shown in Figure 4.12a. However, Figure 4.12b shows that without compression of the feed air at room temperature, only a low working capacity below $0.25 \text{ mmol}_{\text{CO}_2}/\text{g}_{\text{sorbent}}$ is achievable with regeneration at 90°C . When the adsorption is at room temperature, to achieve a working capacity above zero requires regeneration temperatures over 62°C . With pressurization of 5 bar in adsorption, up to $0.8 \text{ mmol}_{\text{CO}_2}/\text{g}_{\text{sorbent}}$ can be obtained. However, compressing large amounts of air may be unpractical and economically infeasible. It is thus clear that the working capacity in the TVSA process is significantly lower compared to isobaric TSA.

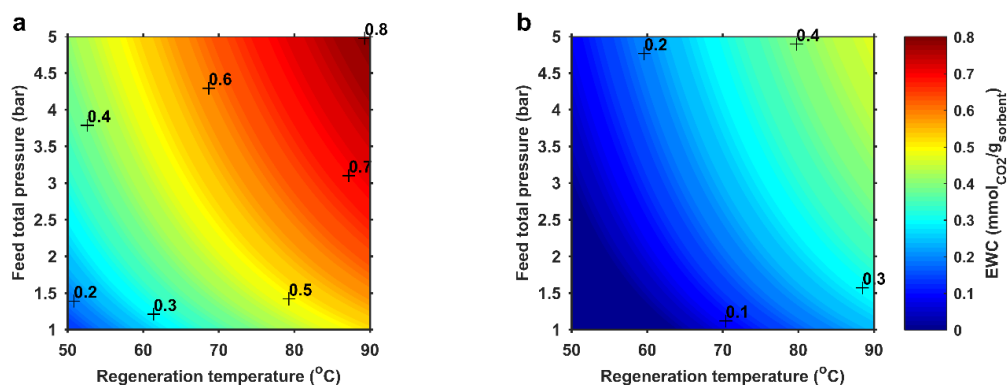


Figure 4.12: Influence of regeneration temperature and compression of the feed on the modelled equilibrium working capacity ($\text{mmol}_{\text{CO}_2}/\text{g}_{\text{sorbent}}$) for temperature-vacuum-swing adsorption for adsorption temperatures of a) -9°C and b) 25°C . The vacuum pressure is 13 mbar, and the feed CO_2 partial pressure is 0.4 mbar at 1 atm. From Article II.

Based on the working capacity analysis, the TVSA process should only be used instead of TSA if production of pure CO_2 is required. For other applications, since the achievable working capacity is larger, isobaric TSA should be used. However, this analysis only considered the equilibrium capacity. Kinetics and energy consumption of the adsorption/desorption process may limit the applicability of different process options. Therefore, a more comprehensive comparison of different regeneration methods was carried out in Article III as discussed in the next section.

4.4 Experimental regeneration method comparison (Article III)

As noted above, an isotherm-based working capacity analysis is limited for regeneration method comparison. Additionally, as discussed in section 2.2, few reports exist where

regeneration options for DAC have been compared, experimentally or otherwise. Using the new experimental device (see section 3.1.3), a series of experiments were done to evaluate the dynamic CO₂ desorption capacity in different conditions. Using the desorption profiles, daily CO₂ productivities and specific energy requirements were evaluated. The effect of different regeneration conditions on the adsorbent degradation rate was evaluated in repeated cycles of adsorption/desorption. This chapter presents the results of regeneration method comparison made in Article III. It should be noted that in the method comparison below, TVSA and TVCSA refer to regeneration schemes that use a purge flow during vacuuming. The conventional TVSA with a closed inlet during regeneration as in the working capacity analysis above is referred to as closed TVSA. A detailed description of the regeneration process schemes is found in section 3.1.4 and Table 3.1.

4.4.1 CO₂ working capacity

The adsorption capacity values obtained at 25 °C from 0.4 mbar CO₂ with the new experimental setup (section 3.1.3) were similar to those measured with the first setup (section 3.1.2), being 0.50-0.53 mmol_{CO₂}/g_{sorbent}. Adsorption was followed by stepwise desorption as described in section 3.1.4. Figure 4.13 shows the experimentally measured working capacity using different regeneration methods and conditions. A comparison of Figure 4.13a and Figure 4.13b shows a good agreement between adsorption and desorption capacity values, although in the 40 ml/min results the total desorption capacity values are slightly higher.

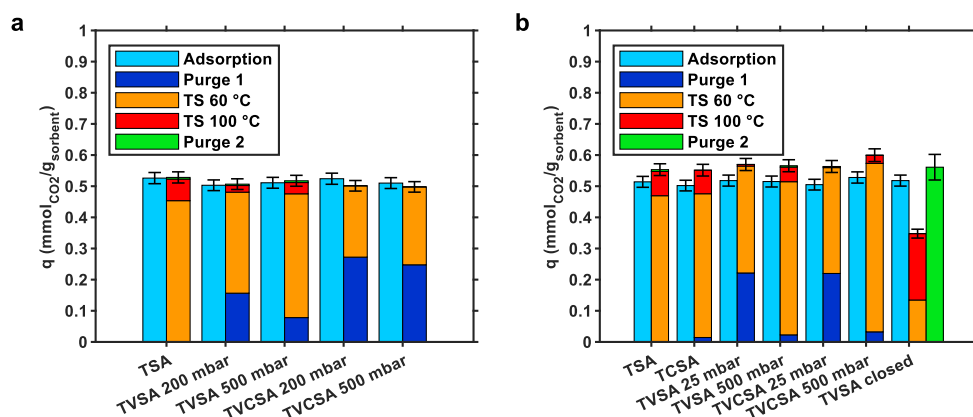


Figure 4.13: Adsorption and desorption CO₂ capacity using a) 1000 ml/min; b) 40 ml/min total flow rate in the desorption phase. ‘Purge 2’ in the closed TVSA process resulted from using an N₂ purge after the closed TVS step with a 1000 ml/min total flow rate. Error bars show the uncertainty. From Article III.

In TSA with 1000 and 40 ml/min flow rates, desorption capacities of 0.45 and 0.47 mmol_{CO₂}/g_{sorbent} were already reached at 60 °C, corresponding to 86% and 85% of the

total desorption capacity. In TVSA and TVCSA methods that couple purge gas with vacuum, a 60 °C temperature swing was enough to achieve over 90% of the total desorption capacity. However, in TVSA with a closed inlet, only 0.13 and 0.35 mmol_{CO₂}/g_{sorbent} were produced using regeneration temperatures of 60 °C and 100 °C, respectively. Additionally, it is worth mentioning, that no capacity was measured during the initial purge step, which consisted of evacuation of the column down to a pressure of 11-12 mbar. Full regeneration in closed TVSA was not achieved without a nitrogen purge.

By comparing these values to the working capacity analysis in section 4.3, it can be deduced that the isotherm-based analysis under-estimates the working capacity somewhat. For example, for TSA the working capacity at 60 °C is about 0.13 mmol_{CO₂}/g_{sorbent} lower in the isotherm-based modelling compared to the corresponding experimental desorption capacity. On the other hand, the isotherm-based working capacity analysis correctly predicted that isothermal vacuuming would not achieve any capacity at reasonable vacuum levels, and that a severe penalty on the working capacity exists when using TVSA with a closed inlet. To improve the accuracy of the isotherm-based analysis, more isotherms above 50 °C might be required. Additionally, in comparison of the results in section 4.3 to those in this section, it should be taken into account that the data in these sections was measured using different experimental setups and with differences in the calculation methods (see section 3.1.5).

Even though a major part of the CO₂ could be desorbed in TSA or TCSA already at 60 °C, the desorption rate was much higher at 100 °C, as shown in Figure 4.14. As shown for TSA in Figure 4.14a and for TCSA in Figure 4.14b, after 60 min of a 60 °C temperature swing, the desorption still continues. When increasing the temperature to 100 °C, the rest of the CO₂ is desorbed in a few minutes. Another way to improve the desorption rate was to apply a vacuum. Even though the working capacity in closed TVSA was low, desorption was completed in a matter of minutes in both temperature swings.

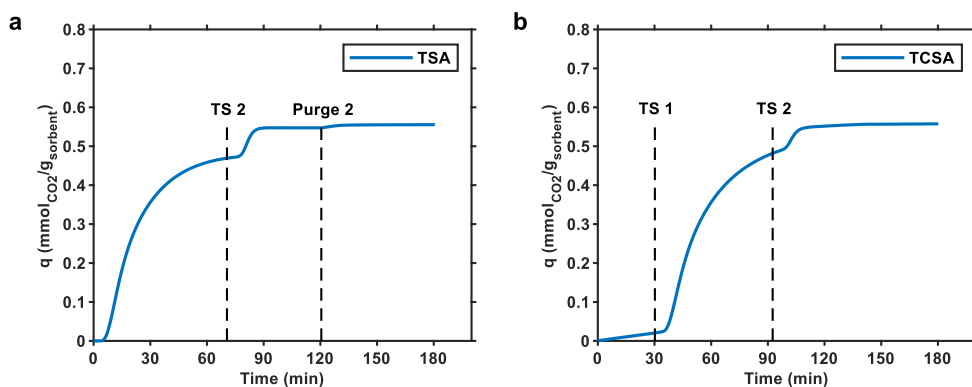


Figure 4.14: Desorption capacity profiles using 40 ml/min flow of a) 400 ppm CO₂; b) 0 ppm CO₂. The temperature of the adsorbent was set to 60 °C a) at start; b) after 'TS 1' and to 100 °C after 'TS 2'. 'Purge 2' refers to switching the flow from 400 ppm to 0 ppm CO₂. From Article III.

A vacuum was also beneficial to the desorption rate in TVSA with a purge gas. As was shown in Figure 4.13, using a purge flow coupled with a vacuum resulted in significant amounts of working capacity even without heating. However, in the low flow rate tests, a lower vacuum of 500 mbar was not enough to achieve a reasonable desorption rate, as shown in Figure 4.15, and thus resulted in a very low working capacity during the initial purge step. This was the case with either TVSA or TVCSA, as shown in Figure 4.15a and Figure 4.15b, respectively. On the other hand, when heating to 60 °C, the desorption rate improved significantly compared to TSA/TCSA even with a low vacuum of 500 mbar. Figure 4.15b shows, that in TVCSA the total working capacity attained during the first 60 min of desorption is 0.47 mmol_{CO2}/g_{sorbent} compared to 0.36 mmol_{CO2}/g_{sorbent} in TCSA. A higher vacuum of 25 mbar improved the desorption rate even more, with almost full regeneration achieved (0.56 mmol_{CO2}/g_{sorbent}) during the first 60 min.

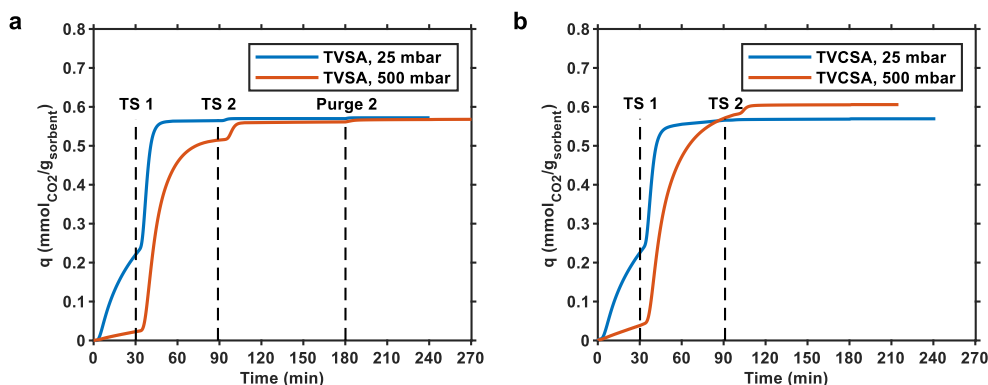


Figure 4.15: Desorption capacity profiles under vacuum using 40 ml/min flow of a) 400 ppm CO₂; b) 0 ppm CO₂. The initial period is vacuuming at 25 °C. The temperature of the adsorbent was set to 60 °C after 'TS 1' and to 100 °C after 'TS 2'. 'Purge 2' refers to switching the flow to pure N₂. From Article III.

4.4.2 Regeneration energy and CO₂ productivity

For TSA, the regeneration-specific energy requirements (SER) were dominated by the sensible heat of the adsorbent and the desorption enthalpy, while the fan energy was negligible due to the low pressure drop. The minimum SER in TSA was 4.2 MJ/kg_{CO2} with a working capacity of 0.47 mmol_{CO2}/g_{sorbent} at a regeneration temperature of 60 °C. Increasing the regeneration temperature to 100 °C increased the SER to 6.4 MJ/kg_{CO2} with a working capacity of 0.55 mmol_{CO2}/g_{sorbent}.

When coupling a vacuum with TSA, the energy requirements increased. Figure 4.16 shows the evolution of the regeneration SER in TVSA with an air purge at two different vacuum levels. Using a 500 mbar vacuum the minimum SER is 6.9 MJ/kg_{CO2} with a working capacity of 0.47 mmol_{CO2}/g_{sorbent}, as shown in Figure 4.16a. However, in this case the point of minimum SER is not necessarily the optimum, since continuing

desorption longer at 60 °C increases the working capacity to 0.51 mmol_{CO2}/g_{sorbent} while increasing the SER to 7.5 MJ/kg_{CO2}. After a temperature increase to 100 °C the working capacity is 0.56 mmol_{CO2}/g_{sorbent} with a SER of 10 MJ/kg_{CO2}.

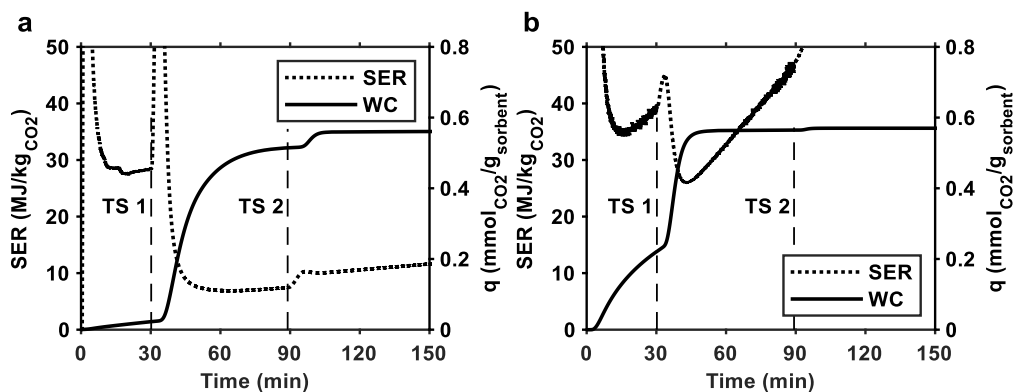


Figure 4.16: Dynamic specific energy requirement (SER) of regeneration and working capacity (WC) for temperature-vacuum swing adsorption with 40 ml/min total flow rate of 400 ppm CO₂ at a) 500 mbar vacuum; b) 25 mbar vacuum.

Using a 25 mbar vacuum increased the desorption rate in TVSA/TVCSA, but also increased the SER rapidly with time, as shown in Figure 4.16b. The minimum regeneration SER is 26 MJ/kg_{CO2} with a working capacity of 0.53 mmol_{CO2}/g_{sorbent}, while 0.56 mmol_{CO2}/g_{sorbent} is attained with SER of 28 MJ/kg_{CO2}. The high SER values are caused by the relatively high vacuum coupled with a high flow rate to adsorbent mass ratio of 40 l/(min·kg). As an example, the flow rate per adsorbent mass ratio is 100 l/(min·kg) during adsorption in the VTT DAC demonstration unit when one blower supplies air to four beds [54].

The SER is strongly dependent on the produced working capacity, but for closed TVSA this effect was pronounced. The regeneration SER after the first temperature swing was 11 MJ/kg_{CO2} and decreased to 9.4 MJ/kg_{CO2} after increasing the regeneration temperature to 100 °C. This is in contrast to other methods, where increase of temperature led to an increase of the SER.

Table 4.4 shows a summary of the SERs and daily CO₂ productivities for different regeneration methods. Because coupling a vacuum with the purge gas increased the desorption rates, the productivities of TVSA/TVCSA at both vacuum levels are higher than those of TCSA. On the other hand, even though the desorption rate in closed TVSA was fast, the daily productivities are low due to the low working capacity. Also, the SER values are higher in closed TVSA compared to low vacuum low temperature TVSA.

Table 4.4: Daily CO₂ productivities and specific energy requirements at 90% and 99% of maximum working capacity at desorption temperatures of 60 °C and 100 °C, respectively. The total flow rate during desorption was 40 ml/min in other experiments except for the closed TVSA and closed TVSA with temperature ramping. All other experiments were done using temperature ramping to 60 °C and then 100 °C except closed TVSA. Data from Article III.

Regeneration method	Regeneration SER (MJ/kgCO ₂)		Productivity (kgCO ₂ /(kg _{adsorbent} ·d))	
	90%, 60°C	99%, 100°C	90%, 60°C	99%, 100°C
TSA	4.5	6.4	0.138*	0.146*
TCSA	4.4	6.3	0.122	0.130
TVSA, 25 mbar	26.2	38.4	0.168	0.161
TVSA, 500 mbar	6.9	10	0.139	0.139
TVCSA, 25 mbar	26.1	41.7	0.168	0.153
TVCSA, 500 mbar	6.2	9.0	0.150	0.148
closed TVSA with T ramp	11.7	8.5	0.042	0.089
closed TVSA	-	7.5	-	0.133

*The method has no purge step after adsorption, therefore productivities are higher than in TCSA.

Improved desorption rates by coupling vacuum and purge gas [218] or steam [129] compared to methods with only a purge gas or a vacuum have also been reported earlier. However, coupling an air purge with a vacuum and temperature swing has not been proposed for DAC, probably due to the dilution of the produced CO₂ and assumed high SER values as found in the 25 mbar case in this work. The SER and CO₂ productivity results suggest that TVSA with a purge gas can be beneficial compared to closed TVSA in terms of both productivity and energy consumption if pure CO₂ is not required. Finally, the effect of different regeneration methods on the cyclic stability of the resin was evaluated, as discussed in the next section.

4.4.3 Cyclic adsorption/desorption tests

Significant differences were found in the cyclic CO₂ capacity drops for different regeneration methods. Using TCSA cycling with adsorption from dry 400 ppm CO₂/N₂ and regeneration at 100 °C with an N₂ purge, the adsorption and desorption capacity dropped from 0.57 to 0.53 mmolCO₂/g_{sorbent} and from 0.53 to 0.51 mmolCO₂/g_{sorbent}, respectively. Applying an air purge with a vacuum increased the capacity drop rates compared to TCSA. Figure 4.17 shows the trends of cyclic capacity in TVSA with regeneration at 60 °C and 100 °C. Comparing Figure 4.17a and Figure 4.17b, it is clear that the capacity drop rate is higher at a higher temperature. With regeneration at 60 °C, the adsorption and desorption capacity dropped from 0.53 to 0.50 mmolCO₂/g_{sorbent}. With a 100 °C regeneration temperature the capacity decreased from 0.52 to 0.45 mmolCO₂/g_{sorbent}. In TVSA cycles with closed inlet during desorption, the adsorption capacity drop was from 0.53 to 0.49 mmolCO₂/g_{sorbent}.

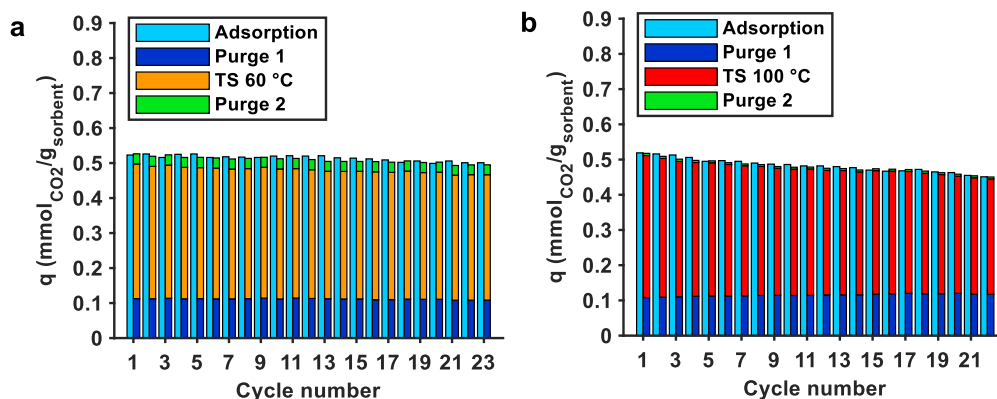


Figure 4.17: The adsorption and desorption capacity in repeated cycles of temperature-vacuum swing adsorption with regeneration at a) 60 °C; b) 100 °C. The adsorption and desorption before 'Purge 2' were done using dry compressed air at 25 °C. 'Purge 2' refers to a dry N₂ purge after a temperature swing. Data from Article III.

In Article IV, a humid cyclic experiment was conducted using the TVCSA scheme, the main results of which are shown in Figure 4.18. Figure 4.18a shows that the CO₂ adsorption and desorption capacity decreased from 0.88 mmol_{CO2}/g_{sorbent} and 0.87 mmol_{CO2}/g_{sorbent} to 0.78 and 0.76 mmol_{CO2}/g_{sorbent}, respectively. Figure 4.18b shows that the H₂O desorption capacity dropped from 3.82 to 2.96 mmol_{CO2}/g_{sorbent}. The variation of the H₂O adsorption capacity seen in Figure 4.18b emphasizes the reasoning for selecting the desorption capacity values for isotherm modelling. The reason for this variation is probably mainly related to the accuracy of the humidity sensor (1% RH) and additional uncertainties related to the calculation of the H₂O adsorption capacities. As discussed in section 3.1.5, the adsorption capacity calculation has a higher uncertainty than desorption capacity calculation. This higher uncertainty is pronounced for the H₂O data, especially due to concentration drops that occurred during the experiments probably due to air remainders in the capillaries and syringes of the humidity calibrator.

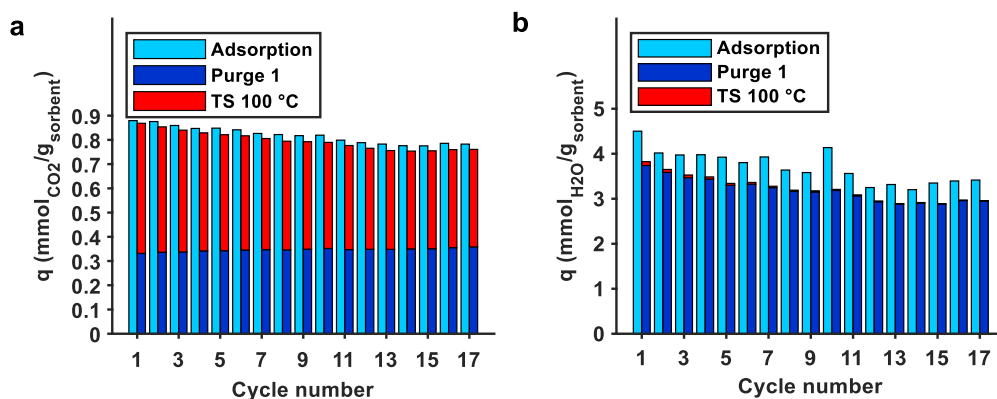


Figure 4.18: Adsorption and desorption capacity of a) CO_2 ; b) H_2O in repeated cycles of temperature-concentration vacuum swing adsorption. The adsorption was done using 400 ppm CO_2 with 2 vol-% H_2O at 25 °C. The regeneration temperature was 100 °C. Data in b) from Article IV.

Table 4.5 summarizes the results of the cyclic experiments. The cyclic capacity drop as a percentage can be argued to be the best metric for comparison of the degradation rate between the regeneration methods. TCSA has the lowest cyclic capacity drops, probably owing to the inert atmosphere during regeneration. When using an air purge with vacuuming, it is notable that the cyclic capacity drop rate is over double with a regeneration temperature of 100 °C compared to 60 °C. This refers to the oxidative degradation of the amines taking place, which has been reported to occur e.g. for linear PEI [99] and resin-supported benzyl amine [219] at temperatures around and even below 100 °C.

The closed TVSA method has a higher capacity drop rate than TVSA with air purge at 60 °C, even though the adsorption column is evacuated prior to heating. Gebald et al. [144] found a 5% capacity decrease in 100 TVSA cycles for an amine-functionalized nanofibrillated cellulose adsorbent. Even though the capacity drop is small, these results indicate that even the closed TVSA method does not prevent amine degradation. While lowering the regeneration temperature would probably reduce the degradation rate, it would also significantly lower the attainable working capacity, as was found in section 4.4.1. It would thus seem that low vacuum, mild temperature TVSA is preferable to the closed TVSA method also in terms of the cyclic stability of the adsorbent.

Table 4.5: The CO₂ capacity decrease in cyclic adsorption/desorption experiments. The capacity drops were determined from the desorption part of the breakthrough curve, except for the closed TVSA method.

Adsorption	Regeneration method	Nr. cycles	CO ₂ capacity drop (mmol _{CO2} /g _{sorbent})	Cyclic CO ₂ capacity drop (%/cycle)
Dry 400 ppm CO ₂ /N ₂	TCSA	19	0.0177	0.18
Dry compressed air	Closed TVSA, 100 °C	23	0.044*	0.36*
Dry compressed air	TVSA, 200 mbar, 60 °C	23	0.0314	0.26
Dry compressed air	TVSA, 200 mbar, 100 °C	22	0.0672	0.59
Humid 400 ppm CO ₂ /N ₂	TVCSA, 200 mbar, 100 °C	17	0.108	0.73

*Determined from the adsorption capacities.

The capacity drop rate of the humid TVCSA method is the highest among the cyclic tests, even though the regeneration was carried out with a dry inert purge. However, in humid adsorption conditions the CO₂ capacity was also much higher, owing to different adsorption mechanism than in dry conditions. Thus, the larger loss of capacity in the humid cyclic experiment could be related to different amine sites being utilized, which are also less stable than those that only capture CO₂ in dry conditions. On the other hand, it could be observed from Figure 4.18, that both the CO₂ and H₂O capacity seemed to stabilize in the last 5-6 cycles. Thus, it is possible that the regeneration method is not fully complete, and thus small amounts of adsorbed species remain in the adsorbent after each cycle until a cyclic steady state is reached. This could be related to more stable species being formed in the humid adsorption of CO₂ on supported amines, as proposed in the literature [80,83]. However, this phenomenon requires more investigation in future work. The regeneration methods done here only in dry conditions should be repeated with humidity present during adsorption. Additionally, FTIR studies of the adsorbed species and the structure of the adsorbent before and after cyclic tests should be done.

4.5 Dynamic modelling of CO₂ adsorption from humid air (Article IV)

In Articles I-III, the study of the CO₂ adsorption process was only based on equilibrium CO₂ capacity modelling or an experimental examination of the regeneration methods. However, an isotherm-based analysis of the equilibrium capacity neglects the effects of kinetics on productivity. Additionally, an experimental comparison is always limited in terms of the available conditions and resources. Modelling the dynamics of the adsorption process is required to answer the critical questions about productivity and the specific energy requirement in variable conditions. In this work, the adsorption of CO₂ from humid air on the amino resin in a fixed-bed column was simulated.

Figure 4.19 shows the results of fitting the dynamic model using the 5-parameter model to experimental CO₂/H₂O adsorption breakthrough data at 25 °C. Figure 4.19a shows that the CO₂ breakthrough profile can be roughly divided into three regions: 1) the lower part

of the curve with fast adsorption before and around breakthrough; 2) the middle part of the curve with roughly linear increase of CO₂ concentration; 3) the upper part of the curve with slowed-down adsorption. The simulated CO₂ breakthrough curves in 1-2 vol-% H₂O cases follow the experimental curves well. However, with 0.2 vol-% H₂O the simulated CO₂ profile shows a delayed increase between 23-60 min, and then increases towards the feed concentration early. In the 2 vol-% H₂O case the CO₂ breakthrough curve is slightly ahead of the experimental curve. Additionally, although not shown in Figure 4.19a, the CO₂ breakthrough curve also reaches saturation early in the 2 vol-% H₂O case.

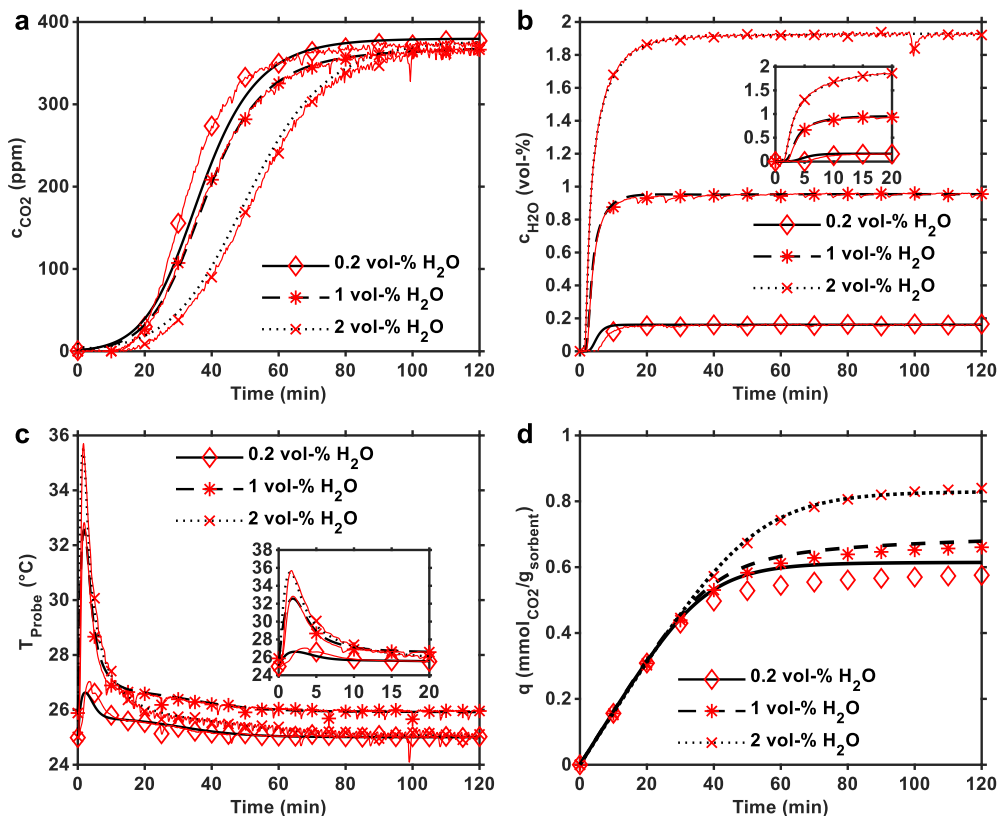


Figure 4.19: Experimental (thin lines with markers) and simulated (lines) a) CO₂ breakthrough profiles; b) H₂O breakthrough profiles; c) bed temperature from a probe 1 cm into the bed; d) CO₂ adsorption capacities from the first two hours of adsorption with initial bed temperature of 25 °C. For the 1 vol-% H₂O experiment, the initial bed temperature was 26 °C. The 5-parameter co-adsorption model was used to model the CO₂ adsorption kinetics. The total flow rate was 500 ml/min. Inserts in b) and c) show the shape of the H₂O breakthrough curves and temperature from the first 20 min of the adsorption phase.

Figure 4.19b shows that the H₂O profiles increase near the inlet concentration in less than 20 min, while the CO₂ profiles only start to increase. The simulated H₂O profiles follow the experimental ones well, but at 0.2 vol-% H₂O breakthrough occurs too early. The

reason for this is that the model under-predicts the H₂O adsorption capacity at this H₂O concentration, which could be related to limited accuracy of the empty volume model for H₂O at low partial pressures (Figure 3.4).

The temperature increase due to adsorption of CO₂ and H₂O is replicated well by the model as shown in Figure 4.19c. The experimental temperatures increase to 27 °C, 32.8 °C and 35.7 °C with 0.2, 1 and 2 vol-% H₂O. The modelled peak temperatures are similar compared to the experimental peaks within 0.5 °C. The temperatures cool down close to the initial bed temperature quickly after reaching the peak temperature. Most of the temperature increase originates from H₂O adsorption. This is apparent when comparing the increase of H₂O capacity of 3.5 mmol_{H₂O}/g_{sorbent} with that of the CO₂ capacity of 0.3 mmol_{CO₂}/g_{sorbent} from 0.2 vol-% H₂O to 2 vol-% H₂O. After all, the estimated heats of adsorption for H₂O and CO₂ are on a similar scale (see Table 4.1, Table 4.2 and Table 4.3). Additionally, a comparison of the temperature and breakthrough profiles shows that the main changes in temperature take place within the first 20 minutes, where the H₂O concentration increases rapidly. Therefore, because the H₂O concentration and consequently the bed temperature are near the initial state before a significant increase of CO₂ concentration takes place, the effect of the H₂O adsorption dynamics on the CO₂ adsorption dynamics can be assumed to be small.

Figure 4.19d shows the experimental and simulated CO₂ adsorption capacity profiles. At 0.2 vol-% H₂O the CO₂ adsorption capacity is over-predicted, which is the main reason why the simulated CO₂ breakthrough profile showed a delayed increase compared to the experimental curve during 23–60 min. This over-prediction originates from using the 5-parameter kinetic model, which also over-predicted the equilibrium CO₂ capacity in the low CO₂ partial pressure region with 0.2 vol-% H₂O (see Figure 4.7). In the 2 vol-% H₂O case, the simulated CO₂ capacity saturates too early, reaching a maximum after 120 min, while the experimental capacity increases for the whole duration of the experiment of five hours.

The experimental adsorption rates calculated from the first 60 min of adsorption are 0.61 and 0.74 mmol_{CO₂}/(g_{sorbent}·h) for 1 and 2 vol-% H₂O, respectively. Therefore, the adsorption rate is improved at a higher humidity content. In the studied conditions, the adsorption rate improvement is due to an improvement of adsorption capacity. However, it is not yet known if the adsorption rate still improves or is retarded at conditions where the improvement of CO₂ adsorption capacity is halted. Based on the literature [42,72] and the humid CO₂ isotherms of the current adsorbent (section 4.2.2), it is not certain if the maximum CO₂ capacity for amine-functionalized adsorbents is reached below 100% relative humidity. However, based on the dry isotherms done in this work (Figure 4.5), the maximum capacity in terms of temperature is expected to be reached at or slightly below -10 °C for the amino resin used in this work. Therefore, the evolution of adsorption rate at low temperature and high humidity conditions should also be investigated.

Based on the fits to the equilibrium CO₂ isotherms (section 4.2.2), it was expected that the breakthrough data fits obtained with the dynamic model could be improved by using

the 7-parameter kinetic model with $t_1=t_2=3$. The comparison of the simulated CO₂ breakthrough profiles at 25 °C using the 5-parameter and 7-parameter models is shown in Figure 4.20. Figure 4.20a shows that at 0.2 vol-% humidity the 7-parameter model improves the simulated breakthrough curve significantly between 20 and 60 min from the start of adsorption. However, both models still show early breakthrough and an overly early increase to the feed concentration in the region of slow adsorption. However, it can be seen from Figure 4.20b that in the 2 vol-% H₂O case the 7-parameter model improves the simulated breakthrough curve throughout. It is especially notable that the simulated curve using the 7-parameter model closely follows the upper part of the curve, and does not lead to early saturation such as with the 5-parameter model.

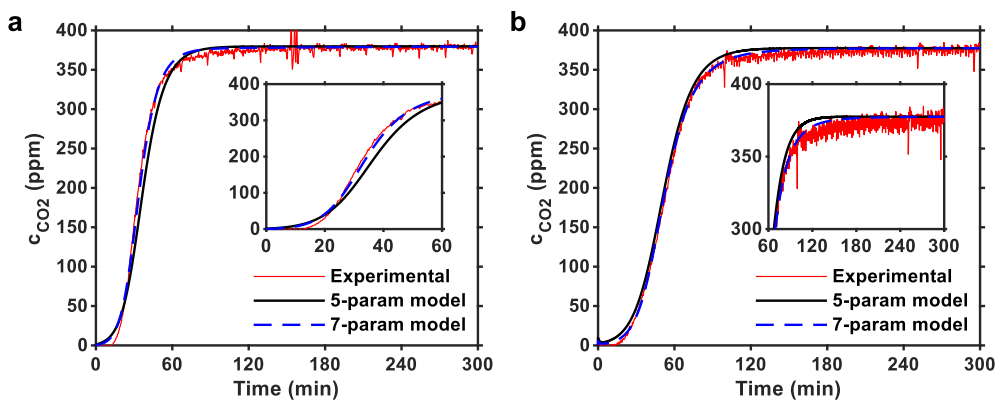


Figure 4.20: Experimental and simulated CO₂ breakthrough profiles using two different kinetic models for CO₂ adsorption at 25 °C in a) 0.2 vol-% H₂O; b) 2 vol-% H₂O. The total flow rate was 500 ml/min.

The dynamic model was also fitted to an almost 2-day adsorption experiment from compressed air humidified with 2 vol-% H₂O with a total flow rate of 100 ml/min, as shown in Figure 4.21. Figure 4.21a shows that while in the 500 ml/min cases the breakthrough of CO₂ occurred during the first 10 min, here it takes place at around 3 hours. The breakthrough time and the middle part of the curve are represented well by both models, but after around 4 hours the 7-parameter model diverges from the experimental data. Even though the 7-parameter model was used above with improved accuracy, here it gives a worse representation of the upper part of the curve than the 5-parameter model.

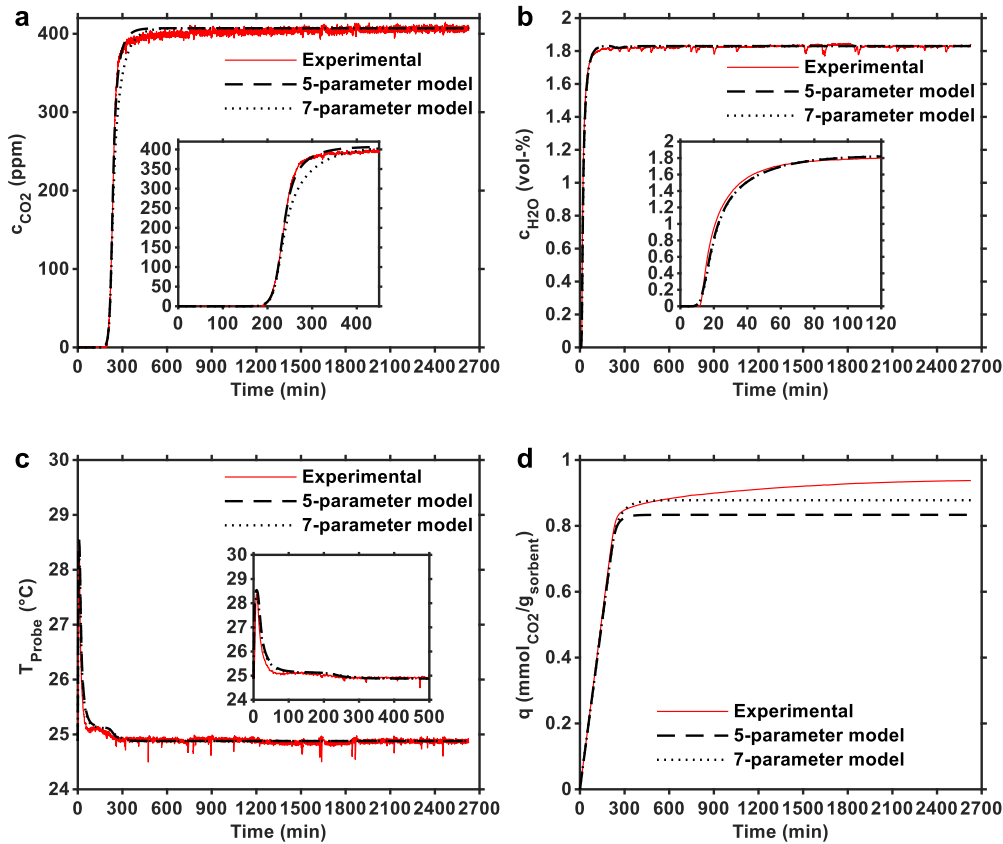


Figure 4.21: Experimental (thin lines with markers) and simulated (lines) a) CO₂ breakthrough profiles; b) H₂O breakthrough profiles; c) bed temperature from probe 1 cm into the bed; d) CO₂ adsorption capacities with a flow rate of 100 ml/min and initial bed temperature of 25 °C. In the 7-parameter co-adsorption model $t_1=t_2=3$.

Otherwise, changing the kinetic model of CO₂ adsorption affects the simulated H₂O profiles and temperature very little, as shown in Figure 4.21b and Figure 4.21c, respectively. The H₂O profiles and the bed temperature are well represented in both simulations. Additionally, Figure 4.21b shows that the adsorbent is nearly saturated with H₂O before CO₂ breakthrough takes place. Moreover, as shown in Figure 4.21c, the largest temperature variations take place before CO₂ breakthrough. This again indicates that the H₂O adsorption dynamics do not significantly affect the shape of the CO₂ profile, at least in the laboratory-scale experiment. The temperature peak is followed by a shoulder, and the reason for this shape is that most of the H₂O adsorption takes place during the first 2 hours, after which adsorption of CO₂ continues. In other words, the shoulder originates mostly from the heat released by CO₂ adsorption that continues longer than H₂O adsorption.

Figure 4.21d shows the main reason for the differences between the experimental and simulated CO₂ breakthrough curves in the 100 ml/min case. The linearly increasing part of the adsorption capacity profile continues roughly linearly even after breakthrough but is followed by a very long and slowly decelerating part. The adsorption rate slow-down is very significant, as 0.81 mmol_{CO₂}/g_{sorbent} is reached in 4 hours, and only 0.12 mmol_{CO₂}/g_{sorbent} in the following 40 hours. The modelled capacity profiles do not follow this region of slow increase, and instead early saturation occurs in both models. Even though the 7-parameter model predicts a closer capacity to the experiment compared to the 5-parameter model, it is still lower by about 0.06 mmol_{CO₂}/g_{sorbent}. Additionally, it seems that equilibrium was still not fully reached in this 2-day experiment.

Table 4.6 shows the parameters of the fixed-bed model fits to experimental breakthrough data. Based on this data, it seems that parameter $k_{f,2}$ increases with humidity, while $k_{f,1}$ does not. This could be related to the humid reaction (reaction 2) becoming more prominent with higher humidity contents, which is expected because the CO₂ adsorption capacity increased with increasing humidity content. However, it should be taken into account that the kinetic parameters are apparent rather than intrinsic, because they combine both reaction kinetics and mass transfer resistance. This is probably one of the main reasons why these kinetic parameters are not identical in the 100 ml/min case compared to the 500 ml/min case at 25 °C, since the external fluid film resistance is affected by the flow rate.

Table 4.6: Parameters of the fixed-bed model fits. The axial dispersion coefficient was calculated by using a correlation, while all the other listed parameters were fitted.

Case and CO ₂ adsorption model	D_L (m ² /s)	$k_{f,1}$ (bar ⁻¹ s ⁻¹ (mol/kg) ^{1-r1}) ^a	$k_{f,2}$ (bar ⁻² s ⁻¹ (mol/kg) ^{1-r2})	$k_{H_2O,LDF}$ (1/s)	K_z (Wm ⁻¹ K ⁻¹)	h (Wm ⁻² K ⁻¹)
0.2 vol-% H ₂ O 25 °C, 5 parameter model	3.50E-04	1.39	1.78	0.94	1.37	16.34
1 vol-% H ₂ O 26 °C, 5 parameter model	3.50E-04	1.44	13.94	0.32	2.10	10.53
2 vol-% H ₂ O 25 °C, 5 parameter model	3.50E-04	0.77	66.66	0.17	1.90	17.25
0.2 vol-% H ₂ O 25 °C, 7 parameter model ($t_1=t_2=3$)	3.50E-04	0.34	2.26	1.10	2.17	11.94
1 vol-% H ₂ O 26 °C, 7 parameter model ($t_1=t_2=3$)	3.50E-04	0.31	5.02	0.41	1.83	10.83
2 vol-% H ₂ O 25 °C, 7 parameter model ($t_1=t_2=3$)	3.50E-04	0.18	8.78	0.16	2.16	18.36
2 vol-% H ₂ O 25 °C, 100 ml/min, 5 parameter model	7.44E-05	3.10	45.99	0.23	1.96	17.91
2 vol-% H ₂ O 25 °C, 100 ml/min, 7 parameter model ($t_1=t_2=3$)	7.44E-05	1.37	6.35	0.38	2.22	19.75

The kinetic and heat transfer parameters were also affected by other limitations of the used models and the experimental setup. The used adsorption column only had one temperature probe inside the column, while measurement from several points would be required for determining the real temperature distribution. In this work, the used dynamic model only considered the dimensions of the adsorbent bed, while for obtaining more generalized fitted parameters valid for scale-up, the dead volume of the column and pipelines should also be taken into account. Here, this was taken into account only in the case of H₂O by adding the adsorption capacity obtained without sample to the modelled H₂O equilibrium capacity (see section 3.2.4). While this method improved the simulation of experimental H₂O concentration profiles, it also affected the heat balance, thus changing the heat transfer parameters. Moreover, the measured CO₂ isotherms were pseudo-equilibrium isotherms, thus underestimating the CO₂ capacity especially in the 100 ml/min case like mentioned above, thus affecting the shape of the simulated breakthrough profiles and the kinetic parameters.

In all experiments, the upper part of the CO₂ breakthrough curve showed a slow approach towards the feed concentration. Especially in the 100 ml/min case, a significant decrease of uptake rate could be observed after a few hours of rapid adsorption. These results highlight the challenges in studying the adsorption of CO₂ from ultra-dilute feeds. Even in the 2-day experiment, a final equilibrium was not established, so the measurement of true equilibrium CO₂ isotherms would be very time and resource consuming. The significant slow-down of CO₂ uptake rate after initial hours of rapid adsorption has also been reported in the literature for other amine-based adsorbents in DAC conditions at 25-36 °C [102,106,187]. In addition to being time and resource-consuming, slowed-down adsorption makes the accurate simulation of the CO₂ breakthrough curve difficult [186].

Overall, the dynamic model with the novel CO₂ adsorption kinetic model led to a very good representation of the experimental adsorption breakthrough data. Even the upper part of the CO₂ breakthrough profile, with a very slow increase towards the feed concentration, was closely simulated in some cases at a 500 ml/min flow rate, especially with the 7-parameter model. This could mostly be attributed to better predictions of the (pseudo-)equilibrium CO₂ capacities compared to the 5-parameter model. In these conditions, the slowed-down adsorption can be attributed to gas diffusion limitations within the adsorbent particles. However, in the 100 ml/min case, the external mass transfer film formed around the adsorbent particles is thicker at the lower flow-rate, therefore slowing down the diffusion of CO₂ from the fluid phase onto the adsorbent surface. Thus, the reason why both models failed in simulating the upper part of the curve may be related to the retarded mass transfer at a lower flow rate, in addition to under-predicting the adsorption capacity. Thus, more accurate modelling of the adsorption kinetics may require a separate diffusion model for this external resistance. The effect of intra-particle diffusion should also be evaluated to find if the proposed kinetic co-adsorption model is adequate for modelling the kinetics within the adsorbent particle [220].

On the other hand, an optimal DAC process is most likely operated in adsorption/desorption cycles that last hours rather than days. The significant slow-down of the adsorption rate after a few hours indicates that targeting equilibrium capacity in the actual process may not be reasonable in terms of the overall economics of the process. After all, the daily CO₂ productivity is reduced if either adsorption or desorption phase is prolonged. Therefore, even the current form of the dynamic model is useful for estimating the specific energy requirement of the adsorption phase and adsorption rate in DAC with the current adsorbent. Additionally, it is expected that the proposed kinetic model can be used for temperature and humidity dependent modelling of CO₂ adsorption from the air using other amine-functionalized adsorbents as well.

5 Conclusions

Direct air capture may play a significant role in the mitigation and reversal of climate change, even already during the following decades. Adsorbent-based DAC using amine-functionalized materials is one of the most promising approaches to capturing CO₂ from the air. This technology can produce pure CO₂ independent of location, while requiring electricity and low-grade heat to operate. However, for large-scale commercialization, the cost of DAC is too high, being up to over 800 €/t_{CO₂} according to some estimates. Some projections estimate that the cost of DAC will decrease from around 300-500 €/t_{CO₂} to well under 100 €/t_{CO₂} in the following few decades. However, significant uncertainties exist in these numbers. Scaling up the technology may also face serious material and energy limitations when aiming at Gt-scale yearly CO₂ removal. These limitations and the high cost of DAC may severely limit the carbon removal and the CCU potential of this technology.

The higher end of the cost estimates can be explained partly with overly pessimistic assumptions, but also by the immaturity of the technology. While amine-based adsorbents enable selective and effective capture of CO₂ from the air and are regenerable at near 100 °C, significant challenges are present in the development of these materials. The combination of a high number of amine groups to achieve high CO₂ adsorption capacity, while maintaining good adsorption kinetics, remains one of the main hurdles. One of the main disadvantages of using supported amines is the degradation of these materials, which can occur via different mechanisms such as oxidation, urea formation, or leaching of the amines or the support material. To gain most of the materials without degrading them, with minimal energy consumption, process design is required.

On the other hand, the high uncertainty in the cost estimates largely originates from the lack of data about the adsorbent materials and the DAC process. The degradation rate of amine-based adsorbents in different conditions relevant to DAC processes has not been studied extensively. Although a significant number of reports discuss the reactions of CO₂ with amines in dry or humid conditions, the effect of humidity on the CO₂ capacity in different DAC conditions has not been comprehensively studied. Especially, the modelling of this phenomenon has been lacking. Moreover, the literature has mainly focused on the study of two process types: the temperature vacuum swing adsorption and steam-stripping processes. Regeneration methods that produce less concentrated CO₂, such as those utilizing air or inert stripping gases, have not been compared in detail. The latter process types may be relevant in applications where pure CO₂ is not required, such as greenhouses and microbial or algae cultivation.

In this thesis, the DAC process was studied using an amine-functionalized resin as the adsorbent material. The amino resin was physicochemically characterized, revealing a surface area of 32 m²/g with a median size of 0.6 μm. FTIR spectroscopy referred to secondary and/or primary amines and ammonium carbamate on the surface of the adsorbent. However, a more detailed study of the capture mechanism of CO₂ in dry and

humid conditions would require the control of conditions during the measurement of the IR spectra.

The CO₂ adsorption performance of the adsorbent was studied in various conditions relevant to direct air capture. The studied amino resin has an adsorption capacity of around 0.5 mmol_{CO₂}/g_{sorbent} at 25 °C in dry DAC conditions, which is in the lower range compared to other reported amine-functionalized adsorbents. However, humidity and cold conditions were found to almost double the adsorption capacity. Of the common adsorption isotherm models, the well-known Toth model yielded the best fit to experimental CO₂ isotherms in ultra-dilute conditions. Using the parameters of the Toth isotherm model fits, the CO₂ working capacity was modelled in different DAC processes.

On the basis of a working capacity analysis, pressure swing adsorption cannot be recommended as a practical process for DAC due to requiring high compression of feed air and/or unreasonably low vacuum pressure during regeneration. While temperature-vacuum swing adsorption with a closed inlet (closed TVSA) during regeneration allows the production of high-purity CO₂, the CO₂ working capacity was almost halved compared to temperature swing adsorption (TSA). From another perspective, similar working capacity values were achievable in TSA operation with a regeneration temperature of 50-60 °C compared to closed TVSA method with a regeneration temperature of 90 °C. Therefore, in terms of working capacity, if only dilute CO₂ is required, the TSA process is preferable to the closed TVSA process. A higher adsorption capacity at low temperature and/or under humid conditions also translated into a higher working capacity. Thus, in terms of the CO₂ working capacity, it would seem that cold climates, e.g., winter conditions in Finland, are beneficial to the DAC process.

To study varying regeneration conditions and to be able to conduct cyclic experiments, an improved laboratory-scale CO₂/H₂O adsorption/desorption device with automatic operation was built. Using this device, different DAC regeneration processes were compared experimentally. The closed TVSA process led to a limited working capacity even with desorption at 100 °C, as expected from the isotherm-based working capacity analysis. The highest CO₂ productivity was obtained using TVSA with a stripping gas, while isobaric TSA had the lowest specific energy requirement. Coupling TVSA with a stripping gas also enabled a lower regeneration temperature of 60 °C, while still achieving higher CO₂ productivity compared to the closed TVSA approach. Consequently, using a mild vacuum of 500 mbar resulted in lower regeneration specific energy requirements than with the closed TVSA process, being around 7 GJ/t_{CO₂} with around 90% adsorbent regeneration. Using a lower regeneration temperature in TVSA with an air purge also led to a better cyclic stability compared to the closed TVSA process with a desorption temperature of 100 °C. Therefore, coupling the TVSA process with an air or inert purge gas can yield better CO₂ productivity, specific energy requirement and adsorbent stability compared to the commonly proposed closed TVSA process. Thus, the experimental comparison confirmed the results of the working capacity analysis in that the closed TVSA process should only be used as a DAC process if pure CO₂ is required.

To model the effect of humidity on the CO₂ capacity in DAC, a novel kinetic model was developed, which is based on the reactions of CO₂ and H₂O with supported amines. This model was used to accurately depict the enhancing effect of humidity on CO₂ adsorption in equilibrium and dynamic conditions. Using the kinetic model, experimental humid CO₂ isotherms were closely modelled. For dynamic simulation of CO₂ adsorption from air, the developed model was used to describe CO₂ adsorption kinetics, and the Guggenheim Anderson De Boer (GAB) isotherm combined with the linear driving force model was used to describe the H₂O adsorption kinetics. At best, the full shape of the CO₂ adsorption breakthrough curves were closely simulated using these models. Therefore, the developed kinetic model offers a new and accurate method to model CO₂ adsorption equilibrium and dynamics in humid conditions. When using the kinetic parameters of the model to describe mass transfer, the model can be used in place of separate isotherm and kinetic models for CO₂ adsorption simulation.

The present work produced important new data about the adsorption-based direct air capture process and its modelling, but is limited in some respects. The cyclic capacity drop in different regeneration processes was determined from only around 20 cycles of adsorption/desorption without probing the possible chemical changes in the adsorbent. The working capacity analysis of different DAC process options was based on equilibrium data, while in a real process, kinetics may become the limiting factor for economic feasibility. On the other hand, the experimental comparison of regeneration methods was only done in dry conditions, and was limited in the number of process parameter choices. The simulation part in this work, while in humid conditions, only focused on the adsorption phase. More comprehensive DAC simulation is needed to evaluate the economic feasibility of different process options, such as the TVSA process that utilizes a purge gas.

Optimization of the DAC process for maximal CO₂ productivity and minimal energy requirement requires the simulation of both adsorption and desorption phases in varying operational conditions. To achieve this, more general model parameters need to be acquired. Experimental CO₂ equilibrium data should be extended to contain points from the full CO₂ partial pressure range. For more generalized treatment of the adsorption/desorption kinetics, the proposed CO₂ kinetics model should be used for the modelling of intrinsic adsorption kinetics, coupled with diffusion models. To improve experimental data on heat transfer, the existing experimental setup could be upgraded with an adsorption column with two-dimensional temperature measurement. Moreover, to minimize the degradation of the adsorbent, more data about the cyclic degradation rates in long-term operation and chemical changes in the adsorbent is required. Thus, more extensive adsorption/desorption cycles coupled with chemical characterization of the adsorbent are needed. Finally, the experimental and modelling work should be done closely tied to adsorbent development.

References

- [1] D. Lüthi, M. Le Floch, B. Bereiter, T. Blunier, J.M. Barnola, U. Siegenthaler, D. Raynaud, J. Jouzel, H. Fischer, K. Kawamura, T.F. Stocker, High-resolution carbon dioxide concentration record 650,000-800,000 years before present, *Nature*. 453 (2008) 379–382. <https://doi.org/10.1038/nature06949>.
- [2] P. Tans (NOAA/GML), R. Keeling (Scripps Institution of Oceanography), www.esrl.noaa.gov/gmd/ccgg/trends/, scrippsco2.ucsd.edu/, (2021).
- [3] V. Masson-Delmotte, P. Zhai, H.O. Pörtner, D. Roberts, J. Skea, P.R. Shukla, A. Pirani, W. Moufouma-Okia, C. Péan, R. Pidcock, S. Connors, J.B.R. Matthews, Y. Chen, X. Zhou, M.I. Gomis, E. Lonnoy, T. Maycock, M. Tignor, T. Waterfield, IPCC, 2018: Summary for Policymakers. In: Global warming of 1.5°C. An IPCC Special Report on the impacts of global warming of 1.5°C above pre-industrial levels and related global greenhouse gas emission pathways, in the context of strengthening the global response, 2018. https://report.ipcc.ch/sr15/pdf/sr15_spm_final.pdf%0Ahttp://www.ipcc.ch/report/sr15/.
- [4] H. Ritchie, M. Roser, CO₂ and Greenhouse Gas Emissions, (2020). <https://ourworldindata.org/co2-and-other-greenhouse-gas-emissions> (accessed April 7, 2021).
- [5] Climate Watch historical GHG emissions, 2021, Washington, DC: World Resources Institute, (2021). <https://www.climatewatchdata.org/ghg-emissions> (accessed August 4, 2021).
- [6] S. Fawzy, A.I. Osman, J. Doran, D.W. Rooney, Strategies for mitigation of climate change: a review, *Environ. Chem. Lett.* 18 (2020) 2069–2094. <https://doi.org/10.1007/s10311-020-01059-w>.
- [7] P. Bains, P. Psarras, J. Wilcox, CO₂ capture from the industry sector, *Prog. Energy Combust. Sci.* 63 (2017) 146–172. <https://doi.org/10.1016/j.pecs.2017.07.001>.
- [8] D. Jansen, M. Gazzani, G. Manzolini, E. Van Dijk, M. Carbo, Pre-combustion CO₂ capture, *Int. J. Greenh. Gas Control.* 40 (2015) 167–187. <https://doi.org/10.1016/j.ijggc.2015.05.028>.
- [9] F. Wu, M.D. Argyle, P.A. Dellenback, M. Fan, Progress in O₂ separation for oxy-fuel combustion—A promising way for cost-effective CO₂ capture: A review, *Prog. Energy Combust. Sci.* 67 (2018) 188–205. <https://doi.org/10.1016/j.pecs.2018.01.004>.
- [10] O. Omoregbe, A.N. Mustapha, R. Steinberger-Wilckens, A. El-Kharouf, H. Onyeaka, Carbon capture technologies for climate change mitigation: A

- bibliometric analysis of the scientific discourse during 1998–2018, *Energy Reports*. 6 (2020) 1200–1212. <https://doi.org/10.1016/j.egy.2020.05.003>.
- [11] I.M. Saeed, P. Alaba, S.A. Mazari, W.J. Basirun, V.S. Lee, N. Sabzoi, Opportunities and challenges in the development of monoethanolamine and its blends for post-combustion CO₂ capture, *Int. J. Greenh. Gas Control*. 79 (2018) 212–233. <https://doi.org/10.1016/j.ijggc.2018.11.002>.
- [12] X. Chen, G. Huang, C. An, Y. Yao, S. Zhao, Emerging N-nitrosamines and N-nitramines from amine-based post-combustion CO₂ capture – A review, *Chem. Eng. J.* 335 (2018) 921–935. <https://doi.org/10.1016/j.cej.2017.11.032>.
- [13] Z. Zhang, Y. Li, W. Zhang, J. Wang, M.R. Soltanian, A.G. Olabi, Effectiveness of amino acid salt solutions in capturing CO₂: A review, *Renew. Sustain. Energy Rev.* 98 (2018) 179–188. <https://doi.org/10.1016/j.rser.2018.09.019>.
- [14] Y. Wang, L. Zhao, A. Otto, M. Robinius, D. Stolten, A review of post-combustion CO₂ capture technologies from coal-fired power plants, *Energy Procedia*. 114 (2017) 650–665. <https://doi.org/10.1016/j.egypro.2017.03.1209>.
- [15] S. Choi, J.H. Drese, C.W. Jones, Adsorbent materials for carbon dioxide capture from large anthropogenic point sources, *ChemSusChem*. 2 (2009) 796–854. <https://doi.org/10.1002/cssc.200900036>.
- [16] European Central Bank, Euro foreign exchange reference rates, US dollar (USD), (2021). https://www.ecb.europa.eu/stats/policy_and_exchange_rates/euro_reference_exchange_rates/html/eurofxref-graph-usd.en.html (accessed November 12, 2021).
- [17] F. Cheng, X. Zhang, K. Mu, X. Ma, M. Jiao, Z. Wang, P. Limpachanangkul, B. Chalermisinsuwan, Y. Gao, Y. Li, Z. Chen, L. Liu, Recent progress of Sn-based derivative catalysts for electrochemical reduction of CO₂, *Energy Technol.* 9 (2021) 1–18. <https://doi.org/10.1002/ente.202000799>.
- [18] J. V. Veselovskaya, P.D. Parunin, O. V. Netskina, L.S. Kibis, A.I. Lysikov, A.G. Okunev, Catalytic methanation of carbon dioxide captured from ambient air, *Energy*. 159 (2018) 766–773. <https://doi.org/10.1016/j.energy.2018.06.180>.
- [19] A. Goepfert, M. Czaun, J.P. Jones, G.K. Surya Prakash, G.A. Olah, Recycling of carbon dioxide to methanol and derived products-closing the loop, *Chem. Soc. Rev.* 43 (2014) 7995–8048. <https://doi.org/10.1039/c4cs00122b>.
- [20] F. Vidal Vázquez, J. Koponen, V. Ruuskanen, C. Bajamundi, A. Kosonen, P. Simell, J. Ahola, C. Frilund, J. Elfving, M. Reinikainen, N. Heikkinen, J. Kauppinen, P. Piermartini, Power-to-X technology using renewable electricity and carbon dioxide from ambient air: SOLETAIR proof-of-concept and improved

- process concept, *J. CO₂ Util.* 28 (2018) 235–246. <https://doi.org/10.1016/j.jcou.2018.09.026>.
- [21] N. Mac Dowell, P.S. Fennell, N. Shah, G.C. Maitland, The role of CO₂ capture and utilization in mitigating climate change, *Nat. Clim. Chang.* 7 (2017) 243–249. <https://doi.org/10.1038/nclimate3231>.
- [22] S. Kaiser, S. Bringezu, Use of carbon dioxide as raw material to close the carbon cycle for the German chemical and polymer industries, *J. Clean. Prod.* 271 (2020) 122775. <https://doi.org/10.1016/j.jclepro.2020.122775>.
- [23] M. Götz, J. Lefebvre, F. Mörs, A. McDaniel Koch, F. Graf, S. Bajohr, R. Reimert, T. Kolb, Renewable Power-to-Gas: A technological and economic review, *Renew. Energy.* 85 (2016) 1371–1390. <https://doi.org/10.1016/j.renene.2015.07.066>.
- [24] D.P. Van Vuuren, A.F. Hof, M.A.E. Van Sluisveld, K. Riahi, Open discussion of negative emissions is urgently needed, *Nat. Energy.* 2 (2017) 902–904. <https://doi.org/10.1038/s41560-017-0055-2>.
- [25] S. Fuss, W.F. Lamb, M.W. Callaghan, J. Hilaire, F. Creutzig, T. Amann, T. Beringer, W. De Oliveira Garcia, J. Hartmann, T. Khanna, G. Luderer, G.F. Nemet, J. Rogelj, P. Smith, J.L.V. Vicente, J. Wilcox, M. Del Mar Zamora Dominguez, J.C. Minx, Negative emissions - Part 2: Costs, potentials and side effects, *Environ. Res. Lett.* 13 (2018) 063002. <https://doi.org/10.1088/1748-9326/aabf9f>.
- [26] K.S. Lackner, P. Grimes, H.J. Ziock, Carbon dioxide extraction from air: Is it an option?, *Proc. 24th Annu. Tech. Conf. Coal Util. Fuel Syst.* (1999) 885–896.
- [27] F.S. Zeman, K.S. Lackner, Capturing carbon dioxide directly from the atmosphere, *World Resour. Rev.* 16 (2004) 157–172.
- [28] R. Socolow, M. Desmond, R. Aines, J. Blackstock, O. Bolland, T. Kaarsberg, N. Lewis, M. Mazzotti, A. Pfeffer, K. Sawyer, J. Siirola, B. Smit, J. Wilcox, Direct air capture of CO₂ with chemicals - A technology assessment for the APS Panel on Public Affairs, APS Physics, 2011.
- [29] R. Baciocchi, G. Storti, M. Mazzotti, Process design and energy requirements for the capture of carbon dioxide from air, *Chem. Eng. Process.* 45 (2006) 1047–1058. <https://doi.org/10.1016/j.cep.2006.03.015>.
- [30] D.W. Keith, G. Holmes, D. St. Angelo, K. Heidel, A process for capturing CO₂ from the atmosphere, *Joule.* 2 (2018) 1573–1594. <https://doi.org/10.1016/j.joule.2018.05.006>.
- [31] G. Holmes, D.W. Keith, An air-liquid contactor for large-scale capture of CO₂ from air, *Philos. Trans. R. Soc. A Math. Phys. Eng. Sci.* 370 (2012) 4380–4403.

- <https://doi.org/10.1098/rsta.2012.0137>.
- [32] Carbon Engineering, subsites: “Our technology”, “Our story”, “News & updates”, (2021). <https://carbonengineering.com/> (accessed November 2, 2021).
- [33] F. Barzagli, C. Giorgi, F. Mani, M. Peruzzini, Screening study of different amine-based solutions as sorbents for direct CO₂ capture from air, *ACS Sustain. Chem. Eng.* 8 (2020) 14013–14021. <https://doi.org/10.1021/acssuschemeng.0c03800>.
- [34] R. Custelcean, N.J. Williams, K.A. Garrabrant, P. Agullo, F.M. Brethomé, H.J. Martin, M.K. Kidder, Direct air capture of CO₂ with aqueous amino acids and solid bis-iminoguanidines (BIGs), *Ind. Eng. Chem. Res.* 58 (2019) 23338–23346. <https://doi.org/10.1021/acs.iecr.9b04800>.
- [35] H. Cai, X. Zhang, L. Lei, C. Xiao, Direct CO₂ capture from air via crystallization with a trichelating iminoguanidine ligand, *ACS Omega.* (2020). <https://doi.org/10.1021/acsomega.0c02460>.
- [36] M. Liu, R. Custelcean, S. Seifert, I. Kuzmenko, G. Gadikota, Hybrid absorption-crystallization strategies for the direct air capture of CO₂ using phase-changing guanidium bases: insights from in operando x-ray scattering and infrared spectroscopy measurements, *Ind. Eng. Chem. Res.* 59 (2020) 20953–20959. <https://doi.org/10.1021/acs.iecr.0c03863>.
- [37] R. Custelcean, K.A. Garrabrant, P. Agullo, N.J. Williams, Direct air capture of CO₂ with aqueous peptides and crystalline guanidines, *Cell Reports Phys. Sci.* 2 (2020) 100385. <https://doi.org/10.26434/chemrxiv.13469985.v1>.
- [38] M. Erans, S.A. Nabavi, V. Manović, Pilot-scale calcination of limestone in steam-rich gas for direct air capture, *Energy Convers. Manag.* X. 1 (2019) 100007. <https://doi.org/10.1016/j.ecmx.2019.100007>.
- [39] M. Erans, S.A. Nabavi, V. Manović, Carbonation of lime-based materials under ambient conditions for direct air capture, *J. Clean. Prod.* 242 (2020). <https://doi.org/10.1016/j.jclepro.2019.118330>.
- [40] K. Li, J.D. Kress, D.S. Mebane, The mechanism of CO₂ adsorption under dry and humid conditions in mesoporous silica-supported amine sorbents, *J. Phys. Chem. C.* 120 (2016) 23683–23691. <https://doi.org/10.1021/acs.jpcc.6b08808>.
- [41] A. Goepfert, H. Zhang, M. Czaun, R.B. May, G.K.S. Prakash, G. a. Olah, S.R. Narayanan, Easily regenerable solid adsorbents based on polyamines for carbon dioxide capture from the air, *ChemSusChem.* 7 (2014) 1386–1397. <https://doi.org/10.1002/cssc.201301114>.
- [42] J.A. Wurzbacher, C. Gebald, N. Piatkowski, A. Steinfeld, Concurrent separation

- of CO₂ and H₂O from air by a temperature-vacuum swing adsorption/desorption cycle, *Environ. Sci. Technol.* 46 (2012) 9191–9198.
- [43] Climeworks, subsite: “CO₂ removal,” (2021). <https://www.climeworks.com> (accessed June 10, 2021).
- [44] M.J. Bos, S. Pietersen, D.W.F.F. Brillman, Production of high purity CO₂ from air using solid amine sorbents, *Chem. Eng. Sci.* X. 2 (2019) 100020. <https://doi.org/10.1016/j.cesx.2019.100020>.
- [45] P.Q. Liao, X.W. Chen, S.Y. Liu, X.Y. Li, Y.T. Xu, M. Tang, Z. Rui, H. Ji, J.P. Zhang, X.M. Chen, Putting an ultrahigh concentration of amine groups into a metal-organic framework for CO₂ capture at low pressures, *Chem. Sci.* 7 (2016) 6528–6533. <https://doi.org/10.1039/c6sc00836d>.
- [46] J.J. Lee, C.H. Chen, D. Shimon, S.E. Hayes, C. Sievers, C.W. Jones, Effect of humidity on the CO₂ adsorption of tertiary amine grafted SBA-15, *J. Phys. Chem. C.* 121 (2017) 23480–23487. <https://doi.org/10.1021/acs.jpcc.7b07930>.
- [47] T. Wang, K.S. Lackner, A. Wright, Moisture swing sorbent for carbon dioxide capture from ambient air, *Environ. Sci. Technol.* 45 (2011) 6670–6675. <https://doi.org/10.1021/es201180v>.
- [48] J. V. Veselovskaya, V.S. Derevschikov, A.S. Shalygin, D.A. Yatsenko, K₂CO₃-containing composite sorbents based on a ZrO₂ aerogel for reversible CO₂ capture from ambient air, *Microporous Mesoporous Mater.* 310 (2021) 110624. <https://doi.org/10.1016/j.micromeso.2020.110624>.
- [49] J. V. Veselovskaya, V.S. Derevschikov, T.Y. Kardash, O.A. Stonkus, T.A. Trubitsina, A.G. Okunev, Direct CO₂ capture from ambient air using K₂CO₃ Al₂O₃ composite sorbent, *Int. J. Greenh. Gas Control.* 17 (2013) 332–340. <https://doi.org/10.1016/j.ijggc.2013.05.006>.
- [50] Climeworks, Climeworks makes history with world-first commercial CO₂ capture plant, (2017). <https://www.climeworks.com/news/today-climeworks-is-unveiling-its-proudest-achievement> (accessed November 10, 2021).
- [51] Norsk e-fuel, (2020). <https://www.norsk-e-fuel.com/en/> (accessed April 19, 2021).
- [52] V. Ruuskanen, G. Givirovskiy, J. Elfving, P. Kokkonen, A. Karvinen, L. Järvinen, J. Sillman, M. Vainikka, J. Ahola, Neo-Carbon Food concept: A pilot-scale hybrid biological–inorganic system with direct air capture of carbon dioxide, *J. Clean. Prod.* 278 (2021) 123423. <https://doi.org/10.1016/j.jclepro.2020.123423>.
- [53] L. Rosa, D.L. Sanchez, G. Realmonte, D. Baldocchi, P. D’Odorico, The water footprint of carbon capture and storage technologies, *Renew. Sustain. Energy Rev.*

- 138 (2021) 110511. <https://doi.org/10.1016/j.rser.2020.110511>.
- [54] C.J.E. Bajamundi, J. Koponen, V. Ruuskanen, J. Elfving, A. Kosonen, J. Kauppinen, J. Ahola, Capturing CO₂ from air: Technical performance and process control improvement, *J. CO₂ Util.* 30 (2019) 232–239. <https://doi.org/10.1016/j.jcou.2019.02.002>.
- [55] S. Deutz, A. Bardow, Life-cycle assessment of an industrial direct air capture process based on temperature–vacuum swing adsorption, *Nat. Energy.* 6 (2021) 203–213. <https://doi.org/10.1038/s41560-020-00771-9>.
- [56] C. Van Der Giesen, C.J. Meinrenken, R. Kleijn, B. Sprecher, K.S. Lackner, G.J. Kramer, A life-cycle assessment case study of coal-fired electricity generation with humidity swing direct air capture of CO₂ versus mea-based postcombustion capture, *Environ. Sci. Technol.* 51 (2017) 1024–1034. <https://doi.org/10.1021/acs.est.6b05028>.
- [57] M.M.J. de Jonge, J. Daemen, J.M. Loriaux, Z.J.N. Steinmann, M.A.J. Huijbregts, Life cycle carbon efficiency of direct air capture systems with strong hydroxide sorbents, *Int. J. Greenh. Gas Control.* 80 (2019) 25–31. <https://doi.org/10.1016/j.ijggc.2018.11.011>.
- [58] C. Breyer, M. Fasihi, C. Bajamundi, F. Creutzig, Direct air capture of CO₂: A key technology for ambitious climate change mitigation, *Joule.* 3 (2019) 2053–2057. <https://doi.org/10.1016/j.joule.2019.08.010>.
- [59] G. Realmonte, L. Drouet, A. Gambhir, J. Glynn, A. Hawkes, A.C. Köberle, M. Tavoni, An inter-model assessment of the role of direct air capture in deep mitigation pathways, *Nat. Commun.* 10 (2019) 1–12. <https://doi.org/10.1038/s41467-019-10842-5>.
- [60] C. Chen, M. Tavoni, Direct air capture of CO₂ and climate stabilization: A model based assessment, *Clim. Change.* 118 (2013) 59–72. <https://doi.org/10.1007/s10584-013-0714-7>.
- [61] S. Chatterjee, K.W. Huang, Unrealistic energy and materials requirement for direct air capture in deep mitigation pathways, *Nat. Commun.* 11 (2020) 10–12. <https://doi.org/10.1038/s41467-020-17203-7>.
- [62] G. Realmonte, L. Drouet, A. Gambhir, J. Glynn, A. Hawkes, A.C. Köberle, M. Tavoni, Reply to “High energy and materials requirement for direct air capture calls for further analysis and R&D,” *Nat. Commun.* 11 (2020) 10–11. <https://doi.org/10.1038/s41467-020-17204-6>.
- [63] H. Azarabadi, K.S. Lackner, Postcombustion capture or direct air capture in decarbonizing US natural gas power?, *Environ. Sci. Technol.* 54 (2020) 5102–

5111. <https://doi.org/10.1021/acs.est.0c00161>.
- [64] J.C. Minx, W.F. Lamb, M.W. Callaghan, S. Fuss, J. Hilaire, F. Creutzig, T. Amann, T. Beringer, W. De Oliveira Garcia, J. Hartmann, T. Khanna, D. Lenzi, G. Luderer, G.F. Nemet, J. Rogelj, P. Smith, J.L. Vicente Vicente, J. Wilcox, M. Del Mar Zamora Dominguez, Negative emissions - Part 1: Research landscape and synthesis, *Environ. Res. Lett.* 13 (2018). <https://doi.org/10.1088/1748-9326/aabf9b>.
- [65] A. Sinha, L.A. Darunte, C.W. Jones, M.J. Realff, Y. Kawajiri, Systems design and economic analysis of direct air capture of CO₂ through temperature vacuum swing adsorption using MIL-101(Cr)-PEI-800 and mmen-Mg₂(dobpdc) MOF adsorbents, *Ind. Eng. Chem. Res.* 56 (2017) 750–764. <https://doi.org/10.1021/acs.iecr.6b03887>.
- [66] K.Z. House, A.C. Baclig, M. Ranjan, E. a. van Nierop, J. Wilcox, H.J. Herzog, Economic and energetic analysis of capturing CO₂ from ambient air, *Proc. Natl. Acad. Sci.* 108 (2011) 20428–20433. <https://doi.org/10.1073/pnas.1012253108>.
- [67] D. Krekel, R.C. Samsun, R. Peters, D. Stolten, The separation of CO₂ from ambient air – A techno-economic assessment, *Appl. Energy.* 218 (2018) 361–381. <https://doi.org/10.1016/j.apenergy.2018.02.144>.
- [68] J. Tollefson, Sucking carbon dioxide from air is cheaper than scientists thought, *Nature.* 558 (2018) 173. <https://doi.org/https://doi.org/10.1038/d41586-018-05357-w>.
- [69] M. Fasihi, O. Efimova, C. Breyer, Techno-economic assessment of CO₂ direct air capture plants, *J. Clean. Prod.* 224 (2019) 957–980. <https://doi.org/10.1016/j.jclepro.2019.03.086>.
- [70] R. Hanna, A. Abdulla, Y. Xu, D.G. Victor, Emergency deployment of direct air capture as a response to the climate crisis, *Nat. Commun.* 12 (2021) 1–13. <https://doi.org/10.1038/s41467-020-20437-0>.
- [71] R. Serna-Guerrero, Y. Belmabkhout, A. Sayari, Modeling CO₂ adsorption on amine-functionalized mesoporous silica: 1. A semi-empirical equilibrium model, *Chem. Eng. J.* 161 (2010) 173–181. <https://doi.org/10.1016/j.cej.2010.04.024>.
- [72] R. Veneman, F. Natalia, Z. Wenying, L. Zhenshan, K. Sascha, W. Brilman, Adsorption of H₂O and CO₂ on supported amine sorbents, *Int. J. Greenh. Gas Control.* 41 (2015) 268–275. <https://doi.org/http://dx.doi.org/10.1016/j.ijggc.2015.07.014>.
- [73] C. Gebald, J. a. Wurzbacher, A. Borgschulte, T. Zimmermann, A. Steinfeld, Single-component and binary CO₂ and H₂O adsorption of amine-functionalized

- cellulose, *Environ. Sci. Technol.* 48 (2014) 2497–2504. <https://doi.org/10.1021/es404430g>.
- [74] M.A. Alkhabbaz, P. Bollini, G.S. Foo, C. Sievers, C.W. Jones, Important roles of enthalpic and entropic contributions to CO₂ capture from simulated flue gas and ambient air using mesoporous silica grafted amines, *J. Am. Chem. Soc.* 136 (2014) 13170–13173. <https://doi.org/10.1021/ja507655x>.
- [75] A. Kumar, D.G. Madden, M. Lusi, K. Chen, E.A. Daniels, T. Curtin, J.J.P. Iv, M.J. Zaworotko, Direct air capture of CO₂ by physisorbent materials, *Angew. Chemie - Int. Ed.* 54 (2015) 1–7. <https://doi.org/10.1002/anie.201506952>.
- [76] E.S. Sanz-Pérez, C.R. Murdock, S.A. Didas, C.W. Jones, Direct capture of CO₂ from ambient air, *Chem. Rev.* 116 (2016) 11840–11876. <https://doi.org/10.1021/acs.chemrev.6b00173>.
- [77] X. Shi, H. Xiao, H. Azarabadi, J. Song, X. Wu, X. Chen, K.S. Lackner, Sorbents for the direct capture of CO₂ from ambient air, *Angew. Chemie - Int. Ed.* 59 (2020) 6984–7006. <https://doi.org/10.1002/anie.201906756>.
- [78] S.A. Didas, M.A. Sakwa-Novak, G.S. Foo, C. Sievers, C.W. Jones, Effect of amine surface coverage on the co-adsorption of CO₂ and water: spectral deconvolution of adsorbed species, *J. Phys. Chem. Lett.* 5 (2014) 4194–4200. <https://doi.org/10.1021/jz502032c>.
- [79] C.H. Chen, D. Shimon, J.J. Lee, F. Mentink-Vigier, I. Hung, C. Sievers, C.W. Jones, S.E. Hayes, The “missing” bicarbonate in CO₂ chemisorption reactions on solid amine sorbents, *J. Am. Chem. Soc.* 140 (2018) 8648–8651. <https://doi.org/10.1021/jacs.8b04520>.
- [80] J. Yu, S.S.C. Chuang, The role of water in CO₂ capture by amine, *Ind. Eng. Chem. Res.* 56 (2017) 6337–6347. <https://doi.org/10.1021/acs.iecr.7b00715>.
- [81] W. Buijs, S. De Flart, Direct air capture of CO₂ with an amine resin: A molecular modeling study of the CO₂ capturing process, *Ind. Eng. Chem. Res.* 56 (2017) 12297–12304. <https://doi.org/10.1021/acs.iecr.7b02613>.
- [82] A.C. Forse, P.J. Milner, J.H. Lee, H.N. Redfearn, J. Oktawiec, R.L. Siegelman, J.D. Martell, B. Dinakar, L.B. Porter-Zasada, M.I. Gonzalez, J.B. Neaton, J.R. Long, J.A. Reimer, Elucidating CO₂ chemisorption in diamine-appended metal-organic frameworks, *J. Am. Chem. Soc.* 140 (2018) 18016–18031. <https://doi.org/10.1021/jacs.8b10203>.
- [83] D.D. Miller, J. Yu, S.S.C. Chuang, Unraveling the structure and binding energy of adsorbed CO₂/H₂O on amine sorbents, *J. Phys. Chem. C.* 124 (2020) 24677–24689. <https://doi.org/10.1021/acs.jpcc.0c04942>.

- [84] S. A. Didas, A.R. Kulkarni, D.S. Sholl, C.W. Jones, Role of amine structure on carbon dioxide adsorption from ultradilute gas streams such as ambient air, *ChemSusChem*. 5 (2012) 2058–2064. <https://doi.org/10.1002/cssc.201200196>.
- [85] J.J. Lee, C.J. Yoo, C.H. Chen, S.E. Hayes, C. Sievers, C.W. Jones, Silica-supported sterically hindered amines for CO₂ capture, *Langmuir*. 34 (2018) 12279–12292. <https://doi.org/10.1021/acs.langmuir.8b02472>.
- [86] J.A. Wurzbacher, C. Gebald, A. Steinfeld, Separation of CO₂ from air by temperature-vacuum swing adsorption using diamine-functionalized silica gel, *Energy Environ. Sci*. 4 (2011) 3584–3592. <https://doi.org/10.1039/c1ee01681d>.
- [87] A. Sayari, Q. Liu, P. Mishra, Enhanced adsorption efficiency through materials design for direct air capture over supported polyethylenimine, *ChemSusChem*. 9 (2016) 2796–2803. <https://doi.org/10.1002/cssc.201600834>.
- [88] D.J.N. Subagyono, Z. Liang, G.P. Knowles, A.L. Chaffee, Amine modified mesocellular siliceous foam (MCF) as a sorbent for CO₂, *Chem. Eng. Res. Des.* 89 (2011) 1647–1657. <https://doi.org/10.1016/j.cherd.2011.02.019>.
- [89] P. Schmidt-winkel, W.W. Lukens, P. Yang, D.I. Margolese, J.S. Lettow, J.Y. Ying, G.D. Stucky, Microemulsion templating of siliceous mesostructured cellular foams with well-defined ultralarge mesopores, *Chem. Mater.* 12 (2000) 686–696. <https://doi.org/10.1021/cm991097v>.
- [90] W. Chaikittisilp, H.J. Kim, C.W. Jones, Mesoporous alumina-supported amines as potential steam-stable adsorbents for capturing CO₂ from simulated flue gas and ambient air, *Energy and Fuels*. 25 (2011) 5528–5537. <https://doi.org/10.1021/ef201224v>.
- [91] J. Wang, H. Huang, M. Wang, L. Yao, W. Qiao, D. Long, L. Ling, Direct capture of low-concentration CO₂ on mesoporous carbon-supported solid amine adsorbents at ambient temperature, *Ind. Eng. Chem. Res.* 54 (2015) 5319–5327. <https://doi.org/10.1021/acs.iecr.5b01060>.
- [92] W. Lu, J.P. Sculley, D. Yuan, R. Krishna, H.-C. Zhou, Carbon dioxide capture from air using amine-grafted porous polymer networks, *J. Phys. Chem.* 117 (2013) 4057–4061. <https://doi.org/10.1021/jp311512q>.
- [93] H. Sehaqui, M.E. Gálvez, V. Becatinni, Y. cheng Ng, A. Steinfeld, T. Zimmermann, P. Tingaut, Fast and reversible direct CO₂ capture from air onto all-polymer nanofibrillated cellulose—polyethylenimine foams, *Environ. Sci. Technol.* 49 (2015) 3167–3174. <https://doi.org/10.1021/es504396v>.
- [94] H. Furukawa, K.E.E. Cordova, M. O’Keeffe, O.M.M. Yaghi, The chemistry and applications of metal-organic frameworks, *Science*. 341 (2013) 1230444.

<https://doi.org/10.1126/science.1230444>.

- [95] L.A. Darunte, A.D. Oetomo, K.S. Walton, D.S. Sholl, C.W. Jones, Direct air capture of CO₂ using amine functionalized MIL-101(Cr), *ACS Sustain. Chem. Eng.* 4 (2016) 5761–5768. <https://doi.org/10.1021/acssuschemeng.6b01692>.
- [96] T.M. McDonald, W.R. Lee, J. a. Mason, B.M. Wiers, C.S. Hong, J.R. Long, Capture of carbon dioxide from air and flue gas in the alkylamine-appended metal-organic framework mmen-Mg₂(dobpdc), *J. Am. Chem. Soc.* 134 (2012) 7056–7065. <https://doi.org/10.1021/ja300034j>.
- [97] N.Y. Huang, Z.W. Mo, L.J. Li, W.J. Xu, H.L. Zhou, D.D. Zhou, P.Q. Liao, J.P. Zhang, X.M. Chen, Direct synthesis of an aliphatic amine functionalized metal-organic framework for efficient CO₂ removal and CH₄ purification, *CrystEngComm.* 20 (2018) 5969–5975. <https://doi.org/10.1039/c8ce00574e>.
- [98] H. Zhang, A. Goepfert, G.K.S. Prakash, G. Olah, Applicability of linear polyethylenimine supported on nano-silica for the adsorption of CO₂ from various sources including dry air, *RSC Adv.* 5 (2015) 52550–52562. <https://doi.org/10.1039/C5RA05428A>.
- [99] S.H. Pang, R.P. Lively, C.W. Jones, Oxidatively-stable linear poly(propylenimine)-containing adsorbents for CO₂ capture from ultradilute streams, *ChemSusChem.* 11 (2018) 2628–2637. <https://doi.org/10.1002/cssc.201800438>.
- [100] S.A. Didas, S. Choi, W. Chaikittisilp, C.W. Jones, Amine-oxide hybrid materials for CO₂ capture from ambient air, *Acc. Chem. Res.* 48 (2015) 2680–2687. <https://doi.org/10.1021/acs.accounts.5b00284>.
- [101] J. Wang, M. Wang, W. Li, W. Qiao, D. Long, L. Ling, Application of polyethylenimine-impregnated solid adsorbents for direct capture of low-concentration CO₂, *AIChE J.* 61 (2015) 972–980. <https://doi.org/10.1002/aic.14679>.
- [102] H.T. Kwon, M.A. Sakwa-Novak, S.H. Pang, A.R. Sujan, E.W. Ping, C.W. Jones, Aminopolymer-impregnated hierarchical silica structures: unexpected equivalent CO₂ uptake under simulated air capture and flue gas capture conditions, *Chem. Mater.* 31 (2019) 5229–5237. <https://doi.org/10.1021/acs.chemmater.9b01474>.
- [103] S. Choi, M.L. Gray, C.W. Jones, Amine-tethered solid adsorbents coupling high adsorption capacity and regenerability for CO₂ capture from ambient air, *ChemSusChem.* 4 (2011) 628–635. <https://doi.org/10.1002/cssc.201000355>.
- [104] Z. Chen, S. Deng, H. Wei, B. Wang, J. Huang, G. Yu, Polyethylenimine-impregnated resin for high CO₂ adsorption: An efficient adsorbent for CO₂ capture

- from simulated flue gas and ambient air, *ACS Appl. Mater. Interfaces*. 5 (2013) 6937–6945. <https://doi.org/10.1021/am400661b>.
- [105] W. Chaikittisilp, R. Khunsupat, T.T. Chen, C.W. Jones, Poly(allylamine) - mesoporous silica composite materials for CO₂ capture from simulated flue gas or ambient air, *Ind. Eng. Chem. Res.* 50 (2011) 14203–14210.
- [106] R.P. Wijesiri, G.P. Knowles, H. Yeasmin, A.F.A. Hoadley, A.L. Chaffee, CO₂ capture from air using pelletized polyethylenimine impregnated MCF silica, *Ind. Eng. Chem. Res.* 58 (2019) 3293–3303. <https://doi.org/10.1021/acs.iecr.8b04973>.
- [107] M.A. Sakwa-Novak, S. Tan, C.W. Jones, Role of additives in composite PEI/oxide CO₂ adsorbents: enhancement in the amine efficiency of supported PEI by PEG in CO₂ capture from simulated ambient air, *ACS Appl. Mater. Interfaces*. 7 (2015) 24748–24759. <https://doi.org/10.1021/acsami.5b07545>.
- [108] X. Zhu, T. Ge, F. Yang, M. Lyu, C. Chen, D. O'Hare, R. Wang, Efficient CO₂ capture from ambient air with amine-functionalized Mg-Al mixed metal oxides, *J. Mater. Chem. A*. 8 (2020) 16421–16428. <https://doi.org/10.1039/d0ta05079b>.
- [109] D.W.F. Brilman, R. Veneman, Capturing atmospheric CO₂ using supported amine sorbents, *Energy Procedia*. 37 (2013) 6070–6078. <https://doi.org/10.1016/j.egypro.2013.06.536>.
- [110] A.R. Sujan, D.R. Kumar, M. Sakwa-Novak, E.W. Ping, B. Hu, S.J. Park, C.W. Jones, Poly(glycidyl amine)-loaded SBA-15 sorbents for CO₂ capture from dilute and ultradilute gas mixtures, *ACS Appl. Polym. Mater.* 1 (2019) 3137–3147. <https://doi.org/10.1021/acsapm.9b00788>.
- [111] D.R. Kumar, C. Rosu, A.R. Sujan, M.A. Sakwa-Novak, E.W. Ping, C.W. Jones, Alkyl-aryl amine-rich molecules for CO₂ removal via direct air capture, *ACS Sustain. Chem. Eng.* 8 (2020) 10971–10982. <https://doi.org/10.1021/acssuschemeng.0c03706>.
- [112] S.J. Park, J.J. Lee, C.B. Hoyt, D.R. Kumar, C.W. Jones, Silica supported poly(propylene guanidine) as a CO₂ sorbent in simulated flue gas and direct air capture, *Adsorption*. 26 (2020) 89–101. <https://doi.org/10.1007/s10450-019-00171-w>.
- [113] A. Goepfert, M. Czaun, R.B. May, G.K.S. Prakash, G.A. Olah, S.R. Narayanan, Carbon dioxide capture from the air using a polyamine based regenerable solid adsorbent, *J. Am. Chem. Soc.* 133 (2011) 20164–20167. <https://doi.org/10.1021/ja2100005>.
- [114] N. Rao, M. Wang, Z. Shang, Y. Hou, G. Fan, J. Li, CO₂ adsorption by amine-functionalized MCM-41: A comparison between impregnation and grafting

- modification methods, *Energy and Fuels*. 32 (2018) 670–677. <https://doi.org/10.1021/acs.energyfuels.7b02906>.
- [115] C. Gebald, J.A. Wurzbacher, P. Tingaut, T. Zimmermann, A. Steinfeld, Amine-based nanofibrillated cellulose as adsorbent for CO₂ capture from air, *Environ. Sci. Technol.* 45 (2011) 9101–9108. <https://doi.org/10.1021/es202223p>.
- [116] R.W. Flaig, T.M. Osborn Popp, A.M. Fracaroli, E.A. Kapustin, M.J. Kalmutzki, R.M. Altamimi, F. Fathieh, J.A. Reimer, O.M. Yaghi, The chemistry of CO₂ Capture in an amine-functionalized metal-organic framework under dry and humid conditions, *J. Am. Chem. Soc.* 139 (2017) 12125–12128. <https://doi.org/10.1021/jacs.7b06382>.
- [117] Y. Belmabkhout, R. Serna-guerrero, A. Sayari, Adsorption of CO₂-containing gas mixtures over amine-bearing pore-expanded MCM-41 silica: application for gas purification, *Ind. Eng. Chem. Res.* 49 (2010) 359–365. <https://doi.org/10.1021/ie900837t>.
- [118] J. Zhu, L. Wu, Z. Bu, S. Jie, B.G. Li, Polyethylenimine-grafted HKUST-type MOF/polyHIPE porous composites (PEI@PGD-H) as highly efficient CO₂ adsorbents, *Ind. Eng. Chem. Res.* 58 (2019) 4257–4266. <https://doi.org/10.1021/acs.iecr.9b00213>.
- [119] S. Choi, T. Watanabe, T.H. Bae, D.S. Sholl, C.W. Jones, Modification of the Mg/DOBDC MOF with amines to enhance CO₂ adsorption from ultradilute gases, *J. Phys. Chem. Lett.* 3 (2012) 1136–1141. <https://doi.org/10.1021/jz300328j>.
- [120] W.R. Lee, S.Y. Hwang, D.W. Ryu, K.S. Lim, S.S. Han, D. Moon, J. Choi, C.S. Hong, Diamine-functionalized metal-organic framework: exceptionally high CO₂ capacities from ambient air and flue gas, ultrafast CO₂ uptake rate, and adsorption mechanism, *Energy Environ. Sci.* 7 (2014) 744–751. <https://doi.org/10.1039/c3ee42328j>.
- [121] L.A. Darunte, Y. Terada, C.R. Murdock, K.S. Walton, D.S. Sholl, C.W. Jones, Monolith-supported amine-functionalized Mg₂(dobpdc) adsorbents for CO₂ capture, *ACS Appl. Mater. Interfaces.* 9 (2017) 17042–17050. <https://doi.org/10.1021/acsami.7b02035>.
- [122] S. Choi, J.H. Drese, P.M. Eisenberger, C.W. Jones, Application of amine-tethered solid sorbents for direct CO₂ capture from the ambient air, *Environ. Sci. Technol.* 45 (2011) 2420–2427. <https://doi.org/10.1021/es102797w>.
- [123] F.Q. Liu, L. Wang, Z.G. Huang, C.Q. Li, W.H. Li, R.X. Li, W.H. Li, Amine-tethered adsorbents based on three-dimensional macroporous silica for CO₂ capture from simulated flue gas and air, *ACS Appl. Mater. Interfaces.* 6 (2014) 4371–4381. <https://doi.org/10.1021/am500089g>.

- [124] G. Qi, L. Fu, E.P. Giannelis, Sponges with covalently tethered amines for high-efficiency carbon capture, *Nat. Commun.* 5 (2014) 1–7. <https://doi.org/10.1038/ncomms6796>.
- [125] M. Jahandar Lashaki, S. Khiavi, A. Sayari, Stability of amine-functionalized CO₂ adsorbents: A multifaceted puzzle, *Chem. Soc. Rev.* 48 (2019) 3320–3405. <https://doi.org/10.1039/c8cs00877a>.
- [126] H. Zerze, A. Tipirneni, A.J. McHugh, Reusable poly(allylamine)-based solid materials for carbon dioxide capture under continuous flow of ambient air, *Sep. Sci. Technol.* 52 (2017) 2513–2522. <https://doi.org/10.1080/01496395.2017.1345943>.
- [127] E.S. Sanz-Pérez, T.C.M. Dantas, A. Arencibia, G. Calleja, A.P.M.A. Guedes, A.S. Araujo, R. Sanz, Reuse and recycling of amine-functionalized silica materials for CO₂ adsorption, *Chem. Eng. J.* 308 (2017) 1021–1033. <https://doi.org/10.1016/j.cej.2016.09.109>.
- [128] W. Li, S. Choi, J.H. Drese, M. Hornbostel, G. Krishnan, P.M. Eisenberger, C.W. Jones, Steam-stripping for regeneration of supported amine-based CO₂ adsorbents, *ChemSusChem*. 3 (2010) 899–903. <https://doi.org/10.1002/cssc.201000131>.
- [129] R.P. Wijesiri, G.P. Knowles, H. Yeasmin, A.F.A. Hoadley, A.L. Chaffee, Desorption process for capturing CO₂ from air with supported amine sorbent, *Ind. Eng. Chem. Res.* 58 (2019) 15606–15618. <https://doi.org/10.1021/acs.iecr.9b03140>.
- [130] X. Zhu, T. Ge, F. Yang, R. Wang, Design of steam-assisted temperature vacuum-swing adsorption processes for efficient CO₂ capture from ambient air, *Renew. Sustain. Energy Rev.* 137 (2021) 110651. <https://doi.org/10.1016/j.rser.2020.110651>.
- [131] V. Stampi-Bombelli, M. van der Spek, M. Mazzotti, Analysis of direct capture of CO₂ from ambient air via steam-assisted temperature–vacuum swing adsorption, *Adsorption*. 26 (2020) 1183–1197. <https://doi.org/10.1007/s10450-020-00249-w>.
- [132] M.A. Sakwa-Novak, C.W. Jones, Steam induced structural changes of a poly(ethylenimine) impregnated γ -alumina sorbent for CO₂ extraction from ambient air, *ACS Appl. Mater. Interfaces*. 6 (2014) 9245–9255. <https://doi.org/10.1021/am501500q>.
- [133] M. Fayaz, A. Sayari, Long-term effect of steam exposure on CO₂ capture performance of amine-grafted silica, *ACS Appl. Mater. Interfaces*. 9 (2017) 43747–43754. <https://doi.org/10.1021/acsami.7b15463>.
- [134] A. Sayari, Y. Belmabkhout, Stabilization of amine-containing CO₂ adsorbents:

- Dramatic effect of water vapor, *J. Am. Chem. Soc.* 132 (2010) 6312–6314.
- [135] S.A. Didas, R. Zhu, N.A. Brunelli, D.S. Sholl, C.W. Jones, Thermal, oxidative and CO₂ induced degradation of primary amines used for CO₂ capture: Effect of alkyl linker on stability, *J. Phys. Chem. C* 118 (2014) 12302–12311. <https://doi.org/10.1021/jp5025137>.
- [136] A. Sayari, Y. Belmabkhout, E. Da'Na, CO₂ deactivation of supported amines: Does the nature of amine matter?, *Langmuir* 28 (2012) 4241–4247. <https://doi.org/10.1021/la204667v>.
- [137] A. Sayari, A. Heydari-Gorji, Y. Yang, CO₂-induced degradation of amine-containing adsorbents: Reaction products and pathways, *J. Am. Chem. Soc.* 134 (2012) 13834–13842. <https://doi.org/10.1021/ja304888a>.
- [138] A. Ahmadalinezhad, A. Sayari, Oxidative degradation of silica-supported polyethylenimine for CO₂ adsorption: insights into the nature of deactivated species., *Phys. Chem. Chem. Phys.* 16 (2014) 1529–1535. <https://doi.org/10.1039/c3cp53928h>.
- [139] S. Bali, T.T. Chen, W. Chaikittisilp, C.W. Jones, Oxidative stability of amino polymer-alumina hybrid adsorbents for carbon dioxide capture, *Energy and Fuels* 27 (2013) 1547–1554. <https://doi.org/10.1021/ef4001067>.
- [140] P. Bollini, S. Choi, J.H. Drese, C.W. Jones, Oxidative degradation of aminosilica adsorbents relevant to postcombustion CO₂ capture, *Energy and Fuels* 25 (2011) 2416–2425. <https://doi.org/10.1021/ef200140z>.
- [141] C. Rosu, S.H. Pang, A.R. Sujan, M.A. Sakwa-Novak, E.W. Ping, C.W. Jones, Effect of extended aging and oxidation on linear poly(propylenimine)-mesoporous silica composites for CO₂ capture from simulated air and flue gas streams, *ACS Appl. Mater. Interfaces* 12 (2020) 38085–38097. <https://doi.org/10.1021/acsami.0c09554>.
- [142] W.C. Wilfong, B.W. Kail, C.W. Jones, C. Pacheco, M.M.L. Gray, Spectroscopic investigation of the mechanisms responsible for the superior stability of hybrid class 1/class 2 CO₂ sorbents: A new class 4 category, *ACS Appl. Mater. Interfaces* 8 (2016) 12780–12791. <https://doi.org/10.1021/acsami.6b02062>.
- [143] M. Parvazinia, S. Garcia, M. Maroto-valer, CO₂ capture by ion exchange resins as amine functionalised adsorbents, *Chem. Eng. J.* 331 (2018) 335–342. <https://doi.org/10.1016/j.cej.2017.08.087>.
- [144] C. Gebald, J. A. Wurzbacher, P. Tingaut, A. Steinfeld, Stability of amine-functionalized cellulose during temperature-vacuum-swing cycling for CO₂ capture from air, *Environ. Sci. Technol.* 47 (2013) 10063–10070.

<https://doi.org/10.1021/es401731p>.

- [145] H. Azarabadi, K.S. Lackner, A sorbent-focused techno-economic analysis of direct air capture, *Appl. Energy*. 250 (2019) 959–975. <https://doi.org/10.1016/j.apenergy.2019.04.012>.
- [146] J.H. Choe, J.R. Park, Y.S. Chae, D.W. Kim, D.S. Choi, H. Kim, M. Kang, H. Seo, Y.-K. Park, C.S. Hong, Shaping and silane coating of a diamine-grafted metal-organic framework for improved CO₂ capture, *Commun. Mater.* 2 (2021) 1–8. <https://doi.org/10.1038/s43246-020-00109-8>.
- [147] E.J. Kim, R.L. Siegelman, H.Z.H. Jiang, A.C. Forse, J.H. Lee, J.D. Martell, P.J. Milner, J.M. Falkowski, J.B. Neaton, J.A. Reimer, S.C. Weston, J.R. Long, Cooperative carbon capture and steam regeneration with tetraamine-appended metal-organic frameworks, *Science*. 369 (2020) 392–396. <https://doi.org/10.1126/science.abb3976>.
- [148] G. Rim, T.G. Feric, T. Moore, A.A. Park, Solvent impregnated polymers loaded with liquid-like nanoparticle organic hybrid materials for enhanced kinetics of direct air capture and point source CO₂ capture, *Adv. Funct. Mater.* 2010047 (2021) 2010047. <https://doi.org/10.1002/adfm.202010047>.
- [149] X. Xu, M.B. Myers, F.G. Versteeg, B. Pejcic, C. Heath, C.D. Wood, Direct air capture (DAC) of CO₂ using polyethylenimine (PEI) “snow”: A scalable strategy, *Chem. Commun.* 56 (2020) 7151–7154. <https://doi.org/10.1039/d0cc02572k>.
- [150] K.A.S. Abhilash, T. Deepthi, R.A. Sadhana, K.G. Benny, Functionalized polysilsesquioxane-based hybrid silica solid amine sorbents for the regenerative removal of CO₂ from air, *ACS Appl. Mater. Interfaces*. 7 (2015) 17969–17976. <https://doi.org/10.1021/acsami.5b04674>.
- [151] H. He, W. Li, M. Zhong, D. Konkolewicz, D. Wu, K. Yaccato, T. Rappold, G. Sugar, N.E. David, K. Matyjaszewski, Reversible CO₂ capture with porous polymers using the humidity swing, *Energy Environ. Sci.* 6 (2013) 488–493. <https://doi.org/10.1039/c2ee24139k>.
- [152] H. He, W. Li, M. Lamson, M. Zhong, D. Konkolewicz, C.M. Hui, K. Yaccato, T. Rappold, G. Sugar, N.E. David, K. Damodaran, S. Natesakhawat, H. Nulwala, K. Matyjaszewski, Porous polymers prepared via high internal phase emulsion polymerization for reversible CO₂ capture, *Polym. (United Kingdom)*. 55 (2014) 385–394. <https://doi.org/10.1016/j.polymer.2013.08.002>.
- [153] X. Shi, Q. Li, T. Wang, K.S. Lackner, Kinetic analysis of an anion exchange absorbent for CO₂ capture from ambient air, *PLoS One*. 12 (2017) 1–12. <https://doi.org/10.1371/journal.pone.0179828>.

- [154] M. Armstrong, X. Shi, B. Shan, K. Lackner, B. Mu, Rapid CO₂ capture from ambient air by sorbent-containing porous electrospun fibers made with the solvothermal polymer additive removal technique, *AIChE J.* 65 (2019) 214–220. <https://doi.org/10.1002/aic.16418>.
- [155] C. Hou, Y. Wu, T. Wang, X. Wang, X. Gao, Preparation of quaternized bamboo cellulose and its implication in direct air capture of CO₂, *Energy and Fuels.* 33 (2019) 1745–1752. <https://doi.org/10.1021/acs.energyfuels.8b02821>.
- [156] J. Song, J. Liu, W. Zhao, Y. Chen, H. Xiao, X. Shi, Y. Liu, X. Chen, Quaternized chitosan/PVA aerogels for reversible CO₂ capture from ambient air, *Ind. Eng. Chem. Res.* 57 (2018) 4941–4948. <https://doi.org/10.1021/acs.iecr.8b00064>.
- [157] X. Shi, H. Xiao, K.S. Lackner, X. Chen, Capture CO₂ from ambient air using nanoconfined ion hydration, *Angew. Chemie.* 128 (2016) 4094–4097. <https://doi.org/10.1002/ange.201507846>.
- [158] J. Song, L. Zhu, X. Shi, Y. Liu, H. Xiao, X. Chen, Moisture swing ion-exchange resin-PO₄ sorbent for reversible CO₂ capture from ambient air, *Energy and Fuels.* 33 (2019) 6562–6567. <https://doi.org/10.1021/acs.energyfuels.9b00863>.
- [159] S. Bali, M.A. Sakwa-Novak, C.W. Jones, Potassium incorporated alumina based CO₂ capture sorbents: Comparison with supported amine sorbents under ultra-dilute capture conditions, *Colloids Surfaces A Physicochem. Eng. Asp.* 486 (2015) 78–85. <https://doi.org/10.1016/j.colsurfa.2015.09.020>.
- [160] R. Rodríguez-Mosqueda, E.A. Bramer, G. Brem, CO₂ capture from ambient air using hydrated Na₂CO₃ supported on activated carbon honeycombs with application to CO₂ enrichment in greenhouses, *Chem. Eng. Sci.* 189 (2018) 114–122. <https://doi.org/10.1016/j.ces.2018.05.043>.
- [161] R. Rodríguez-Mosqueda, E.A. Bramer, T. Roestenberg, G. Brem, Parametrical study on CO₂ capture from ambient air using hydrated K₂CO₃ supported on an activated carbon honeycomb, *Ind. Eng. Chem. Res.* (2018) acs.iecr.8b00566. <https://doi.org/10.1021/acs.iecr.8b00566>.
- [162] R. Rodríguez-Mosqueda, J. Rutgers, E.A. Bramer, G. Brem, Low temperature water vapor pressure swing for the regeneration of adsorbents for CO₂ enrichment in greenhouses via direct air capture, *J. CO₂ Util.* 29 (2019) 65–73. <https://doi.org/10.1016/j.jcou.2018.11.010>.
- [163] A.R. Cuesta, C. Song, pH swing adsorption process for ambient carbon dioxide capture using activated carbon black adsorbents and immobilized carbonic anhydrase biocatalysts, *Appl. Energy.* 280 (2020) 116003. <https://doi.org/10.1016/j.apenergy.2020.116003>.

- [164] A.E. Creamer, B. Gao, Carbon-based adsorbents for postcombustion CO₂ capture: A critical review, *Environ. Sci. Technol.* 50 (2016) 7276–7289. <https://doi.org/10.1021/acs.est.6b00627>.
- [165] K. Sumida, D.L. Rogow, J. a. Mason, T.M. McDonald, E.D. Bloch, Z.R. Herm, T.H. Bae, J.R. Long, Carbon dioxide capture in metal-organic frameworks, *Chem. Rev.* 112 (2012) 724–781. <https://doi.org/10.1021/cr2003272>.
- [166] D.G. Madden, H.S. Scott, A. Kumar, K.J. Chen, R. Sanii, A. Bajpai, M. Lusi, T. Curtin, J.J. Perry, M.J. Zaworotko, Flue-gas and direct-air capture of CO₂ by porous metal-organic materials, *Philos. Trans. R. Soc. A.* 375 (2017). <https://doi.org/10.1098/rsta.2016.0025>.
- [167] N.R. Stuckert, R.T. Yang, CO₂ Capture from the atmosphere and simultaneous concentration using zeolites and amine grafted SBA-15, *Environ. Sci. Technol.* 45 (2011) 10257–10264. <https://doi.org/dx.doi.org/10.1021/es202647a>.
- [168] O. Shekhah, Y. Belmabkhout, Z. Chen, V. Guillerm, A. Cairns, K. Adil, M. Eddaoudi, Made-to-order metal-organic frameworks for trace carbon dioxide removal and air capture, *Nat. Commun.* 5 (2014) 4228–4234. <https://doi.org/10.1038/ncomms5228>.
- [169] S. Mukherjee, N. Sikdar, D. O’Nolan, D.M. Franz, V. Gascón, A. Kumar, N. Kumar, H.S. Scott, D.G. Madden, P.E. Kruger, B. Space, M.J. Zaworotko, Trace CO₂ capture by an ultramicroporous physisorbent with low water affinity, *Sci. Adv.* 5 (2019) 1–8. <https://doi.org/10.1126/sciadv.aax9171>.
- [170] P.M. Bhatt, Y. Belmabkhout, A. Cadiou, K. Adil, O. Shekhah, A. Shkurenko, L.J. Barbour, M. Eddaoudi, A fine-tuned fluorinated MOF addresses the needs for trace CO₂ removal and air capture using physisorption, *J. Am. Chem. Soc.* 138 (2016) 9301–9307. <https://doi.org/10.1021/jacs.6b05345>.
- [171] C.E. Bien, K.K. Chen, S.C. Chien, B.R. Reiner, L.C. Lin, C.R. Wade, W.S.W. Ho, Bioinspired metal-organic framework for trace CO₂ capture, *J. Am. Chem. Soc.* 140 (2018) 12662–12666. <https://doi.org/10.1021/jacs.8b06109>.
- [172] M. Guo, H. Wu, L. Lv, H. Meng, J. Yun, J. Jin, J. Mi, A highly efficient and stable composite of polyacrylate and metal – organic framework prepared by interface engineering for direct air capture, *ACS Appl. Mater. Interfaces.* 13 (2021) 21775–21785. <https://doi.org/10.1021/acsami.1c03661>.
- [173] X. Deng, W. Yang, S. Li, H. Liang, Z. Shi, Z. Qiao, Large-scale screening and machine learning to predict the computation-ready, experimental metal-organic frameworks for CO₂ capture from air, *Appl. Sci.* 10 (2020). <https://doi.org/10.3390/app10020569>.

- [174] P. Xiao, J. Zhang, P. Webley, G. Li, R. Singh, R. Todd, Capture of CO₂ from flue gas streams with zeolite 13X by vacuum-pressure swing adsorption, *Adsorption*. 14 (2008) 575–582. <https://doi.org/10.1007/s10450-008-9128-7>.
- [175] M.T. Ho, G.W. Allinson, D.E. Wiley, Reducing the cost of CO₂ capture from flue gases using pressure swing adsorption, *Ind. Eng. Chem. Res.* 47 (2008) 4883–4890. <https://doi.org/10.1021/ie070831e>.
- [176] R. Haghpanah, A. Majumder, R. Nilam, A. Rajendran, S. Farooq, I.A. Karimi, M. Amanullah, Multiobjective optimization of a four-step adsorption process for postcombustion CO₂ capture via finite volume simulation, *Ind. Eng. Chem. Res.* 52 (2013) 4249–4265. <https://doi.org/10.1021/ie302658y>.
- [177] Q. Yu, J.D.P. Delgado, R. Veneman, D.W.F. Brilman, Stability of a benzyl amine based CO₂ capture adsorbent in view of regeneration strategies, *Ind. Eng. Chem. Res.* 56 (2017) 3259–3269. <https://doi.org/10.1021/acs.iecr.6b04645>.
- [178] W. Brilman, L. Garcia Alba, R. Veneman, Capturing atmospheric CO₂ using supported amine sorbents for microalgae cultivation, *Biomass and Bioenergy*. 53 (2013) 39–47. <https://doi.org/10.1016/j.biombioe.2013.02.042>.
- [179] J.A. Wurzbacher, C. Gebald, S. Brunner, A. Steinfeld, Heat and mass transfer of temperature-vacuum swing desorption for CO₂ capture from air, *Chem. Eng. J.* 283 (2016) 1329–1338. <https://doi.org/10.1016/j.cej.2015.08.035>.
- [180] A.R. Kulkarni, D.S. Sholl, Analysis of equilibrium-based TSA processes for direct capture of CO₂ from air, *Ind. Eng. Chem. Res.* 51 (2012) 8631–8645. <https://doi.org/10.1021/ie300691c>.
- [181] A. Sinha, M.J. Realff, A parametric study of the techno-economics of direct CO₂ air capture systems using solid adsorbents, *AIChE J.* 65 (2019) 1–8. <https://doi.org/10.1002/aic.16607>.
- [182] A. Sinha, L.A. Darunte, C.W. Jones, M.J. Realff, Y. Kawajiri, Correction to “Systems design and economic analysis of direct air capture of CO₂ through temperature vacuum swing adsorption using MIL-101(Cr)-PEI-800 and mmen-Mg₂(dobpdc) MOF adsorbents,” *Ind. Eng. Chem. Res.* (2019). <https://doi.org/10.1021/acs.iecr.6b03887>.
- [183] C. Drechsler, D.W. Agar, Intensified integrated direct air capture - power-to-gas process based on H₂O and CO₂ from ambient air, *Appl. Energy*. 273 (2020) 115076. <https://doi.org/10.1016/j.apenergy.2020.115076>.
- [184] C. Drechsler, D.W. Agar, Investigation of water co-adsorption on the energy balance of solid sorbent based direct air capture processes, *Energy*. 192 (2020) 116587. <https://doi.org/10.1016/j.energy.2019.116587>.

- [185] M.A. Sakwa-Novak, C.J. Yoo, S. Tan, F. Rashidi, C.W. Jones, Poly(ethylenimine)-functionalized monolithic alumina honeycomb adsorbents for CO₂ capture from air, *ChemSusChem*. 9 (2016) 1859–1868. <https://doi.org/10.1002/cssc.201600404>.
- [186] P. Bollini, N.A. Brunelli, S.A. Didas, C.W. Jones, Dynamics of CO₂ adsorption on amine adsorbents. 2. Insights into adsorbent design, *Ind. Eng. Chem. Res.* 51 (2012) 15153–15162. <https://doi.org/10.1021/ie3017913>.
- [187] L.A. Darunte, T. Sen, C. Bhawanani, K.S. Walton, D.S. Sholl, M.J. Realff, C.W. Jones, Moving beyond adsorption capacity in design of adsorbents for CO₂ capture from ultradilute feeds: Kinetics of CO₂ adsorption in materials with stepped isotherms, *Ind. Eng. Chem. Res.* 58 (2019) 366–377. <https://doi.org/10.1021/acs.iecr.8b05042>.
- [188] R. Serna-Guerrero, A. Sayari, Modeling adsorption of CO₂ on amine-functionalized mesoporous silica. 2: Kinetics and breakthrough curves, *Chem. Eng. J.* 161 (2010) 182–190. <https://doi.org/10.1016/j.cej.2010.04.042>.
- [189] M.M. Sadiq, M.P. Batten, X. Mulet, C. Freeman, K. Konstas, J.I. Mardel, J. Tanner, D. Ng, X. Wang, S. Howard, M.R. Hill, A.W. Thornton, A pilot-scale demonstration of mobile direct air capture using metal-organic frameworks, *Adv. Sustain. Syst.* 4 (2020) 1–8. <https://doi.org/10.1002/adsu.202000101>.
- [190] J. Wilcox, P.C. Psarras, S. Liguori, Assessment of reasonable opportunities for direct air capture, *Environ. Res. Lett.* 12 (2017) 065001. <https://doi.org/https://doi.org/10.1088/1748-9326/aa6de5>.
- [191] Q. Yu, D.W.F. Brilman, Design strategy for CO₂ adsorption from ambient air using a supported amine based sorbent in a fixed bed reactor, *Energy Procedia*. 114 (2017) 6102–6114. <https://doi.org/10.1016/j.egypro.2017.03.1747>.
- [192] Q. Yu, W. Brilman, A radial flow contactor for ambient air CO₂ capture, *Appl. Sci.* 10 (2020). <https://doi.org/10.3390/app10031080>.
- [193] W. Zhang, H. Liu, C. Sun, T.C. Drage, C.E. Snape, Capturing CO₂ from ambient air using a polyethyleneimine-silica adsorbent in fluidized beds, *Chem. Eng. Sci.* 116 (2014) 306–316. <https://doi.org/10.1016/j.ces.2014.05.018>.
- [194] C. Drechsler, D.W. Agar, Simulation and optimization of a novel moving belt adsorber concept for the direct air capture of carbon dioxide, *Comput. Chem. Eng.* 126 (2019) 520–534. <https://doi.org/10.1016/j.compchemeng.2019.04.023>.
- [195] S.M.W. Wilson, F.H. Tezel, Direct dry air capture of CO₂ using VTSA with faujasite zeolites, *Ind. Eng. Chem. Res.* 59 (2020) 8783–8794. <https://doi.org/10.1021/acs.iecr.9b04803>.

- [196] G. Santori, C. Charalambous, M.C. Ferrari, S. Brandani, Adsorption artificial tree for atmospheric carbon dioxide capture, purification and compression, *Energy*. 162 (2018) 1158–1168. <https://doi.org/10.1016/j.energy.2018.08.090>.
- [197] W. Jung, K.S. Lee, Isotherm and kinetics modeling of simultaneous CO₂ and H₂O adsorption on an amine-functionalized solid sorbent, *J. Nat. Gas Sci. Eng.* 84 (2020) 103489. <https://doi.org/10.1016/j.jngse.2020.103489>.
- [198] J. Elfving, C. Bajamundi, J. Kauppinen, Characterization and performance of direct air capture sorbent, *Energy Procedia*. 114 (2017) 6087–6101. <https://doi.org/10.1016/j.egypro.2017.03.1746>.
- [199] J. Elfving, C. Bajamundi, J. Kauppinen, T. Sainio, Modelling of equilibrium working capacity of PSA, TSA and TVSA processes for CO₂ adsorption under direct air capture conditions, *J. CO₂ Util.* 22 (2017) 270–277. <https://doi.org/10.1016/j.jcou.2017.10.010>.
- [200] J. Elfving, J. Kauppinen, M. Jegoroff, V. Ruuskanen, L. Järvinen, T. Sainio, Experimental comparison of regeneration methods for CO₂ concentration from air using amine-based adsorbent, *Chem. Eng. J.* 404 (2021) 126337. <https://doi.org/10.1016/j.cej.2020.126337>.
- [201] J. Elfving, T. Sainio, Kinetic approach to modelling CO₂ adsorption from humid air using amine-functionalized resin: Equilibrium isotherms and column dynamics, *Chem. Eng. Sci.* 246 (2021) 116885. <https://doi.org/10.1016/j.ces.2021.116885>.
- [202] Vaisala Oyj, How to measure carbon dioxide, 2019. <https://www.vaisala.com/sites/default/files/documents/VIM-G-How-to-measure-CO2-Application-Note-B211228EN.pdf>.
- [203] Vaisala Oyj, User's guide - Vaisala CARBOCAP® carbon dioxide probe GMP343, (2013). <https://www.vaisala.com/sites/default/files/documents/GMP343 User%27s Guide in English M210514EN.pdf>.
- [204] Bronkhorst, Bronkhorst instruction manual: Mass Flow/pressure meters and controllers for gases and liquids, 2020. <https://www.bronkhorst.com/getmedia/50bed9ce-0445-4eba-9d37-f113ec53cb34/917022-Manual-general-instructions-digital-laboratory-style-and-IN-FLOW.pdf>.
- [205] P. Bollini, N.A. Brunelli, S.A. Didas, C.W. Jones, Dynamics of CO₂ adsorption on amine adsorbents. 1. Impact of heat effects, *Ind. Eng. Chem. Res.* 51 (2012) 15145–15152. <https://doi.org/10.1021/ie301790a>.
- [206] M. Sultan, I.I. El-Sharkawy, T. Miyazaki, B.B. Saha, S. Koyama, T. Maruyama,

- S. Maeda, T. Nakamura, Insights of water vapor sorption onto polymer based sorbents, *Adsorption*. 21 (2015) 205–215. <https://doi.org/10.1007/s10450-015-9663-y>.
- [207] E.J. Quirijns, A.J.B. Van Boxtel, W.K.P. Van Loon, G. Van Straten, Sorption isotherms, GAB parameters and isosteric heat of sorption, *J. Sci. Food Agric.* 85 (2005) 1805–1814. <https://doi.org/10.1002/jsfa.2140>.
- [208] M.S. Shafeeyan, W.M.A.W. Daud, A. Shamiri, A review of mathematical modeling of fixed-bed columns for carbon dioxide adsorption, *Chem. Eng. Res. Des.* 92 (2014) 961–988. <https://doi.org/10.1016/j.cherd.2013.08.018>.
- [209] E. Sonnleitner, G. Schöny, H. Hofbauer, Assessment of zeolite 13X and Lewatit® VP OC 1065 for application in a continuous temperature swing adsorption process for biogas upgrading, *Biomass Convers. Biorefinery*. 8 (2018) 379–395. <https://doi.org/10.1007/s13399-017-0293-3>.
- [210] S.O. Rastegar, T. Gu, Empirical correlations for axial dispersion coefficient and Peclet number in fixed-bed columns, *J. Chromatogr. A*. 1490 (2017) 133–137. <https://doi.org/10.1016/j.chroma.2017.02.026>.
- [211] S. Sircar, J.R. Hufton, Why does the linear driving force model for adsorption kinetics work?, *Adsorption*. 6 (2000) 137–147. <https://doi.org/10.1023/A:1008965317983>.
- [212] W.R. Alesi, J.R. Kitchin, Evaluation of a primary amine-functionalized ion-exchange resin for CO₂ capture, *Ind. Eng. Chem. Res.* 51 (2012) 6907–6915. <https://doi.org/10.1021/ie300452c>.
- [213] Z. Bacsik, N. Ahlsten, A. Ziadi, G. Zhao, A.E. Garcia-bennett, B. Martin-Matute, N. Hedin, Mechanisms and kinetics for sorption of CO₂ on bicontinuous mesoporous silica modified with n-propylamine, *Langmuir*. 27 (2011) 11118–11128.
- [214] A. Danon, P.C. Stair, E. Weitz, FTIR study of CO₂ adsorption on amine-grafted SBA-15: Elucidation of adsorbed species, *J. Phys. Chem.* 115 (2011) 11540–11549.
- [215] G.S. Foo, J.J. Lee, C.H. Chen, S.E. Hayes, C. Sievers, C.W. Jones, Elucidation of surface species through in situ FTIR spectroscopy of carbon dioxide adsorption on amine-grafted SBA-15, *ChemSusChem*. 10 (2017) 266–276. <https://doi.org/10.1002/cssc.201600809>.
- [216] Z. Bacsik, N. Hedin, Effects of carbon dioxide captured from ambient air on the infrared spectra of supported amines, *Vib. Spectrosc.* 87 (2016) 215–221. <https://doi.org/10.1016/j.vibspec.2016.10.006>.

- [217] T. Wang, X. Wang, C. Hou, J. Liu, Quaternary functionalized mesoporous adsorbents for ultra-high kinetics of CO₂ capture from air, *Sci. Rep.* 10 (2020) 21429. <https://doi.org/10.1038/s41598-020-77477-1>.
- [218] R. Serna-Guerrero, Y. Belmabkhout, A. Sayari, Influence of regeneration conditions on the cyclic performance of amine-grafted mesoporous silica for CO₂ capture: An experimental and statistical study, *Chem. Eng. Sci.* 65 (2010) 4166–4172. <https://doi.org/10.1016/j.ces.2010.04.029>.
- [219] M.J. Bos, V. Kroeze, S. Sutanto, D.W.F. Brilman, Evaluating regeneration options of solid amine sorbent for CO₂, *Ind. Eng. Chem. Res.* 57 (2018) 11141–11153. <https://doi.org/10.1021/acs.iecr.8b00768>.
- [220] M.J. Bos, T. Kreuger, S.R.A. Kersten, D.W.F. Brilman, Study on transport phenomena and intrinsic kinetics for CO₂ adsorption in solid amine sorbent, *Chem. Eng. J.* 377 (2019) 120374. <https://doi.org/10.1016/j.cej.2018.11.072>.
- [221] Y. Kuwahara, D.Y. Kang, J.R. Copeland, N. a. Brunelli, S. a. Didas, P. Bollini, C. Sievers, T. Kamegawa, H. Yamashita, C.W. Jones, Dramatic enhancement of CO₂ uptake by poly(ethyleneimine) using zirconosilicate supports, *J. Am. Chem. Soc.* 134 (2012) 10757–10760. <https://doi.org/10.1021/ja303136e>.
- [222] A. Goepfert, H. Zhang, R. Sen, H. Dang, G.K.S. Prakash, Oxidation-resistant, cost-effective epoxide-modified polyamine adsorbents for CO₂ capture from various sources including air, *ChemSusChem.* 12 (2019) 1712–1723. <https://doi.org/10.1002/cssc.201802978>.
- [223] A.R. Sujan, S.H. Pang, G. Zhu, C.W. Jones, R.P. Lively, Direct CO₂ capture from air using poly(ethylenimine)-loaded polymer/silica fiber sorbents, *ACS Sustain. Chem. Eng.* 7 (2019) 5264–5273. <https://doi.org/10.1021/acssuschemeng.8b06203>.
- [224] J.T. Anyanwu, Y. Wang, R.T. Yang, Amine-grafted silica gels for CO₂ capture including direct air capture, *Ind. Eng. Chem. Res.* 59 (2020) 7072–7079. <https://doi.org/10.1021/acs.iecr.9b05228>.
- [225] E.S. Sanz-Pérez, A. Fernández, A. Arencibia, G. Calleja, R. Sanz, Hybrid amine-silica materials: Determination of N content by ²⁹Si NMR and application to direct CO₂ capture from air, *Chem. Eng. J.* 373 (2019) 1286–1294. <https://doi.org/10.1016/j.cej.2019.05.117>.

Appendix A: Literature adsorbent data

Table A1: Experimentally measured CO₂ adsorption capacities of amine-impregnated adsorbents relevant to DAC conditions with near 400 ppm CO₂. B-PEI and L-PEI stand for branched and linear polyethylenimine, respectively. PAA, TEPA and L-PPI stand for polyallylamine, tetraethylenepentamine and linear polypropylenimine, respectively.

Amine/support/additive	Amine loading (mmol _N /g _{sorbent})	T (°C)	Relative humidity	Adsorption capacity (mmolCO ₂ /g _{sorbent})	Reference
PEI/commercial silica	10.5	25	-	2.36	[103]
B-PEI/mesocellular foam (MCF)	10.71	25	-	1.74	[105]
L-PEI/MCF	11.37	25	-	1.05	[105]
PAA/MCF	7.24	25	-	0.86	[105]
B-PEI/SBA-15	9.23	25	-	1.05	[90]
B-PEI/mesoporous alumina	8.66	25	-	1.33	[90]
B-PEI/ mesoporous alumina	11.2	25	-	1.74	[90]
B-PEI/fumed silica	33 w-%	25	-	1.18	[113]
B-PEI/fumed silica	33 w-%	25	67%	1.77	[113]
B-PEI/fumed silica	50 w-%	25	-	1.70	[113]
B-PEI/fumed silica	50 w-%	25	67%	1.41	[113]
B-PEI/zirconosilicate	30 w-%	25	-	0.85	[221]
PEI/commercial resin	50 w-%	25	-	2.26	[104]
TEPA/commercial silica	10	35	-	2.50	[109]
B-PEI ¹ /fumed silica	50 w-%	25	-	2.44	[41]
B-PEI ² /fumed silica	50 w-%	25	-	1.67	[41]
B-PEI/ mesoporous alumina	7.81	30	50%	1.71	[132]
PEI/commercial resin	50 w-%	25	-	1.96	[101]
PEI/commercial resin	50 w-%	25	10%	3.16	[101]
B-PEI/mesoporous carbon	55 w-%	25	-	1.5	[91]
B-PEI/mesoporous carbon/Span 80	55 w-%	25	-	2.25	[91]
B-PEI/mesoporous carbon/Span 80	55 w-%	25	80%	2.58	[91]
PEI/SBA-15	6.36	30	-	0.63	[107]
PEI/SBA-15/polyethylene glycol	5.75	30	-	0.79	[107]
B-PEI/NFC	44 w-%	25	20%	0.5	[93]
B-PEI/NFC	44 w-%	25	80%	2.2	[93]

Table A.1 continued.

Amine/support/additive	Amine loading (mmol _N /g _{sorbent})	T (°C)	Relative humidity	Adsorption capacity (mmol _{CO2} /g _{sorbent})	Reference
PEI/MCM-41	55 w-%	25	-	<1	[87]
PEI/MCM-41/ cetyltrimethylammonium cations	55 w-%	25	-	2.2	[87]
PEI/MCM-41/ cetyltrimethylammonium cations	55 w-%	25	64%	2.2	[87]
PAA/fumed silica ³	50 w-%	21	60-70%	0.72	[126]
L-PPI/SBA-15	8	35	-	1.25	[99]
PEI/hierarchical silica	262 w-%	30	-	2.4	[102]
PEI/hierarchical silica	262 w-%	30	19%	3.36	[102]
B-PEI/MCF pellets	63-66 w-%	46	-	1.8	[106]
B-PEI/MCF pellets	63-66 w-%	46	20%	2.5	[106]
Polyglycidylamine/SBA-15	10.2	35	-	0.6 mmol _{CO2} /g _{SiO2}	[110]
TEPA/commercial silica/epoxide	50 w-%	25	-	1.4	[222]
Pentaethylenehexamine/ commercial silica/epoxide	50 w-%	25	-	1.2	[222]
B-PEI/polymer fibers with silica	41 w-%	35	-	0.6	[223]
B-PEI/polymer fibers with silica	41 w-%	35	46%	1.6	[223]
Alkyl-aryl amines/SBA-15	6.68 (60 w-%)	35	-	0.64 ⁴	[111]
Alkyl-aryl amines/SBA-15	6.68 (60 w-%)	35	30%	1.16	[111]
L-PPI/SBA-15	55 w-%	35	-	0.83	[141]
B-PEI/Mg-Al oxide	67 w-%	25	-	2.27	[108]
PEI/SBA-15	37 w-%	30	-	1.23	[112]
Polypropylene guanidine/SBA-15	50 w-%	30	-	1.12	[112]

¹Molecular weight 800 g/mol. ²Molecular weight 25 000 g/mol. ³450-470 ppm CO₂. ⁴Fixed-bed result.

Table A.2: Experimentally measured CO₂ adsorption capacities of covalently grafted amine-adsorbents relevant to DAC conditions with near 400 ppm CO₂.

Amine/support (additive)	Amine loading (mmol _N /g _{sorbent})	T (°C)	Relative humidity	Adsorption capacity (mmol _{CO2} /g _{sorbent})	Reference
Tri-aminosilane/MCM-41	7.9	25	-	0.98 ¹	[117]
Di-aminosilane/silica gel	2.48	25	-	0.40	[86]
Di-aminosilane/silica gel	2.48	25	40	0.44	[86]
Di-aminosilane/nanofibrillated cellulose (NFC)	4.9	25	40	1.39 ²	[115]
Diamine/MOF Mg ₂ (dobdc)	5.5 w-%	25	-	1.50	[119]
Diamine/MOF Mg ₂ (dobpdc)	3.4 ³	25	-	2.0	[96]
Diamine/MOF Mg ₂ (dobpdc)	3.2 ³	25	-	2.83	[120]
Diamine/MOF Mg ₂ (dobdc)	6.0 ³	25	-	3.89	[45]
Triamine/porous polymer network	8.5	22	-	1.04 ⁴	[92]
Tris(2-aminoethyl)amine (TREN)/MOF MIL-101(Cr)	2.63 mmol _{TREN} /g _{MOF}	25	-	0.35	[95]
TREN ⁵ /MOF MIL-101(Cr)	5.67 mmol _{TREN} /g _{MOF}	25	-	2.8	[95]
PEI ⁶ /MOF MIL-101(Cr)	1.76 mmol _{PEI} /g _{MOF}	25	-	1.35	[95]
Tri-aminosilane/silica gel	5.12	25	-	0.77	[224]
Tri-aminosilane/silica gel	5.12	25	60%	1.10	[224]
Tri-aminosilane/SBA-15	5.7	45	-	0.64	[225]
PEI/polymer+HKUST composite	70 w-%	25	-	1.78	[118]
PEI ⁷ /SBA-15	9.9	25	-	1.72	[122]
L-alanine polymer ⁷ /macroporous silica	10.98	50	-	2.65	[123]

¹Gravimetric result. ²CO₂ concentration 506 ppm. ³Nitrogen that is not bound to open metal sites. ⁴Based on isotherm modelling, not experimental value. ⁵Impregnated in addition to grafted TREN. ⁶PEI partly grafted. ⁷In-situ polymerized.

Publication I

J. Elfving, C. Bajamundi and J. Kauppinen
Characterization and performance of direct air capture sorbent

Reprinted with permission from
Energy Procedia
Vol. 114, pp. 6087-6101, 2017
© 2017, The Authors. Published by Elsevier Ltd.



Available online at www.sciencedirect.com

ScienceDirect

Energy Procedia 114 (2017) 6087 – 6101

Energy

Procedia

13th International Conference on Greenhouse Gas Control Technologies, GHGT-13, 14-18
November 2016, Lausanne, Switzerland

Characterization and performance of direct air capture sorbent

Jere Elfving^{a*}, Cyril Bajamundi^a, Juho Kauppinen^a

^aVTT Technical Research Centre of Finland Ltd., Koivurannantie 1, FI-40101 Jyväskylä, Finland

Abstract

In this paper, a proprietary CO₂ sorbent is characterized and its sorption capacity determined. FTIR-ATR spectroscopy suggests that the sorbent is composed of polystyrene functionalized with primary amine. The Toth isotherm is found to best fit to laboratory-scale CO₂ sorption data in partial pressure range of 0.1-5 mbar. Chemisorption dominates at and below atmospheric CO₂ partial pressure, especially in humid conditions. Humidity promotes total CO₂ capacity by 20-34%. Temperature-dependent Toth model is used to estimate working capacity in different regeneration conditions. Temperature swing adsorption or temperature-vacuum swing adsorption can be utilized in direct air capture conditions, depending on the application.

© 2017 The Authors. Published by Elsevier Ltd. This is an open access article under the CC BY-NC-ND license (<http://creativecommons.org/licenses/by-nc-nd/4.0/>).

Peer-review under responsibility of the organizing committee of GHGT-13.

Keywords: CO₂; direct air capture; adsorbent; Toth isotherm; working capacity

1. Introduction

Direct air capture (DAC) is a branch of technologies developed to capture CO₂ from atmospheric air. Compared to capturing CO₂ from flue gases, DAC is thermodynamically unfavorable ^[1]. To develop feasible DAC processes, energy requirement needs to be minimized and CO₂ capture performance maximized. The most important part of the process is the active material that captures CO₂. Therefore, studying the chemical and physical properties of the active material is of utmost importance.

* Corresponding author. Tel.: +358405710905.
E-mail address: jere.elfving@vtt.fi

Amine-based CO₂ capture in solid sorbents is most often proposed for DAC. The type of amine contributes significantly to the adsorption capacity of the material, and primary amines have been found to perform most effectively in DAC conditions^[2,3]. The type of matrix affects the suitability of the sorbent for different adsorption and desorption conditions. Materials such as silica^[2,4-7], nanocellulose^[8], metal-organic frameworks (MOF)^[9,10] and resins^[11] have been proposed as matrices for amines. Some materials, such as MOFs^[12] perform well in dry conditions but degrade in humid conditions.

On the other hand, humidity can also improve CO₂ adsorption capacity for amine-functionalized sorbents. The mechanism of CO₂ capture in primary or secondary amines is based on the formation of carbamate, requiring two moles of amines for one mole of captured CO₂. In humid conditions, only one mole of amine is required for one mole of CO₂, resulting in higher CO₂ adsorption capacity.^[13] Also, it has been proposed that in humid conditions bicarbonate is formed along with carbamate^[13,14]. Gaining knowledge of the species of adsorption is thus important for better understanding of the capture mechanism.

As the main mechanism in amine-functionalized sorbents is based on chemisorption of CO₂, physisorption of CO₂ is rarely studied. Small amount of CO₂ is physisorbed on materials with high surface areas even in DAC conditions^[15]. Solid polymers such as polystyrene also physically absorb gaseous CO₂^[16]. Often only the adsorption or total desorption capacity is reported, and thus, any capacity by weakly bound CO₂ is reported in the total capacity. It must be taken into account, that physisorbed or physically absorbed CO₂ is desorbed at much milder conditions than chemisorbed CO₂^[15,17]. In a process in which CO₂ purity is striven for, impurities have to be removed prior to desorption step (see Wurzbacher et al.^[18]). If the vacuum pressure is lower than the feed CO₂ partial pressure in this initial step, the weakly bound CO₂ desorbs, and thus the total desorbed amount cannot be utilized. Thus, estimating the contributions of each mechanism can impart about the suitability of the material for a given process.

In this study, a proprietary CO₂ sorbent is physicochemically characterized and its capture capacity studied. Physical properties such as surface area, particle size and surface morphology are examined. The sorbent type and the CO₂ capture mechanism are identified. The CO₂ capacity is studied in both dry and humid conditions. Using the dry sorption data, working capacity contours are constructed to examine different regeneration methods.

The surface morphology of the sorbent was studied with scanning electron microscopy, and the particle size was analyzed by laser diffractometry. BET analysis was conducted to determine surface area. The chemical structure and the adsorption species were studied by examining FTIR spectra by wavenumbers referring to relevant species. The CO₂ capacity of the sorbent was studied with a laboratory-scale setup using very dilute concentrations of CO₂ (100-5000 ppmv) at 25°C, 35°C and 50°C. The data was divided to physical sorption, chemisorption and total desorption data based on different steps in the sorption/desorption cycle. The data was fitted using Langmuir, Freundlich, Sips and Toth adsorption models. To gain temperature-dependent parameters for calculating working capacity, the data was fitted using a previously reported^[19] combined Toth-model.

Nomenclature

DAC	Direct air capture
MOF	Metal-organic framework
BET	Brunauer-Emmett-Teller
FTIR	Fourier transform infrared spectroscopy
ppmv	parts per million by volume
ATR	Attenuated total reflectance
SEM	Scanning electron microscopy
EWC	Estimated working capacity
Nstd	Normalized standard deviation
TCS	Temperature-concentration swing
PSA	Pressure swing adsorption
TSA	Temperature swing adsorption
TVSA	Temperature-vacuum swing adsorption

2. Experimental methods

2.1. Characterization

Hitachi SU3500 scanning electron microscope was used to study surface morphology of the sorbent. Particle size distributions were determined with Malvern Mastersizer 3000 Aero laser diffractometer. The resin sample was dried in a vacuum oven at 120°C for 2 hours prior to the particle size analysis. Surface area was determined with Micromeritics Gemini V by BET analysis. The samples were degasified overnight with FlowPrep 060 prior to the analysis. The BET isotherm plot can be found from Appendix A.

The chemical structure and the sorption mechanism were studied using Perkinelmer Frontier FTIR with Attenuated Total Reflectance (ATR) sampling. The samples were analyzed without pre-treatment with ATR diamond. Due to the sampling method, the study was restricted to examine the sorbent at its equilibrium state with the laboratory atmosphere (with CO₂ and humidity present). The chemical structure of the sorbent and the CO₂ adsorption species were examined by comparing the sorbent ATR-FTIR spectrum to wavenumbers associated with the relevant species. Complete table of used peak wavenumbers, the corresponding species and the references can be found in Appendix B. The spectrum was ATR- and baseline corrected and normalized by setting baseline to 0 and a known polystyrene peak at 2920 cm⁻¹ to 1.

2.2. Fixed-bed experiments

The CO₂ capacity of the sorbent was studied in a laboratory-scale fixed-bed reactor shown in Fig. 1. Approximately 0.5 grams of the sorbent was loaded into the reactor column and fixed with quartz wool. A fresh sample was changed for each isotherm. Pressure drop was measured before and after the sorbent bed.

Nitrogen of purity 5.0 was used as purge gas and as balance gas in different CO₂/N₂ mixtures. Mixture of 1% CO₂/N₂ with purity grade of 3.5/5.0 was used for the CO₂ mixtures. The gas flows were controlled and mixed by an Environics series 2000 computerized multi-component gas mixer. Total gas flow was always maintained at 1 l/min. CO₂-concentration of the gas flow before and after the column was measured by two online FTIR gas analyzers (Gaset). Hovacal digital 122-SP humidifier was used in humid experiments to produce 2 vol-% H₂O to the total gas stream.

A thermocouple measuring the column outer wall temperature was used to control the heating with a PID-controller. Thermocouples were used also to measure the temperature of the sorbent bed and the incoming gas. In dry experiments, the bed temperature was maintained $\pm 1.7^\circ\text{C}$ from the target temperature during sorption, and therefore it could be assumed isothermal. In humid experiments, the bed temperature increased 6.3-11.9°C when the humid CO₂ mixture was introduced into the sorbent column. However, the temperature decreased to the target in less than 8 minutes, and therefore also the humid sorption step could be assumed isothermal.

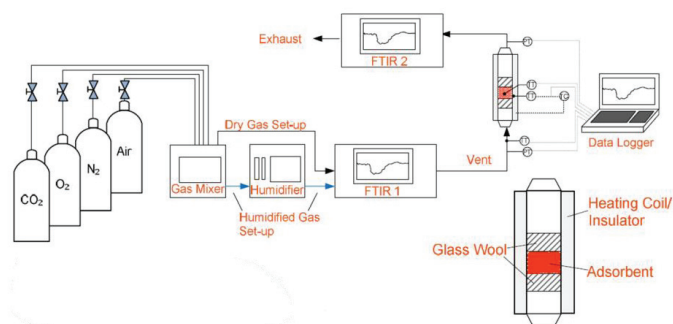


Fig. 1. The experimental setup for CO₂ sorption capacity determination.

Fig. 2 shows a typical pattern of CO₂ concentration measured from the inlet and the outlet gas streams during isotherm tests by online-FTIR. Presorbed species (CO₂ and H₂O) were removed from fresh samples by temperature-concentration swing (TCS) by N₂ purge at 90°C. The sorption step was followed by N₂ purge and heating at 90°C to remove physically bound and chemisorbed CO₂, respectively. The intent was to provide estimates for physical sorption and chemisorption. It is assumed that the physically sorbed CO₂ is removed by only the inert purge step, and the chemisorbed CO₂ is then removed by heating. Therefore, the data gained by the N₂ purge and heating are here referred to as physical sorption data and chemisorption data, respectively. The sum of these is thus referred to as total desorption data.

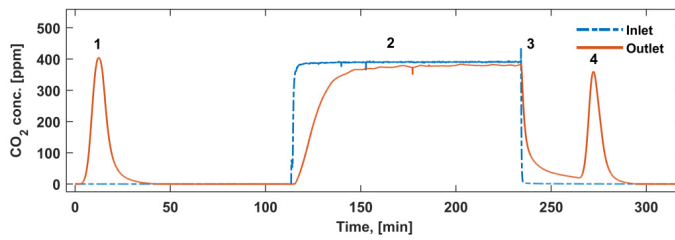


Fig. 2. The experimental steps of CO₂ isotherm tests in a CO₂ concentration profile: 1) the removal of presorbed species (for a fresh sample); 2) 2 hour sorption; 3) 30 min N₂ purge; 4) 1 hour heating.

2.3. Numerical methods

The CO₂ capacities were calculated by integrating the relevant sections in the concentration profiles. All gas flows were computed at 273.15 K and 1 atm by the gas mixer. The captured CO₂ volume was thus calculated by assuming the total flow rate as 1 l/min at all times. Ideal gas law was used to calculate the capacity in moles. The CO₂ flow and the capacity were thus calculated by the following equations:

$$V_{CO_2} = \dot{V}_{tot} \int_{t_0}^t \frac{c_{out} - c_{in}}{m} dt \quad (1)$$

$$q = \frac{p_{tot} \cdot V_{CO_2}}{R \cdot T} \quad (2)$$

where V_{CO_2} is the CO₂ capacity in volume, \dot{V}_{tot} is the total flow rate, t_0 time at the start of the step, t is the time at the end of the step, c_{out} is the concentration of CO₂ in the outlet, c_{in} is the concentration of CO₂ in the inlet, m is the mass of the sample, q is the molar CO₂ capacity, p_{tot} is the total pressure of 1 atm, R is the ideal gas constant, T is 273.15K.

Several well-known isotherm models were used to fit the data:

$$q = \frac{bq_m p}{1 + bp} \quad (3)$$

$$q = kp^{1/n} \quad (4)$$

$$q = \frac{q_m (bp)^{\frac{1}{n}}}{1 + (bp)^{\frac{1}{n}}} \quad (5)$$

$$q = q_m \frac{bp}{[1 + (bp)^t]^{1/t}} \quad (6)$$

where b is the adsorption affinity constant, q_m is the maximum capacity, p is the partial pressure of CO₂, k is a parameter in the Freundlich model, n and t are parameters in the Freundlich, Sips and Toth models. Equations (3), (4), (5) and (6) are Langmuir, Freundlich, Sips and Toth models, respectively.^[20]

An equilibrium model describing both physisorption and chemisorption was proposed by Guerrero et al.^[19]. The model is based on temperature-dependent Toth model and can be given in the form:

$$q = \left[\frac{q_m bp}{(1 + (bp)^t)^{1/t}} \right]_{\text{chemisorption}} + \left[\frac{q_m bp}{(1 + (bp)^t)^{1/t}} \right]_{\text{physisorption}} \quad (7)$$

$$q_m = q_{m,0} \exp \left[\chi \left(1 - \frac{T}{T_0} \right) \right] \quad (8)$$

$$b = b_0 \exp \left[\frac{\Delta H}{RT_0} \left(\frac{T_0}{T} - 1 \right) \right] \quad (9)$$

$$t = t_0 + \alpha \left(1 - \frac{T_0}{T} \right) \quad (10)$$

where χ and α are dimensionless parameters in the temperature-dependent model and ΔH is the isosteric heat of adsorption at zero fractional loading. Thus, the total capacity is the result of fits of the temperature-dependent Toth model to physisorption data and chemisorption data.

The working capacity was calculated in this study using the following equation:

$$EWC = q(p_A, T_A) - q(p_R, T_R) \quad (11)$$

where EWC is the estimated working capacity of the sorbent, $q(p_A, T_A)$ is the capacity gained in feed CO₂ partial pressure and temperature, and $q(p_R, T_R)$ is the capacity gained in corresponding regeneration conditions.

The goodness of fit of different isotherm models was determined by using normalized standard deviation and coefficient of determination. The normalized standard deviation can be given by:

$$Nstd = \sqrt{\frac{\sum [(q - q_{fit}) / q]^2}{N - 1}} \quad (12)$$

where q is the measured value, q_{fit} is the modelled value and N is the number of measurements. Coefficient of determination is given by:

$$R^2 = 1 - \frac{\sum (q - q_{fit})^2}{\sum (q - \bar{q})^2} \quad (13)$$

where R^2 is the coefficient of determination and \bar{q} is the average of the measured values.

3. Results and Discussion

3.1. Characterization

The sorbent is a proprietary resin functionalized with amines. Fig. 3 shows the spherical shape and the macroporous surface of the sorbent. Except for the large pores (up to 20 μm), the surface is relatively smooth and explains partly the low BET surface area of 32 cm^2/g . Laser diffractometer results gave D10, D50 and D90 values of 430 μm , 584 μm and 790 μm , respectively.

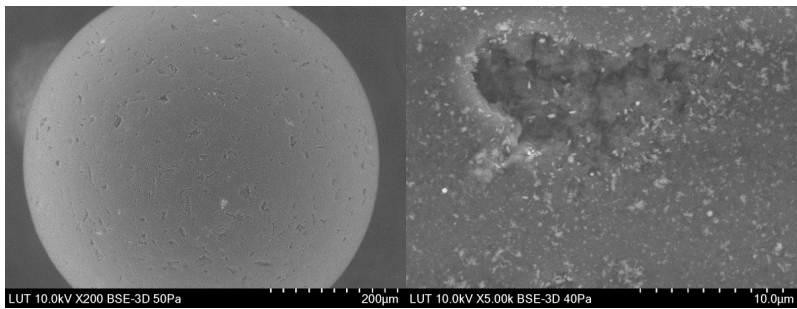


Fig. 3. SEM images of the sorbent surface with 200 X and 5000 X magnifications, respectively.

Fig. 4 shows the FTIR spectrum of the sorbent focused on three wavelength regions of interest. Fig. 4 shows strong evidence that the matrix of the sorbent is composed of polystyrene. Most of the wavenumbers found in literature^[21] that correspond to polystyrene match with a clear peak in the spectrum. Peaks appearing in the wavelength range 3250-3550 cm^{-1} can be attributed to amine N-H stretching^[22]. Two N-H stretch peaks shown in Fig. 4 refer specifically to primary amines^[22].

CO_2 chemisorption by amine species in solid sorbents is suggested to yield mainly carbamate in dry conditions, whereas in humid conditions the formation of bicarbonate is also possible^[13]. Figure 4 shows strong and sharp peaks that match to wavenumbers related to COO^- or NCOO^- vibration or stretching, which correspond to carbamate^[3,17,23,24]. On the other hand, wavenumbers associated with bicarbonate^[17] (HCO_3^-) do not match with any clear peak.

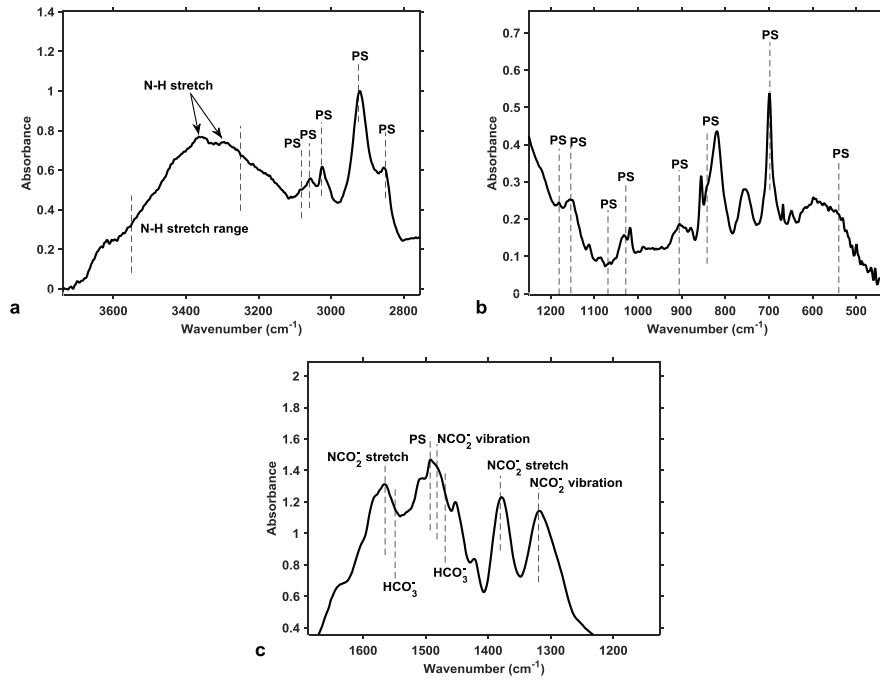


Fig. 4. FTIR spectrum region of the sorbent with peaks corresponding to (a) N-H stretching and polystyrene (PS); (b) polystyrene (PS); (c) NCO₂⁻ stretching, polystyrene (PS) and NCO₂⁻ vibration. The dashed line segments mark wavelength numbers corresponding to chemical species or molecular movements found in the literature^[3,17,21-24].

3.2. Sorption isotherms

Each adsorption isotherm model given in Chapter 2.3 was fitted to the experimental capacity results. Table 1 shows how well each model fitted to the results. Langmuir model gives the worst results for all isotherms, except for chemisorption at 50°C. For this isotherm, the Freundlich model gives the worst results. The Sips model is a combination of Freundlich and Langmuir isotherms, and compared to these gives significantly better correlations and lower uncertainty in all cases. The coefficients of determination are almost equal for both Toth and Sips isotherms. However, the uncertainties are slightly lower for Toth isotherms for physical sorption and total desorption results.

Table 1. Goodness of fit and uncertainty determined for nonlinear Langmuir, Freundlich, Sips and Toth isotherm models fitted to dry CO₂ sorption data.

Type of data	Isotherm model	R ² (25°C/35°C/50°C)	Nstd(%) (25°C/35°C/50°C)
Physical sorption	Langmuir	0.974/0.977/0.983	12.8/14.6/14.4
	Freundlich	0.993/0.989/0.995	8.5/9.3/8.7
	Sips	0.998/0.995/0.999	2.6/5.4/3.0
	Toth	0.999/0.995/0.999	1.9/5.5/2.4
Chemisorption	Langmuir	0.911/0.893/0.872	7.3/7.5/5.6
	Freundlich	0.974/0.970/0.770	4.2/3.9/8.2
	Sips	0.995/0.991/0.880	1.6/2.1/5.3
	Toth	0.995/0.990/0.880	1.6/2.1/5.3
Total desorption	Langmuir	0.924/0.925/0.936	11.0/13.5/14.8
	Freundlich	0.991/0.991/0.992	4.1/4.2/5.5
	Sips	0.999/0.996/0.994	1.3/2.9/3.9
	Toth	0.999/0.995/0.994	1.1/2.9/3.8

The validity of the method used here to quantify physisorption and chemisorption was studied by observing the Toth isotherms shown in Fig. 5. The reaching of a plateau is typical for a chemisorption isotherm, but for physisorption a maximum capacity is not reached for mesoporous adsorbents^[19]. Isotherms in Fig. 5a show strong temperature-dependence, while Fig. 5b isotherms are fairly close to each other. Isotherm plateau for chemisorption isotherms is only realized properly at 50°C. The Langmuir isotherm reaches a plateau in high pressures, which explains why Langmuir fits to the 50°C chemisorption data better than the Freundlich isotherm. In Fig. 5b, the 50°C isotherm has the highest slope in the higher end of the partial pressure region. Therefore, the results suggest that at 50°C both physical sorption and chemisorption were best approximated by the experimental method.

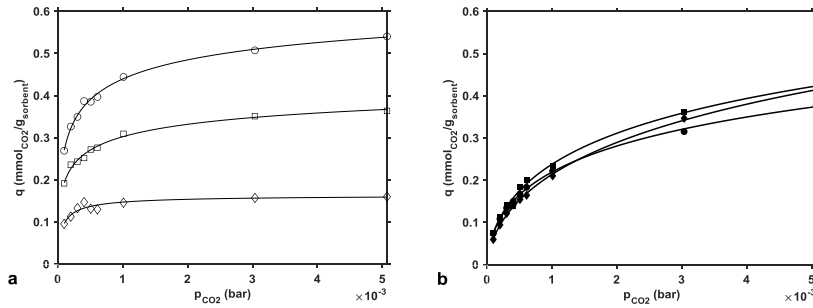


Fig. 5. (a) Chemisorption isotherms and; (b) physical sorption isotherms conducted at 25°C (spheres), 35°C (squares) and 50°C (diamonds).

To best approximate the chemisorption and physical sorption in dry and humid conditions, 50°C was selected as the temperature for comparison. Fig. 6 shows the enhancing effect of humidity on the CO₂ capacity. At 50°C, humidity enhanced physical sorption by 11-18% and chemisorption by 45-54%. The total desorption capacity was enhanced by 20-34%. The benefit from humidity mainly concerns chemisorption because of the promoting effect in the reaction mechanism. The benefit to physical sorption may partly originate from the method, imparting that a portion of the physical sorption data at 50°C is constituted of chemisorbed CO₂. On the other hand, the enhancement can be attributed to increased solubility of the CO₂ in the water-saturated resin structure. In such a case, a significant portion of the physical sorption is based on absorption.

In dry conditions at 50°C, physical sorption becomes the dominant mechanism when the partial pressure of CO₂ reaches 0.38 mbar. At the same temperature in humid conditions, chemisorption is dominant until CO₂ partial pressure is 0.65 mbar. In humid conditions in 0.4 mbar, chemisorption constitutes 55% of the total desorption capacity. Therefore, for this sorbent chemisorption is the most important mechanism of CO₂ capture in DAC conditions.

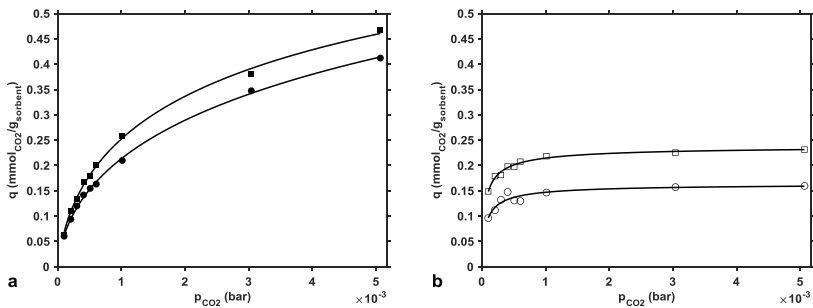


Fig. 6. The Total CO₂ isotherms of physical sorption (a) and chemisorption (b) in dry conditions (spheres) and wet conditions (squares) at 50°C.

Because Toth model gave a very good fit to chemisorption or physical sorption data at each temperature, these data were used for modelling the total capacity. The temperature-dependent combined Toth model (Eq. 7-10) was used to estimate the total desorption. 25°C was selected as the reference temperature. Fig. 7 shows a good fit of the

model to the total desorption data. The normalized standard deviations were 1.3%, 3.2% and 3.8% for 25°C, 35°C and 50°C isotherms, respectively. The corresponding coefficients of determination were 0.998, 0.994 and 0.993.

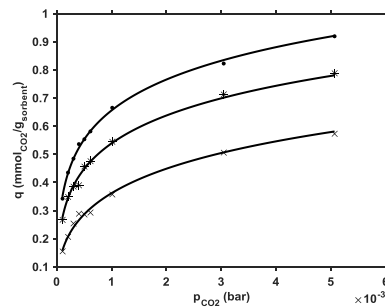


Fig. 7. The combined temperature-dependent Toth model fitted to CO₂ desorption data at 25°C (points), 35°C (asterisks) and 50°C (crosses).

Parameters gained from physical sorption and chemisorption Toth model fits are given in Table 2. The maximum capacities are low compared to previous temperature-dependent fits using amine-functionalized sorbents by Guerrero et al.^[19] and Harlick and Tezel^[25], but show that physical sorption has over two-fold maximum capacity compared to chemisorption. However, the isosteric heat of adsorption at zero loading is higher for physical sorption than for chemisorption. This may impart about the limitation of the experimental method to explain physical sorption and chemisorption in the whole temperature range. However, due to the good correlation between the estimated total desorption given by the model and the experimental total desorption, this model was used for the equilibrium analysis.

Table 2. The parameters of temperature-dependent combined Toth model.

Data	qm ₀ (mmol/g)	b ₀ (1/bar)	t ₀	α	χ	ΔH (kJ/mol)
Physical sorption	1.72	7.60×10 ³	0.234	1.26	2.13	52.5
Chemisorption	0.807	3.25×10 ⁵	0.286	2.00	17.1	35.0

3.3. Equilibrium analysis

The combined Toth model parameters (Table 2) were used to estimate the CO₂ capacity of the sorbent. The EWC was calculated using combinations of sorption and regeneration CO₂ partial pressure and temperature. Equilibrium state in each operation condition was assumed. To model the DAC conditions, the pressures were in the range of 0-0.005 bar. Temperature range of 25-80°C was selected to simulate warm conditions in CO₂ capture and low regeneration temperature, and to avoid excessive extrapolation. Pressure swing- (PSA), temperature swing- (TSA) and temperature-vacuum swing adsorption (TVSA) contours were produced from the EWC matrices. Such as in the process of Wurzbacher et al.^[18], it is assumed here in PSA and TVSA cases that the partial pressure of CO₂ during regeneration is equal to the total pressure due to initial vacuuming.

Although proposed for flue gas CO₂ separation processes^[26,27], PSA is not considered a viable option for direct air capture because of the energy-intensive compression of the feed air^[18,28]. Harlick and Tezel^[25] evaluated EWC in a partial pressure range relevant to post-combustion capture. For example, the EWC was approximately 1.6 mmol/g at 25°C with 10% CO₂ feed regenerated at 1 mbar. Fig. 8 shows that e.g. to gain 0.2 mmol/g of working capacity, the partial pressure of CO₂ already has to be lower than 0.0001 bar (0.1 mbar). The maximum EWC achievable with

desorption at 1 mbar is 0.26 mmol/g, requiring 12.5 bar compression (corresponding to 0.005 bar CO₂) for the incoming air.

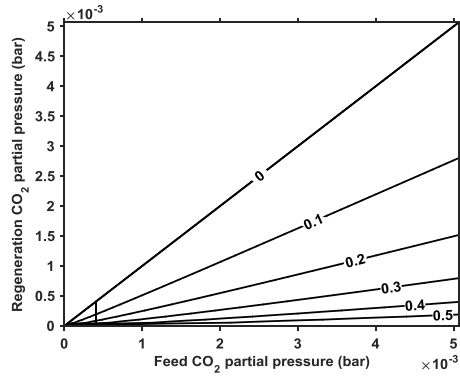


Fig. 8. Expected working capacity (mmol/g) in pressure swing adsorption at 25°C. CO₂ partial pressure corresponding to atmospheric conditions is depicted with a line segment.

Fig. 9 shows the estimated isobaric TSA working capacity of the sorbent. Using atmospheric air as feed at 25°C, 0.44 mmol/g is gained when the regeneration is conducted at 80°C. For comparison, Harlick and Tezel^[25] estimated approximately 1.4 mmol/g at similar feed and regeneration temperatures with 15% CO₂ feed. In Fig. 9, between 50-25°C, with every 5°C of decrease in feed temperature, the working capacity increases by approximately 0.05 mmol/g. Similar trend can be seen when increasing regeneration temperature between 25-55°C. The EWC increases less rapidly by further decreasing the feed temperature and increasing the regeneration temperature. However, maximum theoretical EWC is not yet realized within the temperature range of Fig. 9.

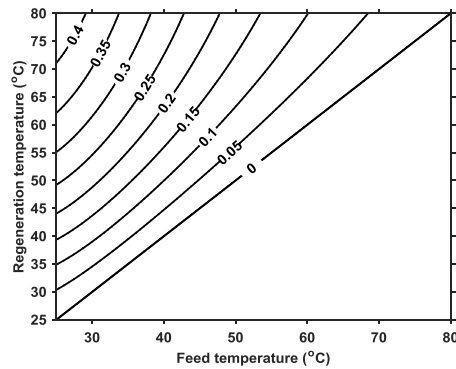


Fig. 9. The expected working capacity (mmol/g) in temperature swing adsorption at CO₂ partial pressure of 0.0004 bar.

Fig. 10 shows a TVSA contour with feed CO₂ concentration corresponding to atmospheric air at 25°C, and variable regeneration conditions. The maximum theoretical EWC is 0.52 mmol/g for DAC with desorption at 80°C. However, this would require a regeneration CO₂ partial pressure of 1×10⁻⁶ bar, which is not reasonable in process scale. If a regeneration pressure of 1 mbar is used, the EWC is lower for TVSA (0.38 mmol/g) than for TSA (0.44

mmol/g) at 80°C regeneration temperature. This is caused by the assumption of CO₂ partial pressure being equal to total (vacuum) pressure in desorption. It is also evident, that to produce at least moderate EWC levels it is not reasonable to lower the regeneration temperature from 80°C. For comparison, in a pressure-temperature swing adsorption contour by Harlick and Tezel [25], the same working capacity of approximately 1.6 mmol/g at 1 mbar vacuum, 25°C feed temperature and 10% CO₂ feed was gained whether the regeneration temperature was 25°C or 150°C. Thus, DAC processes may have less maneuverability for finding an optimum in regeneration pressure and temperature compared to post-combustion capture.

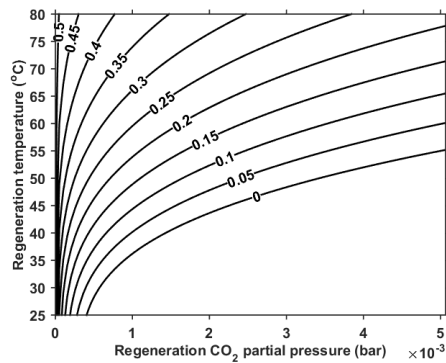


Fig. 10. The working capacity (EWC) (mmol/g) in temperature-vacuum swing adsorption. Feed conditions 25°C and 0.0004 bar partial pressure of CO₂.

4. Conclusions

In this study, a proprietary polymeric sorbent was physically and chemically characterized. The performance of this sorbent was also studied under dry and humid conditions in CO₂ partial pressures up to 5 mbar. The results were divided to physical sorption and chemisorption data by concentration swing and temperature-concentration swing stages. Isotherms in dry conditions at 25°C, 35°C and 50°C were modelled with several well-known isotherm models. Physical sorption and chemisorption data were modelled using a combined temperature-dependent Toth model reported previously in literature. The temperature-dependent model parameters were used to estimate the working capacity of the sorbent in pressure swing adsorption, temperature swing adsorption and temperature-vacuum swing adsorption.

The sorbent was found to exhibit a spherical shape with low surface area of 32 m²/g and median particle size of 0.60 μm. Peaks referring to polystyrene, primary amines and carbamate groups were identified from FTIR spectrum. Toth isotherm was found to fit best to the experimental CO₂ capture capacity data. The method for dividing physical sorption and chemisorption was found to quantify the two mechanisms best at the highest experimental temperature. At 50°C chemisorption was found to be the dominant mechanism at CO₂ partial pressures corresponding to direct air capture (DAC) conditions and below. Humidity enhanced the CO₂ capacity up to 34% at 50°C, and increased the contribution of chemisorption significantly. Pressure swing adsorption (PSA) contour showed that reasonable working capacity was not acquired in an isothermal process until high compression of the feed or unreasonable vacuum for process scale was applied. By estimating temperature swing adsorption (TSA) performance, a maximum working capacity of 0.44 mmol/g was gained in DAC conditions. If reasonable vacuum for process scale temperature-vacuum swing adsorption (TVSA) was also applied, working capacities decreased.

The FTIR results suggest that the material is a polystyrene resin functionalized with primary-amine groups. Because the main mechanism in DAC conditions is chemical adsorption, it is justified to refer to the material as adsorbent. The division to physical sorption and chemisorption data by concentration swing and temperature swing

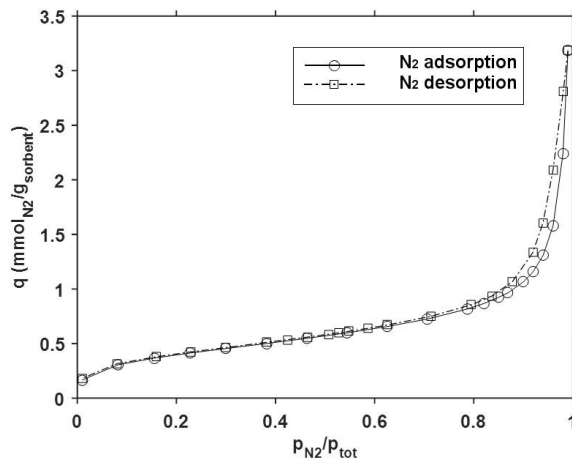
is not a precise method, but can provide estimates by a relevantly easy experimental procedure. A longer concentration swing step would provide more accurate results also at lower temperatures. Based on the analysis of estimated working capacity, the resin presented here is not suitable for pressure swing adsorption in direct air capture. When comparing post-combustion capture and DAC, it is clear that DAC using the current adsorbent requires too high compression of the feed to reach any reasonable EWC levels. Of the different regeneration methods, PSA is affected the most by the huge difference in CO_2 partial pressure of DAC versus post-combustion capture. Using the current adsorbent, temperature swing adsorption using inert gas or steam purge is recommended for highest possible working capacity. However, TVSA should be selected if high purity product is the main goal, because gas purging decreases the CO_2 purity in TSA.

Acknowledgements

This study was conducted as a part of Neo-Carbon Energy project funded by Tekes, the Finnish Funding Agency for Innovation.

The authors would also like to thank Chemical Technology Analysis Services at Lappeenranta University of Technology for co-operating to produce the experimental results in Chapter 3.1.

Appendix A. BET isotherm plot



Appendix B. FTIR reference table

Wavenumber (cm ⁻¹)	Species	Assignment	Reference
540	Polystyrene	-	[21]
698	Polystyrene	-	[21]
842	Polystyrene	-	[21]
906	Polystyrene	-	[21]
1028	Polystyrene	-	[21]
1069	Polystyrene	-	[21]
1154	Polystyrene	-	[21]
1181	Polystyrene	-	[21]
1320-1335	Carbamate	NCOO ⁻ vibration	[3,17,24]
1381-1385	Carbamate	NCOO ⁻ stretch	[3,23]
1469	Bicarbonate	HCO ₃ ⁻	[17]
1482	Carbamate	NCOO ⁻ vibration	[17]
1493	Polystyrene	-	[21]
1549	Bicarbonate	HCO ₃ ⁻	[17]
1564-1565	Carbamate	NCOO ⁻ stretch	[17,23,24]
2850	Polystyrene	-	[21]
2924	Polystyrene	-	[21]
3026	Polystyrene	-	[21]
3026	Polystyrene	-	[21]
3060	Polystyrene	-	[21]
3082	Polystyrene	-	[21]
3250	Amine	N-H stretch range	[22]
3550	Amine	N-H stretch range	[22]

References

- [1] R. Socolow, M. Desmond, R. Aines, J. Blackstock, O. Bolland, T. Kaarsberg, et al., Direct air capture of CO₂ with chemicals - a technology assessment for the APS Panel on public affairs, The American Physical Society, 2011.
- [2] S.A. Didas, A.R. Kulkarni, D.S. Sholl, C.W. Jones, Role of amine structure on carbon dioxide adsorption from ultradilute gas streams such as ambient air, *ChemSusChem*. 2012; 5: 2058–2064.
- [3] M.A. Alkhabbaz, P. Bollini, G.S. Foo, C. Sievers, C.W. Jones, Important roles of enthalpic and entropic contributions to CO₂ capture from simulated flue gas and ambient air using mesoporous silica grafted amines, *J. Am. Chem. Soc.* 2014; 136: 13170–13173.
- [4] S. Choi, J.H. Drese, P.M. Eisenberger, C.W. Jones, Application of amine-tethered solid sorbents for direct CO₂ capture from the ambient air, *Environ. Sci. Technol.* 2011; 45: 2420–2427.
- [5] A. Goepfert, H. Zhang, M. Czaun, R.B. May, G.K.S. Prakash, G.A. Olah, et al., Easily regenerable solid adsorbents based on polyamines for carbon dioxide capture from the air, *ChemSusChem*. 2014; 7: 1386–1397.
- [6] F.Q. Liu, L. Wang, Z.G. Huang, C.Q. Li, W. Li, R.X. Li, et al., Amine-tethered adsorbents based on three-dimensional macroporous silica for CO₂ capture from simulated flue gas and air, *ACS Appl. Mater. Interfaces*. 2014; 6: 4371–4381.
- [7] S. Choi, M.L. Gray, C.W. Jones, Amine-tethered solid adsorbents coupling high adsorption capacity and regenerability for CO₂ capture from ambient air, *ChemSusChem*. 2011; 4: 628–635.
- [8] C. Gebald, J.A. Wurzbacher, P. Tingaut, T. Zimmermann, A. Steinfeld, Amine-based nanofibrillated cellulose as adsorbent for CO₂ capture from air, *Environ. Sci. Technol.* 2011; 45: 9101–9108.
- [9] T.M. McDonald, W.R. Lee, J.A. Mason, B.M. Wiers, C.S. Hong, J.R. Long, Capture of carbon dioxide from air and flue gas in the alkylamine-appended metal-organic framework mmen-Mg₂(dobpdc), *J. Am. Chem. Soc.* 2012; 134: 7056–7065.
- [10] W.R. Lee, S.Y. Hwang, D.W. Ryu, K.S. Lim, S.S. Han, D. Moon, et al., Diamine-functionalized metal-organic framework: exceptionally high CO₂ capacities from ambient air and flue gas, ultrafast CO₂ uptake rate, and adsorption mechanism, *Energy Environ. Sci.* 2014; 7:

- 744–751.
- [11] Z. Chen, S. Deng, H. Wei, B. Wang, J. Huang, G. Yu, Polyethylenimine-impregnated resin for high CO₂ adsorption: An efficient adsorbent for CO₂ capture from simulated flue gas and ambient air, *ACS Appl. Mater. Interfaces*. 2013; 5: 6937–6945.
 - [12] K. Sumida, D.L. Rogow, J.A. Mason, T.M. McDonald, E.D. Bloch, Z.R. Herm, et al., Carbon dioxide capture in metal-organic frameworks, *Chem. Rev.* 2012; 112: 724–781.
 - [13] S. Choi, J.H. Drese, C.W. Jones, Adsorbent materials for carbon dioxide capture from large anthropogenic point sources, *ChemSusChem*. 2009; 2: 796–854.
 - [14] S.A. Didas, M.A. Sakwa-Novak, G.S. Foo, C. Sievers, C.W. Jones, Effect of amine surface coverage on the co-adsorption of CO₂ and water: spectral deconvolution of adsorbed species, *J. Phys. Chem. Lett.* 2014; 5: 4194–4200.
 - [15] A. Kumar, D.G. Madden, M. Lusi, K.-J. Chen, E.A. Daniels, T. Curtin, et al., Direct air capture of CO₂ by physisorbent materials, *Angew. Chemie Int. Ed.* 2015; 54: 1–7.
 - [16] R. Paterson, Y. Yampol'skii, P.G.T. Fogg, A. Bokarev, V. Bondar, O. Ilinich, et al., IUPAC-NIST Solubility Data Series 70. Solubility of Gases in Glassy Polymers, *J. Phys. Chem. Ref. Data*. 1999; 28: 1255–1450.
 - [17] W.R. Alesi, J.R. Kitchin, Evaluation of a primary amine-functionalized ion-exchange resin for CO₂ capture, *Ind. Eng. Chem. Res.* 2012; 51: 6907–6915.
 - [18] J.A. Wurzbacher, C. Gebald, A. Steinfeld, Separation of CO₂ from air by temperature-vacuum swing adsorption using diamine-functionalized silica gel, *Energy Environ. Sci.* 2011; 4: 3584–3592.
 - [19] R. Serna-Guerrero, Y. Belmabkhout, A. Sayari, Modeling CO₂ adsorption on amine-functionalized mesoporous silica: 1. A semi-empirical equilibrium model, *Chem. Eng. J.* 2010; 161: 173–181.
 - [20] D.D. Do, Adsorption analysis: Equilibria and kinetics, in: R.T. Yang (Ed.), London:Imperial College Press;1998: pp. 64–70.
 - [21] L.M. Hanssen, C. Zhu, Wavenumber standards for mid-infrared spectrometry, Reproduced from: J. M. Chalmers, P. R. Griffiths, editors, *Handbook of Vibrational Spectroscopy*, Chichester: Wiley, 2002, Available, n.d.; <https://www.nist.gov/sites/default/files/documents/calibrations/HndBk0>.
 - [22] G. Socrates, *Infrared and Raman Characteristic Group Frequencies: Tables and Charts*, 3rd ed., Chichester:Wiley;2004.
 - [23] Z. Bacsik, N. Ahlsten, A. Ziadi, G. Zhao, A.E. Garcia-bennett, B. Martin-Matute, et al., Mechanisms and kinetics for sorption of CO₂ on bicontinuous mesoporous silica modified with n-propylamine, *Langmuir*. 2011; 27: 11118–11128.
 - [24] A. Danon, P.C. Stair, E. Weitz, FTIR study of CO₂ adsorption on amine-grafted SBA-15: Elucidation of adsorbed species, *J. Phys. Chem.* 2011; 115: 11540–11549.
 - [25] P.J.E. Harlick, F.H. Tezel, Equilibrium analysis of cyclic adsorption processes: CO₂ working capacities with NaY, *Sep. Sci. Technol.* 2005; 40: 2569–2591.
 - [26] M.T. Ho, G.W. Allinson, D.E. Wiley, Reducing the Cost of CO₂ Capture from Flue Gases Using Pressure Swing Adsorption, *Ind. Eng. Chem. Res.* 2008; 47: 4883–4890.
 - [27] S.P. Reynolds, A.D. Ebner, J.A. Ritter, Carbon dioxide capture from flue gas by pressure swing adsorption at high temperature using a K-promoted HTlc: Effects of mass transfer on the process performance, *Environ. Prog.* 2006; 25: 334–342.
 - [28] N.R. Stuckert, R.T. Yang, CO₂ capture from the atmosphere and simultaneous concentration using zeolites and amine-grafted SBA-15, *Environ. Sci. Technol.* 2011; 45: 10257–10264.

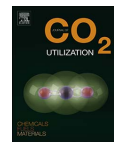
Publication II

J. Elfving, C. Bajamundi, J. Kauppinen and T. Sainio
**Modelling of equilibrium working capacity of PSA, TSA and TVSA processes for
CO₂ adsorption under direct air capture conditions**

Reprinted with permission from
Journal of CO₂ Utilization
Vol. 22, pp. 270-277, 2017
© 2017, Elsevier Ltd.



Contents lists available at ScienceDirect

Journal of CO₂ Utilizationjournal homepage: www.elsevier.com/locate/jcou

Modelling of equilibrium working capacity of PSA, TSA and TVSA processes for CO₂ adsorption under direct air capture conditions

Jere Elfving^{a,*}, Cyril Bajamundi^a, Juho Kauppinen^a, Tuomo Sainio^b^a VTT Technical Research Centre of Finland Ltd., Koivurannantie 1, FI-40101 Jyväskylä, Finland^b Lappeenranta University of Technology, School of Engineering Science, Skinnarilankatu 34, FI-53850 Lappeenranta, Finland

ARTICLE INFO

Keywords:

Direct air capture
CO₂ capture
Working capacity
Equilibrium modelling
Effect of humidity

ABSTRACT

In this study, direct air capture performance of polymeric adsorbent was studied by determining CO₂-isotherms in very dilute conditions (CO₂ partial pressure up to 5 mbar). The effect of cold conditions (0 °C and –10 °C) and humidity on the CO₂ capacity was also studied. The experimental isotherms were used in temperature-dependent equilibrium modelling to simulate equilibrium CO₂ working capacities in pressure-swing adsorption (PSA), temperature-swing adsorption (TSA) and temperature-vacuum swing adsorption (TVSA). Experimental adsorption capacities of 0.80 mmol_{CO₂}/g_{sorbent} and 0.89 mmol_{CO₂}/g_{sorbent} were obtained from 400 ppmv CO₂ in dry cold conditions and at 25 °C in humid conditions, respectively. The highest experimental capacity gained from 400 ppmv CO₂ was 1.06 mmol_{CO₂}/g_{sorbent} in humid cold conditions. In terms of the working capacity, PSA was found not to be a viable process option. Humidity promoted TSA working capacity up to by 0.36 mmol_{CO₂}/g_{sorbent} (78%). TSA could produce larger than 0.5 mmol_{CO₂}/g_{sorbent} working capacity levels even with very low regeneration temperatures (50–60 °C) when adsorbing either in dry cold conditions or humid warm conditions. Such EWC levels with dry TVSA could only be achieved using 90 °C regeneration temperature with adsorption in either cold conditions or from compressed air. Based on these results, TVSA should only be considered in PtX applications requiring high-purity CO₂.

1. Introduction

Wind power and photovoltaic power are very fluctuating in nature, and can generate significant excess electricity when demand is lower than generation [1]. The ever-increasing amount of wind power and photovoltaic power thus leads to a more fluctuating energy generation. In addition to load shifting and grid extension, excess electricity can be managed by storing it by pumped hydro, batteries and flywheels. Excess electricity can also be converted to chemical energy in so-called Power-to-X (PtX) processes. [2, p. 1–5] In addition to chemical conversion processes, biological routes such as greenhouses, microbial and algae cultivation are also potential applications for CO₂ utilization.

Chemical conversion routes in Power-to-X, such as synthesis of methane and methanol, require relatively pure CO₂ flow [2, p. 53–54]. Combustion process flue gases contain impurities such as SO_x, NO_x, halogens, carbon monoxide, chlorides, sulphates and hydrocarbons [3]. Many of these impurities can deactivate the catalyst in methane or methanol synthesis. Sulphur species are especially dangerous, since they can poison a nickel-based catalyst in only a few ppmv [4]. Therefore, the selectivity of the CO₂ capture technology becomes

paramount in point source capture. Otherwise, the product CO₂ may need pre-treatment by a gas-separation unit prior to feeding to the synthesis process. Also, if the PtX-process is not in close proximity to the source of emissions, the CO₂ needs to be transported.

Direct air capture (DAC) evades these disadvantages of post-combustion capture (PCC). As the source of CO₂ is air, CO₂ can be produced almost anywhere, as long as the DAC unit itself is mobile. Capturing CO₂ from air also addresses scattered emissions that are otherwise impossible to control. However, the relatively low concentration of CO₂ in air results to a higher work of separation than in post-combustion capture. Although the thermodynamic minimum work of DAC may be only about three times that of PCC, the economic cost difference may still be significant enough to make DAC unattractive [5]. Instead of solvent-based capture such as using NaOH-solution, which requires high temperature of 800 °C in regeneration [5], solid amine-based materials have been the most reported in DAC-related studies during the past decade [6]. These adsorbents combine highly selective amine groups with porous materials, resulting to much lower temperatures required for regeneration than for example in the NaOH solution-based process [7]. However, in atmospheric conditions the presence of

* Corresponding author.

E-mail address: jere.elfving@vtt.fi (J. Elfving).<http://dx.doi.org/10.1016/j.jcou.2017.10.010>Received 19 April 2017; Received in revised form 25 August 2017; Accepted 11 October 2017
2212-9820/ © 2017 Elsevier Ltd. All rights reserved.

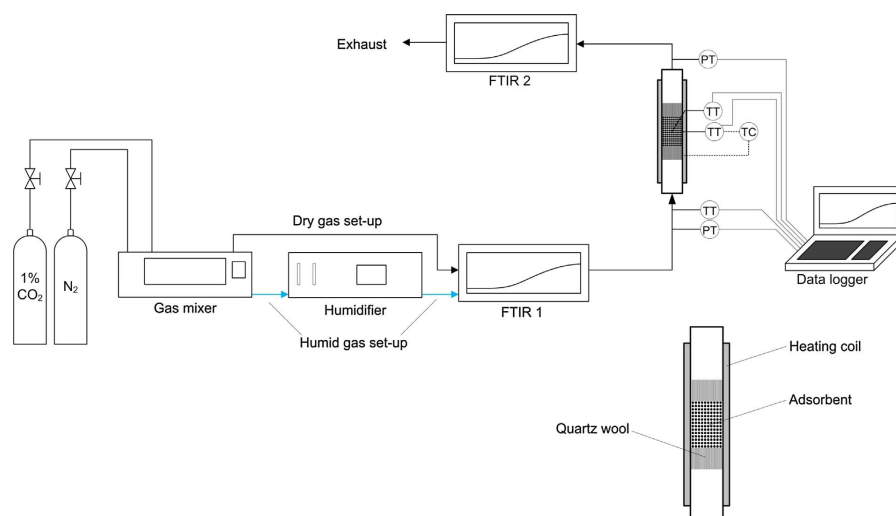


Fig. 1. The experimental set-up for adsorption capacity determination.

humidity can lead to stability issues for some materials [8,9]. If the CO₂ adsorbent is not suitable for operation in varying conditions, the main advantage of DAC is lost.

DAC has only rarely been studied in real atmospheric conditions (see Holmes et al. [10]), not to mention in winter conditions, such as by Wagner et al. [11]. To study the applicability of DAC in northern Europe conditions such as in Finland, the performance needs to be determined also at temperatures appropriate to cold climates.

Humidity can enhance the CO₂ capacity of amine-based sorbents theoretically up to two times the dry capacity [12]. However, experimental results on the effect of humidity vary considerably. The CO₂ capacity of a mesoporous carbon functionalized with polyethylenimine (PEI) only increased from 2.25 in dry conditions to 2.58 mmol_{CO₂}/g_{sorbent} (by 15%) in 80% relative humidity [13]. On the other hand, the capacity of nanofibrillated cellulose functionalized with aminosilane increased from 1.11 mmol_{CO₂}/g_{sorbent} in dry conditions to 2.13 mmol_{CO₂}/g_{sorbent} (by 92%) in 91% relative humidity [14]. Even more drastic effect was found by Sehaqui et al. [15] for a nanofibrillated cellulose sorbent impregnated with PEI, the CO₂ capacity of which increased from approximately 0.5 mmol_{CO₂}/g_{sorbent} in 20% relative humidity to 2.2 mmol_{CO₂}/g_{sorbent} (by over 300%) in 80% relative humidity. Contrary to the results above, Goepfert et al. [16] found a drop in CO₂ capacity from 1.70 mmol_{CO₂}/g_{sorbent} in dry conditions to 1.41 mmol_{CO₂}/g_{sorbent} in 67% relative humidity for a fumed silica sorbent impregnated with PEI. Thus, it is relevant to examine the effect of humidity sorbent-specifically.

Although equilibrium CO₂ adsorption capacity from air may be used for comparison of DAC sorbents, their feasibility under cyclic process conditions cannot be reliably deduced only from the maximum capacity. By using temperature-dependent modelling of CO₂ isotherms at several temperatures, Harlick and Tezel [17] estimated the equilibrium CO₂ working capacity of NaY zeolite in pressure-swing adsorption (PSA), temperature-swing adsorption (TSA) and pressure-temperature-swing adsorption (PTSA). Although representing an ideal case, such analysis can be used to determine the maximum available working capacity in different process conditions.

In this work, adsorption of CO₂ on proprietary adsorbent is studied in conditions relevant to direct air capture; i.e. low temperatures, very

dilute CO₂ partial pressures and the presence of humidity. CO₂ isotherms were determined by laboratory-scale adsorption tests in dry and humid conditions. In earlier work [18], performance of the resin was also studied similarly, and it was found that the Toth isotherm fitted the experimental isotherms best. Therefore, the Toth isotherm was used earlier as well as here to fit experimental CO₂ isotherms. However, the experimental temperature range used in the earlier work was only 25–50 °C. To simulate winter conditions in northern climates such as in Finland, tests in the current work were conducted as low as at –10 °C. To simulate processes with thermal swing, the tests were conducted up to at 90 °C. The enhancing effect of humidity was also studied earlier at 50 °C, but here this was studied at several temperatures, even below the freezing point. Also, the amount of adsorbed water was analyzed in the current work. In the earlier and the current work, the performance of the material in process conditions was modelled by a similar type working capacity analysis as conducted by Harlick and Tezel [17]. Modelled equilibrium working capacity (EWC) contours in PSA, TSA and TVSA were determined by using temperature-dependent modelling. However, the analysis presented here is improved compared to the previous one by using the total desorption capacity instead of sorption capacity in the working capacity modelling. Finally, the analysis is here extended to a wider temperature range as well as the humid TSA case.

2. Materials and methods

2.1. The adsorbent material

The adsorbent studied in this paper is in use in a pilot-scale direct air capture device based on temperature-vacuum-swing adsorption (TVSA) at VTT. The DAC device and the adsorbent were delivered to VTT by Oy Hydrocell Ltd. Research work in VTT on the process and the adsorbent material is ongoing. Material properties of the adsorbent such as physical and chemical structure and the adsorption mechanism were studied previously [18]. Based on Fourier transform infrared (FTIR) spectra, the adsorbent is consisted of polystyrene functionalized with primary amine. The adsorbent particles are spherical with a mean diameter of approximately 0.60 μm and surface area of 32 m²/g. Also, evidence was found from the FTIR spectra that the CO₂ adsorption

mechanism is based on the forming of carbamate. Afterwards, a CHN elemental analysis was also conducted on the adsorbent, in which the nitrogen content was found to be 6.61 m-% of dry weight, which corresponds to 4.72 mmol_N/g_{adsorbent}.

2.2. CO₂ isotherm experiments

CO₂ adsorption measurements were conducted in a laboratory-scale fixed-bed column. The experimental setup is presented schematically in Fig. 1. The adsorption column was built using stainless steel Swagelok parts. Another option using a Liebig-condenser enabled cooling liquid circulation. Approximately 0.5 g of the adsorbent was loaded into the column and fixed with quartz wool. The exact weighed amount of the as-received adsorbent, being the practical mass considering process scale, was used to calculate the adsorption capacity. The sample was changed for each isotherm. Pressure was measured before and after the adsorbent bed.

Nitrogen of purity grade 5.0 was used as purge gas and as balance gas for different CO₂/N₂ mixtures. Mixture of 1% CO₂/N₂ with purity grade of 3.5/5.0 was used with the balance gas to mix different CO₂ compositions. The gas flows were controlled and mixed by an Envirovics series 2000 computerized multi-component gas mixer. Hovacal digital 122-SP humidifier was used in humid experiments to produce 2 vol-% H₂O in the total gas stream. CO₂-concentration of the gas flow before and after the column was measured by two online FTIR-gas analysers (Gaset).

Three different heating/cooling systems were used to achieve isothermal conditions in adsorption depending on the temperature range: 1) heating tape around the column (25 °C, 35 °C, 50 °C, 90 °C); 2) cooling bath containing ice and water (0 °C) or NaCl-solution and ice (−10 °C); 3) Liebig condenser with water (13 °C) or ethylene glycol (−10 °C) circulation. A thermocouple measuring the column outer wall temperature was used to control the heating tape with a PID-controller. Thermocouples were used also to measure the temperature of the adsorbent bed and the incoming gas.

All experiments were carried out using temperature-concentration swing (TCS) adsorption. The experiments consisted of the adsorption step, N₂ purge step and the heating step. Total gas flow rate was 1 l/min in each step. Adsorption was initiated by introducing CO₂/N₂ flow. After 2 h of adsorption, the flow was changed to pure nitrogen to remove physisorbed CO₂ from the tubing, the column and the adsorbent itself. Then, after 30 min, the heating step was initiated by heating up the sample to 90 °C for 1 h. Similar heating step was used to remove preadsorbed species from the fresh adsorbent samples until the CO₂ concentration was below 2 ppmv. The low temperature for desorption was chosen to avoid the degradation of the adsorbent in repeated cycles. Because the adsorption and desorption steps had fixed times, the resulting adsorption capacities are pseudo-equilibrium capacities. The adsorption-desorption profile in a typical experiment can be found in the Supplementary information.

The adsorption capacities were determined at CO₂ partial pressures of 0.1, 0.2, 0.3, 0.4, 0.5, 0.6, 1, 3 and 5 mbar in dry conditions. CO₂ capacities were also determined in humid conditions with 2 vol-% H₂O. For practical reasons, in humid conditions the capacity was determined only at CO₂ partial pressures of 0.2, 0.4, 0.6, 1, 3 and 5 mbar. In order to understand the effect of humidity on the sorption of CO₂, the amount of adsorbed water was also determined at CO₂ partial pressures of 0.4 and 5 mbar.

2.3. Isotherm model

The laboratory-scale dynamic desorption data was used to determine the adsorption capacities in each test. Saturation was not quite reached in the case of 0.1 mbar and 0.2 mbar CO₂ at −10 °C and 0 °C but the values in these cases were obtained by extrapolation of the top part of the breakthrough curve. Calculation of the capacities as well as

uncertainty analysis can be found in the Supplementary information.

The capacities were modelled using the Toth isotherm:

$$q = q_m \frac{bp}{[1 + (bp)^t]^{1/t}} \quad (1)$$

where q is the adsorption capacity, p is the partial pressure of CO₂, q_m , b and t are Toth model parameters. More specifically, q_m refers to the maximum adsorption capacity, b is the adsorption affinity, and t describes the heterogeneity of the adsorption system. These parameters are temperature-dependent, and can be given in the forms:

$$q_m = q_{m,0} \exp\left[\chi\left(1 - \frac{T}{T_0}\right)\right] \quad (2)$$

$$b = b_0 \exp\left[\frac{\Delta H}{RT_0}\left(\frac{T_0}{T} - 1\right)\right] \quad (3)$$

$$t = t_0 + \alpha\left(1 - \frac{T}{T_0}\right) \quad (4)$$

where $q_{m,0}$, b_0 and t_0 are values of the Toth parameters at a reference temperature T_0 , χ and α are dimensionless constants, ΔH is the opposite number of the isosteric heat of adsorption at zero fractional loading, and R is the ideal gas constant. [19, p. 64–69]

The Toth-isotherms were fitted to the experimental data using Matlab. Eqs. (2)–(4) were inserted in Eq. (1) to evaluate the error function, which was minimized using Matlab function *lsqnonlin*. To find the global minimum, function *multistart* was used to generate 50 starting points for the solver. Function tolerance and step tolerance were set to 1·10^{−10}. Forward finite difference method with trust-region-reflective algorithm was used.

Normalized standard deviation is commonly used [14,20,21] to estimate how well isotherm models fit to experimental data. It is calculated according to:

$$\Delta q = \sqrt{\frac{\sum [(q - q_{fit})/q]^2}{N - 1}} \quad (5)$$

where Δq is the normalized standard deviation, q is the measured value and q_{fit} is the modelled value for the CO₂ capacity.

3. Results & discussion

3.1. CO₂ adsorption isotherms

The temperature-dependent Toth model parameters are given in Table 1. The low partial pressure range used in the Toth model has a significant effect on the model parameters, and thus any comparisons made to models with a higher CO₂ partial pressure range would be directional at best. However, the values of parameter ΔH are within reasonable boundaries for CO₂ adsorption on amine-functionalized solid adsorbents. Serna-Guerrero et al. [21] obtained 67.3 kJ/mol in dry conditions for chemisorption data on amine-functionalized silica using the temperature-dependent Toth model. Veneman et al. [22] obtained 86.7 kJ/mol in dry conditions by also using the same model. Zhang et al. [23] measured heats of adsorption between −43 to −53 kJ/mol using different compositions of linear polyethylenimine in

Table 1

The parameters of temperature-dependent Toth model fitted to dry CO₂ adsorption isotherms at −10 °C, 0 °C, 13 °C, 25 °C, 35 °C, 50 °C and 90 °C and humid CO₂ adsorption isotherms at 25 °C, 35 °C, 50 °C and 90 °C.

Data	$q_{m,0}$ (mmol _{CO2} /g _{adsorbent})	b_0 (1/bar)	t_0	α	χ	ΔH (kJ/mol)
Dry	1.71	1.13×10^5	0.265	0.601	4.53	62.2
Humid	1.75	2.60×10^5	0.311	0.046	4.70	67.9

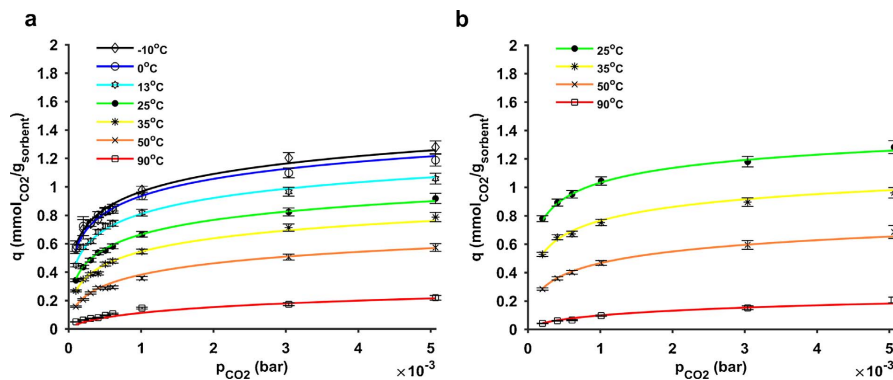


Fig. 2. Temperature-dependent Toth model fit to experimental CO₂ adsorption isotherms in a) dry conditions; b) humid conditions. Markers correspond to experimental points and lines correspond to the model fit. Experimental uncertainty shown by error bars.

fumed silica sorbent.

Fig. 2a and b show a good fit with the temperature-dependent Toth model to the experimental adsorption capacities. The normalized standard deviations for dry data at -10°C , 0°C , 13°C , 25°C , 35°C , 50°C and 90°C were 2.7%, 3.4%, 2.2%, 1.6%, 3.6%, 6.0% and 22%, correspondingly. Although the number of experimental points in the humid isotherms was not very large, the normalized standard deviations of the isotherm fits at corresponding temperatures were good. The normalized standard deviations for humid data at 25°C , 35°C , 50°C and 90°C were 1.3%, 2.4%, 2.2% and 10.6%, respectively. At 90°C , even small absolute errors contributed to high relative error and therefore to relatively high normalized standard deviations.

Fig. 2a shows that cold temperatures are advantageous for DAC in dry conditions. The adsorption capacity is strongly enhanced below room temperature. However, the improvement between 0°C and -10°C is very small, which can be related to gas diffusion limitations or reaching of the maximum capacity in dry conditions. Therefore, this suggests that adsorption temperatures below -10°C do not significantly further improve the adsorption capacity.

CO₂ isotherms were also determined in humid conditions. Comparing Fig. 2b to Fig. 2a shows that humidity significantly enhances the CO₂ capacity between 25°C and 50°C . Fig. 3a shows the quantity of the enhancing effect of humidity on the experimental

results. Another comparison approach is shown in Fig. 3b, which clearly shows that the relative difference of the humid results to the dry results is highest at the lowest CO₂ partial pressures, which is in accordance to results by Gebald et al. [14]. This may result from the fact that at the lowest partial pressures of CO₂ the capture mechanism is dominantly based on chemisorption of CO₂ on amine sites, and the positive effect of humidity stems from increased chemisorption. At 90°C humidity does not have a promoting effect on the CO₂ capacity, however. This can be explained by the high temperature, at which water is no longer significantly captured by the adsorbent as shown in Table 2. Fig. 3 actually shows that the effect of humidity on the capacity is negative, which may originate from experimental uncertainty not explained by the error bars shown in Fig. 2 (see Supplementary information). Table 2 also shows that at 25°C the ratio of sorbed H₂O and CO₂ is highest from humid 400 ppmv CO₂, and at higher temperature the ratio decreases. When comparing the co-adsorption results of H₂O with 400 ppmv CO₂ and 5000 ppmv CO₂, the amount of sorbed H₂O is not clearly higher in 400 ppmv CO₂ results. Therefore, there is no clear indication that H₂O and CO₂ compete for adsorption sites with mixture of 2 vol-% H₂O and dilute concentrations of CO₂. However, to study the competition more comprehensively, single-component H₂O isotherms should be compared with binary component H₂O/CO₂ isotherms, which is out of scope of this article.

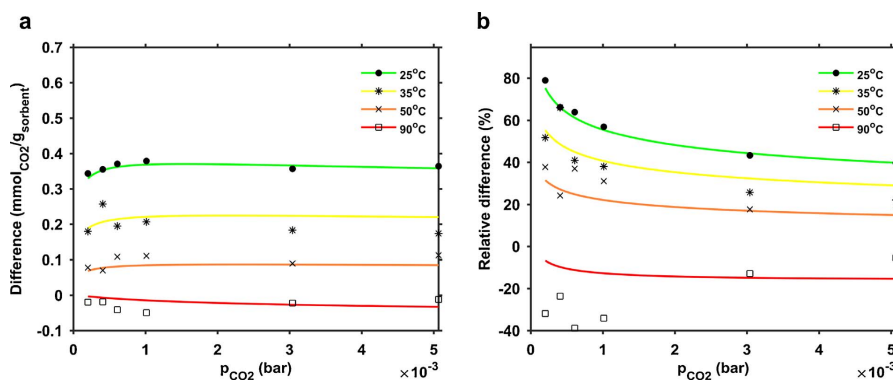


Fig. 3. The a) absolute and b) relative differences of experimental (markers) and modelled (lines) humid adsorption capacities to dry capacities.

Table 2

H₂O capacities at 25 °C, 35 °C, 50 °C and 90 °C with simultaneous adsorption of 400 ppmv or 5000 ppmv CO₂, and the molar ratio of captured H₂O versus CO₂. The molar ratio of H₂O and CO₂ at 90 °C was not calculated due to uncertainty.

Temperature (°C)	400 ppmv CO ₂ /2-vol-% H ₂ O		5000 ppmv CO ₂ /2 vol-% H ₂ O	
	q _{H₂O} (mmol _{H₂O} / g _{sorbent})	q _{H₂O} /q _{CO₂} (mol _{H₂O} / mol _{CO₂})	q _{H₂O} (mmol _{H₂O} / g _{sorbent})	q _{H₂O} /q _{CO₂} (mol _{H₂O} / mol _{CO₂})
25	5.78 ± 0.20	6.5	6.25 ± 0.24	4.9
35	2.66 ± 0.13	4.1	2.43 ± 0.16	2.5
50	1.40 ± 0.10	3.9	1.16 ± 0.08	1.5
90	0.11 ± 0.08	–	0.12 ± 0.13	–

From dry 400 and 5000 ppmv CO₂, the highest experimental adsorption capacities were 0.80 mmol_{CO₂}/g_{sorbent} and 1.28 mmol_{CO₂}/g_{sorbent} at 0 °C and –10 °C, respectively. At 25 °C the CO₂ adsorption capacities from humid 400 and 5000 ppmv CO₂ were 0.89 mmol_{CO₂}/g_{sorbent} and 1.28 mmol_{CO₂}/g_{sorbent}. When comparing the 400 ppmv CO₂ results, the highest value in dry cold conditions at 0 °C is 0.26 mmol/g (48%) higher, and the highest value in humid conditions is 0.35 mmol_{CO₂}/g_{sorbent} (65%) higher than 0.54 mmol_{CO₂}/g_{sorbent} gained in dry conditions at 25 °C. When comparing the 5000 ppmv CO₂ results, the highest values in dry cold conditions and humid warm conditions are both 0.36 mmol_{CO₂}/g_{sorbent} (39%) higher than 0.92 mmol_{CO₂}/g_{sorbent} gained in dry conditions at 25 °C. These results suggest that the effect of humidity in warm air has a greater effect than low temperatures of dry winter air. Also, it seems that the enhancing effect of either humidity or cold temperature decreases when the partial pressure of CO₂ increases.

Although at temperatures below the freezing point the humidity level in atmospheric air is low, it cannot be considered totally dry, as levels in the range of 0.28–0.61 vol-% correspond to relative humidity of 100% between –10 °C to 0 °C. Thus, to study the effect of humidity in cold conditions, an experiment with 0.20 vol-% H₂O and 400 ppmv CO₂ was conducted at –10 °C, corresponding to about 70% relative humidity. Determined from the desorption curve of a similar test cycle as in other experiments, the CO₂ adsorption capacity was 1.06 ± 0.03 mmol/g, thus giving the highest capacity for this material determined so far from 400 ppmv CO₂. The difference between dry and humid capacities at –10 °C (0.29 mmol/g or 38%) is not as high as at 25 °C. However, equilibrium was not attained in the case of CO₂ during this test, as the outlet CO₂ concentration after two hours of adsorption was approximately 360 ppm. Therefore, the actual equilibrium result is even higher. The H₂O desorption result was 7.73 ± 0.21 mmol_{H₂O}/g_{sorbent}, being the highest water capacity measured compared to the 2 vol-% H₂O results in Table 2. The ratio of adsorbed H₂O and CO₂ was also the highest in this test, 7.3.

However, with the experimental setup used in this study it was not possible to simulate the dynamic conditions of a real process. Therefore, although humidity increases the CO₂ capacity in all laboratory conditions studied here, problems may arise due to cycling of adsorption and desorption. Especially if the process is operated such that cold air is blown on the hot bed straight after regeneration, possible moisture present in the chamber may freeze on surfaces. To avoid problems caused by this, the bed should always be desorbed to dryness, as was done in the experiments of this study. Whether such conditions cause significant problems or not could best be studied by pilot-scale experimental cycling campaign conducted in winter.

3.2. Working capacity analysis

In this section, the CO₂ equilibrium working capacity is modelled by utilizing the Toth model parameters shown in Table 1. The equilibrium working capacity can be defined as:

$$EWC = q(p_A, T_A) - q(p_R, T_R) \quad (6)$$

where $q(p_A, T_A)$ is the CO₂ loading at CO₂ partial pressure and temperature of adsorption conditions, and $q(p_R, T_R)$ is the CO₂ loading under regeneration conditions [17]. Using the model parameters, matrices of the CO₂ loading were calculated by vectors of temperature and partial pressure of CO₂. By different combinations of temperature and CO₂ partial pressure, the EWC was calculated in different process conditions. Thus, using the EWC matrices, contours in PSA, TSA and TVSA were determined.

In this analysis equilibrium is assumed in adsorption and regeneration phases. In the TSA case, it is assumed that the composition of the feed air is the same in the adsorption phase as in the regeneration phase, therefore this case is isobaric. In PSA and TVSA cases, when modelling higher or lower than normal atmospheric total pressures, the partial pressure of CO₂ was multiplied accordingly, assuming ideal gas. In PSA and TVSA cases, a hypothetical closed system between an adsorption column and a CO₂ storage tank is assumed in the regeneration stage. Impurities are assumed to be removed by vacuum prior to actual desorption. Thus, the partial pressure of CO₂ is assumed to be equal to total pressure in regeneration in PSA and TVSA. Temperature was in the range of –10 °C to 90 °C in dry conditions, and between 25 °C to 90 °C in humid conditions. For adsorption in this analysis, CO₂ partial pressures up to the experimental higher limit of 0.5 mbar were used. Assuming ideal gas behavior, 0.5 mbar would correspond to 12.5 bar compression of air. For simulating the vacuum conditions, the CO₂ partial pressure was set constant to 13 mbar in regeneration, being a reasonable vacuum pressure achievable by industrial vacuum pumps. Because H₂O isotherms were not determined, modelling of the EWC under humid conditions is here limited to isobaric TSA.

Fig. 4 shows that reaching a significant EWC is challenging in dry DAC conditions by isothermal PSA. Either a very high pressure increase of the feed or a very high vacuum in regeneration is required. Because CO₂ partial pressure is equal to the vacuum pressure in regeneration, no EWC can be gained with 13 mbar vacuum pressure if adsorbing from air. To produce EWC of 0.49 mmol_{CO₂}/g_{sorbent}, regeneration pressure of 1×10^{-6} bar is required. If 1 mbar vacuum was possible and the feed was pressurized to 12.5 bar (5 mbar CO₂ partial pressure), only 0.23 mmol_{CO₂}/g_{sorbent} would be gained.

Fig. 5a shows that the highest working capacities in dry isobaric TSA are expected with adsorption slightly above –10 °C in DAC conditions. This is due to the shape of the isotherms at –10 °C and 0 °C, the difference of which was only slight (Fig. 2a). This is also the cause of a small region in Fig. 5a where positive EWC is possible when the regeneration temperature is lower than the adsorption temperature, and

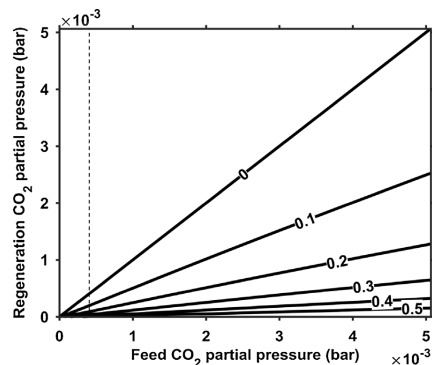


Fig. 4. Contours of modelled equilibrium working capacity (mmol_{CO₂}/g_{sorbent}) in pressure swing adsorption at 25 °C. The dashed line depicts CO₂ partial pressure in air (0.4 mbar).

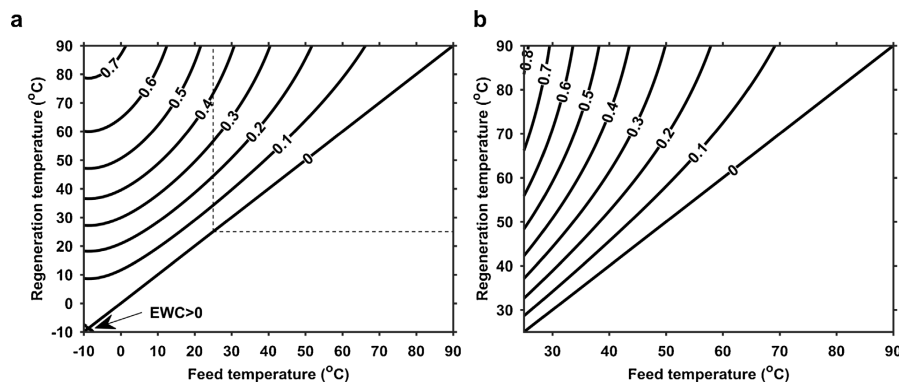


Fig. 5. The contours of modelled equilibrium working capacity ($\text{mmol}_{\text{CO}_2}/\text{g}_{\text{sorbent}}$) in isobaric temperature-swing adsorption at CO_2 partial pressure of 0.4 mbar in a) dry conditions; b) humid conditions with 2 vol-% H_2O . The dashed line segment in a) corresponds to the temperature range in b).

negative EWC is gained when the regeneration temperature is higher than the adsorption temperature. The region is between -10°C to -7.5°C and -10°C to -7.5°C for regeneration and adsorption temperatures, respectively. The EWC level is however very low ($< 0.001 \text{ mmol}_{\text{CO}_2}/\text{g}_{\text{sorbent}}$) in this region. In cold conditions (-10°C to 0°C) every 10°C increase in regeneration temperature in the region $10\text{--}50^\circ\text{C}$ produces $0.1 \text{ mmol}_{\text{CO}_2}/\text{g}_{\text{sorbent}}$ higher EWC. Further increasing the regeneration temperature increases the EWC less substantially. With adsorption below -5°C , regeneration temperature of 50°C leads to EWC of $0.52 \text{ mmol}_{\text{CO}_2}/\text{g}_{\text{sorbent}}$, but capacity of $0.74 \text{ mmol}_{\text{CO}_2}/\text{g}_{\text{sorbent}}$ requires increasing the regeneration temperature up to 90°C . In warm conditions ($20\text{--}30^\circ\text{C}$), a similar pattern is found for regeneration temperatures between 30°C and 50°C . However, the EWC level with a regeneration temperature of 50°C is only $0.19\text{--}0.30 \text{ mmol}_{\text{CO}_2}/\text{g}_{\text{sorbent}}$ in warm adsorption conditions. The highest EWC at 25°C is $0.46 \text{ mmol}_{\text{CO}_2}/\text{g}_{\text{sorbent}}$ when using 90°C in regeneration.

Comparison of Fig. 5a and b shows the strong positive effect of humidity on isobaric TSA working capacity. Almost twice the EWC can be reached in humid conditions with corresponding adsorption and regeneration temperatures. For example, with adsorption at 25°C the maximum EWC in humid isobaric TSA is higher by $0.36 \text{ mmol}_{\text{CO}_2}/\text{g}_{\text{sorbent}}$ (78%) compared to dry conditions. This is the maximum effect of humidity on TSA working capacity in the studied region considering that humidity had the strongest effect on the CO_2 adsorption capacity at the lowest temperature (Fig. 3). The difference is less significant when comparing the EWC gained in humid conditions to the EWC gained in dry cold conditions. However, the maximum humid value is still $0.08 \text{ mmol}_{\text{CO}_2}/\text{g}_{\text{sorbent}}$ (11%) higher than the maximum value in dry cold conditions.

Fig. 5b also shows that much milder regeneration temperatures can be utilized in humid warm conditions ($20\text{--}30^\circ\text{C}$) to gain similar working capacities as in dry warm conditions with regeneration at 90°C . For example, at a regeneration temperature of 50°C , $0.52 \text{ mmol}_{\text{CO}_2}/\text{g}_{\text{sorbent}}$ can be gained in humid conditions with adsorption at 25°C .

Satisfactory EWC levels ($> 0.5 \text{ mmol}_{\text{CO}_2}/\text{g}_{\text{sorbent}}$) can thus be produced with regeneration temperatures as low as $50\text{--}60^\circ\text{C}$ in either dry cold conditions or humid warm conditions. Therefore, low-quality heat could be utilized in regeneration of temperature-swing adsorption.

CO_2 partial pressure was extrapolated with the dry temperature-dependent model to obtain working capacity results in TVSA. As expected, the closed system with 13 mbar vacuum pressure lead to lower working capacities compared to isobaric TSA. Fig. 6 shows that high

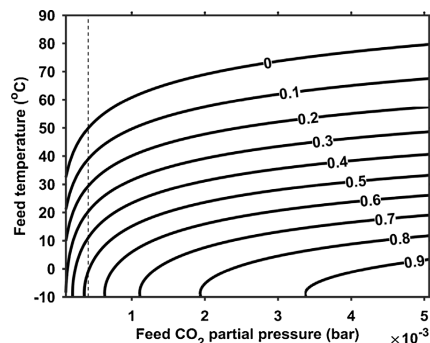


Fig. 6. The contours of modelled equilibrium working capacity ($\text{mmol}_{\text{CO}_2}/\text{g}_{\text{sorbent}}$) in temperature-vacuum-swing adsorption. Regeneration CO_2 partial pressure 13 mbar and temperature 90°C . The dashed line depicts CO_2 partial pressure in air (0.4 mbar).

capacities ($> 0.8 \text{ mmol}_{\text{CO}_2}/\text{g}_{\text{sorbent}}$) are achievable with more than 2 mbar CO_2 partial pressure at -10°C , which corresponds to 5 bar compression of inlet air. EWC obtained at 25°C from air using TVSA ($0.25 \text{ mmol}_{\text{CO}_2}/\text{g}_{\text{sorbent}}$) is 46% lower than for TSA ($0.46 \text{ mmol}_{\text{CO}_2}/\text{g}_{\text{sorbent}}$) with regeneration temperature of 90°C . In the TVSA case, $0.52 \text{ mmol}_{\text{CO}_2}/\text{g}_{\text{sorbent}}$ can be acquired with adsorption temperature between -5°C and -10°C and regeneration temperature of 90°C , which is 30% lower compared to the value obtained using TSA ($0.74 \text{ mmol}_{\text{CO}_2}/\text{g}_{\text{sorbent}}$).

Fig. 7 shows the effect of regeneration temperature and compression of the feed air on the EWC in similar TVSA case as discussed above. For the sake of comparison, contours with two different adsorption temperatures are shown in Fig. 7a and b. It is clearly shown that with warm adsorption conditions (25°C) and low regeneration temperatures ($50\text{--}60^\circ\text{C}$) only small amounts of EWC ($< 0.21 \text{ mmol}_{\text{CO}_2}/\text{g}_{\text{sorbent}}$) can be obtained. With cold adsorption conditions (-9°C), up to $0.54 \text{ mmol}_{\text{CO}_2}/\text{g}_{\text{sorbent}}$ can be produced with moderate compression and 60°C regeneration temperature. However, if the feed air is not compressed, decreasing the regeneration temperature quickly decreases the obtainable EWC below $0.50 \text{ mmol}_{\text{CO}_2}/\text{g}_{\text{sorbent}}$. Thus, without feed compression, it seems that there is little room to adjust the regeneration temperature in TVSA.

When comparing working capacity in TSA and TVSA, it must be

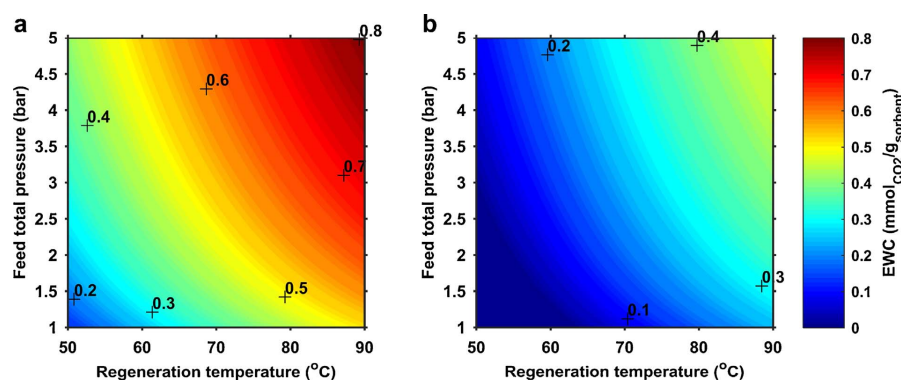


Fig. 7. Influence of regeneration temperature and compression of the feed on modelled equilibrium working capacity ($\text{mmol}_{\text{CO}_2}/\text{g}_{\text{sorbent}}$) in temperature-vacuum-swing adsorption for adsorption temperatures of a) -9°C and b) 25°C . Vacuum pressure is 13 mbar, and feed CO_2 partial pressure is 0.4 mbar at 1 atm.

taken into account that the processes should be considered for different applications. For synthesis processes, air components in the CO_2 produced by TSA may prove problematic [2 p. 53–54]. Therefore, applying temperature swing with vacuuming may be the only viable option for these applications. However, biological applications for CO_2 utilization do not require pure CO_2 . For example, Brillman et al. [24] found that for *Desmodesmus* sp. algae the optimum CO_2 concentration in air was only 1.5%. Brillman et al. were therefore able to utilize direct air capture with thermal swing at only $70\text{--}80^\circ\text{C}$ to produce 2% CO_2 . Considering the penalty to working capacity, TVSA should only be utilized in applications requiring pure CO_2 , whereas in other cases TSA or even TCS should be considered for direct air capture. However, at least for the current adsorbent direct air capture by isothermal PSA does not seem feasible in any case.

4. Conclusions

In this paper, CO_2 isotherms in low partial pressure range were determined to study the effect of different conditions on the performance of polymeric amine-based adsorbent, and to model the equilibrium working capacity in direct air capture. Highest adsorption capacities from dry CO_2 were obtained in cold temperatures (0°C and -10°C). Adding humidity in the gas stream increased the CO_2 capacity from 400 ppmv CO_2 up to 65%. Consequently, the highest experimental capacity of $1.06 \text{ mmol}_{\text{CO}_2}/\text{g}_{\text{sorbent}}$ from 400 ppmv CO_2 was gained in humid cold conditions. However, in a real process humid cold air can cause difficulties. Tests in real atmospheric winter conditions in pilot or process scale are therefore required to prove the applicability of a DAC process to northern Europe winter conditions.

Modelled equilibrium working capacity contours suggest that PSA is not a reasonable process option for DAC with the current sorbent, because EWC levels greater than $0.5 \text{ mmol}_{\text{CO}_2}/\text{g}_{\text{sorbent}}$ could not be achieved without exceeding reasonable boundaries for vacuum pressure. On the other hand, with TSA, EWC levels greater than $0.7 \text{ mmol}_{\text{CO}_2}/\text{g}_{\text{sorbent}}$ were reachable when adsorption conditions were either dry and cold, or warm and humid. Low quality heat at $50\text{--}60^\circ\text{C}$ could also be utilized for TSA to still gain EWC levels above $0.5 \text{ mmol}_{\text{CO}_2}/\text{g}_{\text{sorbent}}$. Comparing dry TSA to dry TVSA with vacuum pressure of 13 mbar, EWC levels were decreased significantly. EWC levels above $0.5 \text{ mmol}_{\text{CO}_2}/\text{g}_{\text{sorbent}}$ with TVSA could only be achieved using 90°C regeneration temperature with adsorption taking place in either cold conditions or from compressed air. Therefore, it is not recommended to decrease the regeneration temperature in TVSA. Based on these results, although TVSA is required for high-purity CO_2

production, TSA can be a more feasible option in applications that only require concentrated CO_2 and can withstand other gas components in air such as N_2 and O_2 .

This analysis considered the performance of different DAC process options only from the view of equilibrium working capacity. The equilibrium working capacity analysis does not take into account the adsorption and desorption rates. Reaching equilibrium working capacities in a DAC process may require too long cycle times to be energetically efficient. The estimation of specific energy requirement from equilibrium working capacity would thus be limited. To estimate the specific energy requirement and to evaluate different DAC process options more comprehensively, in future work also dynamic models will be introduced to support equilibrium-based analysis.

Acknowledgements

This study was conducted as a part of Neo-Carbon Energy and MOPED projects. The Neo-Carbon Energy project is a strategic research opening funded by Tekes, the Finnish Funding Agency for Innovation. The MOPED project is funded by Academy of Finland under grant number 295883. The authors would also like to acknowledge the Tekes-funded SOLETAIR project, in which the production of synthetic fuels using DAC has been demonstrated: <http://www.soletair.fi/>.

Appendix A. Supplementary data

Supplementary data associated with this article can be found, in the online version, at <https://doi.org/10.1016/j.jcou.2017.10.010>.

References

- [1] C.J. Barnhart, M. Dale, A.R. Brandt, S.M. Benson, The energetic implications of curtailing versus storing solar- and wind-generated electricity, *Energy Environ. Sci.* 6 (2013) 2804–2810, <http://dx.doi.org/10.1039/c3ee41973h>.
- [2] M. Lehner, R. Tichler, M. Koppe, H. Steinmüller, *Power-To-Gas: Technology and Business Models*, Springer, 2014, http://dx.doi.org/10.1007/978-3-319-03995-4_1.
- [3] R.T.J. Porter, M. Fairweather, M. Pourkashanian, R.M. Woolley, The range and level of impurities in CO_2 streams from different carbon capture sources, *Int. J. Greenh. Gas Control* 36 (2015) 161–174, <http://dx.doi.org/10.1016/j.ijggc.2015.02.016>.
- [4] A. Kambolis, T.J. Schildhauer, O. Kröcher, CO methanation for synthetic natural gas production, *Chim. Int. J. Chem.* 69 (2015) 608–613, <http://dx.doi.org/10.2533/chimia.2015.608>.
- [5] R. Socolow, M. Desmond, R. Aines, J. Blackstock, O. Bolland, T. Kaarsberg, N. Lewis, M. Mazzotti, A. Pfeffer, K. Sawyer, J. Sirola, B. Smit, J. Wilcox, *Direct Air Capture of CO_2 with Chemicals – A Technology Assessment for the APS Panel on Public Affairs*, APS Physics, 2011.
- [6] E.S. Sanz-Pérez, C.R. Murdock, S.A. Didas, C.W. Jones, Direct capture of CO_2 from

- ambient air, *Chem. Rev.* 116 (2016) 11840–11876, <http://dx.doi.org/10.1021/acs.chemrev.6b00173>.
- [7] S.A. Didas, S. Choi, W. Chaikittisilp, C.W. Jones, Amine-oxide hybrid materials for CO₂ Capture from ambient air, *Acc. Chem. Res.* 48 (2015) 2680–2687, <http://dx.doi.org/10.1021/acs.accounts.5b00284>.
- [8] A. Kumar, D.G. Madden, M. Lusi, K. Chen, E.A. Daniels, T. Curtin, J.J.P. Iv, M.J. Zaworotko, Direct air capture of CO₂ by physisorbent materials, *Angew. Chem. Int. Ed.* 54 (2015) 1–7, <http://dx.doi.org/10.1002/anie.201506952>.
- [9] N.R. Stuckert, R.T. Yang, CO₂ capture from the atmosphere and simultaneous concentration using zeolites and amine-grafted SBA-15, *Environ. Sci. Technol.* 45 (2011) 10257–10264, <http://dx.doi.org/10.1021/es202647a>.
- [10] G. Holmes, K. Nold, T. Walsh, K. Heidele, M.A. Henderson, J. Ritchie, P. Klavins, A. Singh, D.W. Keith, Outdoor prototype results for direct atmospheric capture of carbon dioxide, *Energy Procedia* 37 (2013) 6079–6095, <http://dx.doi.org/10.1016/j.egypro.2013.06.537>.
- [11] A. Wagner, B. Steen, G. Johansson, E. Zanghellini, P. Jacobsson, P. Johansson, Carbon dioxide capture from ambient air using amine-grafted mesoporous adsorbents, *Int. J. Spectrosc.* (2013) 1–8, <http://dx.doi.org/10.1155/2013/690186>.
- [12] S. Choi, J.H. Drese, C.W. Jones, Adsorbent materials for carbon dioxide capture from large anthropogenic point sources, *ChemSusChem* 2 (2009) 796–854, <http://dx.doi.org/10.1002/cssc.200900036>.
- [13] J. Wang, H. Huang, M. Wang, L. Yao, W. Qiao, D. Long, L. Ling, Direct capture of low-concentration CO₂ on mesoporous carbon-supported solid amine adsorbents at ambient temperature, *Ind. Eng. Chem. Res.* 54 (2015) 5319–5327, <http://dx.doi.org/10.1021/acs.iecr.5b01060>.
- [14] C. Gebald, J.A. Wurzbacher, A. Borgschulte, T. Zimmermann, A. Steinfeld, Single-component and binary CO₂ and H₂O adsorption of amine-functionalized cellulose, *Environ. Sci. Technol.* 48 (2014) 2497–2504, <http://dx.doi.org/10.1021/es404430g>.
- [15] H. Sehaqui, M.E. Gálvez, V. Becatini, Y. Cheng Ng, A. Steinfeld, T. Zimmermann, P. Tingaut, Fast and reversible direct CO₂ capture from air onto all-polymer nanofibrillated cellulose/polyethyleneimine foams, *Environ. Sci. Technol.* 49 (2015) 3167–3174, <http://dx.doi.org/10.1021/es504396v>.
- [16] A. Goepfert, M. Czaun, R.B. May, G.K.S. Prakash, G.A. Olah, S.R. Narayanan, Carbon dioxide capture from the air using a polyamine based regenerable solid adsorbent, *J. Am. Chem. Soc.* 133 (2011) 20164–20167, <http://dx.doi.org/10.1021/ja2100005>.
- [17] P.J.E. Harlick, F.H. Tezel, Equilibrium analysis of cyclic adsorption processes: CO₂ working capacities with NaY, *Sep. Sci. Technol.* 40 (2005) 2569–2591, <http://dx.doi.org/10.1080/01496390500283233>.
- [18] J. Elfving, C. Bajamundi, J. Kauppinen, Characterization and performance of direct air capture sorbent, *Energy Procedia* 114 (2017) 6087–6101, <http://dx.doi.org/10.1016/j.egypro.2017.03.1746>.
- [19] D.D. Do, *Adsorption Analysis: Equilibria and Kinetics*, Imperial College Press, London, 1998.
- [20] Z. Chen, S. Deng, H. Wei, B. Wang, J. Huang, G. Yu, Polyethyleneimine-impregnated resin for high CO₂ adsorption: an efficient adsorbent for CO₂ capture from simulated flue gas and ambient air, *ACS Appl. Mater. Interfaces* 5 (2013) 6937–6945, <http://dx.doi.org/10.1021/am400661b>.
- [21] R. Serna-Guerrero, Y. Belmabkhout, A. Sayari, Modeling CO₂ adsorption on amine-functionalized mesoporous silica: 1. a semi-empirical equilibrium model, *Chem. Eng. J.* 161 (2010) 173–181, <http://dx.doi.org/10.1016/j.cej.2010.04.024>.
- [22] R. Veneman, W. Zhao, Z. Li, N. Cai, D.W.F. Brilman, Adsorption of CO₂ and H₂O on supported amine sorbents, *Energy Procedia* 63 (2014) 2336–2345, <http://dx.doi.org/10.1016/j.egypro.2014.11.254>.
- [23] H. Zhang, A. Goepfert, G.K.S. Prakash, G. Olah, Applicability of linear polyethyleneimine supported on nano-silica for the adsorption of CO₂ from various sources including dry air, *RSC Adv.* 5 (2015) 52550–52562, <http://dx.doi.org/10.1039/C5RA05428A>.
- [24] W. Brilman, L. Garcia Alba, R. Veneman, Capturing atmospheric CO₂ using supported amine sorbents for microalgae cultivation, *Biomass Bioenergy* 53 (2013) 39–47, <http://dx.doi.org/10.1016/j.biombioe.2013.02.042>.

Publication III

J. Elfving, J. Kauppinen, M. Jegoroff, V. Ruuskanen, L. Järvinen and T. Sainio
**Experimental comparison of regeneration methods for CO₂ concentration from air
using amine-based adsorbent**

Reprinted with permission from
Chemical Engineering Journal
Vol. 404, pp. 126337, 2021
© 2020, The Authors. Published by Elsevier B.V.



Contents lists available at ScienceDirect

Chemical Engineering Journal

journal homepage: www.elsevier.com/locate/cej

Experimental comparison of regeneration methods for CO₂ concentration from air using amine-based adsorbent



Jere Elfving^{a,*}, Juho Kauppinen^a, Mikko Jegoroff^a, Vesa Ruuskanen^b, Lauri Järvinen^b, Tuomo Sainio^c

^a VTT Technical Research Centre of Finland Ltd., Koivurannantie 1, FI-40101 Jyväskylä, Finland

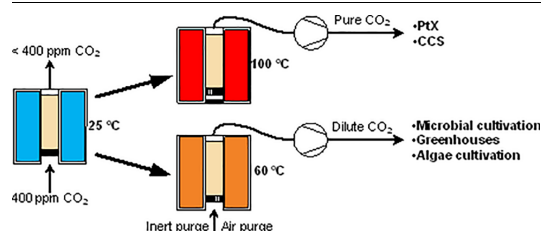
^b Lappeenranta-Lahti University of Technology, School of Energy Systems, Skinnarilankatu 34, FI-53850 Lappeenranta, Finland

^c Lappeenranta-Lahti University of Technology, School of Engineering Science, Skinnarilankatu 34, FI-53850 Lappeenranta, Finland

HIGHLIGHTS

- Only 60 °C coupled with purge gas regenerates amine-based adsorbent by over 85%.
- Coupling purge gas with TVSA is beneficial in terms of CO₂ productivity.
- TVSA with purge gas can have lower specific energy requirement than closed TVSA.
- Using air and 100 °C during regeneration significantly decreases adsorbent capacity.
- Mild temperature TVSA with purge gas is a viable direct air capture process option.

GRAPHICAL ABSTRACT



ARTICLE INFO

Keywords:

Direct air capture
CO₂ adsorption
Adsorbent regeneration
Working capacity
Specific energy requirement
Regenerability

ABSTRACT

Comparison of different regeneration options for direct air capture (DAC) has usually been limited to only consider pure CO₂ production, limiting the process options to e.g. temperature-vacuum swing adsorption (TVSA) or steam-stripping. In this work, detailed experimental comparison is conducted of temperature swing adsorption (TSA/TCSA) and TVSA for DAC. Particularly, TVSA is assessed with air or inert gas purge flow (TVCSA) and without purge flow. The working capacity, regeneration specific energy requirement (SER) and adsorbent regenerability of these processes was compared. For all other studied regeneration options except TVSA without purge flow, over 85% regeneration was obtained already at 60 °C. Isobaric TSA at 60 °C had the lowest regeneration SER of 4.2 MJ/kg_{CO₂}. Coupling TSA with mild vacuum improved desorption rate and increased working capacity from 0.47 to 0.51 mmol_{CO₂}/g_{adsorbent}, requiring 7.5 MJ/kg_{CO₂} for regeneration. Without purge flow, TVSA resulted in only 0.39 mmol_{CO₂}/g_{adsorbent} with the SER of 8.6 MJ/kg_{CO₂} at 100 °C. Due to lower allowable regeneration temperature of 60 °C, mild vacuum TVSA with air flow also had a lower cyclic capacity decrease rate of 0.26%/cycle compared to 0.38%/cycle with TVSA without purge flow at 100 °C. However, using 100 °C with air flow in the TVSA process lead to a significant capacity decrease of 0.6%/cycle. Therefore, using either air or inert purge flow below 100 °C coupled with mild vacuum has benefits over the TVSA process with no inflow in terms of CO₂ productivity, specific energy requirement and adsorbent regenerability. For utilization purposes that require low-concentration CO₂, TVSA with purge flow should thus be considered as a viable regeneration option for direct air capture along with isobaric TSA.

* Corresponding author.

E-mail address: jere.elfving@vtt.fi (J. Elfving).

<https://doi.org/10.1016/j.cej.2020.126337>

Received 28 May 2020; Received in revised form 14 July 2020; Accepted 16 July 2020

Available online 22 July 2020

1385-8947 / © 2020 The Authors. Published by Elsevier B.V. This is an open access article under the CC BY license (<http://creativecommons.org/licenses/by/4.0/>).

1. Introduction

For carbon capture and storage (CCS) or utilization (CCU) purposes, CO₂ capture from flue gases or air has been proposed using various technologies. Aqueous amine solvent-based post-combustion capture (PCC) is a relatively mature technology, but suffers from high heat demand related to the regeneration of the solvent [1,2]. Also, PCC processes based on primary and secondary amines such as monoethanolamine (MEA) may emit amine degradation compounds that are toxic and carcinogenic [3]. Therefore, alternatives such as amino acid salt solutions have been proposed as a more environmentally friendly option to conventional amines [4]. NaOH-based process was the first process type suggested for direct air capture (DAC) [5]. This approach was deemed as highly energy-intensive [6], although pilot-scale results have shown better results for the process type using KOH-solution than the early techno-economic analysis in terms of energy requirement [7]. As an alternative to solvent-based processes, solid adsorbents have been widely studied for both PCC [8–10] and DAC [11]. Solid adsorbent-based DAC has several advantages over the solvent-based solutions such as small unit size and scalability [12], low temperature requirement of usually less than 100 °C [11,13] and fairly simple design, while still being able to produce almost pure CO₂ [11,13].

While physical adsorbents such as activated carbons and metal-organic frameworks (MOF) are reasonable to use in PCC [8,10,14], in DAC they are usually not selective enough, and amine-functionalization of the porous structure is required to obtain higher capacities for the resulting adsorbent [11,15]. CO₂ adsorption capacities for amine-impregnated and amine-grafted adsorbents in PCC conditions (10–15% CO₂) are in the range of 2–5 mmol_{CO₂}/g_{adsorbent} and below 3 mmol_{CO₂}/g_{adsorbent}, respectively [8]. In DAC conditions, amine-impregnated adsorbents usually have 1–2 mmol_{CO₂}/g_{adsorbent}, while for amine-grafted materials the capacities range from 0.1 to even over 2 mmol_{CO₂}/g_{adsorbent} [11]. However, even higher capacities have been obtained in both PCC and DAC conditions, such as 11.8 mmol_{CO₂}/g_{adsorbent} for a mesoporous silica functionalized by surface-initiated amine polymerization from humid 8% CO₂ [16] and 3.89 mmol_{CO₂}/g_{adsorbent} from dry 400 ppm CO₂ for a MOF functionalized with diamines [17]. While a higher CO₂ concentration in PCC leads to higher CO₂ capacities compared to DAC conditions, the difference is not always significant for amine-based adsorbents. For example, a commercial aminoresin Lewatit VP OC 1065 shows fairly steep improvements as a function of CO₂ concentration, having a CO₂ adsorption capacity of 1.06 mmol_{CO₂}/g_{adsorbent} from 400 ppm CO₂, 1.64 mmol_{CO₂}/g_{adsorbent} from 5000 ppm CO₂ at 20 °C [18] and 2.6 mmol_{CO₂}/g_{adsorbent} from 40% CO₂ at 40 °C [19]. However, Lee et al. [20] reported the CO₂ capacities of a diamine-functionalized MOF in dry DAC (0.39 mbar CO₂) and PCC conditions (0.15 bar CO₂) fairly close to each other, being 2.83 and 3.62 mmol_{CO₂}/g_{adsorbent}, respectively. The adsorption capacity of the proprietary aminoresin used in this study has been measured in earlier work [21] to be 0.54 mmol_{CO₂}/g_{adsorbent} in dry DAC conditions and 0.89 mmol_{CO₂}/g_{adsorbent} in humid conditions at 25 °C. It is therefore in the lower end of the reported materials capacity-wise, but is fairly comparable to amine-grafted adsorbents.

Equally important to obtaining a high CO₂ adsorption capacity is regeneration of the adsorbent. One of the most important goals in the regeneration is to maximize CO₂ working capacity, since with low CO₂ capacity the allowable cost of adsorbent drops unrealistically low, making the whole process economically infeasible [22]. While pressure swing adsorption (PSA) may be a viable regeneration option for PCC [10], in DAC this method cannot be used without extensive compression of air or unpractically low vacuum levels [21,23]. Temperature swing adsorption (TSA) is often the method for regeneration of amine-based CO₂ adsorbents in laboratory-scale studies [11]. This method is simple in design, but the disadvantages are that the product CO₂ is diluted and significant oxidative degradation of amine can take place at desorption temperatures slightly above 100 °C [24]. To counter the

oxidative degradation, inert gas can be used instead of air, which can be costly in process scale. An option for using TSA for high-purity CO₂ production is to use pure CO₂ as stripping gas, but in this approach the risk is adsorbent deactivation via urea formation [25,26]. Also, because desorption takes place in a high-concentration CO₂ atmosphere, the working capacity is reduced. A derivative of TSA is steam-stripping, in which saturated steam is used as the inert gas purge and high-purity CO₂ can be produced if water is condensed from the product gas [18,27]. However, a significant drawback in this process is adsorbent deactivation via leaching of the amines [28,29]. This process can also be coupled with vacuum to enhance desorption rate and produce steam at lower than 100 °C temperatures, but leaching of amines by steam remains a problem [30].

Temperature-vacuum swing adsorption (TVSA) process uses coupled vacuum and temperature swing for desorption of CO₂, and can be used to produce near 100% CO₂ from air [13,31]. However, this process reduces the attainable CO₂ working capacity and increases required temperature swing compared to TCSA or TSA [21,23]. This is because in the TVSA process the inlet is closed during desorption to prevent product dilution, which leads to desorption taking place in high-concentration CO₂ atmosphere when CO₂ is produced into the adsorption chamber and the vacuum pump [13,23]. For example, Wurzbacher et al. [23] produced 0.44 mmol_{CO₂}/g_{adsorbent} using TCSA at 90 °C, while using TVSA only produced 0.27 mmol_{CO₂}/g_{adsorbent} with 50 mbar vacuum at 90 °C. With a pilot-scale DAC device using TVSA process, Bajamundi et al. [13] produced only 3.4 kg CO₂ at 80 °C from over 5.6 kg of the CO₂ adsorbed on the aminoresin beds in the best case. Increasing the desorption temperature may help increase the working capacity, but increases energy requirement and the risk of adsorbent thermal degradation. Based on CO₂ isotherms [21], another option for increasing working capacity is to couple air or inert gas flow simultaneously with the TVSA process. Using TVSA coupled with air or inert gas purge has not been proposed for DAC, probably due to assumed high energy requirements of vacuuming and lowered product purity. TVSA with inert gas purge has been compared to steam stripping with vacuum as a regeneration method for DAC in terms of desorption rate [30], but the energy requirement or adsorbent regenerability using this process has not been compared to other options to the authors' best knowledge.

Along with the specific energy requirement and daily working capacity, adsorbent regenerability is one of the most important economic factors of the cyclic DAC process [22]. However, in testing the regenerability of amine-based adsorbents for PCC or DAC applications, cyclic experiments have usually been done with less than 20 cycles [25]. Especially in DAC studies cyclic experiments have been limited with usually less than 10 cycles [32,33], although in some papers over 20 cycles [34] or even 100 cycles [35] have been conducted. From only a few cycles it is hard to deduce anything about the long-term stability of the adsorbent, especially if the uncertainty of the method has not been reported. The long-term regenerability should also be compared between different regeneration options, but the studies comparing regeneration conditions have mainly focused only on degradation mechanisms [19,25,36]. Little to no comparison has been made on the trends of cyclic CO₂ adsorption and desorption capacities in over 20 cycles using different regeneration processes.

Different CO₂ utilization purposes require different CO₂ purities and therefore different DAC process types. High purity of the produced CO₂ is especially important for CO₂ utilization in e.g. Fischer-Tropsch process [37], and may thus require processes such as TVSA. However, many CO₂ utilization purposes exist where there is no need to supply near 100% CO₂, such as greenhouses and microbial and algae cultivation for food or fuels. In greenhouses and especially in closed ones, CO₂ supply is required to not let the CO₂ concentration decrease and reduce plant growth [38]. The use of DAC for greenhouses has been proposed earlier by the use of low-capacity sorbents such as zeolite 13X [39] and alkali metal carbonates [40,41]. Another low-concentration application where DAC has been proposed and tested is microalgae cultivation, in

which Brillman et al. [42] found optimal growth in CO₂ concentration of only 1.5–2%. Also, DAC has been used to supply CO₂ for microbial cultivation to produce edible protein in the Neo-Carbon Food project [43], although the optimal CO₂ concentration for the cultivated microbes is as of yet unknown. With 40–60% capture ratio that is a realistic range for adsorbent based DAC [13], Wilcox et al. [44] estimated the work of separation to rise e.g. from less than around 200 kJ/mol_{CO₂} (4.5 MJ/kg_{CO₂}) to over 550–700 kJ/mol_{CO₂} (12.5–15.9 MJ/kg_{CO₂}) with produced CO₂ purities less than 5% and over 90%, respectively. Thus, these results hint that to lower the cost of DAC, the process should be tailored in terms of required CO₂ purity for each purpose. This requires detailed comparison of all the available regeneration methods and not just the process options that aim to produce pure CO₂.

In this work, an automated and modifiable fixed-bed adsorption-desorption device is used for studying the regeneration options for DAC using temperature-swing adsorption (TSA) and temperature-vacuum swing adsorption (TVSA) processes with and without inlet flow. The purpose of this analysis is to assess whether using regeneration methods with inlet flow such as TSA, leading to low-purity CO₂, show significant working capacity or specific energy requirement benefits compared to the TVSA process without inlet flow during regeneration. Also, combining purge flow such as air or inert gas with the TVSA process is assessed here in DAC conditions using an amine-based adsorbent. Evaluating such process for DAC with amine-based adsorbent using dry air as the purge gas is done here for the first time to the authors' best knowledge. First, the pseudo-equilibrium working capacities are compared for all selected experimental conditions. Then, the working capacity dynamics of these processes are compared, followed by a preliminary assessment of the specific energy requirements. Finally, the progress of cyclic adsorption and desorption capacities are studied over multiple experimental cycles for TCSA and TVSA processes to see the effect of different process options on the regenerability of the amine-based adsorbent.

2. Experimental and calculation methods

2.1. Fixed-bed CO₂ adsorption-desorption setup

The experimental setup used in this study was designed and built in VTT. Schematic of the experimental setup is shown in Fig. 1. The setup has five Bronkhorst mass-flow controllers (MFCs) to reach the wanted inlet gas composition. MFCs 1–3 are mainly used for inert purging gas or air, whereas MFCs 4–5 are mainly used for 100% CO₂, mixtures of CO₂ or air. Fig. 1 shows two different inlet routes to the adsorption column as well as a column bypass route, which are needed e.g. when having to purge the column with N₂ from MFC 1 or 2 while measuring the inlet concentration fed through the column bypass route. Optionally, the inlet gas through inlet route 2 can be humidified, although in this study only dry experiments were done. The inlet gas flow is then led to the adsorption column with two thermocouples. Pressure measurements are located before and after the column. Safety valves are also located before and after the column for the instance of pressure reaching over 6 bar. After the column, the gas flow can be directed through vacuum (< 1 bar) route or overpressure (1–5 bar) route. The total pressure over both routes is controlled by separate Flowserve Kammer pressure control valves either via manual set-point or using the pressure measurement after the column for PID control. At the outlet there are measurements for gas flow rate, humidity, pressure and ppm- and %-scale measurements of CO₂ concentration. All gas flow movements are controlled by 2-way or 3-way magnetic valves.

Fig. 2 shows the structure of the adsorption column, dimensions of the sample chamber and places of the thermocouples. The adsorption column is practically a steel pipe surrounded by a steel jacket, in which cooling or heating liquid flows. The adsorbent sample is placed on the top of a sieve welded into the column and fixed from top by placing quartz wool between the sample and a sieve that is attached to the thermocouple. Temperature of the sample is measured radially from the middle of the sample and axially 10 mm above the lower sieve. Thus, the tip of the thermocouple inside the adsorption column is

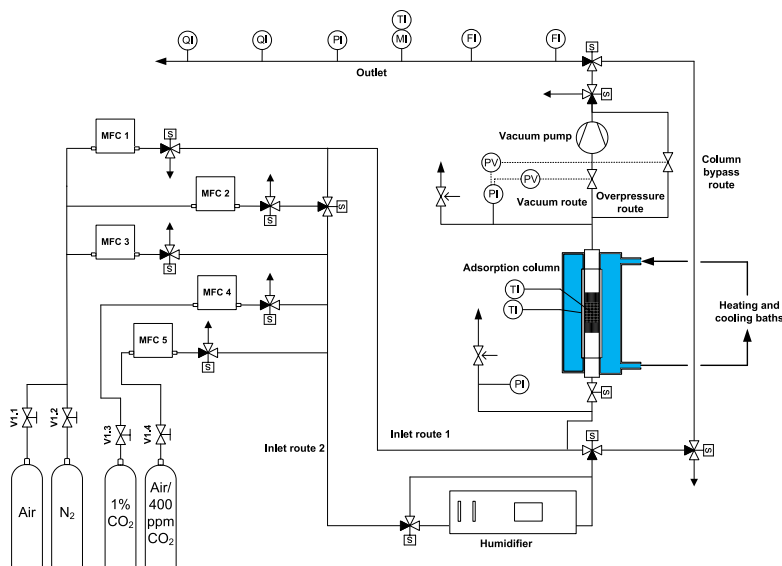


Fig. 1. Experimental setup for fixed-bed adsorption and desorption of CO₂.

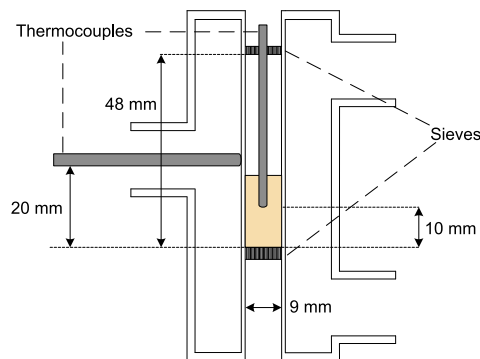


Fig. 2. The adsorption column. The sample in the figure represents volume of 0.5 g of the studied resin.

approximately $\frac{1}{2}$ and $\frac{1}{4}$ from the bottom of the adsorbent for 0.5 g and 1 g samples of the aminoresin used in this study, respectively. Also, temperature is measured from the outer wall of the column 20 mm above the lower sieve. Temperature of the sample is controlled by leading hot or cool liquid to the jacket surrounding the column. For this purpose, separate hot and cool liquid circulations are controlled by two Julabo Corio CD 200F refrigerated/heating circulators. The pass of either cool or hot liquid to the jacket is controlled by 2-way magnetic valves. Currently the operable temperature range is between -10 °C and 105 °C.

All magnetic valves, MFCs, pressure control valves and the vacuum pump are controlled via a LabVIEW-based control and data acquisition program. The program was developed in co-operation between VTT and LUT School of Energy Systems. The program is capable of manual control as well as user-built automatic stepwise sequences. The sequences are built as a spreadsheet that is fed to the program at the start of the experimental run. Each step is run until a fixed time determined in the spreadsheet. The sequence-based control allows to perfectly reproduce the experimental cycles, saves time and resources, and allows to conveniently run continuous cyclic adsorption/desorption. Data sampling rate was 0.5 Hz. Lists of the main components and dimensions of the experimental setup can be found in [Supplementary data](#).

2.2. CO₂ adsorption–desorption experiments

The adsorbent used in this study is a proprietary aminoresin, the characterization of which has been reported earlier in Elfving et al. [45]. In this work, the adsorbent was pre-dried in air at 90 °C. Typically, 0.5 g or 1 g of pre-dried adsorbent was weighed and fixed into the adsorption column with 0.04 g of silica wool below sieve and above the adsorbent. The pre-dried resin had a bulk density of approximately 0.45 g/ml and therefore the sample batch sizes correspond to volumes of 1.1 ml and 2.2 ml. The lower mass was used in cyclic experiments.

For other experiments, to achieve higher dynamic responses during desorption i.e. higher CO₂ concentration and flow-rate peaks, 1 g of adsorbent was used, in which case the sample chamber was almost full. The pre-dried adsorbent still had CO₂ and H₂O adsorbed from air, and in this work these are referred to as pre-adsorbed species.

All experiments were designed beforehand and then run on the sequence-based control in LabVIEW. Because this study focuses on regeneration, the adsorption phase was kept constant in all experimental runs, using 1000 ml/min total flow rate of approximately 400 ppm CO₂ mixed using 1% CO₂ with purities of 3.5 CO₂ and 5.0 N₂, and 5.0 nitrogen at 25 °C. For regeneration, different conditions were used based on each process. The regeneration processes were divided into four steps: 1) ‘Purge 1’ consisting of concentration swing to 0 ppm CO₂ in TCSA coupled with vacuuming in TVCSA, or only vacuuming in TVSA; 2) temperature swing to 60 °C (‘TS 1’); 3) temperature swing to 100 °C (‘TS 2’); 4) concentration swing to 0 ppm CO₂ for TSA and TVSA processes (‘Purge 2’). In TVSA processes with inlet flow, ‘Purge 1’, ‘TS 1’ and ‘TS 2’ were conducted using 400 ppm CO₂. The TVSA process without inlet flow is referred to as ‘closed TVSA’ in this work. Step times were fixed to enable comparison between process steps. The different processes and steps involved are illustrated in [Table 1](#).

For regeneration processes targeting equilibrium or pseudo-equilibrium CO₂ capacities, 1000 ml/min flow rate was used. For studying dynamics more closely, 40 ml/min was chosen as a compromise between fast measurement response and process-relevant flow rate to adsorbent mass ratio. Used vacuum levels were 500 mbar representing a mild-vacuum process, and the minimum achievable at the given flow rate, being 200 mbar with 1000 ml/min and 25 mbar with 40 ml/min. Used inlet gas was either N₂ for concentration swing, 400 ppm CO₂ mixed similarly as in the adsorption phase for 1000 ml/min flow or premixed 400 ppm CO₂ for 40 ml/min flow. Also, compressed dry air with approximately 400 ppm CO₂ was used in the cyclic experiments to find the effect of oxygen on regenerability.

2.3. Calculation of capacities

Here the CO₂ capacities are represented as mmol per gram of dry activated adsorbent, using the mass of pre-adsorbed species (CO₂, H₂O) in each sample to correct the pre-dried sample mass. The mass of pre-adsorbed species was calculated by measuring the CO₂ and H₂O concentrations leaving the sample during initial regeneration phase with 1000 ml/min N₂ flow and heating to 100 °C before the actual experimental cycle. The same procedure was also done without sample, but the resulting masses were negligible, being mainly the contribution of air inside the experimental setup column and lines. The contribution of pre-adsorbed species of the pre-dried sample measured this way was 1.4–2.5 w-%.

Typically, the capacities were calculated based on integration of the CO₂ concentration and flow rate [21,23]. The CO₂ concentration was pressure- and temperature corrected to SATP-conditions (see [Supplementary data](#)). The capacities in the desorption phase were constructed of capacities calculated using ppm-scale measurements when under 5000 ppm, and %-scale measurements when over 5000 ppm. Typically this meant that combination of ppm and %-scale

Table 1

Experimental CO₂ adsorption/desorption processes and step changes. Total inlet gas flow rate was 40 or 1000 ml/min during all phases, except for TVSA closed. For TVSA closed, inlet flow during ‘Purge 2’ was 1000 ml/min.

Process	Adsorption	Time	Purge 1	Time	TS 1	Time	TS 2	Time	Purge 2	Time
TSA	400 ppm CO ₂ , 25 °C	2 h	–	–	60 °C	1 h	100 °C	1 h	0 ppm CO ₂	> 0.5 h
TCSA	400 ppm CO ₂ , 25 °C	2 h	0 ppm CO ₂	0.5 h	60 °C	1 h	100 °C	1.5 h	–	–
TVSA	400 ppm CO ₂ , 25 °C	2 h	400 ppm CO ₂ , vacuum	0.5 h	60 °C	1 h	100 °C	1/1.5 h*	0 ppm CO ₂	> 0.5 h
TVCSA	400 ppm CO ₂ , 25 °C	2 h	0 ppm CO ₂ , vacuum	0.5 h	60 °C	1 h	100 °C	1/1.5 h*	–	–
TVSA closed	400 ppm CO ₂ , 25 °C	2 h	No inflow, vacuum	0.5 h	60 °C	1 h	100 °C	1 h	0 ppm CO ₂	> 0.5 h

* 1 h or 1.5 h for 1000 or 40 ml/min experiments, respectively.

results were used when inlet flow was 40 ml/min in regeneration phase, while only ppm-scale results were used in case of 1000 ml/min flow. Consequently, the results with only 1000 ml/min flow are more accurate than the 40 ml/min results, due to higher uncertainty of the % scale sensor ($< 0.25\% \pm 5\%$ reading) vs. the ppm-scale sensor (± 5 ppm $\text{CO}_2 + 2\%$ reading). Dynamic profiles of both sensors in a 40 ml/min case along with other relevant variable profiles can be found in the [Supplementary data](#).

Instead of measured inlet concentration like in Elfving et al. [21], in this work the inlet concentration was in the form of a step function. In adsorption phase and in desorption with 400 ppm CO_2 inlet flow, the step function value was calculated as a mean value of the concentration of the inlet gas when bypassing the column. Otherwise the step function was set to zero. This is an acceptable approximation, because the effect of dispersion was found to be small, which is shown in a typical experimental cycle in the [Supplementary data](#). However, to gain the most accurate capacity values, the “empty column capacity”, was subtracted from the pseudo-equilibrium and cyclic capacities presented in this work. For the dynamic capacity and specific energy requirement profiles in chapter 3.2, no such correction was used due to very small effect on the final capacity, typically less than 1%.

In closed TVSA runs the calculation was based on only integrating the volume flow rate instead of both volume and concentration due to practical reasons. Due to high amount of vacuumed total volume of about 81 ml compared to the less than 10 ml of produced CO_2 , the produced CO_2 was generated between the adsorption column and the outlet of the vacuum pump. Therefore, no CO_2 was detected in the measurements during this vacuuming stage. The CO_2 capacity of the TVS phase was thus calculated based on the detected flow rate pulse, assuming the pulse detected in the flow-meter is nitrogen. Determination of experimental uncertainty in the calculation of capacities can be found in [Supplementary data](#).

2.4. Calculation of regeneration specific energy requirements

The specific energy requirements calculated in this work are optimal numbers that are based on the experimental dynamic profiles of capacity, temperature, flow rate and vacuum pressure during regeneration phase. The specific energy requirement (SER) at each time point represents the cumulative specific energy requirement calculated based on the experimental vacuum level and temperature at that point, total gas volume flowed until that point, and the desorption CO_2 capacity acquired until that point. The SER values calculated in this work are ideal, and consider no energy losses. The energy requirement of the regeneration phase was calculated by:

$$E_{\text{reg, tot}} = E_{\text{fan}} + E_{s,a} + E_{s,\text{CO}_2} + E_{\text{des,CO}_2} + E_{\text{vac}} \quad (1)$$

where $E_{\text{reg, tot}}$ is the total energy requirement of the regeneration phase, divided into E_{fan} , $E_{s,a}$, E_{s,CO_2} , $E_{\text{des,CO}_2}$ and E_{vac} , which are the energy requirement contributions of air blowers, sensible heat of the adsorbent, sensible heat of adsorbed CO_2 , desorption enthalpy of CO_2 and vacuum, respectively.

The fan energy required to blow air was calculated according to:

$$E_{\text{fan}} = \int \Delta p \dot{V}_{\text{tot}} dt \quad (2)$$

where Δp is the pressure drop along the adsorbent bed and \dot{V}_{tot} is the total flow rate. Pressure drop over the adsorbent bed was here calculated using the Ergun equation:

$$\Delta p = \frac{150 \mu L_{\text{bed}} (1 - \epsilon)^2 v_s}{d_p^2 \epsilon^3} + \frac{1.75 L_{\text{bed}} \rho_g (1 - \epsilon) v_s^2}{d_p \epsilon^3} \quad (3)$$

where μ is the dynamic viscosity, L_{bed} is the length of the adsorbent bed, ϵ is the bed porosity, v_s is the superficial velocity of the gas, d_p is the adsorbent particle size and ρ_g is the gas density [46]. Sensible heat of dry adsorbent was calculated according to:

$$E_{s,a} = m_a c_{p,a} \Delta T \quad (4)$$

where m_a is the mass of adsorbent sample, $c_{p,a}$ is the specific heat capacity of the adsorbent, ΔT is the temperature difference in the temperature swing. Similarly, the sensible heat of desorbed CO_2 could be calculated as:

$$E_{s,\text{CO}_2} = m_{\text{CO}_2} c_{p,\text{CO}_2} \Delta T \quad (5)$$

where m_{CO_2} is the mass of desorbed CO_2 , c_{p,CO_2} is the specific heat capacity of CO_2 . However, the sensible heat of desorbed CO_2 was negligible in the calculations. The desorption heat of CO_2 was calculated using:

$$E_{\text{des,CO}_2} = \int \Delta H \dot{n}_{\text{CO}_2} dt \quad (6)$$

where ΔH is the CO_2 desorption enthalpy, \dot{n}_{CO_2} is the molar flow rate of CO_2 . The energy of the vacuum pump was calculated based on isothermal and irreversible work equation according to [47]:

$$E_{\text{vac}} = -P_{\text{out}} \int \dot{V}_{\text{tot}} dt \left(\frac{P_1}{P_{\text{out}}} - \frac{P_2}{P_{\text{out}}} + \ln \left(\frac{P_2}{P_1} \right) \right) \quad (7)$$

where P_{out} is the mean outlet (ambient) pressure during regeneration, P_1 is the pressure before vacuuming and P_2 is the vacuum pressure at given time point, measured after the column. To gain the specific energy requirements, the total energy requirement in Eq. (1) was then

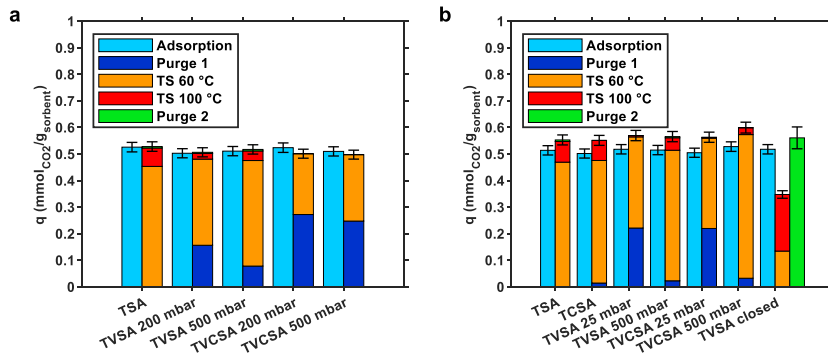


Fig. 3. Adsorption and desorption CO_2 capacities using a) 1000 ml/min; b) 40 ml/min total flow rate in desorption phase. ‘Purge 2’ in TVSA closed resulted from using N_2 purge after the closed TVS step with 1000 ml/min total flow rate. Error bars show the uncertainty.

divided by the produced mass of CO₂ in given experiment. A table with values and/or the source of each constant and variable used for the energy requirement calculations is supplied in the [Supplementary data](#).

3. Results & discussion

3.1. Working capacity comparison

As described in chapter 2.2, adsorption of 400 ppm CO₂ was followed by a stepwise regeneration of the adsorbent. Fig. 3 shows the attained working capacities after each step in the studied regeneration processes. The adsorption capacities are within 0.50–0.53 mmol_{CO₂}/g_{sorbent}. Comparison of Fig. 3b with Fig. 3a shows that the desorption capacities in the runs with 40 ml/min inlet flow are slightly higher than those with 1000 ml/min inlet flow. This difference originates from the different method of capacity calculation in the 40 ml/min results compared to 1000 ml/min results (see chapter 2.3). The total desorption capacities in 1000 ml/min and 40 ml/min cases are in the range of 0.50–0.53 mmol_{CO₂}/g_{sorbent} and 0.55–0.60 mmol_{CO₂}/g_{sorbent}, respectively. Because the total desorption capacities are equal or higher than the adsorption capacities with uncertainty taken into account, regeneration of the adsorbent was complete after each 4-step regeneration process.

Fig. 3a shows that the effect of vacuum level on the initial purge step working capacity is larger for TVSA than for TVCSA in regeneration with 1000 ml/min flow rate. This is an expected result in that the partial pressure of CO₂ for TVCSA is zero with both vacuum levels. In the regeneration experiments with 40 ml/min flow rate, the vacuum level differences were higher. Consequently, Fig. 3b shows much bigger differences in initial purge working capacities between the two vacuum levels compared to Fig. 3a. On the other hand, the equilibrium state in terms of CO₂ partial pressure is still the same in the TVCSA experiments, although the vacuum level is different. The differences in the purge capacities between the two vacuum levels, especially with the lower flow rate, mainly originate from dynamics, since the first step was not carried out until equilibrium.

It is notable that the working capacities are mostly above 90% of the total desorption capacity already with 60 °C temperature swing. Especially in the case of TVCSA with 1000 ml/min inlet flow only negligible desorption was observed at 100 °C. As expected, the largest working capacity differences between 60 °C and 100 °C temperature swing are for TSA, TVCSA and closed TVSA cases. However, even for TSA the working capacities at 60 °C are already 85% and 86% of the total desorption capacity using 40 and 1000 ml/min flow rate during desorption, respectively. However, for closed TVSA the effect of temperature increase from 60 °C to 100 °C is notable, with only 0.13 mmol_{CO₂}/

g_{sorbent} being released at 60 °C. Also, the total desorption capacity released during TVS with closed inlet is only 0.35 mmol_{CO₂}/g_{sorbent}, that is considerably lower than in any of the experiments with inlet flow. Total desorption capacity of 0.56 mmol_{CO₂}/g_{sorbent} in the closed TVSA experiment was obtained when opening the column inlet to nitrogen purge.

The desorption capacity results show that even 60 °C can be used for regeneration with no significant decrease of working capacity compared to 100 °C when using inert purge or 400 ppm CO₂ flow. The result is in line with other studies showing that air [48] or purge flow such as steam under vacuum [30] can be used to fully regenerate amine-based adsorbents even below 100 °C. However, although lower desorption temperatures may be enough to fully regenerate the adsorbent with plenty of time, kinetics may be slowed significantly. Also, possible benefits of coupling vacuum and purging flow during temperature swing steps seem to be minor if only comparing the final working capacities. Therefore, the experimental dynamic capacity profiles are presented below to broaden this comparison to the differences in dynamics. The runs with 1000 ml/min inlet flow in desorption are not discussed in terms of dynamics because the flow rate per mass of adsorbent ratio is too high considering process scale.

3.2. Dynamic capacity profiles

Fig. 4a shows that in TSA regeneration the production of working capacity is delayed at first, taking about 4 min before the capacity starts to increase. This delay could be attributed to three factors: 1) heat transfer from the jacket through the steel wall and into the adsorbent; 2) time spent for the flow to reach the concentration measurements and; 3) CO₂ concentration measurement sensor response time. After this initial period the capacity starts to rise quickly, but slows down eventually, showing that equilibrium state was not reached within 1 h of heating. Fig. 4b shows that the trend for TVCSA is very similar to TSA, except for the start where an almost insignificant amount of CO₂ is removed by cool N₂ purge alone. Therefore, probably even slightly higher capacities are obtainable for TSA/TVCSA already at 60 °C. However, the desorption rates at 60 °C are much slower than at 100 °C. Increasing the temperature to 100 °C quickly increases the working capacities from 0.47 and 0.48 to maximum values of 0.55 and 0.56 mmol_{CO₂}/g_{sorbent} for TSA and TVCSA, respectively. Second purge in TSA increases the working capacity to the same as in TVCSA, 0.56 mmol_{CO₂}/g_{sorbent}. Similar type behavior was reported by Goepfert et al. [48] for a fumed silica-PEI adsorbent, who found that only 12–14% of the adsorption capacity at 25 °C was left at 65 °C. On the other hand, they also reported significantly reduced desorption kinetics below 85 °C, especially at 50–60 °C.

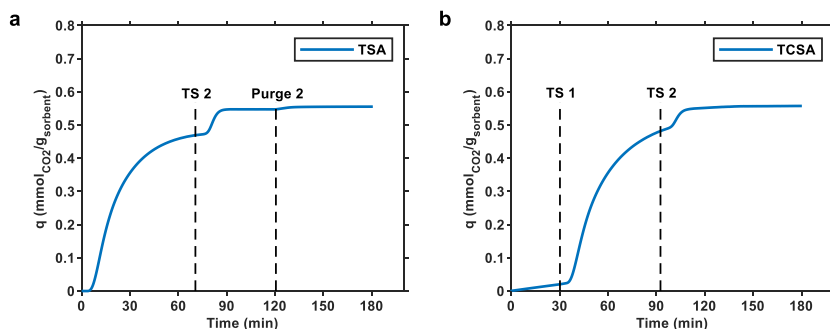


Fig. 4. Desorption capacity profiles using 40 ml/min flow of a) 400 ppm CO₂; b) 0 ppm CO₂. Temperature of the adsorbent was set to 60 °C a) at start; b) after 'TS 1' and to 100 °C after 'TS 2'. 'Purge 2' refers to switching flow from 400 ppm to 0 ppm CO₂.

Fig. 5 shows the clear effect of vacuum level on the capacity profiles of the initial purge phase before any heating. At both vacuum levels, the working capacity is still rising after 30 min of purging, but especially with 25 mbar vacuum a steep rise can be seen for both TVSA and TVCSA processes. The 25 mbar vacuum purge capacity profiles are similar whether using air or nitrogen as purge gas, which can be explained by the very small CO_2 partial pressure difference of 0.01 mbar (10 ppmv) CO_2 in these vacuum conditions. With 500 mbar vacuum the purge-step desorption occurs very slowly for both processes. It was not assessed whether the isothermal purging alone could regenerate the adsorbent fully like it should be based on CO_2 isotherms [21], but it is clear this would take at least several hours, which would probably lead to a very energy-intensive process.

Fig. 5 shows that the first temperature swing to 60 °C leads to a rapid rise of working capacity in both TVSA and TVCSA processes. Comparing the temperature swing steps in TVSA to those of TSA, using even a mild vacuum of 500 mbar clearly enhances the desorption dynamics at 60 °C. For example, with 500 mbar vacuum in TVSA the working capacity gained during 30 min of heating is $0.44 \text{ mmol}_{\text{CO}_2}/\text{g}_{\text{sorbent}}$ while for TSA this is $0.36 \text{ mmol}_{\text{CO}_2}/\text{g}_{\text{sorbent}}$. Using a higher vacuum of 25 mbar leads to even faster desorption. For TVSA with 25 mbar vacuum, over 99% of the maximum capacity at 60 °C is reached within 20 min. However, using 500 mbar vacuum TVSA, this takes over 50 min and equilibrium is not reached after 1 h. The second temperature swing to 100 °C leads to a fast increase of working capacity like in the TSA process. For example, in the TVSA 500 mbar experiment reaching 99% of the maximum capacity at 100 °C takes less than 15 min from the start of 'TS 2'. With the higher vacuum level of 25 mbar the desorption at 100 °C is not significant anymore, which could also be seen from Fig. 3b.

In the closed TVSA runs, initial vacuum purge state produced only negligible amounts of capacity. This is further evidence to proving that isothermal vacuum swing adsorption without compression is not reasonable in DAC [21,23]. Therefore, Fig. 6 shows no observable increase in working capacity in this initial purge phase. However, the temperature swings quickly increase the working capacity with less than 1 min delay, as now there are no delays caused by gas travel time and sensor response like in the other experiments as mentioned above. For TVSA with temperature ramping, it takes about 7 min to reach $0.13 \text{ mmol}_{\text{CO}_2}/\text{g}_{\text{sorbent}}$ in the first temperature swing to 60 °C. A higher temperature increases both working capacity and desorption rate considerably. For TVSA without temperature ramping, the increase from zero to $0.39 \text{ mmol}_{\text{CO}_2}/\text{g}_{\text{sorbent}}$ takes about 5 min. The final working capacity in the temperature ramping case is about $0.04 \text{ mmol}_{\text{CO}_2}/\text{g}_{\text{sorbent}}$ lower than in the experiment without temperature ramp. In addition to experimental uncertainty, the difference may be caused by

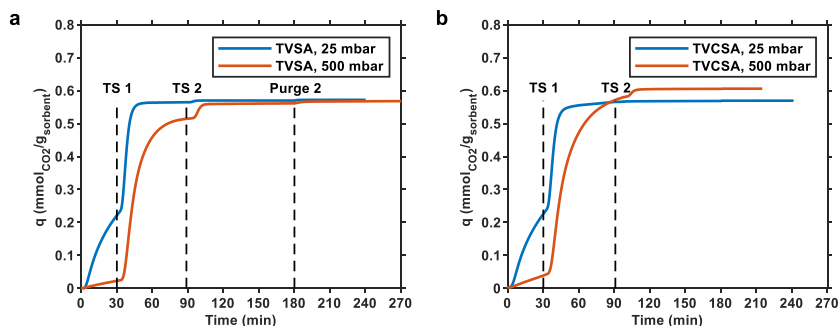


Fig. 5. Desorption capacity profiles under vacuum using 40 ml/min flow of a) 400 ppm CO_2 ; b) 0 ppm CO_2 . The initial period is vacuuming at 25 °C. Temperature of the adsorbent was set to 60 °C after 'TS 1' and to 100 °C after 'TS 2'. 'Purge 2' refers to switching flow to pure N_2 .

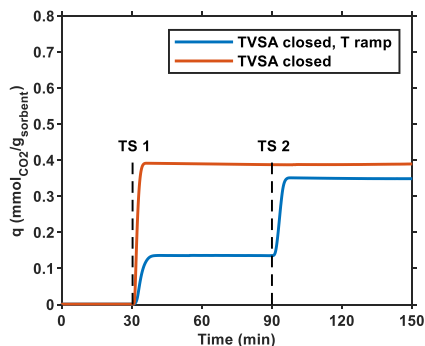


Fig. 6. Desorption capacity profiles in TVSA runs closed from inlet with and without temperature ramping. The initial period is vacuuming at 25 °C. With temperature ramping the temperature of the adsorbent was set to 60 °C after 'TS 1' and to 100 °C after 'TS 2'. Without temperature ramping the temperature was set to 100 °C directly after 'TS 1'.

very slowly continuing desorption of CO_2 after the initial period at 60 °C, in which case the flow rate is under the detection limit of the flow meter.

From the working capacity profiles the promoting effect of high vacuum and temperature on both final working capacities as well as dynamics is clear. Fairly good results were gained with the combination of mild vacuum and temperature as well. In the next chapter, specific energy requirements of TSA and TVSA with 40 ml/min air flow and closed TVSA processes are compared. TVCSA is omitted in the following discussion due to the results being fairly similar with TVSA.

3.3. Specific energy requirements of regeneration

Like explained in chapter 2.4, the following specific energy requirements (SER) are cumulative, taking into account the changes in experimental temperature, vacuum level, CO_2 capacity and gas flow. Because the energy requirement is divided by the capacity obtained until given time point, SER figures start from very high values because the first capacity values are close to zero. Only the contribution of the regeneration phase is taken into account in the following SER numbers because the adsorption phase was similar for all runs. Also, the flow rate during adsorption was 1000 ml/min, resulting in too high flow rate per mass of adsorbent ratio considering process scale. Also, it should be

noted that most of the energy requirement in this analysis resulted from latent heat of adsorbent and vacuum energy. The contribution of fan energy was typically negligible due to short desorption time and low pressure drop over the adsorbent bed of typically below 30 Pa even though the bed height-to-diameter ratio was 4. Therefore, the results of this chapter only apply if the pressure drop is manageable, e.g. below 450 Pa such as in Bajamundi et al. [13], in a tall adsorption column.

The empty volume measured by the flow meter in an evacuation step was 80 ml. The energy consumed in evacuating the empty volume of the system has been subtracted from the total energy requirement in steps where vacuum was used. The reasoning for this is that in a practical process the amount of empty volume in the system would be minimized to reduce capital costs. Also, in a practical process the energy consumed by the evacuation step is only around a few percent of the total energy requirement [49], and therefore shouldn't affect the conclusions of the following specific energy requirement analysis. Working capacity is presented alongside the specific energy values, because working capacity is the meter for estimating daily production of CO₂. Also, working capacity is linked with the produced CO₂ purity in that with a constant flow rate the more produced working capacity within certain time, the higher the average purity is. With 40 ml/min inflow, the purities peaked to 1.3%, 1.8% and 2.7% during the first temperature swing for TSA, TVSA at 500 mbar and TVSA at 25 mbar, respectively. However, the produced CO₂ purities of the current small-scale column do not represent the actual purities in process scale due to high amount of empty volume (see Supplementary data Table S2), and therefore the purities are not shown as a function of time in the following analysis.

Fig. 7 shows that the specific energy requirement for the TSA process reaches the minimum of 4.2 MJ/kg_{CO₂} at the end of the first temperature swing, at which point around 0.47 mmol_{CO₂}/g_{sorbent} has already been reached. After the second temperature swing the SER settles to 6.4 MJ/kg_{CO₂} with working capacity of 0.55 mmol_{CO₂}/g_{sorbent}. Therefore, 17% increase in working capacity (0.08 mmol_{CO₂}/g_{sorbent}) requires about 52% SER increase mainly caused by 40 °C higher desorption temperature. The actual additional SER increase may be even more due to increased cooling demand.

Fig. 8 shows that the SER in TVSA with 25 mbar vacuum rises very sharply with time. After the initial vacuum purge step, rapidly produced CO₂ reduces the SER, reaching the minimum of 26 MJ/kg_{CO₂} at around 43 min. At this point the working capacity is about 0.53 mmol_{CO₂}/g_{sorbent} and still increasing. The working capacity of 0.56 mmol_{CO₂}/g_{sorbent} is reached at 50 min, at which point the SER is already 28 MJ/kg_{CO₂}. After this point the working capacity increases only marginally, but the SER increases significantly. The high specific energy requirement in this case is caused by coupling relatively high vacuum with the fairly high regeneration flow rate to adsorbent mass ratio of 40 l/(min·kg). This ratio e.g. for the DAC demonstration unit reported earlier [13] is around 100 l/(min·kg) during adsorption. The DAC unit total SER was between 44 and 52 MJ/kg_{CO₂} [13], of which the contribution of total regeneration energy has been determined to be around 60–70%. Therefore, the optimal SER values gained in this work with TVSA using 25 mbar vacuum and inlet flow of 40 ml/min are already near the SER of the demonstration unit that is by no means an optimal DAC process. This strongly imparts that the high-vacuum TVSA with purge flow is an unreasonable option for process scale regeneration.

Lowering the vacuum level reduces the SER significantly for TVSA with inlet flow. Although not shown in Fig. 9, after the initial vacuum purge step the SER first increases higher than in TVSA with 25 mbar vacuum, which is caused by slower desorption of CO₂. However, the SER then decreases to the minimum of 6.9 MJ/kg_{CO₂} at 63 min, at which point the reached working capacity is 0.47 mmol_{CO₂}/g_{sorbent}. For comparison, to reach the same working capacity in the TSA required 39% smaller SER. Continuing the desorption until 90 min increases the working capacity to 0.51 mmol_{CO₂}/g_{sorbent} and comes with the SER of 7.5 MJ/kg_{CO₂}. The increase in both SER and working capacity is around 9%. Therefore, in this case stopping the desorption process at SER

minimum cannot be recommended. Although the SER values are significantly lower with the milder vacuum, the process is slowed down. For example, reaching the SER minimum after the start of heating took only 13 min in the 25 mbar process, while for the 500 mbar process this took 33 min. Temperature swing to 100 °C for the 500 mbar TVSA increases the working capacity to 0.56 mmol_{CO₂}/g_{sorbent} and the SER to over 10 MJ/kg_{CO₂}, corresponding to approximately 10% and 33% increases in SER and working capacity, respectively.

Fig. 10 shows that after the initial vacuum purge and first temperature swing, the SER of closed TVSA settles to 11 MJ/kg_{CO₂} with working capacity of 0.14 mmol_{CO₂}/g_{sorbent}. After the second temperature swing the SER settles to 9.4 MJ/kg_{CO₂} with a working capacity of 0.35 mmol_{CO₂}/g_{sorbent}. However, in another experiment where the temperature was directly ramped to 100 °C the maximum working capacity was 0.39 mmol_{CO₂}/g_{sorbent}, with a lower SER value of 8.6 MJ/kg_{CO₂}. Therefore, for closed TVSA using a higher regeneration temperature is not only highly recommended in terms of working capacity, but also beneficial in terms of the specific energy requirement.

Table 2 summarizes the results of working capacity and SER for the different regeneration methods. The results are from a time point after which the desorption rate slows down significantly. With 60 °C and 100 °C temperature swing this point marked reaching 90% and 99% of the maximum working capacity of the step, respectively. With 60 °C temperature swing this point was also at or near the minimum SER value. Also, daily productivities were calculated using these working capacities and the amount of cycles per day. The amount of cycles per day was calculated using a cycle structure with desorption times in Table 2 and fixed adsorption and cooling times of 120 min and 30 min, respectively. In Table 2, TCSA rather than TSA values should be used for comparison of productivities because it has the same initial purge step than other regeneration options. It should also be stressed that comparing the 60 °C productivity values directly with the 100 °C values is not fair in most cases due to temperature ramping in all except 'TVSA closed'. With 60 °C desorption temperature, TCSA has a lower productivity of 0.122 kg_{CO₂}/(kg_{adsorbent}·d) compared to 0.139 and 0.150 kg_{CO₂}/(kg_{adsorbent}·d) for TVSA and TVCSA with mild vacuum, respectively. Because closed TVSA has the lowest working capacities with both desorption temperatures, the productivities are also lower compared to other options, except when using direct heating to 100 °C. Closed TVSA also has higher SER values compared to TSA/TCSA or the mild vacuum TVSA/TVCSA at 60 °C, even with direct heating to 100 °C. On the other hand, the SER values of mild vacuum TVSA/TVCSA are higher than for TSA/TCSA.

Few examples can be found in the literature where purge flow with vacuum is assessed as a regeneration method for amine-based adsorption CO₂ capture. Serna-Guerrero et al. [50] found increased desorption

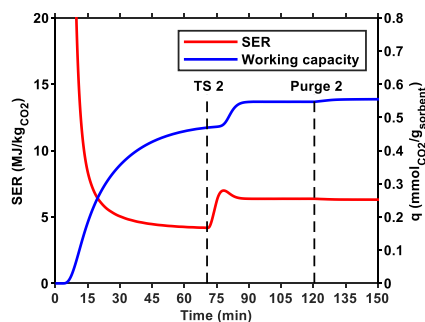


Fig. 7. Dynamic specific energy requirement (SER) and working capacity profiles for temperature-swing adsorption with 40 ml/min total flow rate of 400 ppm CO₂.

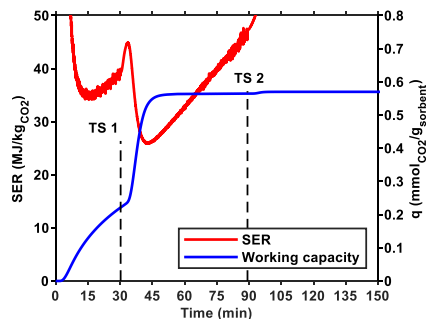


Fig. 8. Dynamic specific energy requirement (SER) and working capacity profiles for temperature-vacuum swing adsorption with 40 ml/min total flow rate of 400 ppm CO_2 and 25 mbar vacuum.

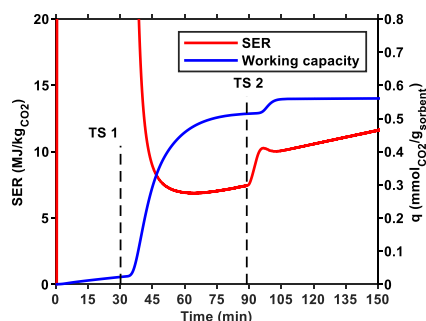


Fig. 9. Dynamic specific energy requirement (SER) and working capacity profiles for temperature-vacuum swing adsorption with 40 ml/min total flow rate of 400 ppm CO_2 and 500 mbar vacuum.

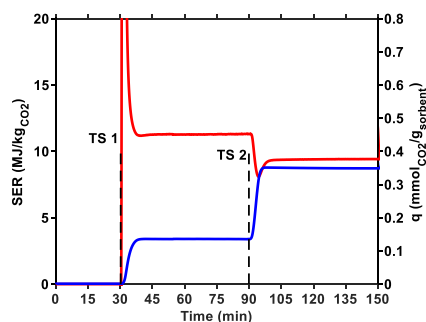


Fig. 10. Dynamic specific energy requirement (SER) and working capacity profiles for temperature-vacuum swing adsorption at 11 mbar vacuum.

rates with an amine-grafted mesoporous silica adsorbent when using purge gas coupled with TVS desorption. On the other hand, Wijesiri et al. [30] found lower desorption rates for the TVS desorption with N_2 purge compared to using steam as purge with a polyethylenimine-functionalized mesoporous silica adsorbent. However, these studies did not assess the total specific energy requirement of the process. Bos et al. [19] compared the regeneration options for biogas upgrading using a

commercial amine-functionalized polystyrene resin, and also considered TVSA case with 100 mbar vacuum and 60 °C with air purge. This option had otherwise low regeneration energy requirement compared to other options, but the contribution of vacuum was almost equal to the heat demand, therefore leading to the highest total energy requirement of the considered cases. Like in this work, Bos et al. found that if only considering SER, TSA/TCSA was the most attractive option.

In a later work, Bos et al. [18] compared regeneration options for DAC, but didn't consider the option with vacuum combined with air or inert gas as purge flow. In dry conditions, they reported much higher SER values for PTSA (closed TVSA) than in this work, even though the reported working capacities of less than 0.25 $\text{mmol}_{\text{CO}_2}/\text{g}_{\text{sorbent}}$ at 91 °C are not very far from those in this work. However, at a higher temperature of 116 °C the SER in Bos et al. was around 10 $\text{MJ}/\text{kg}_{\text{CO}_2}$, which is close to the values in this work. As an interesting result, the specific energy requirement decreased with co-adsorbed water, but increased if steam-stripping was applied. Wurzbacher et al. [31] reported working capacities of 0.32–0.65 $\text{mmol}_{\text{CO}_2}/\text{g}_{\text{sorbent}}$ for (closed) TVSA process in humid conditions in adsorption. They also reported the SER values of 493–640 $\text{kJ}/\text{mol}_{\text{CO}_2}$ (11.2–14.5 $\text{MJ}/\text{kg}_{\text{CO}_2}$), with increase as a function of humidity content in air. Although the boosting effect of humidity on working capacity has been shown also for the sorbent in this work [21], the effect of humidity on SER during regeneration is not obvious, and should be assessed in future work in detail.

Based on the results of chapters 3.2 and 3.3, a mild vacuum TVSA with purge flow doesn't have unreasonably high energy requirement, as long as the purge flow rate is not unreasonably high. Also, even 40 ml/min is high for the sample size of 1 g considering a practical process, and it is possible that significantly lower specific energy requirements are obtainable for TVSA with purging flow when the flow rate and sample size are properly scaled. On the other hand, the boost in productivity from using purge flow during vacuum may still be worth a higher energy requirement. However, it should be taken into account that the differences in productivity between TSA/TCSA vs. TVSA/TVCSA may be smaller in cases where adsorption phase is much longer than desorption, as the effect of desorption rate becomes less significant. On the other hand, the contrary is true for closed TVSA compared to other methods, because less working capacity per cycle means lower daily productivity when the amount of cycles per day is smaller. The results therefore confirm the equilibrium modelling result [21] that the use of closed TVSA process for other utilization purposes than those that require 100% CO_2 cannot be recommended in terms of productivity. Also, because of the lower working capacity, the closed TVSA process has a higher specific energy requirement than the methods utilizing inlet purge flow with or without mild vacuum. However, before assessing adsorbent regenerability, no conclusions of the overall performance of each regeneration method can be made.

3.4. Cyclic experiments

All cyclic experiments done with 19–23 cycles lead to a capacity decrease, which means that the aminoresin studied here started to lose capacity even with a relatively low number of cycles. Significant capacity drops for amine-based adsorbents in only a few cycles have in some cases been measured, while in some cases the sorbent has lasted 100 cycles or more with less than 10% capacity decrease [25]. For example, for the commercial amine-based sorbent Lewatit VP OC 1065, no capacity decrease was noted in 50–60 cycles in various desorption conditions [18,19], and only 4.8% loss of capacity was found in 275 cycles with desorption in N_2 flow at 105 °C [51]. However, in this work, significant differences in adsorbent regenerability were found between the studied regeneration methods.

Fig. 11 shows the slightly decreasing trend of cyclic adsorption and desorption capacity over 19 TCSA cycles. Fig. 11b shows that in adsorption capacities there is a significant drop of about 0.03 mmol/g when comparing the first and third cycles. After this, the adsorption

Table 2

Working capacities, productivities and specific energy requirements at 90% and 99% of maximum working capacity at desorption temperatures of 60 °C and 100 °C, respectively. Total flow rate during desorption was 40 ml/min in other experiments except TVSA closed and TVSA closed with temperature ramp. All other experiments were done using temperature ramping to 60 °C and then 100 °C except TVSA closed. Uncertainties based on uncertainty of capacity.

Regeneration method	WC (mmol _{CO2} /g _{adsorbent})		Time (min)		Productivity (kg _{CO2} /(kg _{adsorbent} d))		Regeneration SER (MJ/kg _{CO2})	
	90%, 60 °C	99%, 100 °C	90%, 60 °C	99%, 100 °C	90%, 60 °C	99%, 100 °C	90%, 60 °C	99%, 100 °C
TSA	0.423 ± 0.014	0.542 ± 0.018	43.9	85.9	0.138 ± 0.005	0.146 ± 0.005	4.5 ± 0.2	6.4 ± 0.2
TCSA	0.434 ± 0.015	0.551 ± 0.019	74.9	117.8	0.122 ± 0.004	0.130 ± 0.004	4.4 ± 0.1	6.3 ± 0.2
TVSA, 25 mbar	0.508 ± 0.017	0.564 ± 0.019 ^a	41.2	72.4	0.168 ± 0.006	0.161 ± 0.005	26.2 ± 0.9	38.4 ± 1.3
TVSA, 500 mbar	0.463 ± 0.016	0.555 ± 0.019	61	102.4	0.139 ± 0.005	0.139 ± 0.005	6.9 ± 0.2	10.0 ± 0.3
TVCSA, 25 mbar	0.509 ± 0.017	0.563 ± 0.019 ^a	42.4	82.5	0.168 ± 0.006	0.153 ± 0.005	26.1 ± 0.9	41.7 ± 1.4
TVCSA, 500 mbar	0.515 ± 0.018	0.599 ± 0.02	68.1	106.7	0.150 ± 0.005	0.148 ± 0.005	6.2 ± 0.2	9.0 ± 0.3
TVSA closed, T ramp	0.122 ± 0.005	0.345 ± 0.014	36.3	95.7	0.042 ± 0.002	0.089 ± 0.004	11.7 ± 0.5	8.5 ± 0.3
TVSA closed	–	0.386 ± 0.016	–	34.6	–	0.133 ± 0.005	–	7.5 ± 0.3

^a Working capacity was already achieved at 60 °C.

capacities show no significant drop for at least the next 6 cycles. The desorption capacities show a fairly steadily decreasing trend rather than a significant drop in the first few cycles. Overall, the drop in capacity over 19 cycles is approximately from 0.57 to 0.53 mmol_{CO2}/g_{adsorbent} (7%) and from 0.53 to 0.51 mmol_{CO2}/g_{adsorbent} (4%) in adsorption and desorption, respectively. The significant drop at the start for the adsorption capacities may be related to incomplete regeneration during the cyclic desorption phases, the effect of which mostly disappears after a couple of cycles, leading to stabilization of the cyclic adsorption capacity. Therefore, the decrease in desorption capacities may be the more reliable metric for long-term regenerability in the TCSA case.

To gain an idea of how high increase of capacity in cyclic conditions can be expected in the worst case, cyclic test was done using TVS regeneration mechanism at 200 mbar vacuum, 100 °C and 1000 ml/min flow of compressed dry air. Fig. 12 shows that the decrease of adsorption and desorption capacities in the TVSA cycles is significant due to coupling high temperature with oxygen-containing gas. Fig. 12a shows an increase in the purge capacities before temperature swing like in the TCSA cycles in Fig. 11, which may be related to positive sensor drift (see Supplementary data). However, both the adsorption and total desorption capacities decrease from approximately 0.52 to 0.45 mmol_{CO2}/g_{adsorbent} (13%) over 22 cycles. It is also notable from these numbers and from Fig. 12b that this time the adsorption and desorption capacities are very close to each other, the maximum difference being within 0.01 mmol_{CO2}/g_{adsorbent}. The main reason for this probably lies in almost complete regeneration due to coupled vacuum and concentration swing with a high flow rate. Also, the method of capacity calculation was changed after the cyclic TCSA run so that instead of measuring the step function (see chapter 2.3) only at the start of the

cyclic experiment, it was measured at the start of each cycle. This method may yield more accurate results and was thus used in the processing of consequent cyclic experiment results.

The same regeneration method was then used for cyclic runs but this time with temperature swing to only 60 °C. Fig. 13 shows that the decrease of both adsorption and total desorption capacities is now only from approximately 0.53 to 0.50 mmol_{CO2}/g_{adsorbent} (6%) in 22–23 cycles. The last three cycles do not show a decreasing trend in capacity, although from this number of cycles it is still too early to draw any conclusions whether the decrease has stabilized or not. Compared to the 100 °C case, the cyclic working capacities with 60 °C temperature swing are slightly smaller, although only less than 10%.

Fig. 14 shows that in the cyclic closed TVSA runs only mild decrease of adsorption capacity took place. It should be noted, that after the closed TVS desorption step the column was purged with nitrogen to fully regenerate the sorbent between each cycle. The desorption capacities shown in Fig. 14a are only the contribution of closed TVS desorption. The adsorption and desorption capacities decrease from approximately 0.53 to 0.49 mmol_{CO2}/g_{adsorbent} (8%) and 0.37 to 0.31 mmol_{CO2}/g_{adsorbent} (16%), respectively. In the desorption capacities most of the decrease takes place between the first two cycles, in which it drops from 0.37 to 0.33 mmol_{CO2}/g_{adsorbent}. If not taking into account this initial drop, the capacity decrease from the second to 23rd cycle is only 0.02 mmol_{CO2}/g_{adsorbent} (6%), being close to the capacity decrease in the adsorption results.

Calculating the desorption capacity loss in percent per cycle, the precise values are 0.18, 0.26, and 0.60%/cycle for TCSA, TVSA with air flow at 60 °C and 100 °C, respectively. For TVSA closed the capacity decrease from adsorption results is 0.38%/cycle. Although the

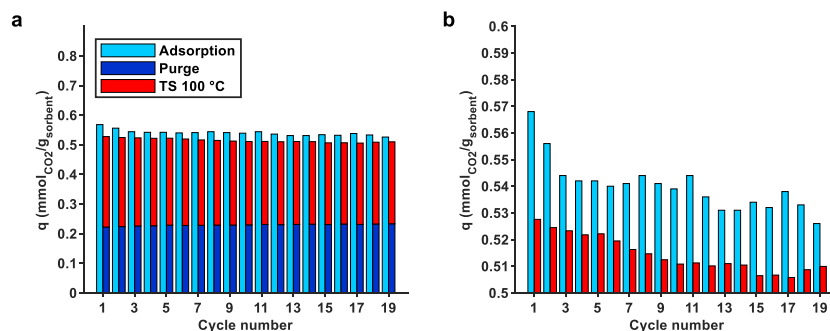


Fig. 11. CO₂ adsorption and desorption capacities in repeated cycles of temperature-concentration swing adsorption. Adsorption was done using 400 ppm CO₂/N₂. b) is a close-up of a).

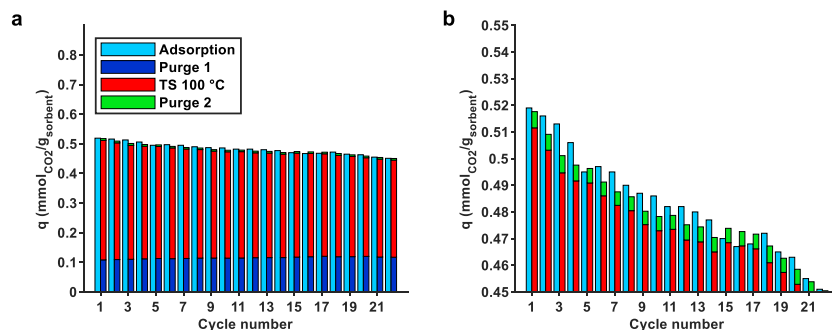


Fig. 12. CO₂ adsorption and desorption capacities in repeated cycles of temperature-vacuum swing adsorption with also concentration swing ('Purge 2') at the end. Adsorption and desorption before 'Purge 2' were done using compressed air. b) is a close-up of a).

desorption in the TCSA process was conducted in inert conditions, the slight capacity decrease is in line with literature, as capacity decrease using inert purge such as N₂ at elevated temperatures has been noted for both impregnated and grafted amine adsorbents [25]. The second-lowest capacity decrease for the 60 °C TVSA with air purge can perhaps be explained with slight oxidative degradation, although for example Bos et al. [19] found that oxidative degradation in a 1 h test did not begin until the temperature was at 70 °C for the commercial Lewatit VP OC 1065. The largest capacity decrease for TVSA with air flow at 100 °C imparts significant oxidative degradation taking place. This is because the capacity loss is much higher than in the 100 °C TCSA cycles, which are devoid of air during desorption.

In the case of the closed TVSA process, no oxygen should be present during desorption due to evacuation of the adsorption column, but the cyclic capacity loss is still higher than in TVSA with air flow at 60 °C. The stability of an amine-functionalized nanofibrillated cellulose sorbent was studied in 100 cycles of closed TVSA cycles by Gebald et al. [35], who reported only 5% of capacity decrease, although at a lower temperature of 90 °C. They also reported that in TVSA operation the degradation was attributed to loss of amines and formation of amides or imides. However, it was unclear whether both were the cause of residual oxygen in the system, or that loss of amines could occur by thermal degradation only. In any case, it seems that degradation of amine-functionalized sorbents cannot be avoided with the closed TVSA method, since lowering the desorption temperature is not a reasonable option due to lowered working capacities.

Based on the working capacity and specific energy requirement

results of this study, regeneration options that utilize purge flow are more flexible in terms of regeneration temperature than the closed TVSA method. To avoid the loss of capacity, the regeneration temperature should be maintained well below 100 °C. In this regard, the mild vacuum TVSA process coupled with purge flow and low temperature seems promising in terms of all studied aspects: working capacity, specific energy requirement and adsorbent regenerability. However, even in mild desorption conditions the cyclic capacity drops per cycle predict only a few hundred cycles before all of the capacity is lost, while in practice the sorbent should withstand thousands if not tens of thousands of cycles with realistic adsorbent costs [22]. On the other hand, it is not known whether the capacity drop follows a linear trend, stabilizes at some point or even accelerates. Also, in inert conditions or in vacuum, the actual mechanism for degradation is less obvious than in the presence of air, and it is not known if for example the vacuum level has an effect on the loss of capacity along with temperature. Therefore, further work is required in cyclic process comparison that takes into account these aspects as well.

4. Conclusions

In this study, a detailed experimental comparison of regeneration methods for CO₂ capture from air was made using an amine-functionalized adsorbent. The experiments were conducted with an automated fixed-bed CO₂ adsorption and desorption device. Especially, the focus was in comparing methods that produce low-purity CO₂ with closed inlet TVSA that produces pure CO₂. The working capacity, dynamics of

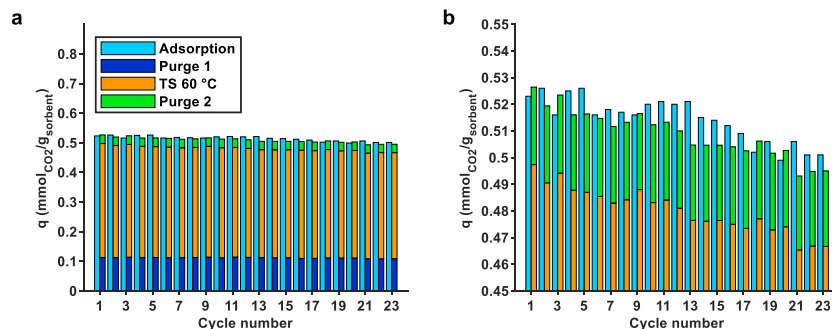


Fig. 13. CO₂ adsorption and desorption capacities in repeated cycles of temperature-vacuum swing adsorption with also concentration swing ('Purge 2') at the end. Adsorption and desorption before 'Purge 2' were done using compressed air. b) is a close-up of a).

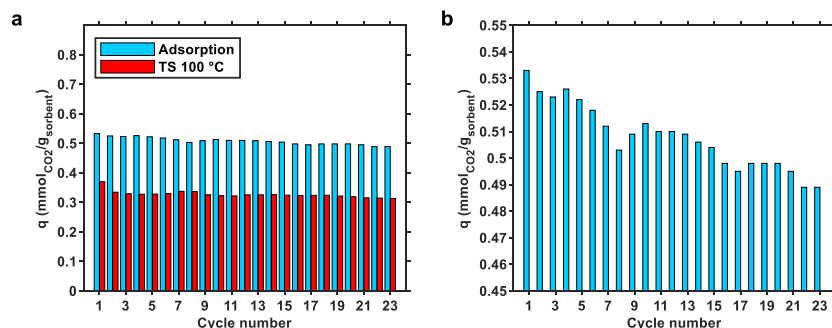


Fig. 14. CO₂ adsorption and desorption capacities in repeated cycles of temperature-vacuum swing adsorption with closed inlet. Adsorption was done using compressed air. After 'TS 100 °C' the sample was fully regenerated by maintaining temperature at 100 °C and purging with nitrogen under vacuum. b) is a close-up of a).

desorption and specific energy requirement were evaluated for TSA, TCSA and TVSA with or without purge flow. Also, regenerability in TCSA and TVSA processes with and without purge flow was studied over 19–23 adsorption and desorption cycles. Coupling vacuum and temperature swing with inlet flow has not been assessed as a regeneration method for DAC in detail before.

Working capacity comparison showed that TSA/TCSA at 60 °C is sufficient to reach 85–86% regeneration, while coupling purge flow with vacuum in TVSA/TVCSA leads to over 90% regeneration. However, using closed TVSA process with no inlet flow left the adsorbent with significant residual loading even at 100 °C. The lowest minimum regeneration specific energy requirement of 4.2 MJ/kg_{CO₂} was achieved with isobaric TSA at 60 °C with the working capacity of 0.47 mmol_{CO₂}/g_{adsorbent}. TVSA at 25 mbar with air flow gave high regeneration SER of over 26 MJ/kg_{CO₂}. However, utilizing a mild vacuum of 500 mbar lead to only 7.5 MJ/kg_{CO₂} with working capacity of 0.51 mmol_{CO₂}/g_{adsorbent}. The TVSA process with no inlet flow had the regeneration SER of 8.6 MJ/kg_{CO₂} with the maximum achievable capacity of only 0.39 mmol_{CO₂}/g_{adsorbent}.

Determination of dynamic working capacity allowed the calculation of daily productivities, which with 60 °C regeneration temperature were 0.122 and 0.150 kg_{CO₂}/(kg_{adsorbent}·d) for TCSA and 500 mbar TVCSA with purge flow, respectively. TVSA with air flow at 500 mbar had a slightly lower productivity than TVCSA of 0.139 kg_{CO₂}/(kg_{adsorbent}·d). The productivity for TVSA with no inlet flow was 0.133 kg_{CO₂}/(kg_{adsorbent}·d) at 100 °C, being lower than for the regeneration options utilizing vacuum coupled with purge flow. In cyclic adsorption/desorption tests the current adsorbent showed a significant capacity loss of 0.6% per cycle at 100 °C with vacuum and air flow. Even with air evacuated out, a capacity loss of 0.38% per cycle was found for the closed inlet TVSA process. Lowering the desorption temperature to 60 °C was highly beneficial for the TVSA method with air flow, because the capacity loss was then only 0.26% per cycle, while still over 90% regeneration was maintained.

The results of this study impart that TVSA coupled with air or inert gas purge flow has clear productivity benefits compared to either isobaric TSA/TCSA or the closed inlet TVSA process. While coupling high vacuum with purge flow leads to unreasonably high energy consumption, mild vacuum can be used to keep the SER lower than in the TVSA process with no inlet flow. The lowest possible specific energy requirements can be obtained using isobaric TSA/TCSA. Flow from the inlet side allows a low regeneration temperature of 60 °C, which cannot be achieved with the closed TVSA process due to drastically reduced working capacity. Even though the column is evacuated of air in the closed TVSA process, degradation of the adsorbent cannot be avoided if even moderate working capacity has to be achieved. Consequently,

mild vacuum TVSA with air flow at 60 °C leads to a better regenerability of the adsorbent. Overall, mild vacuum and temperature TVSA/TVCSA coupled with purge flow seems a viable option for low-concentration CO₂ production from air. The low regeneration temperature also allows the use of process waste heat or district heating in this process or in TSA/TCSA. Therefore, in applications such as greenhouses or microbial and algae cultivation, TSA, TCSA or these coupled with mild vacuum should be the preferred options to the closed TVSA process.

The current study is however limited only to dry conditions with reasonable boundaries for temperature and an upper limit for the flow-rate. In future studies, productivity and specific energy requirement should be assessed as a function of temperature and flow-rate, which could be achieved e.g. by combining experimental work with dynamic modelling. Also, the process scale limitations related to heat transfer, vacuum pumps and purge gas cost should be taken into account. The effect of humidity on process dynamics and specific energy requirement also needs to be evaluated. Adsorbent regenerability should also be studied with a wider set of conditions and even more cycles. Particularly, the different modes of TSA and TVSA should be compared with the steam-stripping method in terms of specific energy requirement and adsorbent regenerability. Also, it should be confirmed whether long-term exposure to desorption conditions or repeated shift between adsorption and desorption conditions is the main driver for degradation. This information would help in deciding whether to maximize daily productivity by maximizing capacity per cycle or by minimizing the cycle duration.

Declaration of Competing Interest

The authors declare that they have no known competing financial interests or personal relationships that could have appeared to influence the work reported in this paper.

Acknowledgements

This study was conducted as a part of projects funded by Academy of Finland under grant numbers 295883 and 329312.

Appendix A. Supplementary data

Supplementary data to this article can be found online at <https://doi.org/10.1016/j.cej.2020.126337>.

References

- [1] Y. Wang, L. Zhao, A. Otto, M. Robinus, D. Stolten, A review of post-combustion CO₂ capture technologies from coal-fired power plants, *Energy Proc.* 114 (2017) 650–665, <https://doi.org/10.1016/j.egypro.2017.03.1209>.
- [2] W. Zhang, H. Liu, Y. Sun, J. Cakstins, C. Sun, C.E. Snape, Parametric study on the regeneration heat requirement of an amine-based solid adsorbent process for post-combustion carbon capture, *Appl. Energy* 168 (2016) 394–405, <https://doi.org/10.1016/j.apenergy.2016.01.049>.
- [3] X. Chen, G. Huang, C. An, Y. Yao, S. Zhao, Emerging N-nitrosamines and N-nitramines from amine-based post-combustion CO₂ capture – A review, *Chem. Eng. J.* 335 (2018) 921–935, <https://doi.org/10.1016/j.cej.2017.11.032>.
- [4] Z. Zhang, Y. Li, W. Zhang, J. Wang, M.R. Soltanian, A.G. Olabi, Effectiveness of amino acid salt solutions in capturing CO₂: A review, *Renew. Sustain. Energy Rev.* 98 (2018) 179–188, <https://doi.org/10.1016/j.rser.2018.09.019>.
- [5] D.W. Keith, M. Ha-Duong, J.K. Stolaroff, Climate strategy with CO₂ capture from the air, *Clim. Change* 74 (2006) 17–45, <https://doi.org/10.1007/s10584-005-9026-x>.
- [6] R. Socolow, M. Desmond, R. Aines, J. Blackstock, O. Bolland, T. Kaarsberg, N. Lewis, M. Mazzotti, A. Pfeffer, K. Sawyer, J. Sirola, B. Smit, J. Wilcox, Direct air capture of CO₂ with chemicals – A technology assessment for the APS Panel on Public Affairs, *APS Phys.* (2011).
- [7] D.W. Keith, G. Holmes, D. St. K.H. Angelo, A process for capturing CO₂ from the atmosphere, *Joule* 2 (2018) 1573–1594, <https://doi.org/10.1016/j.joule.2018.05.006>.
- [8] S. Choi, J.H. Drese, C.W. Jones, Adsorbent materials for carbon dioxide capture from large anthropogenic point sources, *ChemSusChem* 2 (2009) 796–854, <https://doi.org/10.1002/cssc.200900036>.
- [9] S.Y. Lee, S.J. Park, A review on solid adsorbents for carbon dioxide capture, *J. Ind. Eng. Chem.* 23 (2015) 1–11, <https://doi.org/10.1016/j.jiec.2014.09.001>.
- [10] A.E. Creamer, B. Gao, Carbon-based adsorbents for postcombustion CO₂ capture: A critical review, *Environ. Sci. Technol.* 50 (2016) 7276–7289, <https://doi.org/10.1021/acs.est.6b00627>.
- [11] E.S. Sanz-Pérez, C.R. Murdock, S.A. Didas, C.W. Jones, Direct capture of CO₂ from ambient air, *Chem. Rev.* 116 (2016) 11840–11876, <https://doi.org/10.1021/acs.chemrev.6b00173>.
- [12] Climeworks CO₂ capture plant, (2020). <https://www.climeworks.com/our-products/> (accessed February 21, 2020).
- [13] C.J.E. Bajamundi, J. Koponen, V. Ruuskanen, J. Elfving, A. Kosonen, J. Kauppinen, J. Ahola, C.J.E. Bajamundi, J. Koponen, V. Ruuskanen, J. Elfving, A. Kosonen, J. Kauppinen, J. Ahola, Capturing CO₂ from air: Technical performance and process control improvement, *J. CO₂ Util.* 30 (2019) 232–239, <https://doi.org/10.1016/j.jcou.2019.02.002>.
- [14] K. Sumida, D.L. Rogow, J.A. Mason, T.M. McDonald, E.D. Bloch, Z.R. Herm, T.H. Bae, J.R. Long, Carbon dioxide capture in metal-organic frameworks, *Chem. Rev.* 112 (2012) 724–781, <https://doi.org/10.1021/cr2003272>.
- [15] X. Shi, H. Xiao, H. Azarabadi, J. Song, X. Wu, X. Chen, K.S. Lackner, Sorbents for the direct capture of CO₂ from ambient air, *Angew. Chem. Int. Ed.* 59 (2020) 6984–7006, <https://doi.org/10.1002/anie.201906756>.
- [16] G. Qi, L. Fu, E.P. Giannelis, Sponges with covalently tethered amines for high-efficiency carbon capture, *Nat. Commun.* 5 (2014) 1–7, <https://doi.org/10.1038/ncomms6796>.
- [17] P.Q. Liao, X.W. Chen, S.Y. Liu, X.Y. Li, Y.T. Xu, M. Tang, Z. Rui, H. Ji, J.P. Zhang, X.M. Chen, Putting an ultrahigh concentration of amine groups into a metal-organic framework for CO₂ capture at low pressures, *Chem. Sci.* 7 (2016) 6528–6533, <https://doi.org/10.1039/c6sc00936d>.
- [18] M.J. Bos, S. Pietersen, D.W.F.F. Brilman, Production of high purity CO₂ from air using solid amine sorbents, *Chem. Eng. Sci.* 2 (2019) 100020, <https://doi.org/10.1016/j.ces.2019.100020>.
- [19] M.J. Bos, V. Kroeze, S. Sutanto, D.W.F. Brilman, Evaluating regeneration options of solid amine sorbent for CO₂, *Ind. Eng. Chem. Res.* 57 (2018) 11141–11153, <https://doi.org/10.1021/acs.iecr.8b00768>.
- [20] W.R. Lee, S.Y. Hwang, D.W. Ryu, K.S. Lim, S.S. Han, D. Moon, J. Choi, C.S. Hong, Diamine-functionalized metal-organic framework: exceptionally high CO₂ capacities from ambient air and flue gas, ultrafast CO₂ uptake rate, and adsorption mechanism, *Energy Environ. Sci.* 7 (2014) 744–751, <https://doi.org/10.1039/c3ee42328j>.
- [21] J. Elfving, C. Bajamundi, J. Kauppinen, T. Sainio, Modelling of equilibrium working capacity of PSA, TSA and TVSA processes for CO₂ adsorption under direct air capture conditions, *J. CO₂ Util.* 22 (2017) 270–277, <https://doi.org/10.1016/j.jcou.2017.10.010>.
- [22] H. Azarabadi, K.S. Lackner, A sorbent-focused techno-economic analysis of direct air capture, *Appl. Energy* 250 (2019) 959–975, <https://doi.org/10.1016/j.apenergy.2019.04.012>.
- [23] J.A. Wurzbacher, C. Gebald, A. Steinfeld, Separation of CO₂ from air by temperature-vacuum swing adsorption using diamine-functionalized silica gel, *Energy Environ. Sci.* 4 (2011) 3584–3592, <https://doi.org/10.1039/c1ee01681d>.
- [24] A. Ahmadinezhad, A. Sayari, Oxidative degradation of silica-supported poly-ethylenimine for CO₂ adsorption: insights into the nature of deactivated species, *PCP* 16 (2014) 1529–1535, <https://doi.org/10.1039/c3cp53928h>.
- [25] M. Jahandar Lashaki, S. Khavari, A. Sayari, Stability of amine-functionalized CO₂ adsorbents: A multifaceted puzzle, *Chem. Soc. Rev.* 48 (2019) 3320–3405, <https://doi.org/10.1039/c8cs00877a>.
- [26] W. Buijs, Direct air capture of CO₂ with an amine resin: a molecular modeling study of the deactivation mechanism by CO₂, *Ind. Eng. Chem. Res.* 58 (2019) 14705–14708, <https://doi.org/10.1021/acs.iecr.9b02637>.
- [27] W. Li, S. Choi, J.H. Drese, M. Hornbostel, G. Krishnan, P.M. Eisenberger, C.W. Jones, Steam-stripping of supported amine-based CO₂ adsorbents, *ChemSusChem* 3 (2010) 899–903, <https://doi.org/10.1002/cssc.201000131>.
- [28] M.A. Sakwa-Novak, C.W. Jones, Steam induced structural changes of a poly(ethylenimine) impregnated γ -alumina sorbent for CO₂ extraction from ambient air, *ACS Appl. Mater. Interfaces* 6 (2014) 9245–9255, <https://doi.org/10.1021/am501500q>.
- [29] W. Chaikittisilp, H.J. Kim, C.W. Jones, Mesoporous alumina-supported amines as potential steam-stable adsorbents for capturing CO₂ from simulated flue gas and ambient air, *Energy Fuels* 25 (2011) 5528–5537, <https://doi.org/10.1021/ef201224r>.
- [30] R.P. Wijesiri, G.P. Knowles, H. Yeasmin, A.F.A. Hoadley, A.L. Chaffee, Desorption process for capturing CO₂ from air with supported amine sorbent, *Ind. Eng. Chem. Res.* 58 (2019) 15606–15618, <https://doi.org/10.1021/acs.iecr.9b03140>.
- [31] J.A. Wurzbacher, C. Gebald, N. Piatkowski, A. Steinfeld, Concurrent separation of CO₂ and H₂O from air by a temperature-vacuum swing adsorption/desorption cycle, *Environ. Sci. Technol.* 46 (2012) 9191–9198.
- [32] S. Choi, M.L. Gray, C.W. Jones, Amine-tethered solid adsorbents coupling high adsorption capacity and regenerability for CO₂ capture from ambient air, *ChemSusChem* 4 (2011) 628–635, <https://doi.org/10.1002/cssc.201000355>.
- [33] L.A. Darunte, A.D. Oetomo, K.S. Walton, D.S. Sholl, C.W. Jones, Direct air capture of CO₂ using amine functionalized MIL-101(Cr), *ACS Sustain. Chem. Eng.* 4 (2016) 5761–5768, <https://doi.org/10.1021/acsuschemeng.6b01692>.
- [34] A.R. Sujan, S.H. Pang, G. Zhu, C.W. Jones, R.P. Lively, Direct CO₂ capture from air using poly(ethylenimine)-loaded polymer/silica fiber sorbents, *ACS Sustain. Chem. Eng.* 7 (2019) 5264–5273, <https://doi.org/10.1021/acsuschemeng.8b06203>.
- [35] C. Gebald, J.A. Wurzbacher, P. Tingaut, A. Steinfeld, Stability of amine-functionalized cellulose during temperature-vacuum-swing cycling for CO₂ capture from air, *Environ. Sci. Technol.* 47 (2013) 10063–10070, <https://doi.org/10.1021/es401731p>.
- [36] Q. Yu, J.D.P. Delgado, R. Veneman, D.W.F. Brilman, Stability of a benzyl amine based CO₂ capture adsorbent in view of regeneration strategies, *Ind. Eng. Chem. Res.* 56 (2017) 3259–3269, <https://doi.org/10.1021/acs.iecr.6b04645>.
- [37] F. Vidal Vázquez, J. Koponen, V. Ruuskanen, C. Bajamundi, A. Kosonen, P. Simell, J. Ahola, C. Friund, J. Elfving, M. Reinikainen, N. Heikkinen, J. Kauppinen, P. Pierratini, Power-to-X technology using renewable electricity and carbon dioxide from ambient air: SOLETAIR proof-of-concept and improved process concept, *J. CO₂ Util.* 28 (2018) 235–246, <https://doi.org/10.1016/j.jcou.2018.09.026>.
- [38] H.P. Kläring, C. Hauschild, A. Heißner, B. Bar-Yosef, Model-based control of CO₂ concentration in greenhouses at ambient levels increases cucumber yield, *Agric. For. Meteorol.* 143 (2007) 208–216, <https://doi.org/10.1016/j.agrformet.2006.12.002>.
- [39] J. Bao, W.-H. Lu, J. Zhao, X.T. Bi, Greenhouses for CO₂ sequestration from atmosphere, *Carbon Resour. Convers.* 1 (2018) 183–190, <https://doi.org/10.1016/j.crccon.2018.08.002>.
- [40] R. Rodríguez-Mosqueda, J. Rutgers, E.A. Bramer, G. Brem, Low temperature water vapor pressure swing for the regeneration of adsorbents for CO₂ enrichment in greenhouses via direct air capture, *J. CO₂ Util.* 29 (2019) 65–73, <https://doi.org/10.1016/j.jcou.2018.11.010>.
- [41] R. Rodríguez-Mosqueda, E.A. Bramer, G. Brem, CO₂ capture from ambient air using hydrated Na₂CO₃ supported on activated carbon honeycombs with application to CO₂ enrichment in greenhouses, *Chem. Eng. Sci.* 189 (2018) 114–122, <https://doi.org/10.1016/j.ces.2018.05.043>.
- [42] W. Brilman, L. Garcia Alba, R. Veneman, Capturing atmospheric CO₂ using supported amine sorbents for microalgae cultivation, *Biomass Bioenergy* 53 (2013) 39–47, <https://doi.org/10.1016/j.biombioe.2013.02.042>.
- [43] Neo-Carbon Food, (2020). <http://neocarbonfood.fi/> (accessed March 4, 2020).
- [44] J. Wilcox, P.C. Psarras, S. Liguori, Assessment of reasonable opportunities for direct air capture, *Environ. Res. Lett.* 12 (2017) 065001, <https://doi.org/10.1088/1748-9326/aa66e5>.
- [45] J. Elfving, C. Bajamundi, J. Kauppinen, Characterization and performance of direct air capture sorbent, *Energy Proc.* 114 (2017) 6087–6101, <https://doi.org/10.1016/j.egypro.2017.03.1746>.
- [46] M.S. Shafeyan, W.M.A.W. Daud, A. Shamiri, A review of mathematical modeling of fixed-bed columns for carbon dioxide adsorption, *Chem. Eng. Res. Des.* 92 (2014) 961–988, <https://doi.org/10.1016/j.cherd.2013.08.018>.
- [47] A.R. Kulkarni, D.S. Sholl, Analysis of equilibrium-based TSA processes for direct capture of CO₂ from air, *Ind. Eng. Chem. Res.* 51 (2012) 8631–8645, <https://doi.org/10.1021/ie300691c>.
- [48] A. Goepfert, H. Zhang, M. Czaun, R.B. May, G.K.S. Prakash, G.A. Olah, S.R. Narayanan, Easily regenerable solid adsorbents based on polyamines for carbon dioxide capture from the air, *ChemSusChem* 7 (2014) 1386–1397, <https://doi.org/10.1002/cssc.201301114>.
- [49] A. Sinha, L.A. Darunte, C.W. Jones, M.J. Realf, Y. Kawajiri, Systems design and economic analysis of direct air capture of CO₂ through temperature vacuum swing adsorption using MIL-101(Cr)-PEI-800 and mmen-Mg₂(dobdc) MOF adsorbents, *Ind. Eng. Chem. Res.* 56 (2017) 750–764, <https://doi.org/10.1021/acs.iecr.6b03887>.
- [50] R. Serna-Guerrero, Y. Belmabkhout, A. Sayari, Influence of regeneration conditions on the cyclic performance of amine-grafted mesoporous silica for CO₂ capture: An experimental and statistical study, *Chem. Eng. Sci.* 65 (2010) 4166–4172, <https://doi.org/10.1016/j.ces.2010.04.029>.
- [51] M. Parvazinia, S. Garcia, M. Maroto-valer, CO₂ capture by ion exchange resins as amine functionalised adsorbents, *Chem. Eng. J.* 331 (2018) 335–342, <https://doi.org/10.1016/j.cej.2017.08.087>.

Publication IV

J. Elfving and T. Sainio

Kinetic approach to modelling CO₂ adsorption from humid air using amine-functionalized resin: Equilibrium isotherms and column dynamics

Reprinted with permission from
Chemical Engineering Science

Vol. 246, pp. 116885, 2021

© 2021, The Authors. Published by Elsevier Ltd.



Kinetic approach to modelling CO₂ adsorption from humid air using amine-functionalized resin: Equilibrium isotherms and column dynamics

Jere Elfving^{a,*}, Tuomo Sainio^b

^aVTT Technical Research Centre of Finland Ltd., Koivurannantie 1, FI-40101 Jyväskylä, Finland

^bLappeenranta-Lahti University of Technology, School of Engineering Science, Mikkulankatu 19, 15210 Lahti, Finland

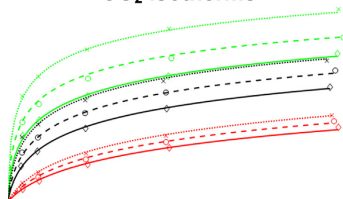
HIGHLIGHTS

- Kinetic model for CO₂ adsorption from humid air on amine-functionalized adsorbent.
- Humid CO₂ adsorption isotherms modelled using the kinetic model.
- Enhancement of CO₂ capacity by humidity captured well by isotherm modelling.
- Dynamic model fitted to fixed-bed data in humid direct air capture conditions.
- Non-isothermal adsorption of CO₂ and H₂O reproduced well by the dynamic model.

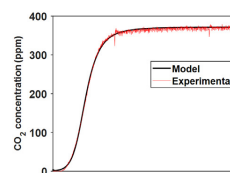
GRAPHICAL ABSTRACT

Modelling humid DAC with novel kinetic model

CO₂ isotherms



CO₂ adsorption dynamics



ARTICLE INFO

Article history:

Received 22 March 2021

Received in revised form 14 June 2021

Accepted 15 June 2021

Available online 22 June 2021

Keywords:

Direct air capture
CO₂ adsorption
H₂O adsorption
CO₂ adsorption
CO₂ isotherms
Kinetic model

ABSTRACT

Humidity can up to double the adsorption capacity of CO₂ in conditions relevant to direct air capture (DAC) on amine-functionalized adsorbents, but the treatment of this phenomenon in isotherm or kinetic models has been all but neglected in the literature. In this work, a kinetic model based on reaction mechanisms of CO₂ adsorption on supported amines in dry and humid conditions is proposed. The kinetic model was used in modelling of humid CO₂ adsorption isotherms and dynamics of fixed-bed CO₂ adsorption from air. The improvement of equilibrium CO₂ capacity by humidity was captured well by the kinetic model, leading to good fits of CO₂ isotherms. At best, the dynamic model closely represented the whole shape of CO₂ adsorption breakthrough curves in several-hour fixed-bed adsorption experiments. Therefore, the proposed kinetic model is expected to be useful in simulation of the DAC process based on supported amine-adsorbents.

© 2021 The Authors. Published by Elsevier Ltd. This is an open access article under the CC BY license (<http://creativecommons.org/licenses/by/4.0/>).

1. Introduction

To not exceed the global warming targets of 1.5 °C or 2 °C by the end of the century requires sharp reduction of global CO₂ emissions to net zero in the coming decades. Any credible scenarios that

can meet these targets require not only CO₂ emission reduction via technologies such as post-combustion capture (PCC), but also the use of carbon removal technologies, among which is capturing CO₂ directly from air. (Coninck et al., 2018) Direct air capture (DAC) usually involves the use of strongly basic solutions or solid sorbents to selectively capture CO₂ from air, followed by the release of CO₂ from the solvent or sorbent in a concentrated form via heating, pressure swing, humidity swing or other methods

* Corresponding author.

E-mail address: jere.elfving@vtt.fi (J. Elfving).

<https://doi.org/10.1016/j.ces.2021.116885>

0009-2509/© 2021 The Authors. Published by Elsevier Ltd.

This is an open access article under the CC BY license (<http://creativecommons.org/licenses/by/4.0/>).

(Sanz-Pérez et al., 2016). As a result, the DAC process can produce pure CO₂ carbon negatively, although the carbon efficiency of DAC is largely dependent on the carbon footprint of the electricity and heat used (de Jonge et al., 2019; Deutz and Bardow, 2021). DAC coupled with carbon storage (DACCS) could reach carbon removal of several GtCO₂/a scale (Breyer et al., 2019; Fuss et al., 2018). On the other hand, DAC can also be combined with different CO₂ utilization technologies (DACCU). DACCU enables a fully renewable energy system by using the produced CO₂ for chemical energy storage in power-to-X (PtX) technologies such as the Fischer-Tropsch process, while producing carbon-neutral fuels for the transport sector (Vidal Vázquez et al., 2018). Another use of DAC is to boost food production in greenhouses (Rodríguez-Mosqueda et al., 2019) or in microbial cultivation (Ruuskanen et al., 2021).

While DAC utilising hydroxide solvents may be an efficient technology for large-scale operation (Keith et al., 2018) and in terms of cost is comparable to solid sorbent technology (Fasih et al., 2019), it is also a fairly complex process with heat demands that cannot be supplied by low-grade waste heat. One type of sorbent-based DAC is the humidity-swing process which utilizes anion-exchange resins, and entails the advantage of sorbent regeneration in atmospheric conditions (Shi et al., 2017; Van Der Giesen et al., 2017). However, water demand during the regeneration phase may limit the geographical applicability of this technology (Van Der Giesen et al., 2017). By contrast, DAC based on amine-functionalized adsorbents does not require water, instead humidity in air is captured, and thus liquid water can be produced (Bajamundi et al., 2019). This process only requires a temperature near 100 °C or less for sorbent regeneration, which enables the use of low-grade waste heat (Bajamundi et al., 2019; Wurzbacher et al., 2016), and can be assembled as scalable modular units (Climeworks, 2021). The adsorbents combine the CO₂-selective amine groups with porous materials such as mesoporous silica, alumina or metal-organic framework (MOF) via impregnation of polyamines, grafting of aminosilanes or surface-initiated polymerization of amines (Sanz-Pérez et al., 2016; Shi et al., 2020).

The co-adsorbed water can be both a nuisance and an advantage in CO₂ capture from air. Co-adsorbed humidity may increase the adsorbent regeneration heat requirement several times compared to dry case with only CO₂ adsorbing (Drechsler and Agar, 2020). Although the energy penalty related to water can be minimized via e.g. heat recovery (Drechsler and Agar, 2020), it is important to be able to evaluate the amount of co-adsorbed H₂O via measuring H₂O isotherms such as in (Veneman et al., 2015; Gebald, 2014). Another negative implication of humidity can be adsorbent degradation, which can occur for example in some metal-organic frameworks (MOFs) (Jahandar Lashaki et al., 2019). On the other hand, humidity may increase the CO₂ adsorption capacity due to a change in the reaction mechanism between CO₂ and amine groups.

Capture of CO₂ in a primary or secondary amine-functionalized adsorbent in dry conditions takes place via formation of an intermediate zwitterion, which can be stabilized by a basic group, such as a neighbouring amine or a water molecule (Sanz-Pérez et al., 2016; Choi et al., 2009; Li et al., 2016). In the case of one primary amine group reacting with CO₂, the formation of the zwitterion can be written as:



In dry conditions, the zwitterion is deprotonated by a neighbouring amine group, resulting in the formation of ammonium carbamate:

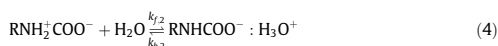


Therefore, in dry conditions, two moles of amine are required to capture one mole of CO₂.

However, the evidence of which species is formed under humid conditions is ambiguous in the literature. For tertiary amines, formation of bicarbonate in humid conditions has been proposed, while in dry conditions tertiary amines cannot capture CO₂ at all (Choi et al., 2009; Lee et al., 2017). For primary and secondary amines, the formation of bicarbonate in humid conditions has also been proposed based on infrared (Didas et al., 2014) and NMR studies (Chen et al., 2018). The formation of bicarbonate from the zwitterion with primary amines in humid conditions would take place via:



However, based on the quantum chemical model by (Li et al., 2016), the mechanism of CO₂ capture in humid conditions more likely leads to hydronium carbamate than bicarbonate:



Hahn et al. (2015) also proposed the formation of a water-stabilized carbamate species based on NMR data. Also, Yu and Chuang (2017) observed the formation of both carbamic acid and hydronium carbamate in humid or wet CO₂ adsorption on tetraethylenepentamine (TEPA) film via in-situ FTIR. Whichever the reactions in Eqs. (3) or (4) or the formation of water-stabilized carbamic acid take place in humid conditions, the result is that only one amine group is required per mole of CO₂, which theoretically boosts the maximum available CO₂ capacity up to double that of dry conditions.

The increase of CO₂ capacity in humid DAC conditions has been reported for different amine-functionalized adsorbents. For a nanofibrillated cellulose (NFC) adsorbent grafted with aminosilanes, Gebald (2014) reported adsorption capacities of 1.11 and 2.13 mmolCO₂/g_{sorbent} at 23 °C using dry and humid (2.5 vol-% H₂O) 400 ppm CO₂, respectively. The improvement of capacity due to humidity was even more heavily promoted at 50 °C, with 0.11 and 1.42 mmolCO₂/g_{sorbent} in dry and humid conditions, respectively. Sayari et al. (2016) found that CO₂ capacity increased with increasing relative humidity (RH) on pore-expanded MCM-41-supported PEI adsorbent, with the highest capacity of 2.92 mmolCO₂/g_{sorbent} achieved at 64% RH, marking a 34% improvement compared to dry conditions (2.18 mmolCO₂/g_{sorbent}). Kumar et al. (2020) used SBA-15 impregnated with 60 w-% of alkyl-aryl amine groups to measure CO₂ capacities of 1.6 and 2.9 mmolCO₂/g_{SiO2} from 400 ppm CO₂ at 35 °C in dry and 30% RH conditions, corresponding to over 81% capacity improvement in humid conditions. For the adsorbent used in this work, CO₂ capacities using 400–5000 ppm CO₂ were 0.54–0.92 mmolCO₂/g_{sorbent} in dry conditions, and 0.89–1.28 mmolCO₂/g_{sorbent} with around 63% RH at 25 °C (Elfving et al., 2017). The improvement of CO₂ capacity by humidity was thus 65% at 400 ppm and 39% at 5000 ppm CO₂. Moreover, based on isotherm modelling, humidity increased the attainable working capacities by up to around 80% in the temperature-swing regeneration process at an adsorption temperature of 25 °C.

However, in some cases, only marginal improvement or even a decrease of capacity in humid conditions has been reported. For example, (Goepfert et al., 2011) reported a capacity increase from 1.18 to 1.77 mmolCO₂/g_{sorbent} in dry and humid (67% RH) conditions for a 33 w-% PEI-loaded fumed silica adsorbent, but with 50 w-% PEI loading, the same experiment resulted in a decrease of capacity from 1.7 to 1.41 mmolCO₂/g_{sorbent}. Also, Wang et al. (2015) measured only modest improvement of CO₂ capacity on a 55 w-% PEI-loaded mesoporous carbon adsorbent from 2.25 to 2.58 mmolCO₂/g_{sorbent} from dry 400 ppm CO₂ and with 80% RH, respec-

tively. On the other hand, sometimes the improvement in humid conditions is more than the theoretical maximum of doubling of the capacity. [Sujan et al. \(2019\)](#) reported only 0.59 mmol_{CO₂}/g_{adsorbent} under dry conditions but 1.6 mmol_{CO₂}/g_{adsorbent} with 85% RH from 400 ppm CO₂ at 35 °C for a 41 w-% PEI-impregnated silica-fiber adsorbent. Also, although not in DAC conditions, [Qi et al. \(2014\)](#) obtained a remarkable capacity of 11.8 mmol_{CO₂}/g_{adsorbent} from 8% CO₂ at 25 °C with 18% relative humidity, but only 0.82 mmol_{CO₂}/g_{adsorbent} in dry conditions in a two-hour experiment. These results impart that, in some cases, the effect of humidity on CO₂ capacity is explained by a change of CO₂ adsorption kinetics rather than a change in equilibrium capacity. In adsorbents with high loading of amine, adsorbed water could act as an additional barrier for diffusion of CO₂ ([Hahn et al., 2015](#); [Si et al., 2019](#)), but on the other hand, humidity could also enhance the flexibility of aminopolymer chains and thus enhance gas diffusion ([Qi et al., 2014](#); [Kolle et al., xxx](#)).

Despite the significant effect of humidity on the capacity and possibly the kinetics of CO₂ adsorption from air on amine-based adsorbents, few attempts have been made to model this phenomenon. Although binary isotherm models for describing competitive CO₂/H₂O adsorption systems have been reported, e.g., Langmuir with Brunauer-Emmett-Teller (BET) ([Wang et al., 2020](#)), these models cannot be used to model CO₂/H₂O adsorption on amine-based adsorbents. The enhancing effect of humidity on CO₂ capacity requires a different approach to isotherm modelling. [Wurzbacher et al. \(2016\)](#) used Toth isotherms measured in dry conditions coupled with an enhancing factor to take into account the effect of humidity on CO₂ capacity. However, the factor was determined from only four measurements using bilinear interpolation, instead of co-adsorption isotherm modelling. Their data was later used by [Stampi-Bombelli et al. \(2020\)](#) to describe the CO₂ adsorption from air in humid conditions using a modified Toth model that takes into account the enhancing effect of humidity. In their model, two additional parameters are introduced, which, combined with H₂O capacity, increase the adsorption affinity and CO₂ maximum capacity under humid conditions. While this approach seems fairly straightforward, only a few isotherm points were reported, and it was not assessed how accurately this model could depict the co-adsorption isotherms.

Another approach to humid CO₂ adsorption modelling on amine-functionalized adsorbents was presented by [Jung and Lee \(2020\)](#), who used the reaction mechanisms of CO₂ and H₂O with amines as a basis to describe the reaction rate equations of CO₂ to carbamate and bicarbonate. In their rate equations, the reaction stoichiometry was neglected, and the reactions have separate maximum capacities, which would mean that two different sites of CO₂ adsorption exist in the adsorbent. Moreover, they used these rate equations as a basis to derive a temperature-dependent co-adsorption isotherm model for CO₂, which resembles the dual-site Langmuir isotherm. They fitted this model to CO₂/H₂O co-adsorption points at 40–70 °C, and showed fairly good representation of the equilibrium data by the model. However, in their data, the CO₂ capacity was lower in humid conditions at CO₂ partial pressures below 0.15 bar at 40–55 °C. Also, the partial pressures of both CO₂ and H₂O were 0.025 bar or higher, so it could not be deduced how well the proposed model depicts lower partial pressure levels or DAC conditions. Therefore, more work is required on finding models that can accurately describe the enhancing effect of humidity on CO₂ adsorption in adsorbent-based DAC.

In this work, a kinetic model based on the kinetics of adsorption and desorption reactions is proposed for CO₂ adsorption from air on amine-functionalized resin. The model includes different mechanisms of CO₂ adsorption in dry and humid conditions on amine-functionalized adsorbents. The model is used to describe adsorption equilibrium isotherms by integrating until equilibrium.

Parameters describing adsorption equilibrium are fitted to (pseudo-)equilibrium CO₂ isotherms measured in humid conditions. The kinetic model is then used in the dynamic simulation of fixed-bed adsorption column to fit mass and heat transfer parameters from experimental CO₂ and H₂O breakthrough curves and temperature data. Adsorption equilibrium of H₂O in the simulation is calculated by the Guggenheim Anderson De Boer (GAB) model fitted to experimental single-component H₂O isotherms. To the authors' best knowledge, this is the first time that an adsorption mechanism-based model has been used to accurately describe the equilibrium and kinetics of CO₂ adsorption in humid DAC conditions.

2. Experimental and modelling methods

2.1. CO₂/H₂O adsorption experiments

In this study, an automated and modifiable fixed-bed adsorption device was used in experimental work. Details of the experimental setup have been previously reported in ([Elfving et al., 2021](#)). Approximately 0.5 g of a proprietary amine-functionalized resin characterized in ([Elfving et al., 2017](#)) was fixed in the column with quartz wool below and above the adsorbent. All experiments were conducted using the temperature-vacuum-concentration swing adsorption (TVCSA) process described in detail below. The samples were first regenerated by temperature-concentration swing (TCS) and vacuum (TVCS) to remove pre-adsorbed CO₂ and H₂O. Regeneration was done with 1000 ml/min of N₂ during TCS and 100 ml/min during TVCS, with a vacuum level of around 50 mbar. The dry weight of the sample used for capacity calculations was gained by subtracting the mass of the pre-adsorbed species from the mass measured before inserting the sample into the column.

Regeneration was followed by CO₂ adsorption using humidified compressed air or 200–4000 ppm CO₂ obtained by mixing 1% CO₂/N₂ and N₂. The gases were humidified using the moisture calibrator Hovacal digital 122-SP. For single-component H₂O isotherms pure N₂ was used as the balance gas, and was humidified similarly as the humid CO₂/N₂ mixtures. Adsorption was carried out for four hours at 25–50 °C. To allow convenient automatic measurement of the single-component H₂O isotherms, H₂O concentrations from 0.16 to 1.86 vol-% were obtained by varying the total flow rate of N₂ from 1000 to 100 ml/min, respectively, while keeping the moisture calibrator set-point constantly at 0.2 vol-%.

The CO₂/H₂O co-adsorption isotherm points were measured at 5 concentrations of CO₂ between 200 and 4000 ppm, at 25–50 °C, and with 3 concentrations of H₂O, the set-points in the moisture calibrator being 0.2 vol-%, 1 vol-% and 2 vol-% H₂O. Each isotherm consisted of 5 consequent adsorption/desorption cycles where the CO₂ partial pressure was varied and temperature and H₂O concentration were kept constant. The sample was changed for each isotherm. The adsorption time for the co-adsorption isotherm experiments was 5–6 h. The flow rate for the first two co-adsorption isotherms (0.2 vol-% H₂O, 25 °C and 35 °C) was only 200 ml/min, but to make sure the CO₂ adsorption was near saturation, the flow rate in the consequent experiments was kept at 500 ml/min. However, even at 25 °C, the difference between the CO₂ capacities gained using 0.2 vol-% H₂O and 200 ml/min were not significantly lower than those measured at 500 ml/min (see [Supplementary Data Fig. S1](#)). Therefore, the two CO₂ isotherms with 0.2 vol-% H₂O at 25 °C and 35 °C measured using 200 ml/min flow rate were used with other isotherms measured using 500 ml/min in the modelling of humid CO₂ adsorption isotherms.

The actual measured concentrations of CO₂ and H₂O were different from the set-points, and for H₂O they were on average

0.16 vol-%, 0.95 vol-% and 1.9 vol-%. However, the variation in the concentrations did not add to the uncertainty of the isotherm points, since partial pressures were used in the isotherm models instead of concentration. The partial pressures p_i of the CO₂ and H₂O isotherm points were calculated by the measured molar fractions y_i (step function concentrations) and column average pressure P_{tot} during adsorption using $p_i = P_{\text{tot}}y_i$. The partial pressures of H₂O in the humid CO₂ isotherms for the three humidity set-points of 0.2 vol-%, 1 vol-% and 2 vol-% were in the range of 0.0016–0.0017 bar, 0.0098–0.0103 bar and 0.0185–0.0205 bar, respectively.

The adsorption phase was followed by complete desorption of the adsorbed species. The desorption phase consisted of purging with N₂ at 1000 ml/min, temperature swing up to 100 °C and vacuuming with 100 ml/min N₂ purge. To find the effect of co-adsorption on water capacity, the experiments with 0.2 vol-% H₂O were run with separate purge steps for CO₂ and H₂O by first stopping the CO₂ flow ('Purge 1'), and then using dry N₂ ('Purge 2'). A slight peak in H₂O concentration during 'Purge 1' was noted in some cases, but the method was deemed too uncertain due to integration of the small peak against the noisy H₂O concentration. The capacities gained this way were in the range of below zero up to only 0.036 mmol_{H₂O}/g_{sorbent}. Therefore, in consequent experiments, the purge steps were combined.

The cyclic humid experiment was done with two-hour adsorption phases using CO₂ and H₂O concentration set-points of 400 ppm and 2 vol-% at 25 °C and a total flow rate of 1000 ml/min. The desorption phase was similar to the one in the co-adsorption experiments. Furthermore, a single experiment with a nearly two-day adsorption phase was done where humidified compressed air with 2 vol-% H₂O and 401 ppm CO₂ was used at a flow rate of 100 ml/min. The calculation of CO₂ and H₂O capacities is discussed in the [Supplementary Data](#). Experimental repeatability was calculated as trend uncertainty from the cyclic experiment (see [Section 3.1](#)), being ± 0.200 mmol_{H₂O}/g_{sorbent} and ± 0.092 mmol_{H₂O}/g_{sorbent} for the H₂O adsorption and desorption capacities, respectively. For adsorption and desorption of CO₂, the repeatability was ± 0.009 mmol_{CO₂}/g_{sorbent} and ± 0.010 mmol_{CO₂}/g_{sorbent}, respectively. A more detailed description of uncertainty with the current experimental device can be found in earlier work ([Elfving et al., 2021](#)).

2.2. Isotherm and kinetic models

The temperature-dependent Toth model ([Do, 1998](#)) has been used for modelling the adsorption of CO₂ on amine-functionalized solid adsorbents ([Veneman et al., 2015](#); [Gebald, 2014](#); [Elfving et al., 2017](#); [Serna-Guerrero et al., 2010](#)), but also for water adsorption on porous adsorbents ([Wang and LeVan, 2009](#); [Qasem and Ben-Mansour, 2018](#)). However, the Toth isotherm lacks the multilayer adsorption behaviour encountered in porous adsorbents such as nanofibrillated cellulose ([Gebald, 2014](#); [Stampi-Bombelli et al., 2020](#)) or polystyrene-based resin ([Veneman et al., 2015](#)) that have been functionalized with amines. For describing the H₂O adsorption on amine-functionalized adsorbents, the Brunauer Emmett Teller (BET) ([Drechsler and Agar, 2020](#)) and the GAB ([Gebald, 2014](#)) isotherms have been used. However, the typical form of BET model has no temperature dependency. Therefore, the GAB-isotherm is used in this work to model H₂O adsorption on the aminoresin:

$$q_{\text{H}_2\text{O}} = \frac{q_{\text{m,mono}}CK(p_{\text{H}_2\text{O}}/p_{\text{H}_2\text{O,sat}})}{(1 - K(p_{\text{H}_2\text{O}}/p_{\text{H}_2\text{O,sat}}))(1 + K(p_{\text{H}_2\text{O}}/p_{\text{H}_2\text{O,sat}})(C - 1))} \quad (5)$$

where $q_{\text{H}_2\text{O}}$ is the H₂O adsorption capacity at partial pressure $p_{\text{H}_2\text{O}}$ and water saturation vapour pressure of $p_{\text{H}_2\text{O,sat}}$ and $q_{\text{m,mono}}$ is the

monolayer adsorption capacity of H₂O. Parameters C and K are temperature-dependent:

$$C = C_0 \exp\left(\frac{\Delta H_C}{R_{\text{id}}T}\right) \quad (6)$$

$$K = K_0 \exp\left(\frac{\Delta H_K}{R_{\text{id}}T}\right) \quad (7)$$

where C_0 and K are dimensionless parameters and ΔH_C and ΔH_K are adsorption enthalpies of monolayer and multilayer adsorption. ([Gebald, 2014](#); [Stampi-Bombelli et al., 2020](#); [Sultan et al., 2015](#); [Quirijns et al., 2005](#)) Because ΔH_C can be expected to be positive and ΔH_K negative ([Sultan et al., 2015](#); [Quirijns et al., 2005](#)), the lower boundary of ΔH_C and the upper boundary of ΔH_K were fixed at zero during isotherm fitting.

Based on reactions presented in Eqs. (1)–(4), the adsorption rates of CO₂ in dry and humid conditions can be described with the following equations:

$$r_1 = k_{f,1}[\text{R-NH}_2]^2[\text{CO}_2] - k_{b,1}[\text{RNHCOO}^- : \text{RNH}_3^+] \quad (8)$$

$$r_2 = k_{f,2}[\text{R-NH}_2][\text{CO}_2][\text{H}_2\text{O}] - k_{b,2}[\text{RNHCOO}^- : \text{H}_3\text{O}^+] \quad (9)$$

where k_f and k_b are the kinetic constants of forward and backward reactions, respectively. Square brackets refer to the concentrations of the respective reaction species. Subscripts 1 and 2 refer to the reactions in dry and humid conditions, respectively. Although the rate Eq. (9) for reaction 2 shows the formation of hydronium carbamate in humid conditions (Eq. (4)), another option is bicarbonate formation (Eq. (3)), as discussed above. Similarly to ([Jung and Lee, 2020](#)), the amine species concentration $[\text{R-NH}_2]$ is the solid-phase concentration of available amine sites for adsorption of CO₂, while the concentrations of CO₂ and H₂O are replaced with the respective partial pressures. Also, the product concentrations $[\text{RNHCOO}^- : \text{RNH}_3^+]$ and $[\text{RNHCOO}^- : \text{H}_3\text{O}^+]$ are replaced with the solid-phase concentrations of CO₂ of q_{1,CO_2} and q_{2,CO_2} , i.e. the CO₂ adsorption capacity for reactions 1 and 2, respectively. However, contrary to ([Jung and Lee, 2020](#)), the available amine sites concentration is here calculated from balance $q_m - 2q_{1,\text{CO}_2} - q_{2,\text{CO}_2}$, with common maximum capacity of amine sites q_m being available for both reactions. In other words, reaction 1 consumes two amine sites per mole of CO₂, and reaction 2 consumes only one amine site per mole of CO₂. The backward reaction rate constant can be written in terms of the adsorption affinity b as $k_b = k_f/b$. Therefore, the resulting mass balance equations are written as:

$$\frac{dq_{1,\text{CO}_2}}{dt} = k_{f,1}(q_m - 2q_{1,\text{CO}_2} - q_{2,\text{CO}_2})^2 p_{\text{CO}_2} - \frac{k_{f,1}}{b_1} q_{1,\text{CO}_2} \quad (10)$$

$$\frac{dq_{2,\text{CO}_2}}{dt} = k_{f,2}(q_m - 2q_{1,\text{CO}_2} - q_{2,\text{CO}_2}) p_{\text{CO}_2} p_{\text{H}_2\text{O}} - \frac{k_{f,2}}{b_2} q_{2,\text{CO}_2} \quad (11)$$

The total rate of change in CO₂ adsorption $dq_{\text{tot,CO}_2}/dt$ is then calculated by a sum of the reaction rate Eqs. (10) and (11). The adsorption affinity is temperature-dependent:

$$b_1 = b_{0,1} \cdot \exp\left(\frac{-\Delta H_1}{R_{\text{id}} \cdot T_0} \cdot \left(\frac{T_0}{T} - 1\right)\right) \quad (12)$$

$$b_2 = b_{0,2} \cdot \exp\left(\frac{-\Delta H_2}{R_{\text{id}} \cdot T_0} \cdot \left(\frac{T_0}{T} - 1\right)\right) \quad (13)$$

where $b_{0,1}$ and $b_{0,2}$ are the reference adsorption affinities at reference temperature T_0 , while $-\Delta H_1$ and $-\Delta H_2$ are the opposite numbers of isosteric heats of adsorption for reactions 1 and 2, respectively.

Eqs. (10) and (11) coupled with the temperature dependency of the adsorption affinity are referred to later in this work as the 5-

parameter co-adsorption model. In this model, the exponents of the available amine site concentration in reactions 1 and 2 originate from the reaction stoichiometry.

It is also possible to fit these exponents from experimental data. Denoting the exponents by t_1 and t_2 gives:

$$\frac{dq_{1,\text{CO}_2}}{dt} = k_{f,1}(q_m - 2q_{1,\text{CO}_2} - q_{2,\text{CO}_2})^{t_1} p_{\text{CO}_2} - \frac{k_{f,1}}{b_1} q_{1,\text{CO}_2} \quad (14)$$

$$\frac{dq_{2,\text{CO}_2}}{dt} = k_{f,2}(q_m - 2q_{1,\text{CO}_2} - q_{2,\text{CO}_2})^{t_2} p_{\text{CO}_2} p_{\text{H}_2\text{O}} - \frac{k_{f,2}}{b_2} q_{2,\text{CO}_2} \quad (15)$$

Eqs. (12)–(15) are in this work referred to as the 7-parameter co-adsorption model. The 5-parameter and 7-parameter co-adsorption models were used to model the CO₂ adsorption kinetics in humid conditions.

The co-adsorption models were fitted to all the humid CO₂ desorption isotherm data at 25–50 °C to find equilibrium parameters q_m , b_1 , b_2 , $-\Delta H_1$, $-\Delta H_2$, and additionally t_1 and t_2 in the case of the 7-parameter model. Given sufficient time, the equilibrium state is determined by the ratio of forward and backward rate constants rather than their absolute values. Therefore, the forward kinetic parameters can be set to arbitrary values (here $k_{f,1} = k_{f,2} = 1$) while ensuring that the equilibrium state is reached by integrating long enough in time. At a later stage, the forward kinetic parameters can be estimated from kinetic data by using the previously determined values for the equilibrium parameters. In this work, dynamic CO₂ breakthrough data was used to estimate the kinetic constants by using the fixed-bed model, as described in the next section.

To calculate the total equilibrium CO₂ capacity when fitting the models to CO₂ isotherms, the kinetic models were integrated for a sufficiently long time to reach equilibrium using the 'ODE15s' - solver in Matlab. The relative and absolute tolerances for the ODE solver 'RelTol' and 'AbsTol' were $1 \cdot 10^{-10}$. The isotherm fitting for both single-component H₂O GAB isotherms and the co-adsorption models was done by using the 'lsqnonlin' - optimization function with termination tolerances 'Tolfun' and 'TolX' of $1 \cdot 10^{-10}$. To help find global minima, the 'MultiStart' function in Matlab was utilized for the fitting of the H₂O isotherms with 100 starting points, while for the 5-parameter model, 50 starting points were used. In the case of the 7-parameter model, the fitted parameters of the 5-parameter model were used as the starting points.

2.3. Fixed-bed adsorption column model

A dynamic model was written for non-isothermal co-adsorption of CO₂ and H₂O in a column packed with the amine-functionalized resin. Mass and heat balance equations along the axial direction of the bed were solved by using the method of lines in Matlab. Ideal gas law was used for gas phase calculations such as calculating partial pressures from concentrations. Since this work only considers the adsorption phase and low concentrations of CO₂ and H₂O, gas velocity along the bed is constant in this model. Possible adsorption of N₂ or O₂ from compressed air is not taken into account due to non-existent or negligible competition with CO₂ or H₂O due to physical adsorption mechanism, near atmospheric pressure (see Table 1) and the low surface area of the resin of 32 m²/g (Elfving et al., 2017). Moreover, the total pressure is constant in the model, since the effect of the pressure drop along the bed on partial pressures of CO₂ and H₂O was assumed to be negligible. For example, in experiments with a 500 ml/min total flow rate, the average pressure drop across the bed during adsorption was 230 Pa at 25 °C and 180 Pa at 35 °C with 2 vol-% H₂O and

Table 1

Parameters used in the fixed-bed modelling. NIST database values were obtained with the 'refpropm' - user-built function in Matlab and REFPROP software using corresponding inlet gas composition, temperature and total pressure.

Quantity	Parameter	Value	Source
Adsorbent bed properties			
L_{bed}	Bed length	0.017–0.018 m	Calculated from column dimensions and bulk density
R_{bed}	Bed radius	0.0045 m	Column inner radius
ϵ	Bed voidage	0.375	Adsorbent SDS
ρ_B	Bulk density	450 kg/m ³	Measured
R_p	Particle radius	$3 \cdot 10^{-4}$ m	From particle size distribution median (Elfving et al., 2017)
ρ_p	Particle density	720 kg/m ³	Calculated from voidage and bulk density
$c_{p,a}$	Specific heat capacity of adsorbent	1580 J/(kg K)	From (Sonnleitner et al., 2018). Resin matrix similar type.
Inlet gas properties			
$y_{\text{CO}_2,\text{feed}}$	Feed molar fraction of CO ₂	0.00037–0.00040	Measured
$y_{\text{H}_2\text{O},\text{feed}}$	Feed molar fraction of H ₂ O	0.0016–0.0193	Measured
T_{feed}	Feed gas temperature	298–308 K	Set equal to measured bed temperature
ρ_g	Gas mixture density	1.13–1.20 kg/m ³	NIST database
v_i	Interstitial velocity	0.070–0.349 m/s	Calculated from flow rate and voidage
ν	Kinematic viscosity of gas mixture	$1.48 \cdot 10^{-5}$ m ² /s	NIST database
c_{p,CO_2}	Molar heat capacity of CO ₂	851–861 J/(mol K)	NIST database
$c_{p,\text{H}_2\text{O}}$	Molar heat capacity of H ₂ O	4180 J/(mol K)	NIST database
$c_{p,g}$	Specific heat capacity of gas mixture	1050–1060 J/(kg K)	NIST database
Process conditions			
T_w	Column wall temperature	298–308 K	Set equal to measured bed temperature
P_{tot}	Total pressure in the column	1.03–1.07 10^5 Pa	Measured

around 370 ppm CO₂. Thermal equilibrium between the solid and gas phases was assumed. Bed properties such as voidage, adsorbent density and specific heat capacity are constant. Also, case-dependent thermodynamic properties of the gas such as kinematic viscosity, gas density and specific heat capacity were calculated for the inlet gas in each case based on gas composition, total pressure and temperature, but are constant within each simulation case. The solid phase and gas phase properties as well as initial and boundary conditions can be found in Table 1.

The component material balance can be represented as:

$$\frac{\partial c_i}{\partial t} = D_L \frac{\partial^2 c_i}{\partial z^2} - v_i \frac{\partial c_i}{\partial z} - \frac{\rho_B}{\epsilon} \frac{\partial q_i}{\partial t} \quad (16)$$

where c_i is the concentration of species i , t is time, D_L is the axial dispersion coefficient, z is axial dimension, v_i is the interstitial velocity, ρ_B is the adsorbent bed bulk density and ϵ is the bed porosity (Bollini et al., 2012; Shafeeyan et al., 2014; Haghpanah et al., 2013). Several correlations exist for calculating the axial dispersion coefficient, but here the Chung & Wen correlation was used:

$$D_L = \frac{2R_p v_i \epsilon}{0.2 + 0.011 Re^{0.48}} \quad (17)$$

where R_p is the adsorbent particle radius and Re is the Reynold's number calculated by $Re = 2R_p v_i \rho_i / \nu$, where ν is the kinematic viscosity of the inlet gas mixture (Rastegar and Gu, 2017). The kinetics of total CO₂ adsorption arise from the sum of Eqs. (10) and (11) or (14) and (15), as explained above. However, as the adsorption of H₂O was described with the GAB isotherm model, the linear driving force model (Sircar and Hufton, 2000) was used to describe the water adsorption kinetics:

$$\frac{d\bar{q}_i}{dt} = k_{i,\text{LDF}}(q_{i,\text{eq}} - \bar{q}_i) \quad (18)$$

where \bar{q}_i is the average capacity of species i in the adsorbent particle, $k_{i,\text{LDF}}$ is the linear driving force kinetic constant and $q_{i,\text{eq}}$ is the equilibrium capacity of species i , arising from the isotherm model. Specifically, in the fixed-bed model $q_{i,\text{eq}}$ is the local equilibrium capacity depending on the partial pressure of species i and temperature in the gas arriving to the given grid point at time t .

The heat balance is a simplified form of the model used by Haghpanah et al. (2013) in that gas velocity and pressure are constant. Also, in this work, there is no separate heat balance at the column wall, since the wall temperature along radial and axial directions was assumed to be uniform. The heat balance takes into account convection and dispersion along the axial direction of the bed, sensible heat of the adsorbed molecules, exothermic heat of adsorption and heat transfer between the bed and the column wall:

$$\begin{aligned} & \frac{1-\varepsilon}{\varepsilon} \rho_p (c_{p,a} + c_{p,\text{CO}_2} q_{\text{tot},\text{CO}_2} + c_{p,\text{H}_2\text{O}} q_{\text{H}_2\text{O}}) \frac{\partial T}{\partial t} \\ &= \frac{K_z}{\varepsilon} \frac{\partial^2 T}{\partial z^2} - \rho_g c_{p,g} v_i \frac{\partial T}{\partial z} - \frac{1-\varepsilon}{\varepsilon} \rho_p \left(c_{p,\text{CO}_2} \frac{dq_{\text{tot},\text{CO}_2}}{dt} + c_{p,\text{H}_2\text{O}} \frac{dq_{\text{H}_2\text{O}}}{dt} \right) T \\ & \quad - \frac{1-\varepsilon}{\varepsilon} \rho_p \left(-\Delta H_1 \frac{dq_{1,\text{CO}_2}}{dt} + (-\Delta H_2) \frac{dq_{2,\text{CO}_2}}{dt} + (-\Delta H_{\text{TotH}_2\text{O}}) \frac{dq_{\text{H}_2\text{O}}}{dt} \right) - \frac{2h}{\varepsilon R_{\text{bed}}} (T - T_w) \end{aligned} \quad (19)$$

where ρ_p is the adsorbent particle density, $c_{p,a}$ is the specific heat capacity of the adsorbent, c_{p,CO_2} and $c_{p,\text{H}_2\text{O}}$ are the molar heat capacities of CO₂ and H₂O, respectively, K_z is the axial effective heat conductivity, ρ_g is the gas density, $c_{p,g}$ is the specific heat capacity of the gas, h is the overall heat transfer coefficient between the bed and the column wall, R_{bed} is the adsorbent bed radius and T_w is the wall temperature.

At the inlet boundary, the Danckwert's boundary condition was used:

$$D_L \frac{\partial C_i}{\partial z} \Big|_{z=0} = -v_i (C_{i,\text{feed}} - C_i|_{z=0}) \quad (20)$$

where $C_{i,\text{feed}}$ is the feed concentration of species i , and $C_i|_{z=0}$ is the concentration of species i at the column inlet boundary. At the outlet boundary, the boundary condition is:

$$\frac{\partial C_i}{\partial z} \Big|_{z=L} = 0 \quad (21)$$

where L is bed length. Analogously for the heat balance, the inlet boundary condition (Haghpanah et al., 2013; Farooq and Ruthven, 1990) is:

$$K_z \frac{\partial T}{\partial z} \Big|_{z=0} = -\varepsilon v_i \rho_g c_{p,g} (T_{\text{feed}} - T|_{z=0}) \quad (22)$$

and the outlet boundary condition:

$$\frac{\partial T}{\partial z} \Big|_{z=L} = 0 \quad (23)$$

As for initial conditions, the adsorbent bed is regenerated ($q_{\text{H}_2\text{O}} = 0$; $q_{\text{CO}_2,1} = 0$; $q_{\text{CO}_2,2} = 0$; $q_{\text{CO}_2,\text{tot}} = 0$) and emptied from adsorbing species ($C_{\text{CO}_2} = 0$; $C_{\text{H}_2\text{O}} = 0$), temperature in the column is equal to column wall and inlet gas temperature ($T = T_w = T_{\text{feed}}$). Discretization of

the ODEs was done via finite difference method. Details of the discretization can be found in Supplementary Data.

As mentioned above, the desorption isotherm data of CO₂ and H₂O was corrected by empty column desorption capacities, which was then used for fitting the equilibrium parameters of the CO₂ kinetic model (Eqs. (10)–(15)) and the GAB model parameters for H₂O. Therefore, when using these models in the dynamic fixed-bed model, the simulated adsorption breakthrough curves would lead to an early breakthrough in comparison to the measured adsorption breakthrough curves. For CO₂ near 400 ppm, this is not significant (see Supplementary Data of (Elfving et al., 2021)), but for H₂O, the effect of the empty column needs to be accounted for in the model. Therefore, empty column adsorption capacities were measured at several H₂O concentrations, and a Langmuir isotherm model was fitted to this data. The capacity calculated from this model was added to the H₂O equilibrium capacity in Eq. (18). The model fit and parameters are shown in Supplementary Data Fig. S2.

The fixed-bed model was fitted to scaled dynamic experimental data to find parameters $k_{f,1}$, $k_{f,2}$, $k_{\text{H}_2\text{O,LDF}}$, K_2 and h . The used experimental data was CO₂ and H₂O breakthrough curves and the temperature of the bed measured approximately 1 cm into the bed. The data fitting was done by using the Matlab function "lsqcurvefit" with termination tolerances 'FunTol' and 'ToIX' of $1 \cdot 10^{-8}$ and $1 \cdot 10^{-10}$. The number of control volumes in all simulations was 200. Equations for scaling the data are found in the Supplementary Data.

3. Results & discussion

3.1. Humid cyclic experiment

Earlier, only dry cyclic experiments (Elfving et al., 2021) have been done with the resin studied in this work. Therefore, to find the capacity decrease rate and repeatability in humid conditions, a cyclic TVCSA run with 2 vol-% H₂O and 370–380 ppm CO₂ was done, and the results are shown in Fig. 1. Fig. 1a shows good agreement of cyclic adsorption and desorption capacities, with difference of the two falling below 0.02 mmol_{CO2}/g_{sorbent}. However, Fig. 1c shows that the H₂O adsorption capacities are clearly higher than the desorption capacities by 0.29–0.93 mmol_{H2O}/g_{sorbent}. The main reasons for this difference probably lie in humidity sensor accuracy ($\pm 1\%$ RH) and additional uncertainty related to calculating the H₂O adsorption capacities, which is discussed in more detail in Supplementary Data (Calculation of experimental capacities).

The CO₂ adsorption and desorption capacities decreased from around 0.87 mmol_{CO2}/g_{sorbent} to 0.77 mmol_{CO2}/g_{sorbent} and 0.76 mmol_{CO2}/g_{sorbent} in 17 cycles, respectively. The exact capacity drops corresponded to 11.1% and 12.4% or 0.65%/cycle and 0.73%/cycle for adsorption and desorption, respectively. Meanwhile, the H₂O desorption capacities decreased from 3.82 to 2.96 mmol_{H2O}/g_{sorbent}, which corresponds to a 22.6% drop, or 1.33%/cycle. In earlier work (Elfving et al., 2021), the greatest CO₂ capacity drop found in dry conditions of 0.60%/cycle was gained when using temperature-vacuum swing adsorption with air purge at 100 °C, being on similar scale to the results above. On the other hand, the capacity drop in dry conditions using TCS regeneration was only 0.18%/cycle (Elfving et al., 2021). Since the regeneration in the humid cyclic experiment was conducted using dry gases, and the resin was mostly dry by the time temperature swing was started, leaching of amines by moisture should not be the cause of the capacity drops. It can be observed from Fig. 1b and 1d that in the last 5–6 cycles the capacities seem to stabilize. This could refer to the least stable amine sites being deactivated or removed first, causing the initial rapid decrease of capacity. On the other

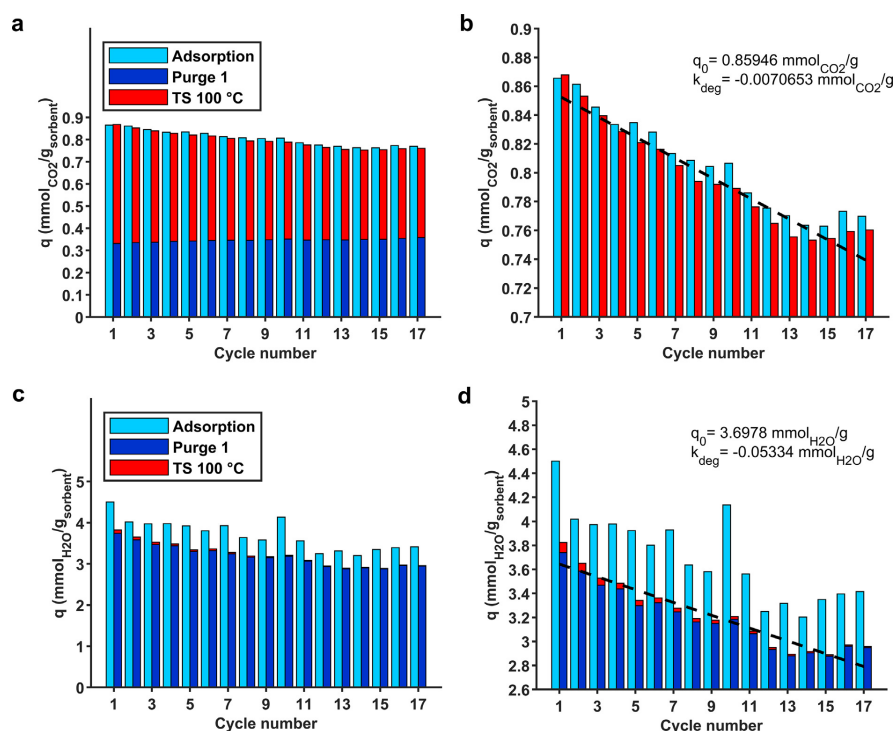


Fig. 1. CO₂ and H₂O adsorption and desorption capacities in repeated cycles of temperature-concentration-vacuum swing adsorption. Sub-figures b) and d) are close-ups from a) and c), respectively, and show the linear fit and parameters to total desorption capacities.

hand, this could also be due to the regeneration method not being fully complete, leaving small amounts of CO₂ and H₂O adsorbed after each cycle until cyclic steady-state is reached. This could be due to more stable species formed between CO₂ and amines under humid adsorption conditions, as suggested by infrared spectroscopy studies (Yu and Chuang, 2017; Miller et al., 2020). However, the real reason for the capacity drop rates requires further investigation in future work.

Regardless of the reason for the capacity drops, the implication for the isotherm results is the same, and requires data correction. Fig. 1b and 1d show a linear fit to the desorption capacities of CO₂ and H₂O with coefficients of determination of 0.94 and 0.90, respectively. Although the capacity drops are not linear for the last cycles, these linear functions give an estimate of the capacity drop rate for CO₂ and H₂O in humid conditions. Therefore, this data was used to correct the isotherm point data below as described in Supplementary Data (equation S1).

3.2. H₂O isotherms

Fig. 2 shows the experimental H₂O desorption data and the GAB isotherm fit gained for the amine-functionalized polystyrene resin. The isotherm data in Fig. 2a shows that at 35 °C and 50 °C, the H₂O capacity progresses almost linearly with increasing partial pressure. However, at 25 °C, the isotherm shows a type III isotherm shape, corresponding to multilayer H₂O adsorption. Similar beha-

viour of H₂O adsorption on amine-functionalized adsorbents has been reported for, e.g., Lewatit VP OC 1065 (Veneman et al., 2015) and aminosilane-functionalized NFC (Gebald, 2014). Fig. 2b shows that the H₂O isotherms seem to be a function of relative humidity rather than both temperature and relative humidity. However, as data was not gathered from the total relative humidity range due to the risk of water condensation in the experimental device lines, it was “safer” to use the temperature-dependent GAB model.

Table 2 shows the GAB isotherm parameters. For the heat balance of the fixed-bed model, the isosteric heat of adsorption was calculated at zero loading via $-\Delta H_{H_2O,0} = \Delta H_c + \Delta H_K + \Delta H_{H_2O,vap}$ (Gebald, 2014; Sultan et al., 2015; Quirijns et al., 2005), where $\Delta H_{H_2O,vap}$ is the heat of H₂O vaporization of 44.1 kJ/mol_{H₂O}, resulting in 50.7 kJ/mol_{H₂O}. Another method to estimate the isosteric heat of adsorption is from the Clausius Clapeyron equation by fitting $\ln(p_{H_2O})$ derived from GAB isotherm vs. $1/T$ (see e.g. (Sultan et al., 2015)), resulting in 50.1 kJ/mol_{H₂O} near zero loading (1E-6 mmol_{H₂O}/g_{sorbent}). These values are comparable with, e.g., 43 kJ/mol_{H₂O} for Lewatit VP OC 1065 (Veneman et al., 2015) and 48.8 kJ/mol_{H₂O} for amine-functionalized NFC (Gebald, 2014). Thus, the adsorption enthalpy of -50.7 kJ/mol_{H₂O} is used in the heat balance of the dynamic model in this work.

Fig. 2 also shows H₂O desorption capacities from the co-adsorption isotherm experiments where 370–380 ppm CO₂ was adsorbed simultaneously. These points are in good agreement with

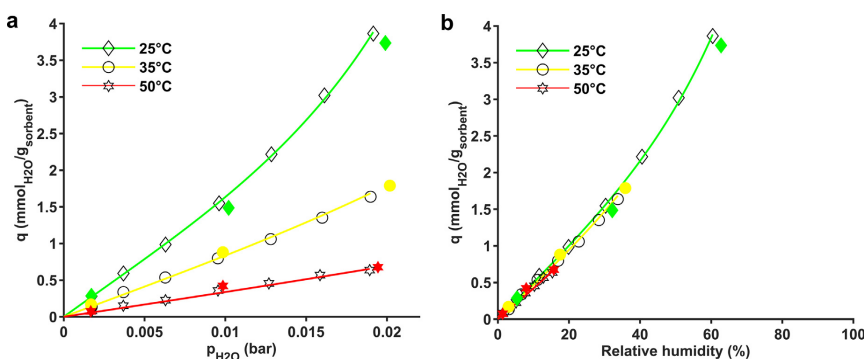


Fig. 2. Single-component H₂O desorption isotherms. Filled markers show H₂O desorption capacities in co-adsorption of 370–380 ppm CO₂ and humidity.

Table 2

Parameters of the GAB model fitted to single-component H₂O desorption isotherms, and the isosteric heat of H₂O adsorption at zero loading.

$q_{m,mono}$ (mmol _{H₂O} /g _{sorbent})	C_0	K_0	ΔH_c (kJ/mol)	ΔH_k (kJ/mol)	$-\Delta H_{H_2O,0}$
2.58	0.155	0.871	6.6	0	50.7

the single-component H₂O isotherm fits, and thus there is no need for a separate co-adsorption model in terms of H₂O adsorption in DAC conditions. Even with 4000 ppm CO₂, the resulting desorption capacities for H₂O were not significantly lower or higher than the single-component data, being 3.94 mmol_{H₂O}/g_{sorbent}, 1.75 mmol_{H₂O}/g_{sorbent} and 0.75 mmol_{H₂O}/g_{sorbent} at 25 °C, 35 °C and 50 °C, respectively. The corresponding single-component points were 3.87 mmol_{H₂O}/g_{sorbent}, 1.64 mmol_{H₂O}/g_{sorbent} and 0.64 mmol_{H₂O}/g_{sorbent}. The results thus refer to CO₂ having a negligible effect on H₂O adsorption in terms of capacity at least with dilute CO₂. Similar behaviour was found for the amine-functionalized resin Lewatit VP OC 1065, even though H₂O is mostly adsorbed by the amine groups in amine-functionalized hydrophobic resins (Veneman et al., 2015). A possible reason for the unaffected H₂O capacity by CO₂ is that the groups that capture CO₂ also capture H₂O via the bicarbonate or hydronium carbamate formation as presented in Eqs. (3) and (4), respectively.

3.3. CO₂/H₂O co-adsorption isotherms

Even though the temperature-dependent Toth model has been used previously to model the CO₂ desorption isotherms of the aminoresin in both humid and dry conditions with excellent fits (Elfving et al., 2017; Elfving et al., 2017), the model lacks the effect of H₂O. Therefore, to model the CO₂ adsorption in variable temperature and humidity conditions, the model based on reaction kinetics of CO₂ and amines as presented in Eqs. (10)–(15) was used. As described in Section 2.2, the CO₂ adsorption rate equations were integrated to find the equilibrium capacities of CO₂, and the model was fitted to humid isotherm data of CO₂.

Fig. 3 shows the experimental humid CO₂ isotherms and the fit of the 5-parameter co-adsorption model of Eqs. (10)–(13). Overall, the 5-parameter model captures the temperature- and humidity dependency of the data well. The best fits to experimental data are obtained at 1 vol-% H₂O, with the modelled isotherms being very close to the experimental points. At 2 vol-%, some divergence from experimental data is shown especially in the low partial pressure region, with the model underestimating the capacity. At 25 °C,

19.9 mbar H₂O and 0.39 mbar CO₂, the experimental CO₂ capacity is 0.875 mmol_{CO₂}/g_{sorbent} and the model value is 0.827 mmol_{CO₂}/g_{sorbent}. With 0.2 vol-% H₂O the isotherm fit diverges more from the experimental data especially at 25 °C by overestimating the capacity below 0.001 bar and underestimating it above this partial pressure. The experimental CO₂ capacity at 25 °C at 0.4 mbar CO₂ and 1.7 mbar H₂O is 0.572 mmol_{CO₂}/g_{sorbent} while the model estimate is 0.632 mmol_{CO₂}/g_{sorbent}. Therefore, in DAC conditions at 25 °C, the model leads to a higher relative error of 10.5% at 0.2 vol-% H₂O vs. 5.5% at 2 vol-% H₂O.

To find whether the model fit to isotherm data could be improved, a 7-parameter model given by Eqs. (12)–(15) was used, where the exponents of the available amine site concentration are fitted parameters t_1 and t_2 instead of based on reaction stoichiometry as in the 5-parameter model. By letting the exponent parameters vary freely in the fitting procedure, it was expected that these parameters would increase, thus increasing the order of the model and explaining the data better. Fig. 4 shows the fit obtained with the 7-parameter co-adsorption model with relaxed boundaries of parameters t_1 and t_2 . It is obvious that the model describes the experimental data excellently with the fitted exponential parameters of $t_1 = 10.56$ and $t_2 = 14.42$.

A variation of the 7-parameter model where the upper boundaries of the exponent parameters were set to 3 was also fitted to experimental data. This was done to limit the computational effort that could be expected to increase with high values of the exponential parameters. The fitted exponential parameters were found to be optimum at their upper limits, resulting in $t_1 = t_2 = 3$. Fig. S3 shows that while not yielding an almost perfect fit like the model with relaxed boundaries (Fig. 4), setting the upper boundaries of t_1 and t_2 to 3 resulted in a much better fit than with the 5-parameter model. Only at 25 °C with 0.2 vol-% H₂O at CO₂ partial pressures higher than 0.002 bar can the model be observed to significantly diverge from the experimental isotherm. Therefore, it seems that increased reaction order of the co-adsorption model also leads to a better fit of the isotherm data.

All the co-adsorption model-fit parameters are given in Table 3. Comparing the 5-parameter model maximum capacity of free

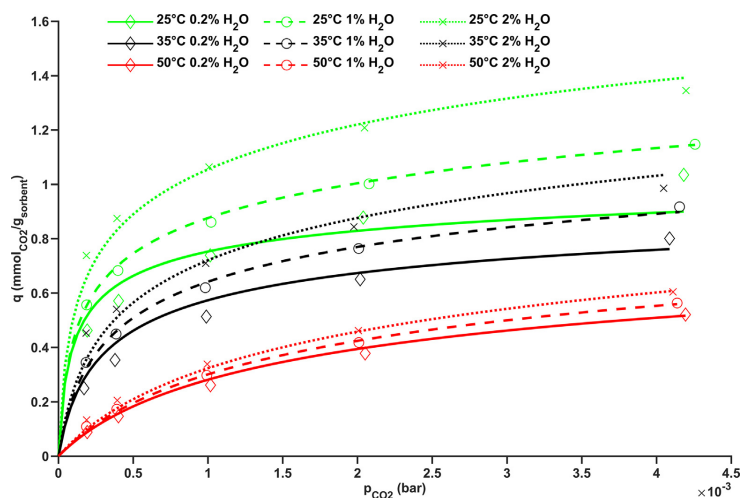


Fig. 3. Experimental (markers) and modelled (lines) CO_2 isotherms using the 5-parameter co-adsorption model.

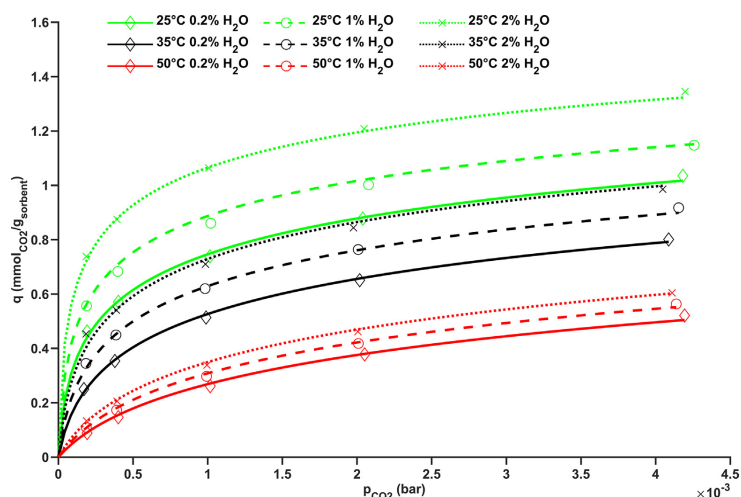


Fig. 4. Experimental (markers) and modelled (lines) CO_2 isotherms using the 7-parameter co-adsorption model with relaxed upper boundaries for parameters t_1 and t_2 .

amine sites q_m of $1.91 \text{ mmol}_{\text{amine}}/\text{g}_{\text{sorbent}}$ to the amine content $4.72 \text{ mmol}_{\text{N}}/\text{g}_{\text{sorbent}}$ of the resin (Elfving et al., 2017) imparts that around 40% of the total amine capacity is available for CO_2 . The 7-parameter model values for q_m are higher, and it is not deducible from the current data how accurately this parameter represents the value of free amine sites available for CO_2 capture. The isosteric heats of adsorption for the reactions in dry and humid conditions are $82\text{--}98 \text{ kJ}/\text{mol}_{\text{CO}_2}$ and $112\text{--}127 \text{ kJ}/\text{mol}_{\text{CO}_2}$, respectively. The values for the humid reactions are higher, which is not expected if comparing the net reaction enthalpies of hydronium carbamate or bicarbonate and ammonium carbamate pathways (Li et al.,

2016). However, (Miller et al., 2020) observed that while ammonium carbamate has a higher binding energy than hydronium carbamate, the hydrated form of hydronium carbamate has a binding energy higher than that of ammonium carbamate. Also, (Yu and Chuang, 2017) suggested the formation of hydrogen-bonded water/ammonium carbamate in humid CO_2 adsorption conditions on a TEPA film, which has a higher binding energy than ammonium carbamate. Comparing the values with literature, the isosteric heats of adsorption in reaction pathway 2 are somewhat high compared to other results for CO_2 capture on supported amines, such as $62\text{--}68 \text{ kJ}/\text{mol}_{\text{CO}_2}$ for the aminoresin in this study using the Toth

Table 3
Parameters of the kinetic co-adsorption models in isotherm data fitting.

Model	q_m (mmol _{amine} /g _{adsorbent})	$b_{0,1}$ (bar ⁻¹ (mol/kg) ^{1-t1})	$b_{0,2}$ (bar ⁻² (mol/kg) ^{1-t2})	t_1	t_2	$-\Delta H_1$ (kJ/mol)	$-\Delta H_2$ (kJ/mol)	$k_{t,1}^a$ (bar ⁻¹ s ⁻¹ (mol/kg) ^{1-t1})	$k_{t,2}^a$ (bar ⁻² s ⁻¹ (mol/kg) ^{1-t2})
5-parameter	1.91	3.199E+03	7.461E+04	2	1	98.0	111.5	1	1
7-parameter	2.61	4.200E+02	2.540E+04	3 ^b	3 ^b	85.0	123.4	1	1
7-parameter	6.98	9.224E-06	7.372E-07	10.56	14.42	81.7	126.7	1	1

^a Parameter value fixed.

^b Parameter upper boundary fixed to 3.

model (Elfving et al., 2017), 87 kJ/mol_{CO2} for Lewatit VP OC 1065 (Veneman et al., 2015), 73 kJ/mol_{CO2} for NFC functionalized with aminosilane (Gebald, 2014) and around 90 kJ/mol_{CO2} for primary or secondary amine-containing SBA-15 (Alkhabbaz et al., 2014). The isosteric heats of adsorption from the co-adsorption models were used in the fixed-bed model heat balances to account for the adsorption heat of CO₂ from both ammonium carbamate and bicarbonate or hydronium carbamate formation.

It should be noted that the high values of t_1 and t_2 gained from the fitting of the 7-parameter model are probably not physically justified. It is known that amine-functionalized adsorbents are complex systems with multiple presented reaction pathways between CO₂, H₂O and amines as discussed in the introduction. In supported amine adsorbents, energetically different CO₂ adsorption sites can exist due to different amine groups and the hydrocarbon chains and groups linked to them (Alkhabbaz et al., 2014; Lee et al., 2018). However, there is no data on the current adsorbent to support the resulting high reaction orders of over 10. Especially, it can be deduced that in the case of the 7-parameter model, the resulting fitted t_1 and t_2 values do not represent the stoichiometry of the system. Therefore, the physicality of the exponent parameters in the case of the 7-parameter model fits is questionable, especially when no limits are set for these parameters.

The CO₂ capacity results gained from the lab-scale experiments and those given by the derived kinetic models exceed the results gained from pilot-scale experiments with the same adsorbent in real humid atmospheric conditions (Vidal Vázquez et al., 2018; Ruuskanen et al., 2021; Bajamundi et al., 2019). For example, during the DAC device performance campaigns the amount of adsorbed CO₂ varied between 0.5 and 0.7 mmol_{CO2}/g_{adsorbent}, while temperature and relative humidity varied in the range of 15–20 °C and 39–78% (Bajamundi et al., 2019). However, the amount of pure CO₂ produced was only around 0.2–0.3 mmol_{CO2}/g_{adsorbent}. This is due to incomplete regeneration of the resin in pilot-scale experiments using temperature-vacuum swing adsorption (TVSA) with desorption at around 80 °C. In dry laboratory-scale tests, this regeneration method (closed TVSA) was found to produce incomplete regeneration even at 100 °C (Elfving et al., 2021). In the pilot-scale experiments, TVSA was followed by a short temperature swing by flowing air through the hot beds leading to more desorbed but uncollected CO₂, which explains why the pilot-scale adsorption results are higher than the amounts produced. However, this TS-step was still not enough to completely regenerate the adsorbent due to low temperature, short desorption time and the presence of CO₂ in the feed. Therefore, to compare the capacities gained using the current model parameters to results gained in real ambient conditions with the same aminoresin, a more complete regeneration of the resin beds via use of, e.g., TVSA with steam stripping (Stampi-Bombelli et al., 2020; Sinha et al., 2017) or inert purge would be required.

3.4. Fixed-bed modelling of co-adsorption

To evaluate how well the kinetic co-adsorption model of CO₂ can be used to simulate adsorption column dynamics, the 5-

parameter and 7-parameter co-adsorption models as well as the single-component H₂O GAB isotherm model were used in the source terms of the fixed-bed model described in Section 2.3. Here, the 7-parameter model with $t_1 = t_2 = 3$ was used in addition to the 5-parameter model in the fixed-bed data fitting.

Fig. 5 shows the results of the fixed-bed model fit to experimental data using the 5-parameter co-adsorption model. As seen in Fig. 5a, the CO₂ breakthrough profiles can be roughly divided into three regions: 1) the initial period of fast adsorption before and just after breakthrough with no increase or slow increase of CO₂ concentration; 2) a region of roughly linear concentration increase; 3) a region where adsorption slows down significantly, and the CO₂ concentration increases very slowly towards the feed concentration. The slowed-down kinetics may be due to CO₂ slowly reaching amine sites that are less easily accessed within the adsorbent pores, which become more hindered as more CO₂ is adsorbed. On the other hand, the resin has a fairly moderate amine loading of 4.7 mmol_N/g_{adsorbent} (Elfving et al., 2017) and adsorption of CO₂ on the aminoresin is clearly more equilibrium-controlled than diffusion-controlled such as in highly-loaded materials (Sayari et al., 2016; Goepfert et al., 2011). Another reason for the slowed-down kinetics than hindered amine sites may lie in the particle size distribution, with bigger particles taking longer to saturate than particles with a size close to the median of 0.6 mm (Elfving et al., 2017) or smaller.

Fig. 5a shows that at 25 °C in each humidity case, the model shows immediate breakthrough, while the experimental breakthrough times are between 10 and 13 min. After the initial period, the simulated CO₂ breakthrough curve at 0.2 vol-% H₂O shows a significantly delayed increase at around 23–60 min, while the other simulated curves follow the experimental data well. The result is expected due to the overestimation of the CO₂ adsorption capacity at 0.2 vol-% H₂O by the 5-parameter model (see Fig. 3). Also, in the last kinetic region, the simulated breakthrough curves in 0.2 vol-% and 2 vol-% H₂O cases reach the inlet concentration too early. However, at 1 vol-% H₂O, the model is also able to simulate the slowly increasing region with good accuracy, as shown in Fig. 54a.

Fig. 5b shows that the H₂O concentrations increase to near the inlet concentration in under 20 min, even at the lowest level of humidity. After one hour, there is very little change in the breakthrough profiles. It seems that the H₂O desorption isotherm coupled with the empty adsorption column model (see Fig. S2) underestimates the H₂O adsorption capacity at the lowest humidity content. Otherwise, the simulated H₂O breakthrough curves follow the experimental data well.

Fig. 5c shows that the magnitude of temperature increase is heavily dependent on the humidity content, and that this difference is well represented by the co-adsorption fixed-bed model. Experimental and simulated peak temperatures in the 2 vol-% case are around 35.5–35.7 °C, while in the 0.2 vol-% case, these are only around 26.5–27 °C. A 5–7 times higher temperature increase in the highest compared to lowest humidity content suggests that most of the released heat results from H₂O adsorption rather than CO₂ adsorption. After all, the CO₂ capacity is only around

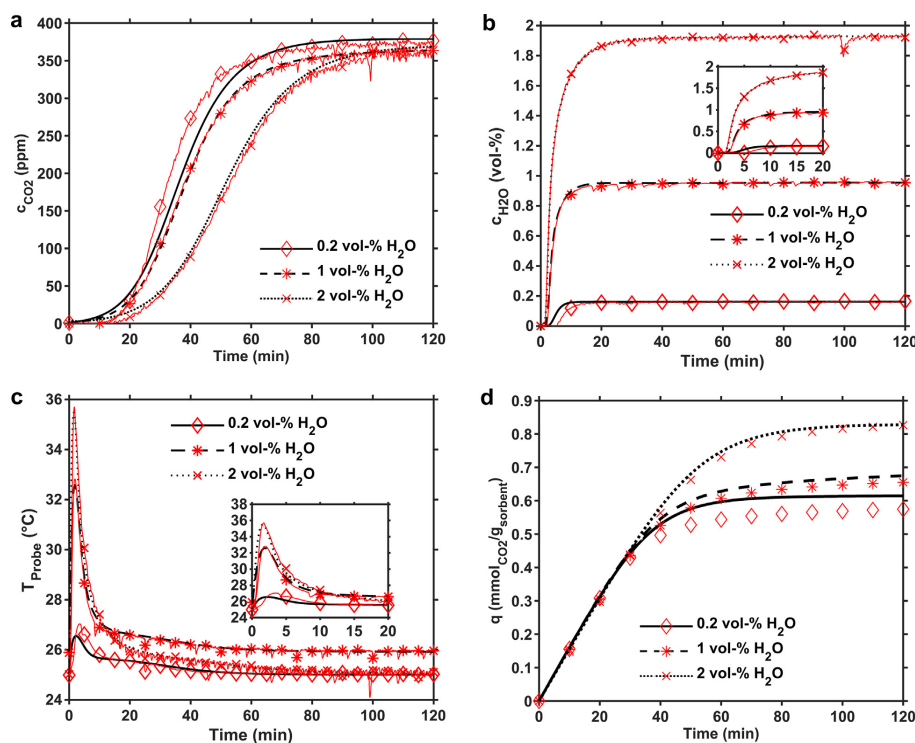


Fig. 5. Experimental (thin lines with markers) and simulated (lines) a) CO₂ breakthrough profiles; b) H₂O breakthrough profiles; c) bed temperature from probe 1 cm into the bed; d) CO₂ adsorption capacities from the first two hours of adsorption with initial bed temperature of 25 °C. For the 1 vol-% H₂O experiment, the initial bed temperature was 26 °C. The 5-parameter co-adsorption model was used to model CO₂ adsorption kinetics. The total flow rate was 500 ml/min. Inserts in b) and c) show the shape of the H₂O breakthrough curves and temperature from the first 20 min of the adsorption phase.

0.3 mmol_{CO₂}/g_{sorbent} higher at 2 vol-% than at 0.2 vol-% H₂O, while the H₂O capacity is higher by over 3.5 mmol_{CO₂}/g_{sorbent}. Also, as the heats of adsorption for the humid CO₂ adsorption reaction (Table 3) are comparable to the dry reaction heats of adsorption, the released heat per mole of adsorbed CO₂ is not significantly higher in humid vs. dry conditions. After the peak temperatures are reached, the decreasing temperature trends are also similar in simulated and experimental data. As the temperature changes are linked to the changes in H₂O concentration, the changes take place mostly in the first 20 min, therefore only affecting the initial region of CO₂ adsorption.

Fig. 5d shows that the dynamic CO₂ capacities appear similar until around 26–30 min, when the curves start to diverge. After this point, as expected from the CO₂ breakthrough profiles, the simulated CO₂ capacity curves of 0.2 vol-% and 2 vol-% cases reach their maximum values too early. In the 2 vol-% H₂O case, the simulated CO₂ capacity is around 0.83 mmol_{CO₂}/g_{sorbent} at 120 min, after which practically no change is predicted. However, the experimental adsorption capacity continues to increase slowly up to 0.86 mmol_{CO₂}/g_{sorbent} at five hours of adsorption. It should be taken into account that the experimental adsorption capacity curves were calculated via integration of the experimental breakthrough profiles, while the simulated capacity curves were calculated by co-

adsorption models based on desorption capacities. Therefore, these capacity curves are never exactly the same.

Fig. 6a shows that at 35 °C, the simulated breakthrough curves follow the overall shape of the experimental curves closely for both 1 vol-% and 2 vol-% humidity cases. As in the 25 °C case, the model curves show immediate breakthrough, but the experimental breakthrough times are around 6–7 min. The initial kinetic region is better approximated by the model in the 2 vol-% case. However, the middle kinetic region is very closely followed by the model in both cases. In the region of slow adsorption rate (the upper part of the curve), the model slightly overestimates the concentration at first in both cases. However, the differences are only a few ppm or less.

Fig. 6b shows that the simulated H₂O breakthrough curves are again close to the experimental ones in the 1 and 2 vol-% H₂O cases. The breakthrough times are similar in simulated and experimental curves, all being close to 1 min. At around 6–30 min, a drop in H₂O concentration in the experimental data is visible, the reason for which is discussed in the Supplementary Data. As expected from the lower H₂O capacities at higher temperature and lower relative humidity, the temperature peaks are around 2–3 °C smaller than in the 25 °C case as shown in Fig. 6c. The experimental and simulated peak temperatures are around 40 °C at 1 vol-% H₂O and 42.5–43.5 °C at 2 vol-% H₂O.

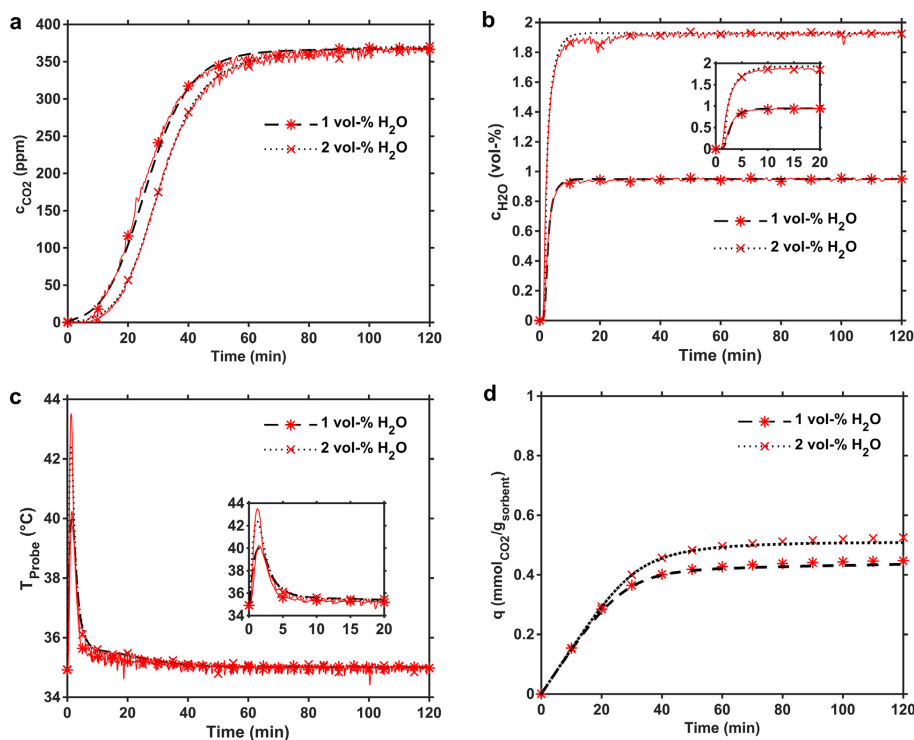


Fig. 6. Experimental (thin lines with markers) and simulated (lines) a) CO₂ breakthrough profiles; b) H₂O breakthrough profiles; c) bed temperature from probe 1 cm into the bed; d) CO₂ adsorption capacities from the first two hours of adsorption with initial bed temperature of 35 °C. The 5-parameter co-adsorption model was used to model CO₂ adsorption kinetics. The total flow rate was 500 ml/min. Inserts in b) and c) show the shape of the H₂O breakthrough curves and temperature from the first 20 min of the adsorption phase.

Fig. 6d shows that at 35 °C, the capacity profiles of 1 and 2 vol-% humidity cases start to diverge roughly 10 min from the start, with the model predictions following the experimental adsorption capacities closely for the first 120 min. However, similarly as to the case in a 25 °C setting, the model fails to predict the slowly increasing capacity trend after 120 min in the 2 vol-% H₂O case at 35 °C. However, in the 1 vol-% H₂O case, the modelled capacity increases gradually for the total duration of the experiment. The reason for these differences between humidity levels is apparent from the 5-parameter co-adsorption model fit (Fig. 3), where at each temperature the CO₂ capacity in DAC conditions (0.4 mbar CO₂) was best represented at 1 vol-% humidity.

To compare the adsorption rates, the experimental adsorption rates calculated from the first 30 min of adsorption are approximately 0.87 and 0.88 mmol_{CO2}/(g_{sorbent}·h) at 1 and 2 vol-% H₂O at 25 °C, and 0.73 and 0.80 mmol_{CO2}/(g_{sorbent}·h) at 1 and 2 vol-% H₂O at 35 °C, respectively. If calculated from the first 60 min of adsorption, the values are 0.61 and 0.73 mmol_{CO2}/(g_{sorbent}·h) at 1 and 2 vol-% H₂O at 25 °C, and 0.43 and 0.50 mmol_{CO2}/(g_{sorbent}·h) at 1 and 2 vol-% H₂O at 35 °C, respectively. Therefore, lower temperature and higher humidity content improve the CO₂ adsorption rate due to higher equilibrium adsorption capacity. Hahn et al., 2015 found that at levels of humidity content above 5 vol-%, the adsorption kinetics were retarded due to formation of water film

around the adsorbent, thus limiting diffusion. Based on the results above, this might not be the case in DAC conditions, although studying CO₂ adsorption near 100% relative humidity is warranted.

Although the experimental dynamic adsorption data was mostly described well by the simulations using the 5-parameter model as discussed above, it is also clear that the shortcomings of the 5-parameter model in modelling of the CO₂ adsorption capacity translated into inaccuracies in the dynamic model. This can be deduced because the H₂O and temperature profiles were predicted well by the simulation and because the changes mostly took place before significant changes in CO₂ concentration started, as was shown above. Also, the worst CO₂ breakthrough simulations occurred when the CO₂ capacity was severely under- or overpredicted by the model. Thus, it could be expected that an improved co-adsorption model, that fits the isotherm data better than the 5-parameter model, should also yield a more accurate simulation of the adsorption process when used in the fixed-bed model. To this end, the 7-parameter co-adsorption model with $t_1 = t_2 = 3$ (Fig. S3) was used in the fixed-bed model.

Fig. 7 shows an overall better simulation of the CO₂ breakthrough with the 7-parameter model compared to using the 5-parameter model. Fig. 7a shows that the 7-parameter co-adsorption model improves the fit of the simulated CO₂ breakthrough curves, especially in the 0.2 vol-% H₂O case. At 0.2 vol-%

H₂O, the second kinetic region between 23 and 52 min is now closely represented by the model. In the slow adsorption region after 52 min, the model shows early saturation at 0.2 vol-%, but at 1 and 2 vol-% this region is also well represented by the model (also see Fig. S4). This is a clear improvement from using the 5-parameter co-adsorption model, which led to early saturation at 2 vol-% humidity. This is also seen in the capacity curves in Fig. 7b, where capacity in the 2 vol-% case keeps increasing after 120 min. Compared to the 5-parameter model results at 2 vol-% H₂O and 25 °C, where practically no change was observed after two hours, the simulated capacity here still increases from around 0.86 mmol_{CO2}/g_{sorbent} at two hours to almost 0.88 mmol_{CO2}/g_{sorbent} at five hours.

To find the effect of flow rate on the CO₂ adsorption process, a nearly 2-day adsorption from humidified compressed air was done using a low flow rate (100 ml/min). Fig. 8 shows the experimental and simulated results of this run using the 5-parameter and 7-parameter ($t_1 = t_2 = 3$) kinetic models in the fixed-bed model. As shown in Fig. 8a, the CO₂ breakthrough ($c_{CO_2}/c_{CO_2,feed} > 0.01$) is well predicted by both models, and occurs at 192–194 min in the experiment and at around 180–190 min in the simulations. In the second kinetic region using the 7-parameter model, a significant divergence of the simulated breakthrough curve from the experimental curve is seen after around 230 min. On the other hand, both simulated curves reach saturation too early, being at 401 ppm after around 14 h of adsorption, while the experimental concentration is around 395 ppm at this point.

By the time CO₂ breakthrough occurs, the experimental H₂O profile is almost at the inlet H₂O concentration as shown in Fig. 8b. Overall, the simulated H₂O curve represents the experimental profile well, although the feed concentration is reached somewhat early. The differences between the simulated and experimental H₂O breakthrough curves are only a few hundred ppm at highest, and their effect on CO₂ adsorption dynamics can be assumed negligible. The magnitude of temperature increase is captured well by the simulations as shown in Fig. 8c, where both the experimental and simulated probe temperatures reach a peak of around 28.5 °C. The figure also shows an interesting shape of the temperature profile not clearly seen in the 500 ml/min experiments. At around 80–280 min, a shoulder appears with a temperature of 25.1–25.2 °C before cooling down to 24.9 °C. The cause of this shoulder is evident when comparing it with the CO₂ breakthrough data, imparting that this delay in cooling is caused by the heat released from the adsorption of CO₂.

The difference between the experimental and simulated adsorption capacities in the 2-day run can be seen from Fig. 8d. It is clear that both models underpredict the experimental pseudo-equilibrium capacity of 0.92 mmol_{CO2}/g_{sorbent}, which is probably the main reason why the simulated CO₂ breakthrough profiles represented the slow kinetic region poorly. However, it is notable here that although the 7-parameter co-adsorption model gives a closer estimation of the pseudo-equilibrium CO₂ capacity, the breakthrough curves fitted using this model are worse than by using the 5-parameter model. This is contrary to the results found for the 500 ml/min cases, and imparts that the 7-parameter model does not necessarily give a better estimation of the adsorption kinetics, although the isotherm fit is significantly improved compared to the 5-parameter model. On the other hand, in the case of the 7-parameter model, the selection of the upper boundary for the exponential parameters during isotherm fitting was arbitrary, and it should be assessed in more detail how these affect the performance of the model in different hydrodynamic conditions. However, as flow rate affects the mass transfer resistances in CO₂ adsorption, the reason for the worse performance of both models in the low flow rate case may in part be caused by the lack of separate diffusional models for CO₂. This will be discussed in more detail later in the text.

In terms of the CO₂ breakthrough curve shape and challenges in simulating the slow approach to feed concentration encountered with each of the models, similar observations have been reported in the literature. Bollini et al. (2012) found the LDF kinetic model combined with the Toth isotherm insufficient to describe CO₂ adsorption kinetics on adsorbents with high amine loadings. Better results were obtained by using a heterogeneous model that takes into account two diffusion mechanisms in the adsorbent: fast diffusion in the pores and slow diffusion in the aminopolymer phase. However, even with this heterogeneous model their results showed premature saturation, failing to represent the upper part of the CO₂ breakthrough curve. Serna-Guerrero and Sayari (2010) used the Toth isotherm model and Avrami kinetic model for CO₂ adsorption in dry flue-gas conditions on amine-grafted silica. Their simulation also shows an excessively fast approach of saturation in some experiments, although they attributed this to experimental error rather than actual kinetic behaviour. Jung and Lee (2020) used a reaction mechanism-based kinetic model such as in this work to simulate the CO₂ adsorption breakthrough curves in humid flue gas conditions on PEI-functionalized silica. Also in their

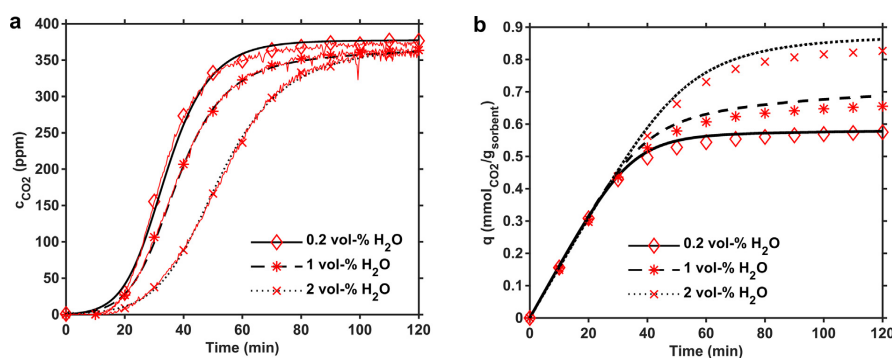


Fig. 7. Experimental (thin lines with markers) and simulated (lines) a) CO₂ breakthrough profiles; b) CO₂ adsorption capacities from the first two hours of adsorption. The 7-parameter co-adsorption model with $t_1 = t_2 = 3$ was used to model CO₂ adsorption kinetics. The total flow rate was 500 ml/min. Initial bed temperature was 25 °C, except for 1 vol-% H₂O experiment where it was 26 °C.

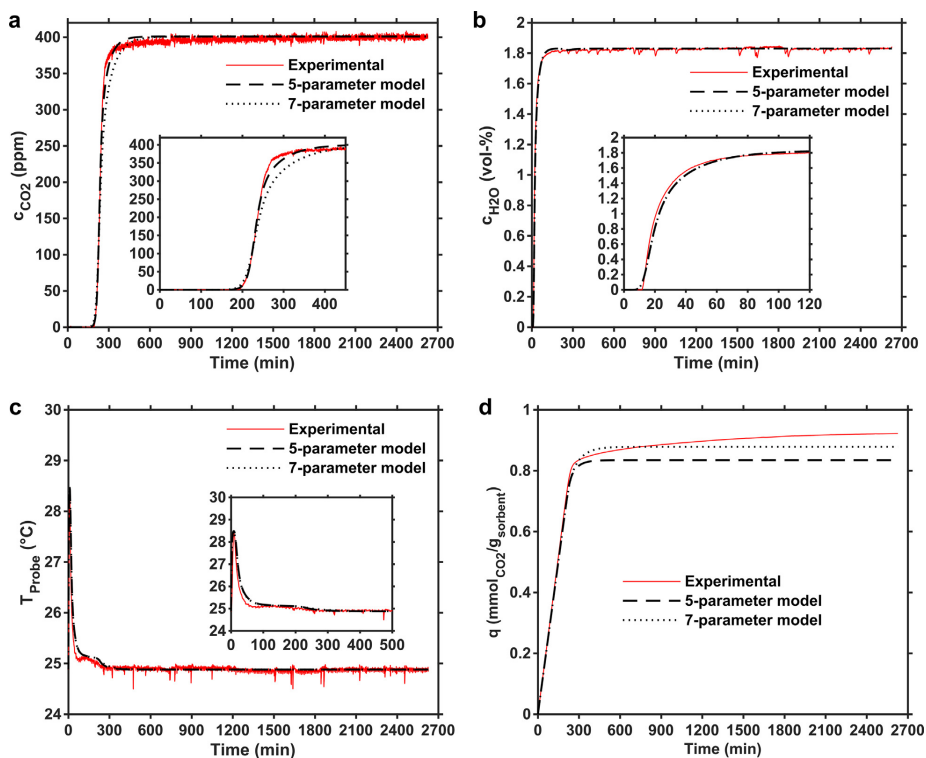


Fig. 8. Experimental (thin lines with markers) and simulated (lines) a) CO₂ breakthrough profiles; b) H₂O breakthrough profiles; c) bed temperature from probe 1 cm into the bed; d) CO₂ adsorption capacities with a flow rate of 100 ml/min and initial bed temperature of 25 °C. In the 7-parameter co-adsorption model $t_1 = t_2 = 3$.

work, the simulations often seemed to show early increase of the CO₂ concentration to feed conditions compared to experimental data, although the difference did not seem pronounced.

Since the concentration of adsorbate affects the velocity of the concentration fronts and the shape of the breakthrough curves, the best reference data for this study would be acquired under DAC conditions. Even though DAC on supported amine adsorbents has been simulated in several studies (Wurzbacher et al., 2016; Stampi-Bombelli et al., 2020; Sinha et al., 2017; Darunte et al., 2019), comparisons of fixed-bed models to experimental data are rare, especially under humid conditions. Darunte et al. (2019) reported the modelling of CO₂ adsorption on diamine-functionalized Mg₂(dobpdc) MOF adsorbent, which had an interesting isotherm shape requiring splitting of both the isotherm model and the kinetic regions into two parts. By combining LDF and Avrami models, they simulated the CO₂ breakthrough profiles in dry DAC conditions, exhibiting a comparison to experimental data. However, due to the peculiar shape of the CO₂ isotherms and breakthrough curves, their results are difficult to compare with those observed with typical type-1 or Langmuir-shape isotherms. Stampi-Bombelli et al. (2020) found somewhat good representation by their fixed-bed model prediction of the CO₂ adsorption breakthrough curve in humid DAC conditions using the modified Toth isotherm and the LDF kinetic model. However, due to use of

a very flat-shaped adsorbent bed with a height-to-width ratio of 1/8, the shape of the breakthrough curve was very different from those reported in this work, making it difficult to make any comparisons of the kinetics.

The CO₂ adsorption simulations in DAC (Wurzbacher et al., 2016; Stampi-Bombelli et al., 2020; Sinha et al., 2017; Darunte et al., 2019) or PCC conditions (Bollini et al., 2012; Shafeeyan et al., 2014; Haghpanah et al., 2013) typically rely on the use of separate isotherm and kinetic models. Although the most important aspect of the current kinetic approach is the ability to model the effect of humidity on CO₂ adsorption, this approach may also lead to other advantages over the conventional approach with separate isotherm and kinetic models. To study these differences, a comparison was made between the Toth isotherm coupled with the LDF kinetic model and the kinetic approach of the current work, which can be found in the Supplementary Data. Fig. S6 shows that while the differences are fairly small, the 5-parameter and 7-parameter models give a better prediction of the overall shape of the CO₂ breakthrough curve, especially when the model capacity prediction matches the experimental one. Additionally, the 5-parameter and 7-parameter models have comparable computational times with the Toth + LDF model. While higher-order kinetic models such as the Avrami model may give a better representation of the breakthrough curve than the LDF model, they can

be expected to lead to higher computational effort. Further, given that more complex isotherm models are required to take humidity into account like the 5/7-parameter models do, thus further increasing the computational cost, the kinetic approach presented in the current work also seems numerically more advantageous compared to using separate models for equilibrium and kinetics. In the conventional approach, an improved kinetic model such as the Avrami model, and an isotherm model taking humidity into account, also come with additional uncertainty related to the additional parameters required.

The best-fit parameters of the fixed-bed model are given in Table 4. The kinetic parameter $k_{f,2}$ increases compared to $k_{f,1}$ with humidity, which could result from shift to bicarbonate or hydronium carbamate formation as humidity content increases. Additionally, the $k_{f,2}$ parameter is lower at 35 °C at both 1 and 2 vol-% H₂O. The decreased value of the $k_{f,2}$ parameter is probably related to retarded adsorption reaction kinetics rather than mass transfer, since higher temperature should increase mass transfer. This is observed in the case of the Toth + LDF model fit, where the LDF kinetic parameter is higher at 35 °C compared to 25 °C. However, it should be taken into account that the kinetic parameters for the three models are apparent rather than intrinsic, combining all the mass transfer resistances as well as CO₂ adsorption reaction kinetics.

The $k_{f,1}$ and $k_{f,2}$ values in the 500 ml/min case are not identical to those in the 100 ml/min case at 25 °C, while these should be constant with flow rate if the parameters only described adsorption reaction kinetics and intraparticle diffusion. While intraparticle diffusion and the adsorption reaction kinetics are not affected by hydrodynamic conditions such as flow rate (Ruthven, 1984), the external fluid film resistance can be expected to be much higher in the 100 ml/min experiment compared to the 500 ml/min experiments. Therefore, the results impart that external fluid film resistance around the adsorbent particle has a significant effect on the kinetics at least in the studied conditions. Therefore, in addition to the proposed co-adsorption models, a more accurate and generalized treatment of the adsorption kinetics requires addi-

tional models that take into account the diffusion of CO₂ in the adsorbent particle. This includes diffusion through the external film of the particle and intraparticle diffusion. Of these, the film mass transfer is probably more important, but it should also be assessed if diffusional resistances inside the particle can be neglected or not, such as in Bos et al. (Bos et al., 2019).

Other limitations related to the models and the experimental device also existed, which should be taken into account when comparing the parameters in Table 4. The adsorption column only had one temperature probe, and therefore it was not possible to record axial distribution of temperature, which could affect the adsorption rate in the fixed-bed. The estimated value of the K_s parameter was typically near its initial value, which was 2 W/(m·K) in all of the data fittings. To find the true temperature distribution and its effect on the adsorption process, experimental data would be required from several points along the column in the axial direction. Moreover, the way that the effect of the empty volume on the H₂O material balance is taken into account (see Section 2.3) increases the released heat, affecting the overall heat transfer coefficients represented by h . In this work, only the adsorbent bed was simulated, but in future work, a detailed model of the dead volume in the experimental device should be included. Also, in the 100 ml/min case, both kinetic models yielded lower CO₂ adsorption capacities than determined experimentally, which also had an effect on the dynamic model fit and thus the kinetic parameters.

The overall shape of CO₂ adsorption breakthrough curves was simulated well by the 5/7-parameter models used in this work. When the pseudo-equilibrium isotherm points were close to the model values, even the upper part of the breakthrough curve was closely represented. However, when using a low flow rate of 100 ml/min leading to extended adsorption time, difficulties arose in reproducing the shape of the entire breakthrough curve. The co-adsorption model equilibrium parameters were obtained by fitting to pseudo-equilibrium isotherms rather than true equilibrium data. The kinetic parameters of the co-adsorption models, $k_{f,1}$ and $k_{f,2}$, were obtained by fitting the dynamic model to CO₂ breakthrough data, without separately taking into account diffusional

Table 4

Parameters of the fixed-bed model fits at different temperatures, humidities and flow rates. The axial dispersion coefficient was calculated by using a correlation, while all the other listed parameters were fitted.

Case and CO ₂ adsorption model	D_t (m ² /s)	$k_{f,1}$ (bar ⁻² s ⁻¹ (mol/kg) ^{1+τ_1}) ^a	$k_{f,2}$ (bar ⁻² s ⁻¹ (mol/kg) ^{1+τ_2})	$k_{H_2O,LDF}$ (1/s)	K_s (Wm ⁻¹ K ⁻¹)	h (Wm ⁻² K ⁻¹)
0.2 vol-% H ₂ O 25 °C 5 parameter model	3.50E-04	1.37	1.71	0.99	1.74	17.78
1 vol-% H ₂ O 26 °C 5 parameter model	3.50E-04	1.48	12.67	0.38	2.12	10.51
2 vol-% H ₂ O 25 °C 5 parameter model	3.50E-04	0.92	58.74	0.22	2.10	17.34
1 vol-% H ₂ O 35 °C 5 parameter model	3.52E-04	1.35	2.06	0.26	1.96	19.65
2 vol-% H ₂ O 35 °C 5 parameter model	3.51E-04	1.78	14.54	0.88	1.96	36.25
0.2 vol-% H ₂ O 25 °C 7 parameter model ($\tau_1 = \tau_2 = 3$)	3.50E-04	0.35	2.33	1.22	1.96	11.87
1 vol-% H ₂ O 26 °C 7 parameter model ($\tau_1 = \tau_2 = 3$)	3.50E-04	0.32	4.94	0.39	2.0	10.13
2 vol-% H ₂ O 25 °C 7 parameter model ($\tau_1 = \tau_2 = 3$)	3.50E-04	0.20	8.53	0.20	2.10	18.90
2 vol-% H ₂ O 35 °C 7 parameter model ($\tau_1 = \tau_2 = 3$)	3.51E-04	0.45	3.57	1.60	3.12	33.12
2 vol-% H ₂ O 25 °C, 100 ml/min 5 parameter model	7.44E-05	3.81	30.25	0.11	2.03	18.13
2 vol-% H ₂ O 25 °C, 100 ml/min 7 parameter model ($\tau_1 = \tau_2 = 3$)	7.44E-05	0.69	5.03	0.10	2.10	18.59
2 vol-% H ₂ O 25 °C Toth + LDF	3.50E-04	0.0012 s ⁻¹	–	0.29	1.86	16.67
2 vol-% H ₂ O 35 °C Toth + LDF	3.51E-04	0.0018 s ⁻¹	–	0.20	1.89	30.13

^a For Toth + LDF, the LDF kinetic constant reported.

resistances in the adsorbent particle. Therefore, perfect simulation of the breakthrough curves for very long adsorption runs would probably require true equilibrium isotherms determined from adsorption capacities measured for several days, and possibly a separate model of CO₂ diffusion in the adsorbent. On the other hand, one may argue that adsorption steps lasting several days instead of several hours would not be economically viable, as an optimized DAC process is most likely operated with much shorter cycles. Therefore, the strong representation of the experimental fixed-bed data in this work already warrants the use of these co-adsorption models in simulation of humid DAC to study the dynamics of CO₂ adsorption and the related specific energy requirement.

4. Conclusions

In this work, CO₂ adsorption from air was simulated by using a kinetic model which takes into account the effect of humidity, the study of which has been all but neglected in scientific literature so far. Pseudo-equilibrium CO₂ isotherms in humid conditions with partial pressures of CO₂ and H₂O relevant to DAC were measured experimentally at 25–50 °C on an amine-functionalized resin. The kinetic co-adsorption model based on reaction mechanisms of CO₂ with amines in dry and humid conditions was used to calculate the equilibrium CO₂ capacities and fitted to the experimental isotherm data. To account for the adsorption of humidity, the temperature-dependent GAB model was fitted to experimental single-component H₂O isotherms. The co-adsorption model accounting for CO₂ adsorption kinetics and the GAB model coupled with the linear driving force model describing H₂O adsorption kinetics were then used in a dynamic non-isothermal model. This model was fitted against experimental CO₂ and H₂O breakthrough curves and adsorption column temperature in DAC conditions. A humid cyclic adsorption/desorption experiment was also done to find the capacity drop rate.

In the cyclic experiment, a CO₂ capacity drop of approximately 0.7%/cycle was measured, which necessitated the correction of experimental isotherm data to account for the drop in capacity. The H₂O isotherms were well approximated by the GAB isotherm with multilayer H₂O adsorption behavior. In all studied CO₂ partial pressures and temperatures, increased humidity content led to an increase in CO₂ capacity. This phenomenon was captured well by the proposed kinetic co-adsorption model, of which three variations with different reaction orders were used. The 5-parameter model with reaction order based on reaction stoichiometry gave an overall good fit to the isotherms, but at the lowest humidity content of 0.2 vol-% led to overprediction of the CO₂ capacity at partial pressures lower than 0.001 bar. The so-called 7-parameter model with a higher but arbitrary reaction order yielded an almost perfect fit to the isotherm data. In fitting the fixed-bed model to dynamic experimental data, the simulated breakthrough curves and adsorption column temperature were close to the experimental ones. It was found that the accuracy of the CO₂ isotherm fit given by the kinetic co-adsorption model significantly affected the accuracy of the simulated CO₂ breakthrough curves. Using the 7-parameter kinetic model in the dynamic model also yielded close representation of the whole CO₂ breakthrough profile in cases where the 5-parameter model failed.

The present work used pseudo-equilibrium CO₂ isotherm data from several-hour experiments and used the co-adsorption models directly to model the kinetics of CO₂ adsorption without separately accounting for the effect of diffusional resistances in the adsorbent particle. Possibly due to these reasons, at a lower flow rate of 100 ml/min, the fixed-bed model fit represented the CO₂ breakthrough time well but failed to simulate the long, slowly increasing

upper part of the concentration profile. Therefore, for determining mass-transfer parameters valid for scale-up, the effect of diffusional resistances in the adsorbent particle should be assessed in future studies. To realistically account for heat transfer in different bed shapes, 2-D simulation coupled with temperature measurement from several points in axial and radial directions should be used. To include desorption, the current parameters of the co-adsorption kinetic models may be used as a first estimate, but for more accurate simulation of CO₂ production, adsorption capacities measured at higher partial pressures of CO₂ should also be included in the isotherm fitting.

Nevertheless, even in the current form, 1-D fixed-bed adsorption simulation with the proposed co-adsorption kinetic models help assess critical parameters of CO₂ adsorption in humid DAC conditions such as adsorption rate and specific energy requirement in different conditions. Moreover, based on a preliminary comparison, using the proposed models to simulate CO₂ adsorption kinetics instead of separate isotherm and kinetic models can yield both improved accuracy and numerical advantage. For purposes of scaling up, the proposed kinetic models can be combined with existing mass-transfer models. Thus, the presented co-adsorption models are expected to be generally useful in the modelling of CO₂ adsorption kinetics on amine-functionalized adsorbents.

CRedit authorship contribution statement

Jere Elfving: Conceptualization, Methodology, Software, Validation, Formal analysis, Investigation, Data curation, Writing - original draft, Writing - review & editing, Visualization, Project administration, Funding acquisition. **Tuomo Sainio:** Methodology, Writing - review & editing, Supervision.

Declaration of Competing Interest

The authors declare that they have no known competing financial interests or personal relationships that could have appeared to influence the work reported in this paper.

Acknowledgements

This study was conducted as a part of the DAC2.0 project funded by the Academy of Finland under grant number 329312.

The authors would also like to thank Dr. Harri Nieminen for his useful comments on the manuscript.

Appendix A. Supplementary material

Supplementary data to this article can be found online at <https://doi.org/10.1016/j.ces.2021.116885>.

References

- Coninck, H., Revi, A., Babiker, M., Bertoldi, P., Buckeridge, M., Cartwright, A., Dong, W., Ford, J., Fuss, S., Hourcade, J.-C., Ley, D., Mechler, R., Newman, P., Revokatova, A., Schultz, S., Steg, L., Sugiyama, T., 2018. IPCC special report - Global warming of 1.5 °C: Chapter 4 - Strengthening and implementing the global response. https://www.ipcc.ch/site/assets/uploads/sites/2/2019/05/SR15_Chapter4_Low_Res.pdf.
- Sanz-Pérez, E.S., Murdock, C.R., Didas, S.A., Jones, C.W., 2016. Direct capture of CO₂ from ambient air. *Chem. Rev.* 116, 11840–11876. <https://doi.org/10.1021/acs.chemrev.6b00173>.
- de Jonge, M.M.J., Daemen, J., Loriaux, J.M., Steinmann, Z.J.N., Huijbregts, M.A.J., 2019. Life cycle carbon efficiency of direct air capture systems with strong hydroxide sorbents. *Int. J. Greenh. Gas Control.* 80, 25–31. <https://doi.org/10.1016/j.ijggc.2018.11.011>.
- Deutz, S., Bardow, A., 2021. Life-cycle assessment of an industrial direct air capture process based on temperature-vacuum swing adsorption. *Nat. Energy.* 6, 203–213. <https://doi.org/10.1038/s41560-020-00771-9>.

- Breyer, C., Fasih, M., Bajamundi, C., Creutzig, F., 2019. Direct air capture of CO₂: A key technology for ambitious climate change mitigation. *Joule*, 3, 2053–2057. <https://doi.org/10.1016/j.joule.2019.08.010>.
- Fuss, S., Lamb, W.F., Callaghan, M.W., Hilaire, J., Creutzig, F., Amann, T., Beringer, T., De Oliveira Garcia, V., Hartmann, J., Khanna, T., Luderer, G., Nemet, G.F., Rogelj, J., Smith, P., Vicente, J.L.V., Wilcox, J., Del Mar Zamora Dominguez, M., Minx, J.C., 2018. Negative emissions - Part 2: Costs, potentials and side effects. *Environ. Res. Lett.* 13. <https://doi.org/10.1088/1748-9326/aabf9f> 063002.
- Vidal Vázquez, F., Koponen, J., Ruuskanen, V., Bajamundi, C., Kosonen, A., Simell, P., Ahola, J., Frilund, C., Elfving, J., Reinikainen, M., Heikkinen, N., Kauppinen, J., Piermartini, P., 2018. Power-to-X technology using renewable electricity and carbon dioxide from ambient air: SOLETAIR proof-of-concept and improved process concept. *J. CO₂ Util.* 28, 235–246. <https://doi.org/10.1016/j.jcou.2018.09.026>.
- Rodríguez-Mosqueda, R., Rutgers, J., Bramer, E.A., Brem, G., 2019. Low temperature water vapor pressure swing for the regeneration of adsorbents for CO₂ enrichment in greenhouses via direct air capture. *J. CO₂ Util.* 29, 65–73. <https://doi.org/10.1016/j.jcou.2018.11.010>.
- Ruuskanen, V., Givirovsky, G., Elfving, J., Kokkonen, P., Karvinen, A., Järvinen, L., Sillman, J., Vainikka, M., Ahola, J., 2021. Neo-Carbon Food concept: A pilot-scale hybrid biological–inorganic system with direct air capture of carbon dioxide. *J. Clean. Prod.* 278. <https://doi.org/10.1016/j.jclepro.2020.123423> 123423.
- Keith, D.W., Holmes, G., St Angelo, D., Heidel, K., 2018. A process for capturing CO₂ from the atmosphere. *Joule* 2, 1573–1594. <https://doi.org/10.1016/j.joule.2018.05.006>.
- Fasih, M., Efimova, O., Breyer, C., 2019. Techno-economic assessment of CO₂ direct air capture plants. *J. Clean. Prod.* 224, 957–980. <https://doi.org/10.1016/j.jclepro.2019.03.086>.
- Shi, X., Li, Q., Wang, T., Lackner, K.S., 2017. Kinetic analysis of an anion exchange adsorbent for CO₂ capture from ambient air. *PLoS One*, 12, 1–12. <https://doi.org/10.1371/journal.pone.0179828>.
- Van Der Giesen, C., Meinenken, C.J., Kleijn, R., Sprecher, B., Lackner, K.S., Kramer, G., 2017. A life-cycle assessment case study of coal-fired electricity generation with humidity swing direct air capture of CO₂ versus mea-based postcombustion capture. *Environ. Sci. Technol.* 51, 1024–1034. <https://doi.org/10.1021/acs.est.6b05028>.
- Bajamundi, C.J.E., Koponen, J., Ruuskanen, V., Elfving, J., Kosonen, A., Kauppinen, J., Ahola, J., 2019. Capturing CO₂ from air: Technical performance and process control improvement. *J. CO₂ Util.* 30, 232–239. <https://doi.org/10.1016/j.jcou.2019.02.002>.
- Wurzbacher, J.A., Gebald, C., Brunner, S., Steinfeld, A., 2016. Heat and mass transfer of temperature-vacuum swing desorption for CO₂ capture from air. *Chem. Eng. J.* 283, 1329–1338. <https://doi.org/10.1016/j.cej.2015.08.035>.
- ClimeWorks, 2021. "CO₂ removal." (2021). <https://www.climeWorks.com> (accessed June 10, 2021).
- Shi, X., Xiao, H., Azarabadi, H., Song, J., Wu, X., Chen, X., Lackner, K.S., 2020. Sorbents for the direct capture of CO₂ from ambient air. *Angew. Chemie - Int. Ed.* 59, 6984–7006. <https://doi.org/10.1002/anie.201906756>.
- Drechsler, C., Agar, D.W., 2020. Investigation of water co-adsorption on the energy balance of solid sorbent based direct air capture processes. *Energy*, 192. <https://doi.org/10.1016/j.energy.2019.116587> 116587.
- Veneman, R., Natalia, F., Wenyang, Z., Zhenhan, L., Sascha, K., Brilman, W., 2015. Adsorption of H₂O and CO₂ on supported amine sorbents. *Int. J. Greenh. Gas Control*, 41, 268–275. <https://doi.org/http://dx.doi.org/10.1016/j.ijggc.2015.07.014>.
- Gebald, C., Wurzbacher, J.A., Borgschulte, A., Zimmermann, T., Steinfeld, A., 2014. Single-component and binary CO₂ and H₂O adsorption of amine-functionalized cellulose. *Environ. Sci. Technol.* 48, 2497–2504. <https://doi.org/10.1021/es40439g>.
- Jahandar Lashaki, M., Khiavi, S., Sayari, A., 2019. Stability of amine-functionalized CO₂ adsorbents: A multifaceted puzzle. *Chem. Soc. Rev.* 48, 3320–3405. <https://doi.org/10.1039/c8cs00877a>.
- Choi, S., Drese, J.H., Jones, C.W., 2009. Adsorbent materials for carbon dioxide capture from large anthropogenic point sources. *ChemSusChem* 2, 796–854. <https://doi.org/10.1002/cssc.200900036>.
- Li, K., Kress, J.D., Mebane, D.S., 2016. The mechanism of CO₂ adsorption under dry and humid conditions in mesoporous silica-supported amine sorbents. *J. Phys. Chem. C* 120, 23683–23691. <https://doi.org/10.1021/acs.jpcc.6b08808>.
- Lee, J.J., Chen, C.H., Shimon, D., Hayes, S.E., Sievers, C., Jones, C.W., 2017. Effect of humidity on the CO₂ adsorption of tertiary amine grafted SBA-15. *J. Phys. Chem. C* 121, 23480–23487. <https://doi.org/10.1021/acs.jpcc.7b07930>.
- Didas, S.A., Sakwa-Novak, M.A., Foo, G.S., Sievers, C., Jones, C.W., 2014. Effect of amine surface coverage on the co-adsorption of CO₂ and water: spectral deconvolution of adsorbed species. *J. Phys. Chem. Lett.* 5, 4194–4200. <https://doi.org/10.1021/jz502032c>.
- Chen, C.H., Shimon, D., Lee, J.J., Mentink-Vigier, F., Hung, I., Sievers, C., Jones, C.W., Hayes, S.E., 2018. The "missing" bicarbonate in CO₂ chemisorption reactions on solid amine sorbents. *J. Am. Chem. Soc.* 140, 8648–8651. <https://doi.org/10.1021/jacs.8b04520>.
- Hahn, M.W., Steib, M., Jentys, A., Lercher, J.A., 2015. Mechanism and kinetics of CO₂ adsorption on surface bonded amines. *J. Phys. Chem. C* 119, 4126–4135. <https://doi.org/10.1021/jp512001t>.
- Yu, J., Chuang, S.S.C., 2017. The role of water in CO₂ capture by amine. *Ind. Eng. Chem. Res.* 56, 6337–6347. <https://doi.org/10.1021/acs.iecr.7b00715>.
- Sayari, A., Liu, Q., Mishra, P., 2016. Enhanced adsorption efficiency through materials design for direct air capture over supported polyethylenimine. *ChemSusChem* 9, 2796–2803. <https://doi.org/10.1002/cssc.201600834>.
- Kumar, D.R., Rosu, C., Suján, A.R., Sakwa-Novak, M.A., Ping, E.W., Jones, C.W., 2020. Alkyl-aryl amine-rich molecules for CO₂ removal via direct air capture. *ACS Sustain. Chem. Eng.* 8, 10971–10982. <https://doi.org/10.1021/acscuschemeng.0c03706>.
- Elfving, J., Bajamundi, C., Kauppinen, J., Sainio, T., 2017. Modelling of equilibrium working capacity of PSA, TSA and TVSA processes for CO₂ adsorption under direct air capture conditions. *J. CO₂ Util.* 22, 270–277. <https://doi.org/10.1016/j.jcou.2017.10.010>.
- Goepfert, A., Czaun, M., May, R.B., Prakash, G.K.S., Olah, G.A., Narayanan, S.R., 2011. Carbon dioxide capture from the air using a polyamine based regenerable solid adsorbent. *J. Am. Chem. Soc.* 133, 20164–20167. <https://doi.org/10.1021/ja2100005>.
- Wang, J., Huang, H., Wang, M., Yao, L., Qiao, W., Long, D., Ling, L., 2015. Direct capture of low-concentration CO₂ on mesoporous carbon-supported solid amine adsorbents at ambient temperature. *Ind. Eng. Chem. Res.* 54, 5319–5327. <https://doi.org/10.1021/acs.iecr.5b01060>.
- Suján, A.R., Pang, S.H., Zhu, G., Jones, C.W., Lively, R.P., 2019. Direct CO₂ capture from air using poly(ethylenimine)-loaded polymer/silica fiber sorbents. *ACS Sustain. Chem. Eng.* 7, 5264–5273. <https://doi.org/10.1021/acscuschemeng.8b06203>.
- Qi, G., Fu, L., Giannelis, E.P., 2014. Sponges with covalently tethered amines for high-efficiency carbon capture. *Nat. Commun.* 5, 1–7. <https://doi.org/10.1038/ncomms6796>.
- Si, W., Ye, S., Zhang, D., Yang, B., Hou, Y., Li, Z., Zhang, X., Zhu, J., Lei, L., 2019. Kinetics and mechanism of low-concentration CO₂ adsorption on solid amine in a humid confined space. *Can. J. Chem. Eng.* 97, 697–701. <https://doi.org/10.1002/cjce.23257>.
- Kolle, J.M., Fayaz, M., Sayari, A. Understanding the effect of water on CO₂ adsorption (accepted). *Chem. Rev. Article ASAP*. <https://doi.org/10.1021/acs.chemrev.0c00762>.
- Wang, Z., Goyal, N., Liu, L., Tsang, D.C.W., Shang, J., Liu, W., Li, G., 2020. N-doped porous carbon derived from polypyrrole for CO₂ capture from humid flue gases. *Chem. Eng. J.* 396. <https://doi.org/10.1016/j.cej.2020.125376> 125376.
- Stampi-Bombelli, V., van der Spek, M., Mazzotti, M., 2020. Analysis of direct capture of CO₂ from ambient air via steam-assisted temperature–vacuum swing adsorption. *Adsorption* 26, 1183–1197. <https://doi.org/10.1007/s10450-020-00249-w>.
- Jung, W., Lee, K.S., 2020. Isotherm and kinetics modeling of simultaneous CO₂ and H₂O adsorption on an amine-functionalized solid sorbent. *J. Nat. Gas Sci. Eng.* 84. <https://doi.org/10.1016/j.jngse.2020.103489> 103489.
- Elfving, J., Kauppinen, J., Jegoroff, M., Ruuskanen, V., Järvinen, L., Sainio, T., 2021. Experimental comparison of regeneration methods for CO₂ concentration from air using amine-based adsorbent. *Chem. Eng. J.* 404. <https://doi.org/10.1016/j.cej.2020.126337> 126337.
- Elfving, J., Bajamundi, C., Kauppinen, J., 2017. Characterization and performance of direct air capture sorbent. *Energy Procedia*, 114, 6087–6101. <https://doi.org/10.1016/j.egypro.2017.03.1746>.
- Do, D.D., 1998. *Adsorption analysis: Equilibria and kinetics*. Imperial College Press.
- Serna-Guerrero, R., Belmakhout, Y., Sayari, A., 2010. Modeling CO₂ adsorption on amine-functionalized mesoporous silica: 1. A semi-empirical equilibrium model. *Chem. Eng. J.* 161, 173–181. <https://doi.org/10.1016/j.cej.2010.04.024>.
- Wang, Y., LeVan, M.D., 2009. Adsorption equilibrium of carbon dioxide and water vapor on zeolites 5A and 13X. *J. Chem. Eng. Data*, 54, 2839–2844. <https://doi.org/10.1021/je800900a>.
- Qasem, N.A.A., Ben-Mansour, R., 2018. Adsorption breakthrough and cycling stability of carbon dioxide separation from CO₂/N₂/H₂O mixture under ambient conditions using 13X and Mg-MOF-74. *Appl. Energy*, 230, 1093–1107. <https://doi.org/10.1016/j.apenergy.2018.09.069>.
- Sultan, M., El-Sharkawy, I.I., Miyazaki, T., Saha, B.B., Koyama, S., Maruyama, T., Maeda, S., Nakamura, T., 2015. Insights of water vapor sorption onto polymer based sorbents. *Adsorption*, 21, 205–215. <https://doi.org/10.1007/s10450-015-9663-y>.
- Quirjns, E.J., Van Bortel, A.J.B., Van Loon, W.K.P., Van Straten, G., 2005. Sorption isotherms, GAB parameters and isosteric heat of sorption. *J. Sci. Food Agric.* 85, 1805–1814. <https://doi.org/10.1002/jsfa.2140>.
- Sonnleitner, E., Schöny, G., Hofbauer, H., 2018. Assessment of zeolite 13X and Lewatit® VP OC 1065 for application in a continuous temperature swing adsorption process for biogas upgrading. *Biomass Convers. Biorefinery*, 8, 379–395. <https://doi.org/10.1007/s13399-017-0293-3>.
- Bollini, P., Brunelli, N.A., Didas, S.A., Jones, C.W., 2012. Dynamics of CO₂ adsorption on amine adsorbents. 1. Impact of heat effects. *Ind. Eng. Chem. Res.* 51, 15145–15152. <https://doi.org/10.1021/ie301790a>.
- Shafeeyan, M.S., Daud, W.M.A.W., Shamiri, A., 2014. A review of mathematical modeling of fixed-bed columns for carbon dioxide adsorption. *Chem. Eng. Res. Des.* 92, 961–988. <https://doi.org/10.1016/j.cherd.2013.08.018>.
- Haghpahan, R., Majumder, A., Nilam, R., Rajendran, A., Farooq, S., Karimi, I.A., Amanullah, M., 2013. Multiobjective optimization of a four-step adsorption process for postcombustion CO₂ capture via finite volume simulation. *Ind. Eng. Chem. Res.* 52, 4249–4265. <https://doi.org/10.1021/ie302658y>.
- Rastegar, S.O., Gu, T., 2017. Empirical correlations for axial dispersion coefficient and Peclet number in fixed-bed columns. *J. Chromatogr. A* 1490, 133–137. <https://doi.org/10.1016/j.chroma.2017.02.026>.

- Sircar, S., Hufton, J.R., 2000. Why does the linear driving force model for adsorption kinetics work? *Adsorption*. 6, 137–147. <https://doi.org/10.1023/A:1008965317983>.
- Farooq, S., Ruthven, D.M., 1990. Heat effects in adsorption column dynamics. 2. Experimental validation of the one-dimensional model. *Ind. Eng. Chem. Res.* 29, 1084–1090. <https://doi.org/10.1021/ie00102a020>.
- Miller, D.D., Yu, J., Chuang, S.S.C., 2020. Unraveling the structure and binding energy of adsorbed CO₂/H₂O on amine sorbents. *J. Phys. Chem. C* 124, 24677–24689. <https://doi.org/10.1021/acs.jpcc.0c04942>.
- Alkhabbaz, M.A., Bollini, P., Foo, G.S., Sievers, C., Jones, C.W., 2014. Important roles of enthalpic and entropic contributions to CO₂ capture from simulated flue gas and ambient air using mesoporous silica grafted amines. *J. Am. Chem. Soc.* 136, 13170–13173. <https://doi.org/10.1021/ja507655x>.
- Lee, J.J., Yoo, C.J., Chen, C.H., Hayes, S.E., Sievers, C., Jones, C.W., 2018. Silica-supported sterically hindered amines for CO₂ capture. *Langmuir*. 34, 12279–12292. <https://doi.org/10.1021/acs.langmuir.8b02472>.
- Sinha, A., Darunte, L.A., Jones, C.W., Realf, M.J., Kawajiri, Y., 2017. Systems design and economic analysis of direct air capture of CO₂ through temperature vacuum swing adsorption using MIL-101(Cr)-PEI-800 and mmen-Mg₂(dobpdc) MOF adsorbents. *Ind. Eng. Chem. Res.* 56, 750–764. <https://doi.org/10.1021/acs.iecr.6b03887>.
- Bollini, P., Brunelli, N.A., Didas, S.A., Jones, C.W., 2012. Dynamics of CO₂ adsorption on amine adsorbents. 2. Insights into adsorbent design. *Ind. Eng. Chem. Res.* 51, 15153–15162. <https://doi.org/10.1021/ie3017913>.
- Serna-Guerrero, R., Sayari, A., 2010. Modeling adsorption of CO₂ on amine-functionalized mesoporous silica. 2: Kinetics and breakthrough curves. *Chem. Eng. J.* 161, 182–190. <https://doi.org/10.1016/j.cej.2010.04.042>.
- Darunte, L.A., Sen, T., Bhawanani, C., Walton, K.S., Sholl, D.S., Realf, M.J., Jones, C.W., 2019. Moving beyond adsorption capacity in design of adsorbents for CO₂ capture from ultradilute feeds: Kinetics of CO₂ adsorption in materials with stepped isotherms. *Ind. Eng. Chem. Res.* 58, 366–377. <https://doi.org/10.1021/acs.iecr.8b05042>.
- Ruthven, D.M., 1984. *Principles of adsorption and adsorption processes*. Wiley.
- Bos, M.J., Kreuger, T., Kersten, S.R.A., Brilman, D.W.F., 2019. Study on transport phenomena and intrinsic kinetics for CO₂ adsorption in solid amine sorbent. *Chem. Eng. J.* 377. <https://doi.org/10.1016/j.cej.2018.11.072> 120374.

ACTA UNIVERSITATIS LAPPEENRANTAENSIS

966. YANCHUKOVICH, ALEXEI. Screening the critical locations of a fatigue-loaded welded structure using the energy-based approach. 2021. Diss.
967. PETROW, HENRI. Simulation and characterization of a front-end ASIC for gaseous muon detectors. 2021. Diss.
968. DONOGHUE, ILKKA. The role of Smart Connected Product-Service Systems in creating sustainable business ecosystems. 2021. Diss.
969. PIKKARAINEN, ARI. Development of learning methodology of additive manufacturing for mechanical engineering students in higher education. 2021. Diss.
970. HOFFER GARCÉS, ALVARO ERNESTO. Submersible permanent-magnet synchronous machine with a stainless core and unequal teeth widths. 2021. Diss.
971. PENTTILÄ, SAKARI. Utilizing an artificial neural network to feedback-control gas metal arc welding process parameters. 2021. Diss.
972. KESSE, MARTIN APPIAH. Artificial intelligence : a modern approach to increasing productivity and improving weld quality in TIG welding. 2021. Diss.
973. MUSONA, JACKSON. Sustainable entrepreneurial processes in bottom-of-the-pyramid settings. 2021. Diss.
974. NYAMEKYE, PATRICIA. Life cycle cost-driven design for additive manufacturing: the frontier to sustainable manufacturing in laser-based powder bed fusion. 2021. Diss.
975. SALWIN, MARIUSZ. Design of Product-Service Systems in printing industry. 2021. Diss.
976. YU, XINXIN. Contact modelling in multibody applications. 2021. Diss.
977. EL WALI, MOHAMMAD. Sustainability of phosphorus supply chain – circular economy approach. 2021. Diss.
978. PEÑALBA-AGUIRREZABALAGA, CARMELA. Marketing-specific intellectual capital: Conceptualisation, measurement and performance. 2021. Diss.
979. TOTH, ILONA. Thriving in modern knowledge work: Personal resources and challenging job demands as drivers for engagement at work. 2021. Diss.
980. UZHEGOVA, MARIA. Responsible business practices in internationalized SMEs. 2021. Diss.
981. JAISWAL, SURAJ. Coupling multibody dynamics and hydraulic actuators for indirect Kalman filtering and real-time simulation. 2021. Diss.
982. CLAUDELIN, ANNA. Climate change mitigation potential of Finnish households through consumption changes. 2021. Diss.
983. BOZORGMEHRI, BABAK. Finite element formulations for nonlinear beam problems based on the absolute nodal coordinate formulation. 2021. Diss.
984. BOGDANOV, DMITRII. Transition towards optimal renewable energy systems for sustainable development. 2021. Diss.
985. SALTAN, ANDREY. Revealing the state of software-as-a-service pricing. 2021. Diss.

986. FÖHR, JARNO. Raw material supply and its influence on profitability and life-cycle assessment of torrefied pellet production in Finland – Experiences from pilot-scale production. 2021. Diss.
987. MORTAZAVI, SINA. Mechanisms for fostering inclusive innovation at the base of the pyramid for community empowerment - Empirical evidence from the public and private sector. 2021. Diss.
988. CAMPOSANO, JOSÉ CARLOS. Integrating information systems across organizations in the construction industry. 2021. Diss.
989. LAUKALA, TEIJA. Controlling particle morphology in the in-situ formation of precipitated calcium carbonate-fiber composites. 2021. Diss.
990. SILLMAN, JANI. Decoupling protein production from agricultural land use. 2021. Diss.
991. KHADIM, QASIM. Multibody system dynamics driven product processes. 2021. Diss.
992. ABDULKAREEM, MARIAM. Environmental sustainability of geopolymer composites. 2021. Diss.
993. FAROQUE, ANISUR. Prior experience, entrepreneurial outcomes and decision making in internationalization. 2021. Diss.
994. URBANI, MICHELE. Maintenance policies optimization in the Industry 4.0 paradigm. 2021. Diss.
995. LAITINEN, VILLE. Laser powder bed fusion for the manufacture of Ni-Mn-Ga magnetic shape memory alloy actuators. 2021. Diss.
996. PITKÄOJA, ANTTI. Analysis of sorption-enhanced gasification for production of synthetic biofuels from solid biomass. 2021. Diss.
997. MASHLAKOV, ALEKSEI. Flexibility aggregation of local energy systems—interconnecting, forecasting, and scheduling. 2021. Diss.
998. NIKITIN, ALEKSEI. Microwave processes in thin-film multiferroic heterostructures and magnonic crystals. 2021. Diss.
999. VIITALA, MIRKA. The heterogeneous nature of microplastics and the subsequent impacts on reported microplastic concentrations. 2021. Diss.
1000. ASEMOKHA, AGNES. Understanding business model change in international entrepreneurial firms. 2021. Diss.
1001. MUSTO, JIRI. Improving the quality of user-generated content. 2021. Diss.
1002. INKERI, EERO. Modelling of component dynamics and system integration in power-to-gas process. 2021. Diss.
1003. GARIFULLIN, AZAT. Deep Bayesian approach to eye fundus image segmentation. 2021. Diss.



ISBN 978-952-335-764-8
ISBN 978-952-335-765-5 (PDF)
ISSN-L 1456-4491
ISSN 1456-4491
Lappeenranta 2021